UNIVERSITÀ DEGLI STUDI DELL'INSUBRIA

Dipartimento di Scienza e Alta Tecnologia- DiSAT

PhD in physics and astrophysics

XXXVIII cycle

Oriented crystals: an innovative approach to electromagnetic calorimetry

---

Author:
Alessia Selmi

Supervisors:
Prof.ssa Michela Prest
Università degli Studi dell'Insubria

Dott. Erik Vallazza
INFN–Sezione di Milano Bicocca

CONTENTS

INTRODUCTION

Calorimeters play a crucial role in high-energy, nuclear, and astroparticle physics. Originally developed for the study of cosmic rays, they have evolved substantially over the years: conceived primarily to measure the energy of electrons, photons, and hadrons, they now fulfill multiple tasks that make them fundamental detectors in modern experiments.
Many high-energy and astroparticle experiments rely on high-resolution, homogeneous electromagnetic calorimeters based on scintillating crystals, in which the energy of the incident particle is determined by detecting the scintillation light produced by the electromagnetic shower it initiates. Despite the central role of crystals in homogeneous calorimeters, the influence of the crystalline lattice, and its orientation, on the characteristics of the electromagnetic shower development is typically ignored.
An innovative approach to electromagnetic calorimetry is the use of oriented crystals. Depending on the orientation of the crystalline lattice with respect to the incident particle trajectory, the crystal can appear either as an amorphous medium or as an ordered array of lattice planes or atomic strings. In the latter case, the features of the electromagnetic processes are strongly modified. The particle experiences an effective electromagnetic field generated by the coherent sum of the contributions of many atoms, giving rise to phenomena that depend on the particle energy and incidence angles.
The dependence of the electromagnetic interactions on the crystal orientation has been hypothesized since the beginning of the XX century. The first comprehensive theoretical treatment of the interaction of charged particles in oriented crystals was given by Lindhard who demonstrated that when a charged particle trajectory is aligned within a small angle to the crystallographic planes or axes, the particle transverse motion becomes bound by the continuous potential, and it follows a periodic motion inside the lattice, i.e. the particle is channeled. The periodicity of the particle motion modifies the features of the electromagnetic processes inside the crystal: both photon emission by charged particles and pair production by photons in oriented crystals differ substantially from the corresponding processes in amorphous media.
The features of the channeling radiation depend strongly on the particle energy; at high energies (tens of GeV and above), the nearly constant and extremely intense lattice field acting on the particle, leads to an enhancement of the bremsstrahlung and pair production cross sections and thus to an enhancement of the electromagnetic shower development. The first experimental investigation of such strong field induced enhancement of the radiation emission in an oriented inorganic scintillator was performed only recently and provided the foundation for the R&D of the first prototype of a homogeneous electromagnetic calorimeter based on oriented crystals which is the subject of this thesis work.
An overview of the calorimeters used for the energy measurement in high energy physics,

with particular emphasis on homogeneous electromagnetic calorimeters, and a detailed description of the electromagnetic shower development and the detection mechanisms employed in calorimetry are provided in the first chapter.
The second chapter is divided in two parts: the first part summarizes the main features of the crystalline lattice and briefly describes how standard electromagnetic processes are modified in oriented crystals. The second part of the chapter focuses on the recent experimental studies performed on coherent effects in oriented crystals, which provided the basis for the R&D described in this thesis.
This work has been performed in the framework of the ORiEnted calOrimeter (OREO) project[1], with the aim of assembling and characterizing a first homogeneous electromagnetic calorimeter based on oriented lead tungstate ($PbWO_4$) crystals.
OREO consists of a 3×3 matrix of 5 radiation length oriented crystals followed by non-oriented crystals; it is a homogeneous calorimeter with a transverse segmentation, a feature that can be exploited to enhance the discrimination between electromagnetically interacting particles and hadrons. In fact, in oriented crystals, the strong coherent field modifies only the electromagnetic processes, while the nuclear interaction length is unaffected by the lattice orientation. Consequently, the development of the electromagnetic shower in the upstream layer is accelerated when it is oriented, whereas hadrons interact similarly in both random and axial orientations.
The R&D of the OREO calorimeter consisted in different steps, performed during the years;

- First, the modification of the features of the electromagnetic shower development has been experimentally investigated in a single $PbWO_4$ crystal. The enhancement in the electromagnetic shower development and thus the reduction of the radiation length has been quantified. Furthermore, an alignment procedure has been standardized to ensure that the crystal is adequately positioned for the beam to impinge along the crystallographic axis. These studies were performed in 2022.

- The second step consisted in demonstrating the possibility of aligning a layer of crystals along the same crystallographic direction. This was performed with two prototypes: a single 3×1 row and a 2×2 matrix of $PbWO_4$ oriented crystals, both coupled to SiPM matrices in two dedicated beamtests in 2023.

- Finally, the OREO calorimeter has been assembled and tested in 2024 over a wide range of energies to study the linearity and the improvement in the energy resolution.

The description of the $PbWO_4$ crystals and the photodetection systems employed during the years in several beamtests performed at CERN, is presented in the third chapter along with the OREO calorimeter design. The second part of the chapter describes the experimental setup employed to investigate the strong field effect and to characterize the OREO calorimeter.
Each of the remaining three chapters presents the experimental results from the analysis of data collected in the beamtests performed at CERN between 2022 and 2024.

1 Istituto Nazionale di Fisica Nucleare - National Institute for Nuclear Physics (INFN) CSNV, National Scientific Committee V and since 2024, part of subtask 1.3.4 within the DRD Calo Collaboration at CERN [1].

The preliminary study of the beam characteristics, the characterization of the detectors in the experimental setup, a brief description of the CERN beamtest facility where the data have been collected, and the Geant4 simulation employed in the analysis are presented in the appendices.

1

CALORIMETRY FOR ENERGY MEASUREMENTS IN PARTICLE PHYSICS

In nuclear and particle physics, calorimetry refers to the detection of particles and the measurement of their properties through the total absorption in a block of instrumented material, called calorimeter. In such a detector, the process of measurement through which the particle properties are determined is destructive[1].

In modern particle physics experiments, calorimeters are designed to fulfill multiple tasks. They measure not only the energy of charged particles but also those of photons and neutral hadrons. They are indispensable for the measurement of particle jets and for the reconstruction of the complete event properties, which can provide indirect detection of neutrinos and their energy through a measurement of the event missing energy. The ability to provide fast signals that are easy to process and to interpret, makes calorimeters central components of the trigger systems in high-energy physics experiments. Calorimeters are also important for the identification of the particle type, using information on the longitudinal and transverse shape of the energy deposit to separate electrons, photons, hadrons and muons.

In the past, calorimeters played a crucial role in many important discoveries, such as the experimental observation of the Higgs boson [2, 3], the discovery of the intermediate vector bosons $W^{\pm}$ and Z^0 [4–6] and the observation of the ν-oscillation effects [7].

Calorimeters exist in a wide variety: the choice of the technology and the detector parameters for a specific application depends on many factors including the nature of the particle, the physics processes under investigation and the available budget.

They can be divided into electromagnetic and hadronic calorimeters, based on the particle type and on the different nature of the involved physical processes. In most collider experiments, electrons and photons are measured in the electromagnetic calorimeter, whereas hadrons and jets are measured using the combined response of the electromagnetic calorimeter and the hadronic calorimeter.

Calorimeters can be furthered classified, according to their construction technique, into sampling and homogeneous calorimeters. In sampling calorimeters the function of absorption and signal generation are performed by different materials: a passive medium, typically a high density material that degrades the shower, and an active medium that generates the signals. On the other hand, in a homogeneous calorimeter the entire volume contributes to the signal: the same material both absorbs the particles and generates the

1 Except for muons, which are not typically fully absorbed in experiment calorimeters.

detector signal. In collider experiments, homogeneous calorimeters are typically used as electromagnetic calorimeters; in non accelerator experiments or in neutrino physics, homogeneous calorimeters, where the sensitive medium can be water or ice, scintillator, a noble liquid or the atmosphere itself, are used to detect both the electromagnetic and hadronic showers.
In general, the detailed design is set by the target energy range and the performance requirements (e.g., resolution, granularity, timing), balanced against overall size, cost, and operating conditions.
The OREO collaboration has assembled a prototype of homogeneous electromagnetic calorimeter based on oriented inorganic scintillator crystals. The physics of the particle interaction with oriented crystals will be presented in the next chapter. In this chapter, the general characteristics of electromagnetic calorimeters are discussed, with particular attention on homogeneous calorimeters. In the first part of the chapter the physics of the electromagnetic shower is described in detail, while the second part is dedicated to the different mechanisms through which the calorimeter signals are generated, both in homogeneous and in sampling calorimeters. Finally, the performance characteristics of homogeneous electromagnetic calorimeters are described.

1.1 THE PHYSICS OF THE ELECTROMAGNETIC SHOWER DEVELOPMENT

To understand the physics of the electromagnetic shower development, it is essential to know how electrons, positrons, and photons interact with matter.
The first part of this section reviews such interaction mechanisms while in the second part a simplified model for the electromagnetic shower development is introduced.

1.1.1 ELECTRONS AND POSITRONS INTERACTION IN MATTER

The energy loss mechanisms for electrons and positrons are governed by the well understood laws of Quantum ElectroDynamics (QED).
Figure 1.1 shows the fractional energy loss per radiation length X_0[2] in lead as a function of the electron or positron energy. At low energy, electrons and positrons primarily lose energy via ionization. Already at energies above 10 MeV the main source of energy loss of electrons and positrons is bremsstrahlung, which is the emission of electromagnetic radiation resulting from the interaction with the electron field generated by the atomic nuclei. The bremsstrahlung theory has been introduced by Bethe and Heitler [9]; the cross section

2 The radiation length X_0 is defined as: (a) the mean distance over which a high-energy electron loses all but 1/e of its energy via bremsstrahlung, and (b) 7/9 of the mean free path for pair production by a high-energy photon (more details in Section 1.2) [8].

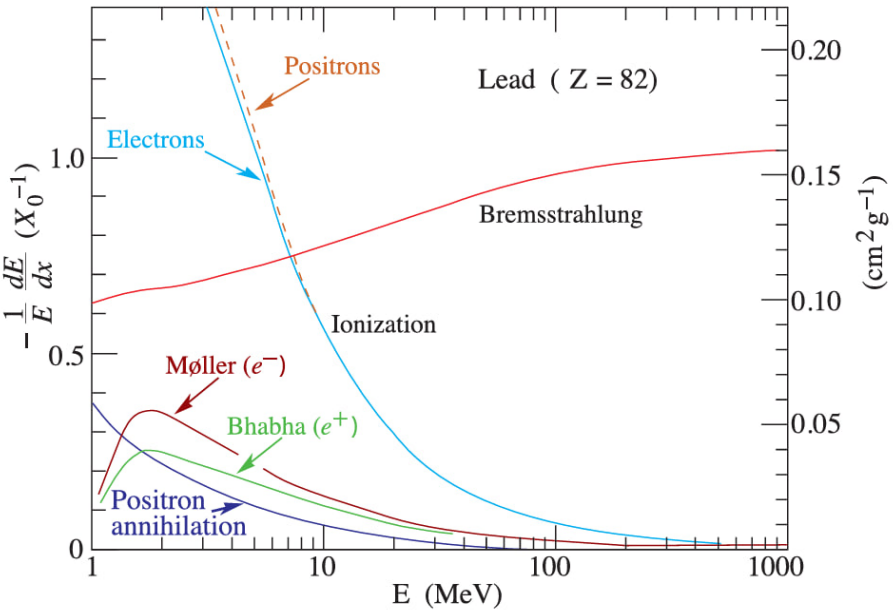

Figure 1.1: Fractional energy loss per radiation length in lead as a function of the electron or positron energy.

for the emission of a photon of energy $\hbar\omega = E_0 - E_1$, $E_1 = E_1(\omega, E_0)$ being the final energy of the parent particle, is:

$$\Phi(\omega; E_0) \propto \alpha\, Z^2 r_p^2 \frac{1}{\hbar\,\omega\, E_0^2}\left[\left(E_0^2 + E_1^2 - \frac{2}{3}E_0E_1\right)\ln\left(\frac{183}{Z^{1/3}}\right) + \frac{E_0E_1}{9}\right]. \tag{1.1}$$

where:

- $\alpha \sim 1/137.036$ is the fine-structure constant [10];
- $r_p \propto 1/(mc^2)^2$ is the classical particle radius. This factor introduces a strong dependence on the particle mass; bremsstrahlung plays a role for any charged particle crossing matter. However, for heavier charged particles such radiative process is suppressed[3].

The cross section is quadratically dependent on the atomic number of the nucleus, Z. The energy spectrum of the radiated photons falls off as $1/\hbar\omega$; it can extend all the way to the energy of the radiating particle, but in general each emitted photon carries only a small fraction of this energy.
In the bremsstrahlung process, the electron (or positron) undergoes a change in direction; this deviation depends on the angle and the energy of the emitted photons, that depend on the strength of the Coulomb field (i.e, the Z of the absorber material). An estimate of the average emission cone aperture angle of the emitted photons is given by $1/\gamma = mc^2/E_0$. This means that the higher the energy of the primary electron (or positron), the smaller the angle at which photons are emitted.
In general, the ionization loss rate varies only logarithmically with the electron energy,

3 For muons, the second lightest particles, the bremsstrahlung cross section is $\sim 1/43000$ of the electron one.

while the energy loss rate via bremsstrahlung is proportional to E_0. The energy at which the two loss rates are equal is defined as the critical energy $E_c = E_c(Z)$. An alternative definition of the critical energy, originally formulated by Rossi [11], defines E_c as the energy at which the ionization per radiation length equals the electron energy:

$$(\Delta E)_{\text{ion}} \mathrm{X}_0 = E_0 \tag{1.2}$$

This definition is equivalent to the first one with the approximation

$$\left[\frac{dE_0}{dx}\right]_{\text{brem}} = \frac{E_0}{\mathrm{X}_0} \tag{1.3}$$

The two definitions are illustrated in the case of copper in Figure 1.2. An estimate of this

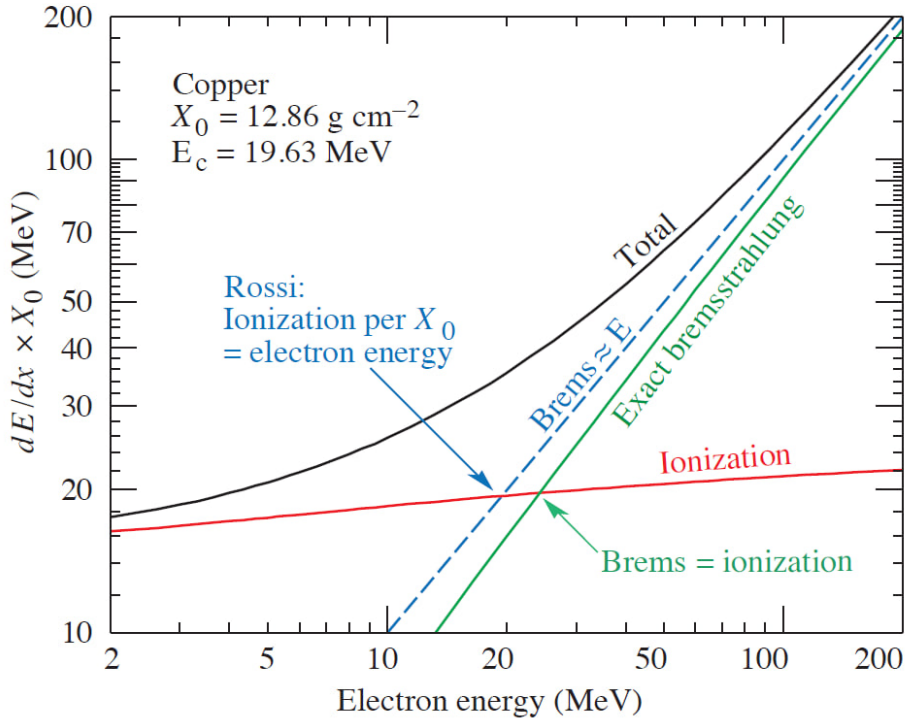

Figure 1.2: The two definitions of the critical energy E_c.

critical energy is given by [8]:

$$E_c = \frac{610(710)\text{MeV}}{Z + 1.24(0.92)} \tag{1.4}$$

for solids (gas). The higher the atomic number of the target, the lower the energy threshold for radiation emission to become dominant.

1.1.1.1 THE RADIATION FORMATION LENGTH

The formation of bremsstrahlung radiation takes a finite time, and hence a finite distance, before a photon emitted by an accelerating electron is fully formed and can propagate freely. In particular, the photon must be separated from the parent electron by at least one wavelength, $\lambda = 2\pi c/\omega$, where ω is the radiation angular frequency. This follows

from the small longitudinal momentum transfer to the scattering center, which, given the Heisenberg uncertainty principle, implies a large uncertainty in the electron longitudinal position.
The distance the parent electron has to travel during the emission of a photon is called the radiation formation length l_f [12]. One way to compute the formation length is to consider the distance required for the emitted photon to be separated from the emitting particle by one reduced wavelength:

$$l_f = \frac{2\gamma^2 c}{\omega} \tag{1.5}$$

As a consequence, higher-energy photons are formed over shorter distances, and hence in a shorter time, whereas more energetic electrons emit a photon having a $\hbar\omega$ energy in a broader space interval.
If the electron dynamics is disturbed within the radiation formation length, the radiation emission process can be altered. In particular, when a charged particle crosses a crystalline lattice, several different coherent mechanisms take place, depending on the energy scale and on the misalignment angle, that alter the radiation emission. Details are provided in Section 2.1.

1.1.2 PHOTONS INTERACTION IN MATTER

Three major possible interaction mechanisms contribute to the energy deposit process by photons in matter: photoelectric effect, incoherent (Compton) scattering and electron-positron pair production.
Photon interactions are fundamentally different from the ones experienced by electrons and positrons; unlike electrons and positrons, which slow down gradually through many small interactions with the atoms of the absorber, photons are either completely absorbed or scattered of a significant angle.
The following section describes the three mechanisms of photons interaction with matter.

1.1.2.1 PHOTOELECTRIC EFFECT

In the photoelectric effect, an atom absorbs a photon and emits an electron with a kinetic energy

$$E_{e^-} = h\nu - E_b \tag{1.6}$$

where E_b is the binding energy of the electron in its original shell (Figure 1.3). For photon energies above a few hundred keV, the photoelectron carries most of the incident photon energy. The atom is left in an excited state with a vacancy and returns to the ground state by emitting characteristic X-rays or Auger electrons, which are monoenergetic electrons produced by the internal absorption of characteristics X-rays by the atom.
The photoelectric cross section scales with Z^n, with $n \approx 4 - 5$. Such strong dependence of the photoelectric absorption probability on the atomic number of the absorber is the reason why high Z materials are preferred for photon detectors such as in γ-ray spectroscopy. The

cross section also scales with the photon energy as $E^{-7/2}$, meaning that the photoelectric effect is the most probable interaction at low photon energies.

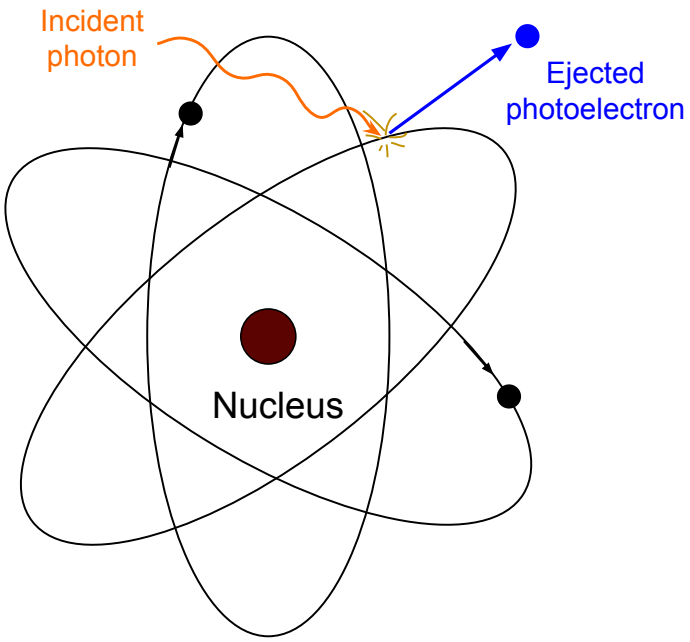

Figure 1.3: Scheme of the photoelectric effect.

1.1.2.2 COMPTON SCATTERING

In the Compton process (Figure 1.4), a photon is scattered by an atomic electron of the absorber material. The photon transfers a portion of its energy to the electron[4]; the scattered photon energy $h\nu'$ is determined by its scattering angle θ:

$$h\nu' = \frac{h\nu}{1 + \frac{h\nu}{m_0c^2}(1 - \cos\theta)} \tag{1.7}$$

where m_0c^2 is the rest mass energy of the electrons (0.511 MeV). When $\theta = \pi$, the energy of the scattered photon $h\nu'$ reaches its minimum. On the other hand, for very small scattering angles, very little energy is transferred.
The cross section for Compton scattering is given by [8]:

$$\frac{d\sigma}{d\Omega} = Z\, r_0^2 \left(\frac{1}{1 + \alpha\,(1 - \cos\theta)}\right)^2 \left(\frac{1 + \cos^2\theta}{2}\right) \left(1 + \frac{\alpha^2(1 - \cos\theta)^2}{(1 + \cos^2\theta)\,[1 + \alpha\,(1 - \cos\theta)]}\right) \tag{1.8}$$

Compton scattering is the most likely interaction for photons with energies from a few hundred keV up to about 5 MeV. In this range, this differential cross section is approximately flat in the backward hemisphere ($\theta > \pi/2$) and increases toward a maximum at

4 The electrons in the Compton scattering are treated as free electrons: all the atomic binding effects and many-body interactions of bound electrons in atomic or molecular systems are neglected in the scattering process. This approximation is valid if the energy of the photons is large enough compared to the binding energy.

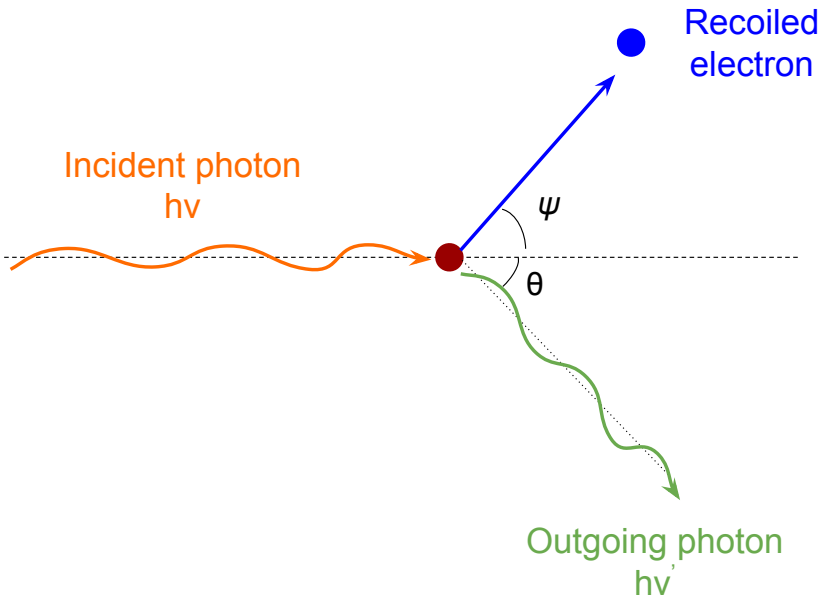

Figure 1.4: Scattering Compton of a photon with a free electron.

$\theta = 0$ (forward scattering).
It is proportional to Z, showing much less importance of the dependence on the number of the target electrons in the nuclei of the absorber material than the cross section for the photoelectric effect.
The cross section for Compton scattering decreases increasing the photon energy as $\sim 1/E$.

1.1.2.3 PAIR PRODUCTION

As the energy of the photon exceeds twice the electron rest mass, the production of an electron-positron pair becomes energetically possible. The interaction takes place in the Coulomb field of a nucleus; for low-Z materials and at high energies, e^+e^- creation in the field of the atomic electrons also contributes significantly to the total pair production cross section. During the process, the photon is absorbed in the Coulomb field of the nucleus and converted into an e^+e^- pair (Figure 1.5). The photon energy in excess, above the $2m_ec^2$ required to create the pair, goes into kinetic energy shared by the electron and the positron. In the medium, electrons and positrons produce bremsstrahlung radiation as well as ionization. The positrons eventually annihilate with an electron, producing two new photons (each with an energy of 511 keV). The cross section increases with the energy and reaches an asymptotic value for energies of the order of GeV.

1.1.2.4 RELATIVE IMPORTANCE OF THE DIFFERENT INTERACTION MECHANISMS

The relative importance of the mechanisms through which photons interact with matter depends strongly on the photon energy and on the absorber atomic number Z.

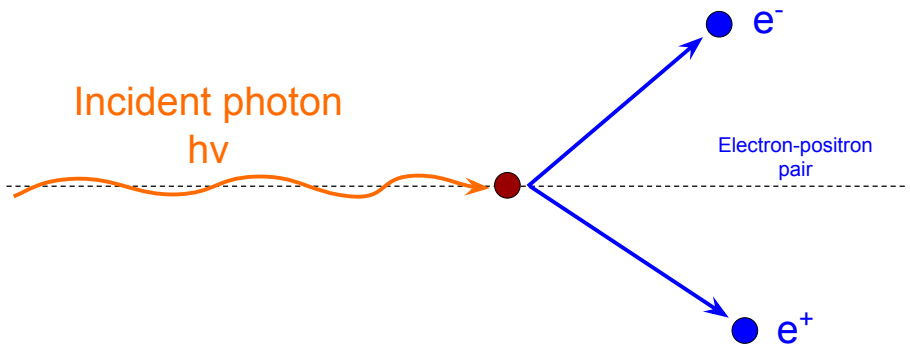

Figure 1.5: Scheme of the pair production mechanism.

Figure 1.6 shows the energy dependence of the three interaction processes. The photoelec-

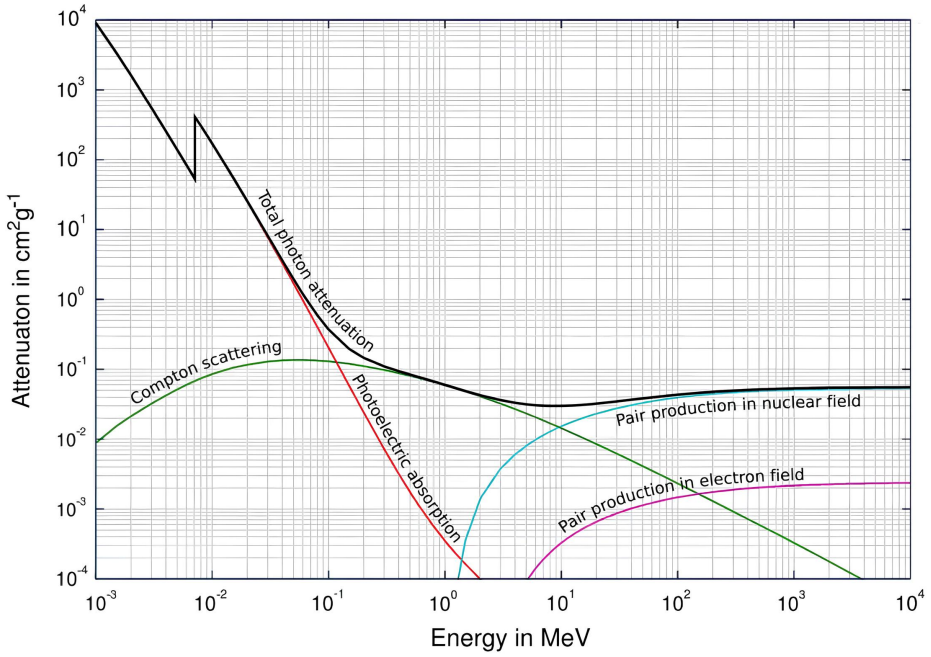

Figure 1.6: Energy dependence of the different photons interaction mechanisms with matter.

tric effect dominates at low energies; as the energy of the incident photon increases, its cross section decreases rapidly and Compton scattering becomes the dominant process. In high-Z materials, the role of Compton scattering is comparatively reduced with respect to photoelectric absorption and pair production. Pair production becomes the dominant process at high energies.
All these interaction mechanisms are fundamental for understanding the physics of an electromagnetic shower development in electromagnetic calorimetry.

1.2 A MODEL FOR THE ELECTROMAGNETIC SHOWER DEVELOPMENT

Multi GeV electrons and positrons interact with matter via bremsstrahlung. The majority of photons produced by bremsstrahlung are very soft[5], and are absorbed through successive Compton scattering until the final absorption via the photoelectric effect. Photons carrying enough energy may create e^+e^- pairs; when the positron comes at rest, it annihilates with an electron and two 511 keV photons are created.
The result of such interactions is a shower that consists of thousands of electrons, positrons and photons (Figure 1.7). Overall, in the electromagnetic shower development process most of the deposited energy comes from the ionization of the many Compton electrons and photoelectrons.
The calorimetric signals are generated through different mechanisms, depending on the calorimeter material, which will be described in Section 1.3.
The longitudinal and lateral development of an electromagnetic shower can be described

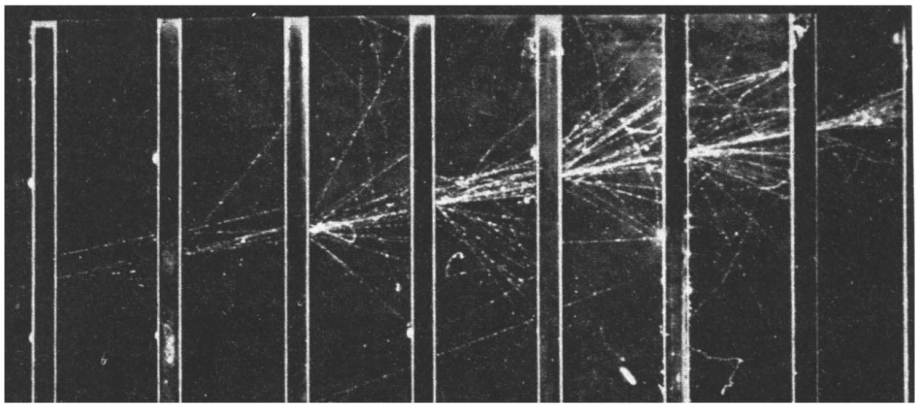

Figure 1.7: Photo of an electromagnetic shower in a cloud chamber with lead absorbers [13].

in terms of two parameters: the radiation length X_0, and the Molière radius ρ_M, which depend only on the characteristics of the material.

1.2.1 THE RADIATION LENGTH

The radiation length X_0 is defined as the mean distance x over which a high-energy ($\gg$ 1 GeV) electron loses all but 1/e of its original energy E_0 via bremsstrahlung:

$$\langle E(x) \rangle = E_0 \exp(-x/X_0) \tag{1.9}$$

5 A considerable fraction, up to 40 %, of the energy carried by 10 GeV electrons is deposited by shower particles with an energy below 1 MeV [8].

Similarly, a photon beam of initial intensity I_0 crossing a block of material is absorbed mainly through pair production. Its mean intensity after a thickness x is

$$\langle I(x) \rangle = I_0 \exp\left[-\frac{7}{9}\frac{x}{X_0}\right] \tag{1.10}$$

This implies that the mean free path of high energy photons is equal to $\frac{9}{7}\ X_0$.
The radiation length can be expressed as a function of the atomic number Z and weight of the material A as [8]:

$$X_0 \simeq \frac{716.4\,\mathrm{g\,cm^{-2}}\,A}{Z\,(Z+1)\,\ln(287/\sqrt{Z})} \tag{1.11}$$

By expressing the dimension of the absorber in units of X_0, material-dependent effects are, in first approximation, eliminated.
The mean longitudinal profile of the electromagnetic shower can be described in terms of the radiation length [14]:

$$\frac{dE}{dt} = E_0 \frac{b\,(bt)^{a-1}e^{-bt}}{\Gamma(a)} \tag{1.12}$$

where $t \equiv x/X_0$, a and b are dimensionless shape parameters that depend, on average, on the particle type (electron/positron or photon) and energy.
Figure 1.8 shows the simulated shower longitudinal profiles in lead tungstate, as a function of the material thickness (expressed in radiation lengths), for incident electrons of energy 1 GeV, 10 GeV, 100 GeV, 1 TeV [15].
The energy deposited per unit thickness initially increases with the depth in the material.

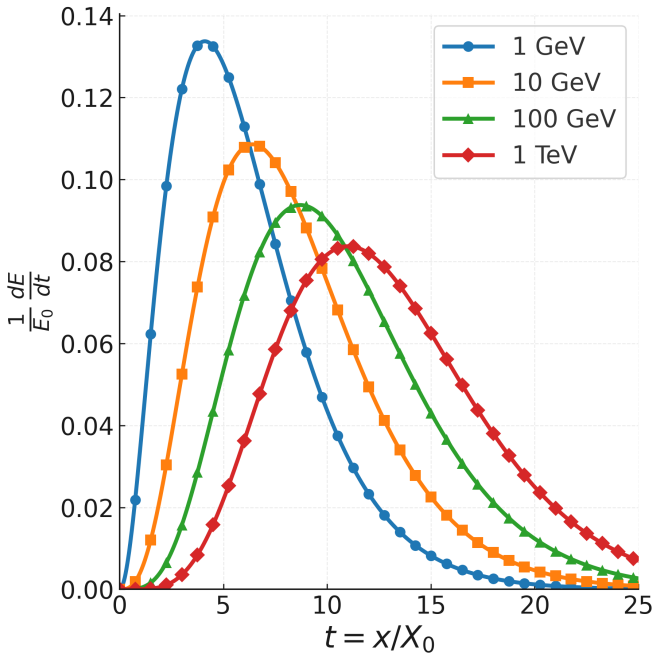

Figure 1.8: Simulated shower longitudinal profiles in lead tungstate, as a function of the material thickness (expressed in radiation lengths), for incident electrons of energy 1 GeV, 10 GeV, 100 GeV, 1 TeV [15].

The shower maximum $t_{\max}$

$$t_{\max} \approx \ln\left(\frac{E_0}{E_c}\right) + t_0 \tag{1.13}$$

with E_c the critical energy (Equation 1.2) and $t_0 \approx -0.5$ ($+0.5$) for electrons (photons), is reached when the average energy of the shower particles equals the critical energy. Beyond this maximum, the number of shower particles, and thus the energy deposited in the detector per unit thickness, gradually decreases and, at some point, no further multiplication takes place. As the Z of the absorber material increases, the shower maximum shifts to a greater depth, and the shower profile decays more slowly beyond the shower maximum. This is because in high Z material, the production of electron-positron pairs and the emission of bremsstrahlung photons continues down to much lower energies than in low-Z materials.
Equation 1.13 shows a logarithmic energy dependence of the longitudinal shower profile: thus, the thickness of the detector depends weakly on the energy of the incident particle. The thickness of the calorimeter needed to contain 95 % of the energy of the shower is

$$t_{95\%} = \approx t_{\max} + 0.08Z + 9.6 \tag{1.14}$$

In calorimeters with a total thickness $\gtrsim 25\, X_0$, the longitudinal leakage beyond the active volume is typically $< 1\%$ for incident electrons up to ~ 300 GeV.
Table 1.1 lists the values of the radiation length of some of the most used scintillator materials in calorimetry. In general, electromagnetic calorimeters are very compact detectors: for instance, lead tungstate has a radiation length of 0.89 cm, a value that allows the electromagnetic calorimeter of the Compact Muon Solenoid (CMS) experiment to reach 26 X_0 in only ~ 23 cm.

1.2.2 THE MOLIÈRE RADIUS

The Molière radius is defined in terms of the radiation length and the critical energy:

$$\mathrm{R_M(g/cm)} = 21 \text{ MeV } \frac{\mathrm{X_0}}{E_c} \tag{1.15}$$

Typically, $\sim$ 85-90 % of the shower is deposited in a cylinder with a radius $\mathrm{R_M}$ around the shower axis.
Such lateral spread of the electromagnetic shower is caused by the fact that, in general, the shower particles contributing to the calorimeter signal are isotropically distributed with respect to the particle that initiated the shower; however, electromagnetic showers are quite narrow: for most calorimeters $\mathrm{R_M}$ is of the order of a few centimeters.
When designing a calorimeter, it is important that the detector is large enough to contain the shower of interest. Shower particles escaping from the detector represent a source of fluctations that may affect the precision of the measurement.

1.3 DETECTION MECHANISMS

In this section, the different mechanisms through which calorimetric signals are generated, both in homogeneous and in sampling calorimeters, are described.
Particular emphasis will be given to the scintillation and Cherenkov mechanisms, which are characteristic of lead tungstate, the crystalline material selected by the OREO Collaboration for the oriented calorimeter.

1.3.1 SCINTILLATION

Historically used as the first physics process for the generation of calorimetric signals, scintillation remains one of the most useful detection mechanisms used today in many particle physics experiments.
Scintillation is the mechanism of light photons emission upon the absorption of ionizing radiation; when charged particles cross matter, they lose energy through the electromagnetic interaction with atomic electrons producing ionization and excitation. The resulting excited atomic or molecular states are unstable and quickly return to the ground state, releasing the excitation energy as visible or ultraviolet photons. The scintillation light is converted into an electrical signal by photodetectors such as PhotoMultipliers Tube (PMT) [16] or Silicon PhotoMultipliers (SiPM) [17].
Based on the different physical mechanisms of light emission, scintillators can be divided into organic and inorganic scintillators [18]. The use of organic scintillators for homogeneous calorimeters is very limited, mainly because they are not dense enough, whereas they are commonly chosen as the active medium for sampling calorimeters, such as for the UA1 and UA2 electromagnetic calorimeters [19, 20].
The choice of the scintillator material and the photodetectors depends on the specific goals of the experiment. Table 1.1 summarizes the main properties of the crystals most commonly used for (past and present) high-energy physics applications. One of the first hermetic electromagnetic calorimeters to operate at a e^+e^- collider, the Stanford Positron Electron Accelerating Ring (SPEAR) at the Stanford Linear Accelerator Center (SLAC), was the Crystal Ball detector, a 4π detector consisting of NaI(Tl) crystals.
CsI has been widely used in many experiments, such as BaBar [21], Belle [22], and CLEO [23].
Lead tungstate has become one of the most widely used scintillation materials in modern particle physics experiments. In the last three decades, $PbWO_4$-based calorimeters have been considered in the design of several experiments in a wide range of energies and geometries, such as in the CMS electromagnetic calorimeter [24] (Figure 1.9) and in the A Large Ion Collider Experiment (ALICE) at CERN [25] and in the antiProton ANnihilation at DArmstadt ($\overline{\text{P}}$ANDA) experiment [26].
As shown in Table 1.1, lead tungstate exhibits some features which make it particularly suited to the Large Hadron Collider (LHC) and high energies environment: it has a very

	NaI(Tl)	CsI(Tl)	CsI	BGO	$PbWO_4$
Density (g/cm^3)	3.67	4.53	4.53	7.13	8.28
X_0(cm)	2.59	1.85	1.85	1.12	0.89
R_M (cm)	4.5	3.8	3.8	2.4	2.2
Decay time (ns)	250	1000	10	300	5
slow component			36		15
Emission peak (nm)	410	565	305	410	440
slow component			480		
Light yield (γ/MeV)	4×10^4	5×10^4	4×10^4	8×10^3	1.5×10^2
Photoelectron yield (relative to NaI)	1	0.4	0.1	0.15	0.01
Rad. hardness (Gy)	1	10	10^3	1	10^5

Table 1.1: Main properties of the crystals commonly used (in the past and at present) for homogeneous electromagnetic calorimeters in accelerator experiments.

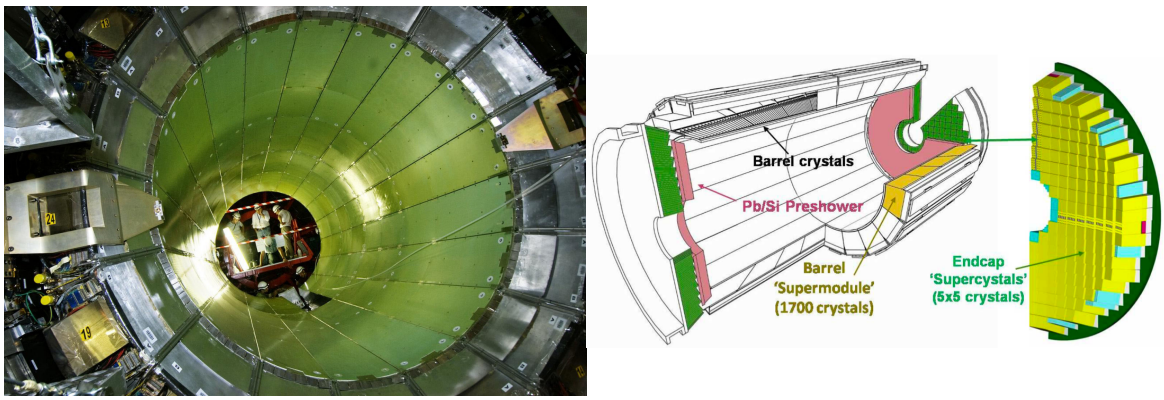

Figure 1.9: (left) Photo and (right) scheme of the CMS electromagnetic calorimeter.

short radiation length, a small Molière radius (Section 1.2), high radiation resistance and fast response. Furthermore, differently from many other inorganic scintillators, lead tungstate is radiation tolerant and non-hygroscopic. The main drawback is that the light yield is quite modest, which requires a careful optimization of the light collection and photodetector readout.

Generally, these high-Z scintillator crystals are employed as an amorphous material and the crystalline lattice influence is typically ignored. The OREO Collaboration has selected lead tungstate for the construction of the first prototype of an oriented crystal based calorimeter for its aforementioned characteristics. The main physical and crystalline properties of $PbWO_4$ and $PbWO_4$-Ultra-Fast (UF) will be discussed in Section 3.1.

Apart from scintillation, lead tungstate presents an additional, very prompt light component from Cherenkov emission, a mechanism that will be described in the next section.

1.3.2 CHERENKOV RADIATION

When a charged particle travels faster than the speed of light in a given medium ($\beta n > 1$, with n the refractive index of the medium and β the ratio of the velocity of the charged particles in the medium to that of light in vacuum), it loses energy emitting Cherenkov radiation.
The radiation is emitted at a characteristic angle, the Cherenkov angle $\theta_C = \arccos(n\beta)^{-1}$, along the direction of the particle velocity; therefore this radiation is confined to the surface of a cone with a vertex angle θ_C (Figure 1.10). The spectrum of the Cherenkov radiation

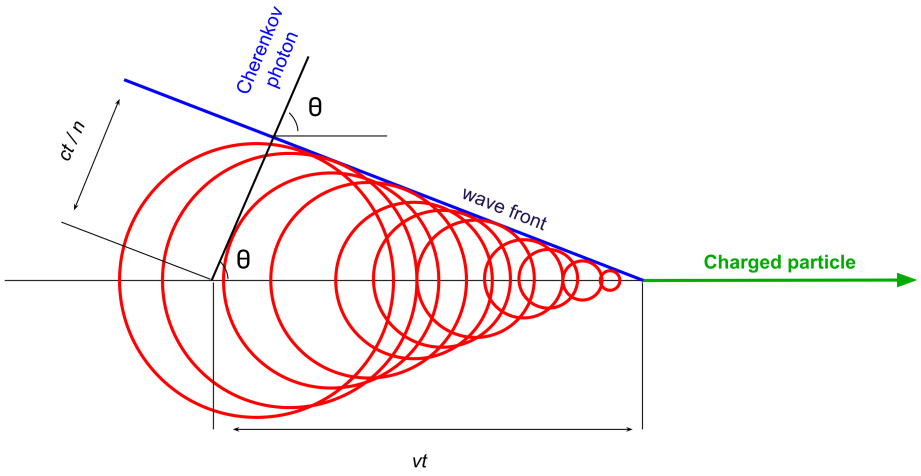

Figure 1.10: Cherenkov radiation scheme. In the time t, the particle travels a distance vt, while the light it emits travels a distance ct/n. The wavefronts of the light emitted by such particle form a cone with half-opening angle θ_C.

exhibits a characteristic $1/\lambda^2$ dependence; the emission is therefore concentrated in the short-wavelength region of the spectrum. The blue emitted light is converted into an electric signal by a photodetector in optical contact with the Cherenkov medium.
Since a minimum particle velocity is required in a given medium to generate Cherenkov light, Cherenkov detectors have an inherent discrimination capability that is unique among radiation detectors.
A very important aspect of the Cherenkov mechanism is that the light is emitted in a very short time, typically of the order of picoseconds in solids or liquids. In general, the timing properties of a Cherenkov detector are limited by the photodetection system. Therefore, Cherenkov detectors, including calorimeters, are the optimal choice in experiments in which high speed is required.
The most important drawback of Cherenkov detectors is the low intensity of the produced light: the number of photons emitted per electron in common Cherenkov media is only a few hundreds per MeV. This corresponds to a visible-light yield about 100 times smaller than that of an efficient scintillator.
Lead glass (PbO) is cheap and easy to handle and therefore has been widely used in the past for high energy physics applications, for example in the Omni-Purpose Apparatus for LEP (OPAL) experiment at the Large Electron–Positron Collider (LEP) [27].

Water Cherenkov detectors, such as Super-Kamiokande [28] have played and are playing a central role in particle and astroparticle physics. Large volumes of ultrapure water are instrumented with dense arrays of PMTs, which record the characteristic blue Cherenkov light emitted by the relativistic charged particles crossing the medium. Examples of experiments that use a natural environment to create huge water Cherenkov detectors include the NEutrino Mediterranean Observatory (NEMO) [29], the Neutrino Extended Submarine Telescope with Oceanographic Research Project (NESTOR) [30], the Cubic Kilometre Neutrino Telescope (KM3NeT) [31] in the Mediterranean Sea, and the IceCube [32] experiment in the Antarctic ice.

1.3.3 IONIZATION

As mentioned before, when charged particles cross matter they lose energy through the electromagnetic interaction with atomic electrons producing ionization and excitation. In the case of ionization, ion pairs are produced; each ion pair consists of a free electron and the corresponding positive ion of the absorber atom from which the electron has been totally removed. The collection of these free electrons is used as the signal generation mechanism in a wide variety of particle detectors.
Calorimeters based on noble liquids, such as liquid argon, as active media have been used in particle physics experiments since the 1970s. The A Toroidal LHC Apparatus (ATLAS) calorimeter [33] is one of the largest liquid argon sampling calorimeters operating today. Unlike scintillating crystals, noble liquids are very radiation hard; this property has played an important role in the choice of the ATLAS sampling electromagnetic calorimeter. A very large homogeneous liquid argon system is operating as a Time Projection Chamber (TPC) in the ICARUS experiment [34]. Liquid argon is indeed cheap, abundantly available and the required purity levels can be easily achieved and maintained. Other noble liquids, such as krypton and xenon, are much more expensive, although with a higher density, and are therefore limitedly used. One example is the electromagnetic sampling calorimeter of the NA48 experiment at CERN, which uses liquid krypton as active medium [35].
A different type of ionization calorimeters is based on solid state semiconductors like silicon, germanium and gallium. These calorimeters are rarely used in high-energy physics experiments since they are expensive and therefore not suited to large systems. They have an excellent intrinsic resolution that is optimal for low-energy particles, whereas at high energy other effects like leakage and response non uniformities dominate.

1.4 THE ENERGY RESOLUTION OF A HOMOGENEOUS ELECTROMAGNETIC CALORIMETER

Calorimeters measure the particle energy; the precision of this measurement is called energy resolution. The main advantage of homogeneous electromagnetic calorimeters is their excellent energy resolution, which is due to the fact that the whole energy of the incident

particle is deposited in the active medium, in contrast with sampling calorimeters. In an ideal homogeneous calorimeter, the intrinsic energy resolution is due to the fluctuations of the total length of the tracks of the ionizing particles in the shower [36]. Since the shower development is a stochastic process, the absolute uncertainty on the total track length is proportional to its square root, which results in an uncertainty on the measured energy:

$$\frac{\sigma_E}{E} = \frac{1}{\sqrt{E_0}} \tag{1.16}$$

where E_0 is the original particle energy. IN fact, the energy resolution of a real calorimeter is deteriorated by other contributions and can be modelled as [36]

$$\frac{\sigma_E}{E} = \sqrt{\left(\frac{a}{\sqrt{E}}\right)^2 + \left(\frac{b}{E}\right)^2 + c^2} \tag{1.17}$$

where the first, second and third term under the square root are the stochastic, noise and constant term respectively. An example of energy resolution curve is presented in Figure 1.11

In particular:

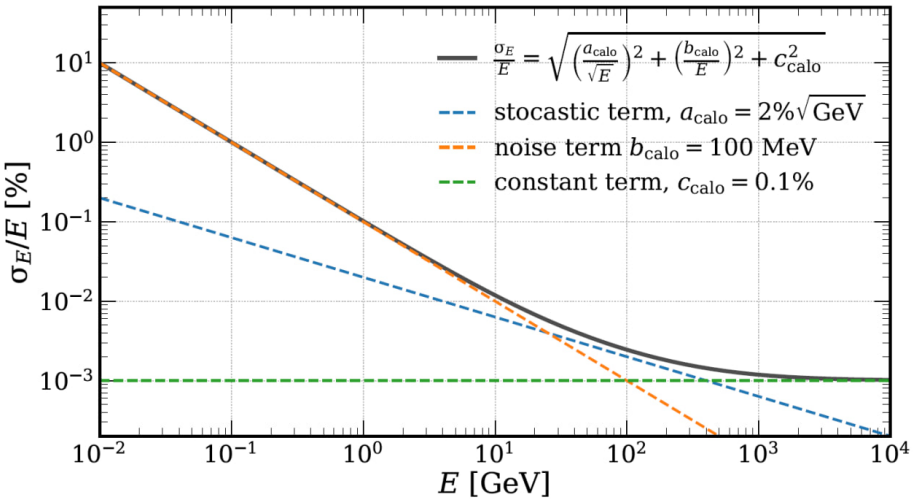

Figure 1.11: Example of an energy resolution curve (solid gray curve); the single terms are shown as dashed curves.

- The stochastic term a accounts for the fluctuations in the shower development inside the detector volume. In homogeneous calorimeters, these fluctuations are particularly small because the entire shower develops within the active material, allowing most of the initial energy to be measured. This term represents the intrinsic energy resolution (Equation 1.16), weighted by the Fano factor and is of the order of a few$\%/\sqrt{\text{GeV}}$ for homogeneous calorimeters, around ten times smaller than the values found in modern sampling calorimeters [36].

- The noise term b includes the contribution from the electronic noise and depends on the detector technology; scintillation and Cherenkov threshold detectors can achieve small levels of noise by properly choosing the photodetection system [36].

- The constant term c includes the contributions that do not depend on the energy of the particle, such as non uniformities in the calorimeter response, caused by factors such as the detector geometry, the mechanical imperfections, the readout variations, the temperature changes, aging, or radiation damage. The constant term becomes dominant at very high energies and in general should be kept at the level of 1% or smaller [36].

Additional contributions that degrade the energy resolution come from the transverse and lateral leakage, as well as from losses in hermeticity caused by possible gaps between detector channels. These quantities should be minimized as much as possible in the design of a homogeneous calorimeter.
Semiconductor calorimeters have an excellent intrinsic resolution: the energy gap between the valence and conduction band is very narrow, typically of the order of 1 eV, one order of magnitude less than the energy needed to produce one electron-ion pair in gases and two orders of magnitude less than the energy required for the production of one photoelectron in scintillator materials. However, as already mentioned, they are rarely used in high-energy physics experiments.
Cherenkov calorimeters usually have a worse energy resolution than other types of homogeneous calorimeters. This is mainly due to the small light yield. The lead glass calorimeter used in the OPAL experiment at LEP achieved an energy resolution of $\sim 5\%/\sqrt{E}$ [27]. Inorganic scintillators present a very high energy resolution: the electromagnetic calorimeter of the CMS experiment has an energy resolution with a stochastic term of $3.3\%/\sqrt{E}$, a constant term of 0.27%, and a noise term of $0.19\%/E$ [15].

The electromagnetic interactions of a particle with a crystalline lattice differ from those in amorphous media. The next chapter describes how standard electromagnetic processes are modified in oriented crystals. Furthermore, a review on recent experimental studies on coherent effects in oriented crystals, which provided the basis for the construction of the OREO calorimeter, is given.

2

TOWARD ORIENTED CRYSTAL BASED CALORIMETRY

The physics of the electromagnetic interactions between a particle and a crystalline medium differs from what happens in an amorphous material.
Depending on the crystalline lattice orientation with respect to the incident particles trajectory, the crystal can appear either as an amorphous medium or as an ordered array of lattice planes or atomic strings. In the latter case, the particle experiences an effective electromagnetic field that is the result of the coherent sum of all the single atoms contributions, which results in different phenomena that depend on the particles energy and on the incidence angles. Such phenomena have been discovered and studied over the years.
The dependence of the electromagnetic interactions on the crystal orientation has been hypothesized since the beginning of the XX century. In 1912 J. Stark, in a paper on the interaction of accelerated protons with a crystal lattice, suggested that some directions in a crystalline lattice are more transparent than others to the passage of charged particles [12, 37].
The first comprehensive theoretical treatment of such phenomenon, called channeling, was given later, in 1965, by Lindhard, who introduced the continuum approximation to describe the average crystalline potentials. He demonstrated that when a charged particle trajectory is aligned within a small angle to the crystallographic planes or axes, the particle transverse motion becomes bound by the continuous potential, and it follows a periodic motion inside the lattice [38].
The crystalline lattice also affects the features of the electromagnetic radiation emitted by electrons and positrons; indeed, the probability of photon emission from charged particles and the probability of pair production by photons in oriented crystals differ from those of the corresponding processes in amorphous media.
This chapter is divided in two parts: the first part summarizes the main features of the crystalline lattice and briefly describes how standard electromagnetic processes are modified in oriented crystals. The second part of the chapter focuses on the recent experimental studies performed on coherent effects in oriented crystals, which provided the basis for the construction of the OREO prototype.

2.1 ELECTROMAGNETIC INTERACTIONS IN ORIENTED CRYSTALS

In the following sections, the crystalline lattice is described, and the energy-dependent modifications of the electromagnetic interactions in oriented crystals are presented. Particular attention is given to the processes at high energies (above a few tens of GeV), in the so-called strong field regime, and to the enhancement of electromagnetic radiation arising from the interaction of particles with the strong crystalline field in axially oriented crystals.

2.1.1 THE CRYSTALLINE LATTICE

A crystal is a solid with a highly ordered structure, characterized by invariance under discrete spatial translations. It is described by [39] (Figure 2.1):

- the Bravais lattice: an infinite set of points in space that is invariant under a discrete set of translations; the structure appears identical when viewed from any lattice point. It identifies only the geometry of the periodic structure. There are 14 distinct three-dimensional Bravais lattices that define all the possible translational symmetries in crystalline solids;
- a basis: which may consist of a single atom or a group of atoms, molecules, or ions with defined positions relative to a lattice point. By placing the basis on every point of the Bravais lattice, the actual crystal structure is generated;
- a unit cell: the smallest volume of space which, when translated through all the vectors of the Bravais lattice, can reproduce the entire crystal structure. It contains exactly one lattice point (primitive cell) or an integer number of lattice points (conventional cell), together with the corresponding basis.

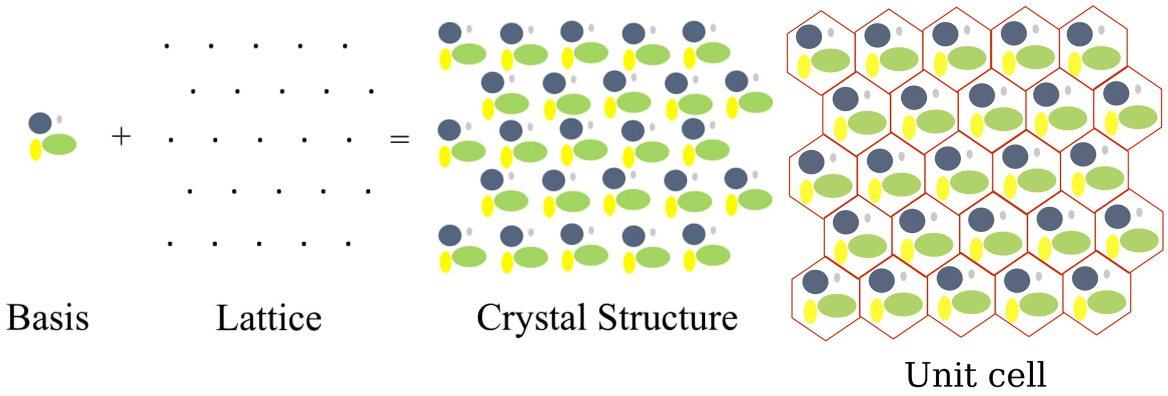

Figure 2.1: Simplified scheme of the crystalline structure.

The crystalline planes are uniquely identified by the Miller indices (hkl) via

$$\frac{h\,x}{a_0} + \frac{k\,y}{b_0} + \frac{\ell\,z}{c_0} = 1\,, \tag{2.1}$$

where (x, y, z) are the coordinates along the crystallographic axes and (a_0, b_0, c_0) are the lattice parameters along x, y, z, so that the plane intercepts the three axes at a_0/h, b_0/k, and c_0/ℓ.
The (h, k, l) constants are the Miller indices, and they uniquely characterize a set of parallel planes, each one corresponding to a different value of n.
The following notation has been adopted:

- (h, k, l) denotes a plane, according to Equation 2.1;
- $[h, k, l]$ denotes an axis, i.e. the direction perpendicular to the corresponding (h, k, l) plane;
- $\langle h, k, l \rangle$ indicates the set of all the axes identical to $[h, k, l]$, due to the symmetries of the crystal structure such as the invariance under rotation.

Figure 2.2 shows a crystalline lattice with different orientations with respect to the page axis: (a) all the main axes and planes are oriented at a large angle with respect to the page axis, thus the lattice appears and behaves like an unordered structure, i.e. an amorphous medium. This condition is called random orientation; (b) the (001) plane; (c) the $\langle 100 \rangle$ axis and (d) the [001] axis.

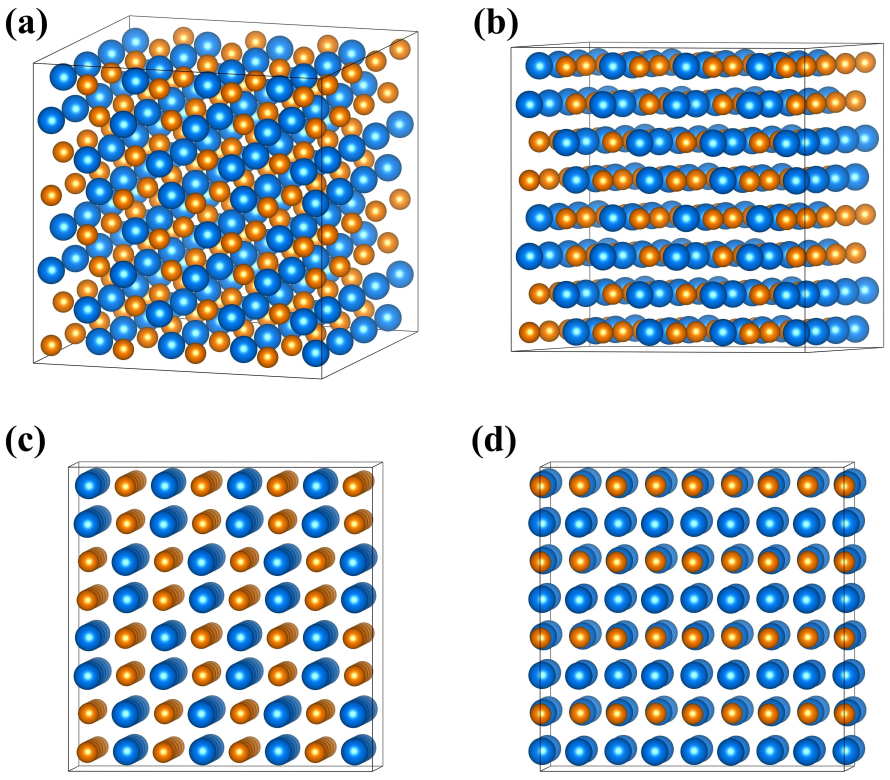

Figure 2.2: Example of a crystalline lattice in different orientations: (a) random, (b) in the (001) plane, (c) in the $\langle 100 \rangle$ and (d) in the [001] axis.

2.1.2 PARTICLE DYNAMICS IN AN ORIENTED CRYSTAL

A major contribution to the quantitative description of the particles motion in crystals was given by Lindhard [38]. In his work he recognized that the Bethe-Bloch description of the stopping power [8], valid for amorphous media with a uniform target density, was no longer valid for the description of particles travelling in a crystal.
In particular, the features of the coherent interactions experienced by the particle in an oriented crystal can be described by a continuum potential, obtained by averaging the screened Coulomb fields along rows or planes.
The single-axis continuum potential U_{ax} is obtained by integrating the single-atom potential along the entire atomic string:

$$U_{ax}(x,y) \equiv U_{ax}(r_\perp) = \frac{1}{d_{ax}} \int_{-\infty}^{+\infty} V_{atom}^{th}\left(\sqrt{r_\perp^2 + z^2}\right) \, dz \tag{2.2}$$

where $r_\perp = \sqrt{x^2 + y^2}$ is the transverse distance from the string and d_{ax} is the interatomic spacing along the axis.
Similarly, the single-plane continuum potential U_{pl} is given by:

$$U_{pl}(x) \;=\; n_{atom}\, d_{pl} \int_{-\infty}^{+\infty}\int_{-\infty}^{+\infty} V_{atom}^{th}\left(\sqrt{x^2 + y^2 + z^2}\right) \, dy\, dz \tag{2.3}$$

where n_{atom} is the atomic number density[1] and d_{pl} is the interplanar spacing.
Since the axial potential does not depend on the coordinate along the axis, z, the motion along z can be considered free and the longitudinal translational energy $E_z = p_z^2/(2m)$ is conserved. Under elastic interaction with the continuum potential, the total particle energy E_0 is conserved as well, and the dynamics separates into a free longitudinal motion and a transverse motion governed by $U_{ax}(r_\perp)$:

$$E_\perp = E_0 - E_z = \frac{p_\perp^2}{2m\gamma} + U(r_\perp) \tag{1.11}$$

where:

- $p_\perp$ is the transverse momentum;
- $\gamma = \dfrac{1}{\sqrt{1-\beta^2}} = \dfrac{E_0}{mc^2}$ is the Lorentz factor;
- β is the speed in units of the speed of light c, with $v = \beta\, c$;
- $U = U_{ax}^{tot}$ ($-\,U_{ax}^{tot}$) for positively (negatively) charged particles.

Figure 2.3 (left) shows the potential generated by a single atomic string in a tungstate crystal, in the transverse plane with respect to the $\langle 111 \rangle$ axis. Depending on the initial

1 The atomic number density, n_{atom}, is the number of atoms per unit volume of the material:

$$n_{atom} \;=\; \frac{\rho\, N_A}{A}$$

where ρ is the mass density, A the molar mass, and N_A the Avogadro constant.

energy of the incident particle $E_\perp$ with respect to the height of the string potential barrier U_0, different trajectories in the transverse plane may be observed, as shown in Figure 2.3 (right)[2]:

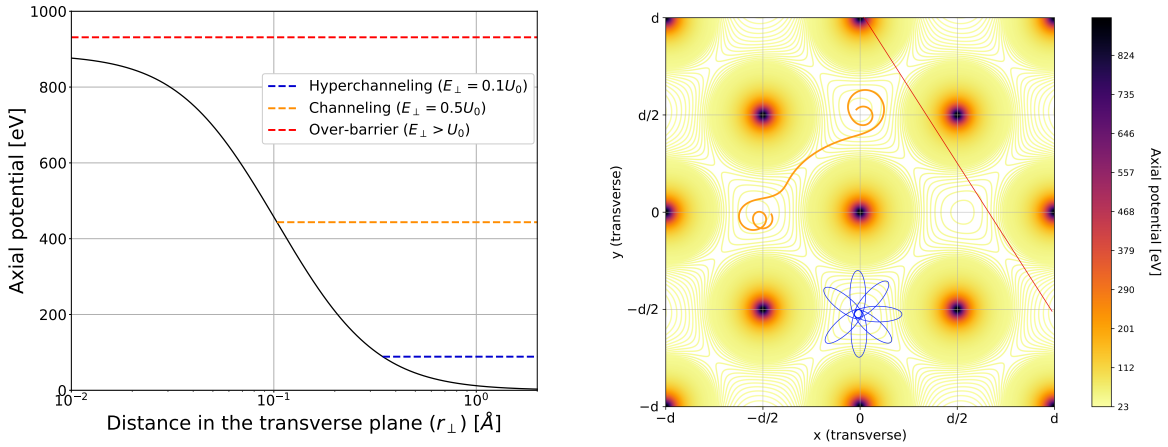

Figure 2.3: (left) Potential generated by a single atomic string in a tungstate crystal, in the transverse plane with respect to the $\langle 111 \rangle$ axis. (right) Contour plot of the axial potential. The colored lines (blue, orange, red) show the different possible motions in the lattice, depending on the initial energy of the particle [40].

- if $E_\perp \ll U_0$ (blue curves), the particle is trapped at the bottom of the potential well and oscillates in the transverse plane (rosette orbits). This condition is called hyperchanneling.

- if $E_\perp \lesssim U_0$ (orange curve), the particle is still trapped in the potential well: it is forced into a trajectory which is partly oscillating around a potential well, partly propagating across the adjacent strings. In both these cases, the particle is (completely or partially) bound to follow specific trajectories. Such condition is called channeling (Figure 2.4).

  Lindhard evaluated the angular acceptance of the channelling phenomenon:

$$\theta_c \sim \sqrt{\frac{2U_0}{pv}} \tag{2.4}$$

  where $p = (p_\perp, p_z)$ is the particle initial momentum, v the modulus of its initial velocity. It can be seen that a higher-potential axis features a broader angular acceptance and that the angular acceptance decreases as the energy of the incident particle increases. In general, in case of high-Z, high-density crystals, values around 500 μrad (100 μrad) are attained at a few GeV ($\sim$ 100 GeV).

  Scattering events inside the medium can break the conservation of the transverse energy and the particle may eventually escape from its bound state. This process is called dechanneling (Figure 2.5). Further details on the channeling phenomenon can be found in [12, 38, 42, 43].

2 Positive particles are considered.

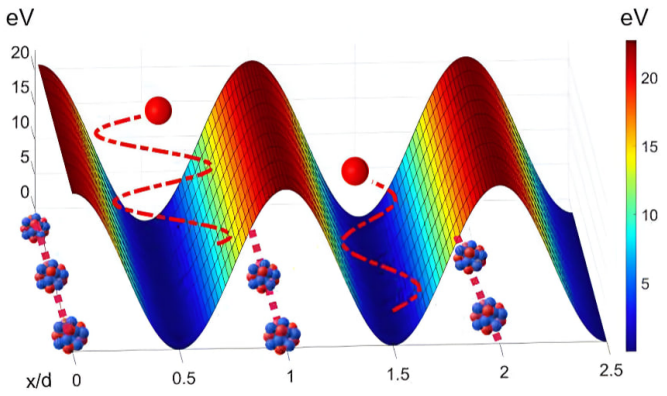

Figure 2.4: Sketch of the continuum potential for a set of atomic planes and the resulting planar channeling of positively charged particles. The horizontal coordinate x/d is the distance x perpendicular to the planes, normalized to the interplanar spacing d, while the vertical axis y indicates the direction parallel to the lattice plane. The potential shows maxima along the nuclei on the atomic planes; positive particles cross the crystal while oscillating in the wells between adjacent planes [41].

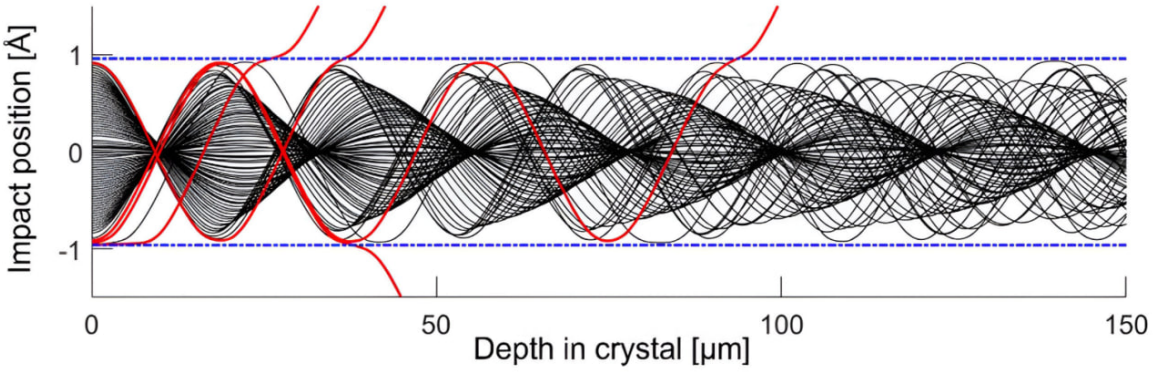

Figure 2.5: Monte Carlo simulation for a 180 GeV proton planar channeling. The blue lines indicate the atomic planes position; the black lines represent the channeled particles orbits and the red lines indicate the dechanneled particles [41].

- if $E_\perp \gtrsim U_0$ (red curve), the particle is unbound and is free to propagate above the lattice structure. This motion is called over-barrier. Such motion differs from the motion of a particle in an amorphous medium; in particular, some physical processes are still affected by the continuum string potential. More details are provided in Section 2.1.4.

2.1.3 RADIATION EMISSION IN ORIENTED CRYSTALS

When electrons or positrons interact with an oriented crystal, the coherence between the periodic interactions with the lattice leads to a modification of the electromagnetic radiation emitted with respect to that of standard bremsstrahlung, described in Section 1.1.1. The properties of the emitted radiation depend on the energy and on the incidence angle of the particle.

2.1.3.1 CHANNELING RADIATION

Channeling radiation is the electromagnetic radiation emitted by electrons or positrons crossing a crystal under channeling conditions: when the particle enters the crystal with an incidence angle smaller than the Lindhard critical angle (Equation 2.4) relative to a crystallographic axis or plane, the continuum potential confines its transverse motion into small oscillations within the potential well, leading to coherent photon emission.
This phenomenon was first predicted by Kumakhov in [44].
Channeling radiation can be classified depending on the incident particle energy [12]:

- at energies below about 100 MeV, the particle oscillating in the potential well can be treated as an electric dipole in the transverse plane; the emitted spectrum shows an enhancement with respect to standard bremsstrahlung and exhibits peaks associated with the quantization of the transverse bound states of the well. A more detailed description of the features of the channeling radiation at low energy can be found in [45];

- between $\sim$ 100 MeV and a few GeV, the number of available states increases significantly and their relative spacing decreases. This allows to describe the photon production classically, as a dipole-like emission process. The electromagnetic radiation is emitted in the forward direction relative to the particle trajectory, summing up as it happens in an undulator[3]. The channeling radiation spectrum, as well as the undulator one, exhibits well-defined peaks at specific harmonic numbers (Figure 2.6).

- at a few GeV and above, which is the case of major interest for this thesis, the dipole approximation cannot be applied anymore because relativistic effects, that must be taken into account in the transverse motion, also affect the longitudinal motion. In the particles rest frame, the axial (or planar) electric field is Lorentz-boosted, therefore the channeling radiation production is locally equivalent to the emission of radiation from a particle moving in an intense and constant field (strong field regime) i.e., synchrotron radiation. Figure 2.7 presents the synchrotron radiation spectrum: the harmonic peaks are no more present and the spectrum presents a hardening at high energy. As the angular frequency ω approaches the critical frequency ${\omega_c}$[4], an exponential decrease becomes evident. More details are provided in Section 2.1.4.

2.1.3.2 COHERENT BREMSSTRAHLUNG

If the particle is in an over-barrier state, i.e. an electron or positron is incident on the lattice axis with an angle larger than θ_C, but small enough for the continuum approximation to be valid, the periodic interactions with the potential generated by different axes and planes

3 An undulator is a device composed of dipole magnets with alternating polarity.
4 The critical frequency is computed as:

$$\omega_c = \frac{3c1\gamma^3}{2R} \tag{2.5}$$

where R is the curvature radius of the impinging particle.

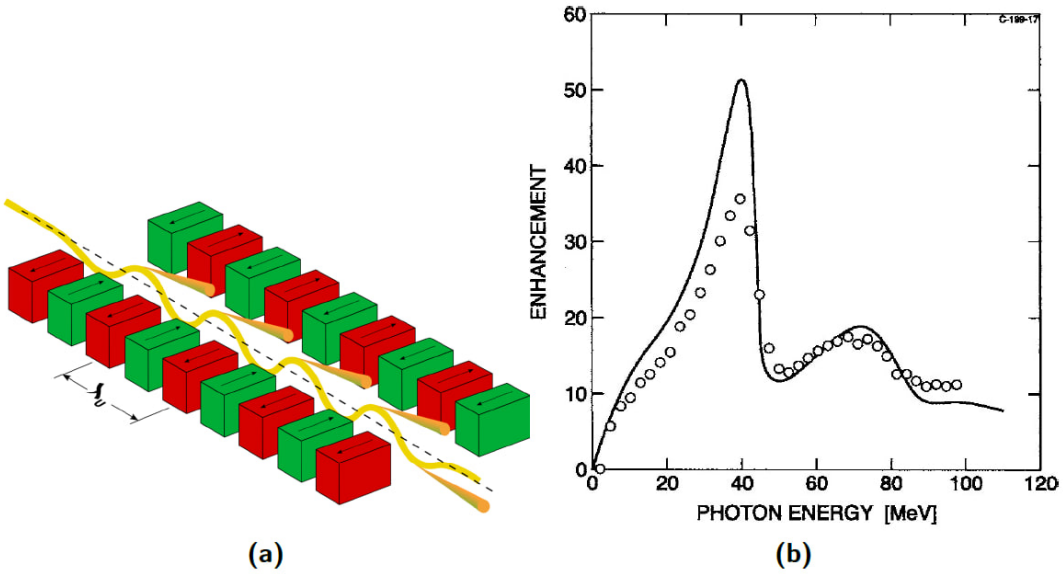

Figure 2.6: (a) Working scheme of an undulator; the colored blocks are magnets with alternating polarity, λ_u is the magnet pitch. The light cones are emitted in the forward direction. (b) Channeling radiation spectrum for a 6.7 GeV positron incident parallel to the (110) plane in a silicon crystal. Empty dots represent the experimental data, while the solid line represents the theoretical curve [12].

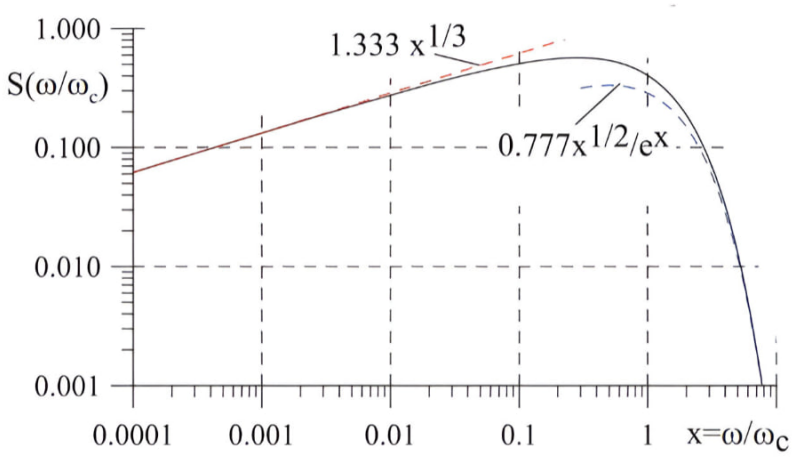

Figure 2.7: Synchrotron radiation spectrum as a function of the angular frequency ω normalized to the critical value ω_c [46].

lead to the production of photons, with a smaller intensity than the channeling radiation value but larger than the standard bremsstrahlung prediction. Such phenomenon is called coherent bremsstrahlung.

The effect of the periodic structure plays an important role for bremsstrahlung radiation: when the electron crosses the crystal planes periodically along the interatomic distance d, it can scatter coherently on many target atoms along its way. The coherence in scattering causes the radiation emission, that adds coherently at every plane crossing. The periodic perturbation of the straight-line path by the planar potential will cause the emission of radiation. The enhancement of the radiation over standard bremsstrahlung is a consequence of the correlation of the deflections by crystal atoms. A complete treatment

of the phenomenon of coherent bremsstrahlung can be found in [47, 48].

Figure 2.8 shows a scheme of the different radiative processes, for an electron or positron incident on the axis (or plane) of an oriented crystal, as a function of the incidence angle and energy.

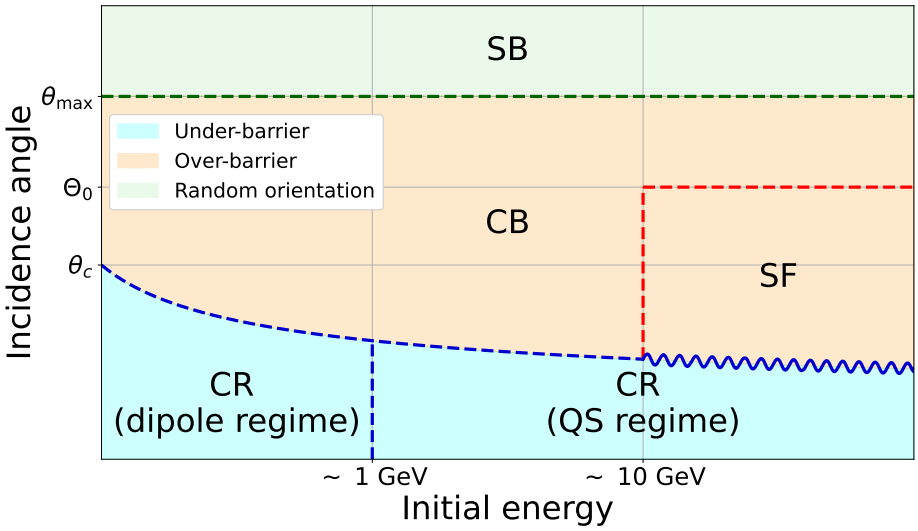

Figure 2.8: Scheme of the radiative processes of a charged particle incident on the axis of an oriented crystal, as a function of the incidence angle and energy. θ_c is the channeling critical angle, Θ_0 the strong field critical angle (Section 2.1.4) and θ_{max} the angle beyond which directional effects in oriented crystals are negligible. The wavy blue line indicates that, in the strong field regime, the features of the emitted radiation are identical, for both channeled and over-barrier electrons.

2.1.4 STRONG FIELD IN A CRYSTAL AND SHOWER ENHANCEMENT

At an energy high enough, the lattice potential in the particle rest frame is Lorentz-boosted and can reach and even overcome a critical value:

$$\mathcal{E}_0 = \frac{m_e^2 c^3}{e\hbar} \sim 1.32 \times 10^{16} \text{ V/cm} \tag{2.6}$$

the so-called Schwinger critical field, i.e., the threshold for nonlinear quantum-electrodynamical effects to occur [49]. Macroscopic strong electromagnetic fields occur naturally only in astrophysical environments such as supernovae and pulsars [12, 50, 51]. It was during the Seventies and Eighties that the possibility of observation of the effects of QED in strong crystalline fields started to be considered. The strong field reached in the high-energy interactions with a crystalline lattice in the incident particle frame provides an easy, stable and relatively large-scale way to study the nonlinear quantum-electrodynamical effects.

As already mentioned, in presence of crystalline strong fields, electromagnetic processes

are modified compared with the bremsstrahlung and pair production at lower energies and in amorphous media; in particular such an intense field induces an enhancement of the quantum radiation emission probability with respect to the Bethe-Heitler description. The creation of an $e^{\pm}$ pair by a high-energy photon increases as well.
Such effects open the way to several technological applications in high energy physics and to the development of future detectors, such as the OREO calorimeter prototype described in this work.

2.1.4.1 THE STRONG FIELD REGIME IN ORIENTED CRYSTALS

The strong field regime is attained when:

$$\chi = \frac{\gamma \mathcal{E}_{\text{lab}}}{\mathcal{E}_0} \tag{2.7}$$

where $\mathcal{E}_{\text{lab}}$ is the continuous axial electric field in the laboratory frame and γ is the Lorentz factor[5]. In order for the strong field regime to be attained, χ must be greater than 1. However, it has been found that the quantum corrections to the classical synchrotron spectrum are already visible for $\chi > 0.1$ [12].
In his work, Baier [52] provided an estimate for the strong field parameter χ as a function of the main lattice properties and the impinging particle:

$$\chi \sim \frac{U_0 \gamma \hbar c}{(mc^2)^2 a_s} \tag{2.8}$$

where a_s is the atomic screening distance. The strong field effect intensity depends linearly on the lattice potential U_0 and on the incident particle energy (γ). For instance, for an electron of 5.6 GeV entering the $PbWO_4$ $\langle 001 \rangle$ axis, $\chi \sim 0.2$, while for an electron of 120 GeV $\chi \sim 4$ [53].

2.1.4.2 ELECTROMAGNETIC RADIATION IN STRONG FIELD REGIME

When a particle travels inside an oriented crystal, the extremely intense lattice field is approximately constant over long sections of the particle path. In the so-called constant-field approximation, the variation of the particle velocity is constant along the whole formation length, which at high energies becomes several orders of magnitude larger than the interatomic distance. This nearly constant field acting on the particle during the radiation formation process leads to the emission of quantum synchrotron-like radiation, in which photons may be emitted with a considerable fraction of the electron energy. The trajectory is indeed locally well described as a segment of a circular path: the particle propagates in the same way as under the effect of a uniform magnetic field, i.e., like in a synchrotron.

5 For photons, γ can be replaced with $\gamma_{\text{PP}} = \hbar\omega / m_e c^2$, $\hbar\omega$ being the incident photon energy.

The characteristic scale over which the electromagnetic processes are enhanced by strong field effects has been introduced by Baier [54]:

$$\Theta_0 = \frac{U_0}{mc^2} \tag{2.9}$$

It has to be noted that Θ_0 is independent on the initial energy and, on the other hand, strongly depends on the lattice potential. Figure 2.9 shows the values of the average axial potential well depth, U_0, for the two strongest (i.e., higher charge-density) $PbWO_4$ axes, $\langle 100 \rangle$ and $\langle 001 \rangle$. The corresponding angular acceptance Θ_0 is ~ 0.9 mrad for both axes.
Comparing it with the critical angle for channelling (Equation 2.4), leads to:

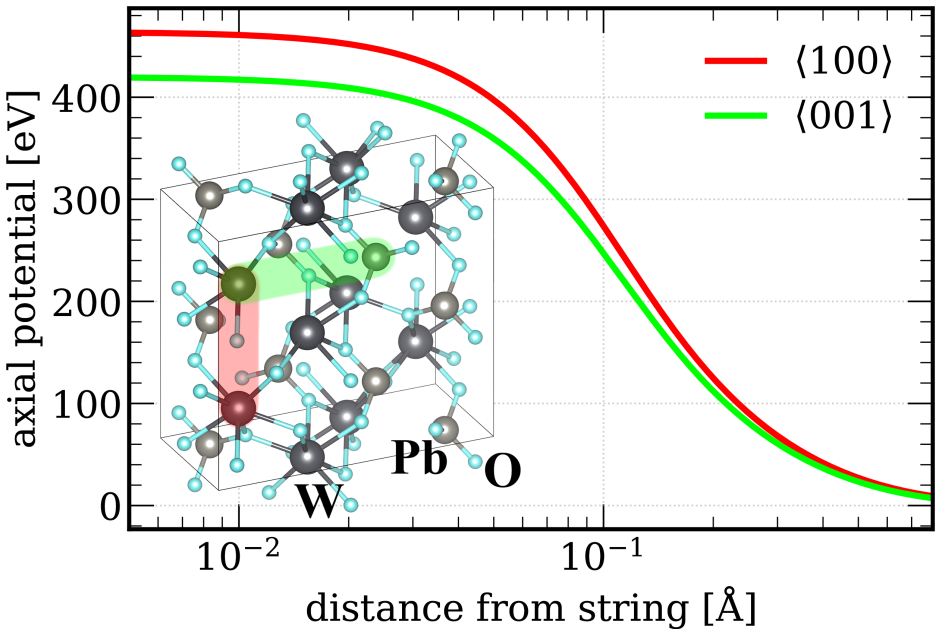

Figure 2.9: Average continuous axial potential felt by positrons (opposite sign for electrons) for two of the main $PbWO_4$ axes as a function of the distance in the transverse direction from the atomic string.

$$\frac{\Theta_0}{\theta_c} = \frac{1}{mc^2}\sqrt{\frac{E_0 U_0}{2}} \tag{2.10}$$

The higher the incident particle energy and the stronger the crystalline potential, the more dominant the strong field effects are over channelling.

2.1.4.3 PAIR PRODUCTION IN STRONG FIELD REGIME

Since photons are neutrally charged, pair production could be expected to be identical in an amorphous medium and in an oriented crystal. However, the e^+e^- pair production is affected by the interaction with the electric field, generated by the crystalline structure of a target material while the pair is created.
The creation of an e^+e^- pair by a high-energy photon crossing matter is closely related, by crossing symmetry, to the emission of electromagnetic radiation by electrons or positrons

in the same energy range.
Figure 2.10 shows the Feynman diagrams associated to these two processes. Similarly to the standard bremsstrahlung process, it is possible to define a pair production formation length as the average distance required to transversely separate the created e^+e^- pair by two Compton wavelengths (with $\lambda_c = \hbar/(mc)$, where m is the electron mass):

$$\ell_f^{\mathrm{PP}} \;=\; 2\,\gamma_p\,\lambda_c \tag{2.11}$$

where $\hbar\omega$ is the photon energy and $\gamma_p = \hbar\omega/(mc^2)$ is the Lorentz factor associated with the emitted pair. The radiation formation length grows as the parent charged particle energy grows: the higher the initial photon energy, the shorter the propagation of the virtual e^+e^- pair before becoming real.
The lattice electric field is able to influence the lepton pair while it is still in the virtual

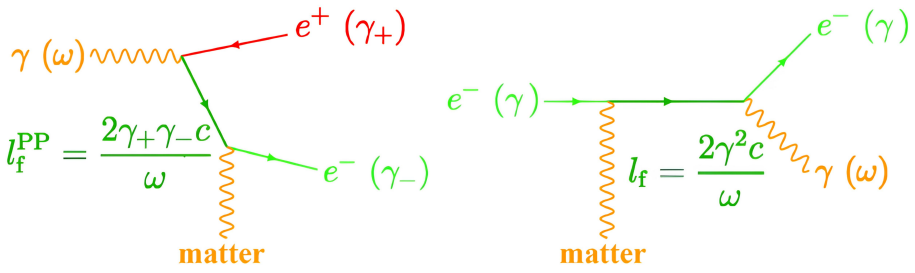

Figure 2.10: Feynman diagrams of the electron-positron pair production (left) and bremsstrahlung (right).

state (i.e., the internal green line in Figure 2.10); for such reason the pair production yield undergoes a pronounced enhancement with respect to the purely incoherent case when the strong field regime is reached. This enhancement can be categorized into two different regimes, depending on the photon incidence angle:

- for an incidence angle $< \Theta_0$, the constant field approximation can be applied in the same way as in treating the synchrotron-like radiation case, and the so-called strong field pair production regime is attained. Figure 2.11 shows the trend of the strong field pair production probability per unit distance as a function of the incident photon energy, for different target materials;

- for angles larger than Θ_0, the constant field approximately breaks down. The resulting process is called coherent pair production: similarly to the coherent bremsstrahlung, in this regime there is a smaller enhancement of the pair production probability, with respect to the standard pair production yield.

Further details can be found in [54–57].

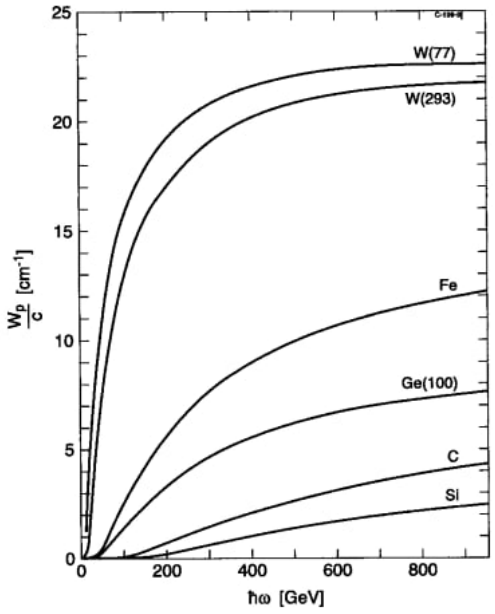

Figure 2.11: Strong field pair production probability for unit distance as a function of the incident photon energy. The photon impinges along the ⟨111⟩ axis for C, Si, Fe, and W, and along ⟨110⟩ for Ge. Temperatures different from room temperature are indicated in brackets [55].

2.1.4.4 ELECTROMAGNETIC SHOWER DEVELOPMENT IN ORIENTED CRYSTALS

The increase of the bremsstrahlung and pair production cross section due to the strong field leads to an enhancement of the electromagnetic shower development, i.e., to a larger production of secondary particles per unit of length, with respect to the case of an amorphous or randomly oriented medium. In the case of a scintillating crystal, such as lead tungstate, this results in a larger number of scintillating photons emitted inside the medium per unit of shower depth.

Figure 2.12 presents the simulated energy deposit of a 120 GeV electron in randomly (top) and axially (bottom) oriented $PbWO_4$ as a function of depth. Due to the enhancement of the bremsstrahlung and pair production, when on axis, the shower is more compact along the longitudinal direction, with the maximum of the shower located significantly closer to the target front.

The reduction of the shower length in crystals can be seen as the reduction of the effective radiation length values with respect to the standard values obtained in case of amorphous or randomly oriented media.

Already after the first particle interaction, the average energy of each secondary particle decreases after each electromagnetic interaction. Furthermore, such secondary particles are produced with a non-zero angle relative to the shower axis. As a result, at the more advanced stages of the shower development, the full strong field regime is maintained only for a subset of particles; the largest enhancement appears within the first few radiation lengths, whereas downstream the shower development becomes increasingly similar to the one in an amorphous medium or randomly oriented crystal.

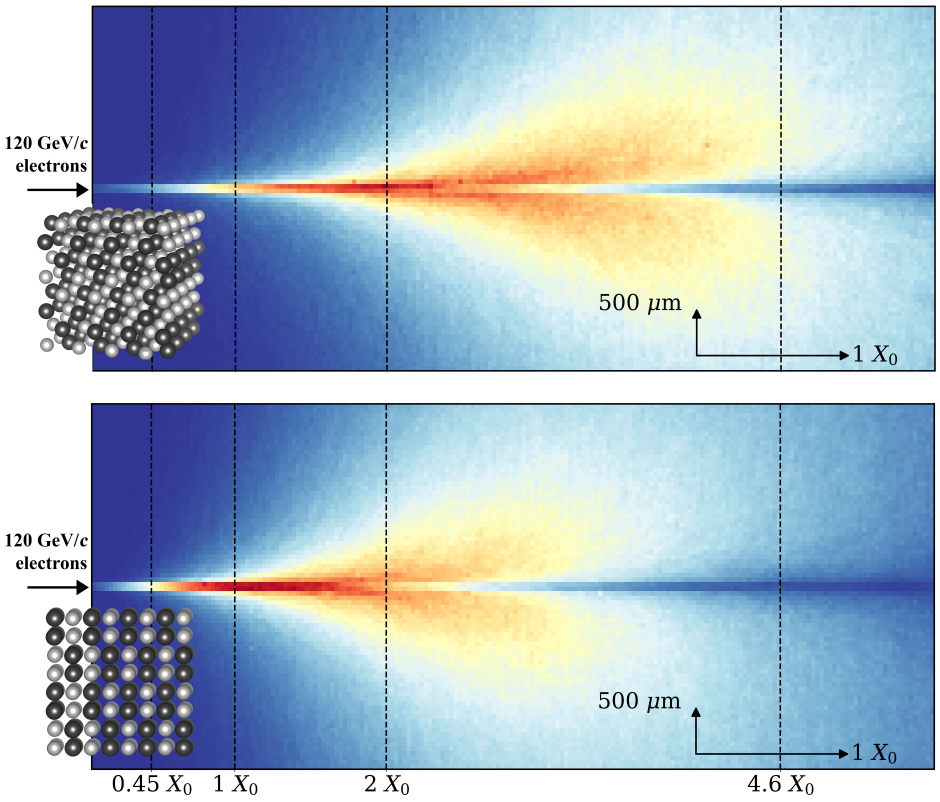

Figure 2.12: Simulated energy density deposited in an electromagnetic shower initiated by 120 GeV electrons as a function of the position inside a randomly (top) and axially (bottom) oriented $PbWO_4$ crystal.

2.2 PRELIMINARY STUDIES ON ORIENTED CRYSTALS

The first experimental evidences of a modification of the features of the electromagnetic radiation emitted by electrons in crystals as a function of the lattice orientation came in 1959-1960 [58–61].

Experimental investigations of the strong field effects on the electromagnetic processes in oriented crystals only started in the 1980s, for both pair production and radiation emission. They were initially focused on very thin ($\lesssim$ 1 mm) silicon, germanium and diamond crystals [62, 63].

Studies on high Z, high-density metallic materials, such as iridium and tungsten, were performed starting from the 1990s, with the aim of developing compact photon converters and high-intensity positron sources. In these studies, only optically opaque and relatively thin crystals were examined [64–66].

The first investigation of the strong field induced enhancement of the radiation emission in an oriented inorganic scintillator was performed only recently, during 2017-2018, by the Axial and quasi-axial coherent interaction between charged particle beams and crystals (AXIAL) project[6], where the enhancement of the radiation from 120 GeV electrons incident on the $\langle 001 \rangle$ axis of a 0.45 X_0 thick $PbWO_4$ has been studied. However, no direct

6 Project of INFN. Experimental teams from the INFN sections of Ferrara and Milano Bicocca and from Laboratori Nazionali di Legnaro were involved in this collaboration.

measurement of the energy deposited inside the crystal sample was performed [67].
A direct measurement of the enhancement of the electromagnetic shower development that occurs in oriented crystals in the full strong regime was performed for the first time recently (2021-2022) by the STrOng cRystalline electroMagnetic field (STORM) collaboration.
This section summarizes the most important results obtained in recent years on the studies on the enhancement of the electromagnetic shower development in oriented lead tungstate, which provided the basis for the construction of the OREO prototype.

2.2.1 EXPERIMENTAL INVESTIGATION OF STRONG FIELD EFFECTS IN ORIENTED CRYSTALS

Four $PbWO_4$ crystal samples of different thickness were studied in 2021-2022 by the STORM collaboration: 0.45, 1, 2, 4.6[7] X_0. Details on the crystals characteristics can be found in [68, 69].
The studies were performed on the H2 extracted beamline at the CERN Super Proton Synchrotron (Appendix C) with a 120 GeV electron beam. The 1 X_0 crystal was also probed with a tagged photon beam with an energy of 5-100 GeV (more details can be found in [40]).
Each crystal was coupled to a SiPM to directly measure the enhancement of the scintillation light inside the crystal itself, because of the shower acceleration caused by the strong crystalline field. Further details in [68].

2.2.1.1 THE EXPERIMENTAL SETUP

Figure 2.13 shows the experimental setup used to study coherent effects in oriented crystals. The same configuration was employed to collect the data with the OREO prototype. A comprehensive description will be provided in Section 3.2.
It consists of:

- a high-resolution tracking system based on silicon microstrip detectors to reconstruct the particle trajectory;
- the crystalline samples installed on a high-precision multi-stage goniometer, to align the crystal with the beam direction;
- a homogeneous electromagnetic calorimeter to measure the energy of the particles emerging from the crystals.

For the measurement with tagged photons, a copper target with a thickness of 1 mm (0.07 X_0) was used to generate bremsstrahlung photons from the incident 120 GeV electrons.

7 The same crystal has been characterized in this work (Chapter 4).

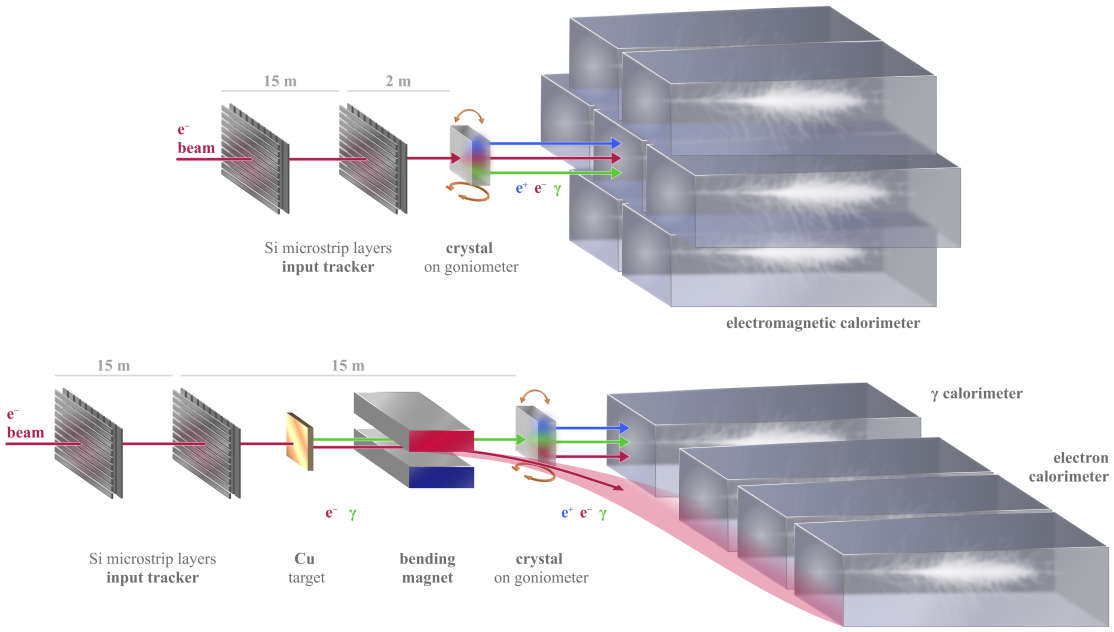

Figure 2.13: Scheme of the experimental setup for (top) the measurement with electrons and with (bottom) tagged photons. The tagged photon beam is produced through a copper converter; the primary electron beam, which exits from the converter, is deflected by the bending magnet and then absorbed by a spectrometer, which is composed of several lead glass calorimeters. The energy of the photons impinging on the crystals is estimated as the difference between the energy of the primary beam and the one measured by the spectrometer [40, 69, 70].

2.2.1.2 ENHANCEMENT OF THE ELECTROMAGNETIC SHOWER DEVELOPMENT

The electromagnetic shower development has been studied as a function of the crystal thickness measuring the scintillation light produced in the crystals with the SiPMs.

Figure 2.14a presents the energy deposited in the random orientation ($E^{\text{rnd}}_{\text{dep}}$) and when the particle incidence beam is aligned with the crystallographic axis, i.e. in the axial orientation ($E^{\text{ax}}_{\text{dep}}$). The energy deposited in the axial orientation increases more rapidly than $E^{\text{rnd}}_{\text{dep}}$, reaching higher values within the first few radiation lengths due to the acceleration of the electromagnetic shower development.

The Monte Carlo simulations were performed using the Geant4 toolkit [71], modified to include the strong field effects (Appendix B). The simulations well reproduce the experimental results, allowing the investigation of the deposited energy for depths larger than 4.6 X_0.

The difference between the energy deposited in the axial and random orientation presented in Figure 2.14b, increases with the crystal thickness.

The ratio between the energy deposited in axial and random orientation is presented in Figure 2.14c; such ratio reaches a maximum value of approximately 3.6 at a depth of 2 X_0[8]. Beyond the maximum the ratio decreases monotonically: the energy of the secondary particles produced during the development of the electromagnetic shower decreases, reducing the intensity of the strong field effects they experience. As a result, further on

8 The simulations indicate the peak at 1.7 X_0.

in the shower development, the cascade evolves similarly to that in a randomly oriented crystal.

Figure 2.15 shows the average energy deposit inside the 1 X_0 crystal sample by the photon

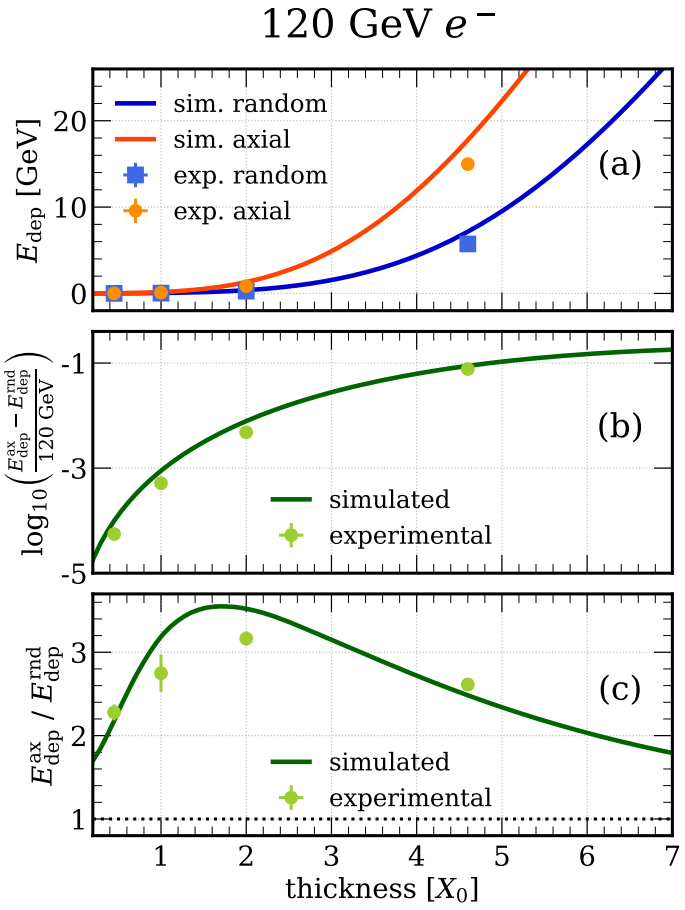

Figure 2.14: Energy deposited by a 120 GeV electron beam as a function of the crystal thickness. (a) Mean E_{dep} in axial and random orientation. (b) Difference between E^{rnd}_{dep} and E^{ax}_{dep} normalized to the beam energy. (c) Ratio between E^{rnd}_{dep} and E^{ax}_{dep}. The solid curves were obtained with simulations [68, 69].

beam as a function of the inferred photon energy[9] (E^{inf}_{γ}) for different incidence angles with respect to the crystallographic axis. The energy deposited in the axial orientation increases significantly with E^{inf}_{γ}, confirming that:

- The enhancement of the pair production cross-section is the same for incident electrons and photons and increases with the energy of the incident particle.
- For incidence angles larger than the strong field acceptance Θ_0, there is still an enhancement of the pair production cross-section, due to the coherent pair production and coherent bremsstrahlung phenomena.

This experimental study of the acceleration of electromagnetic showers provides the foundation for the R&D of the OREO electromagnetic calorimeter, which will be described in the next chapter.

9 Computed as explained in [40, 69].

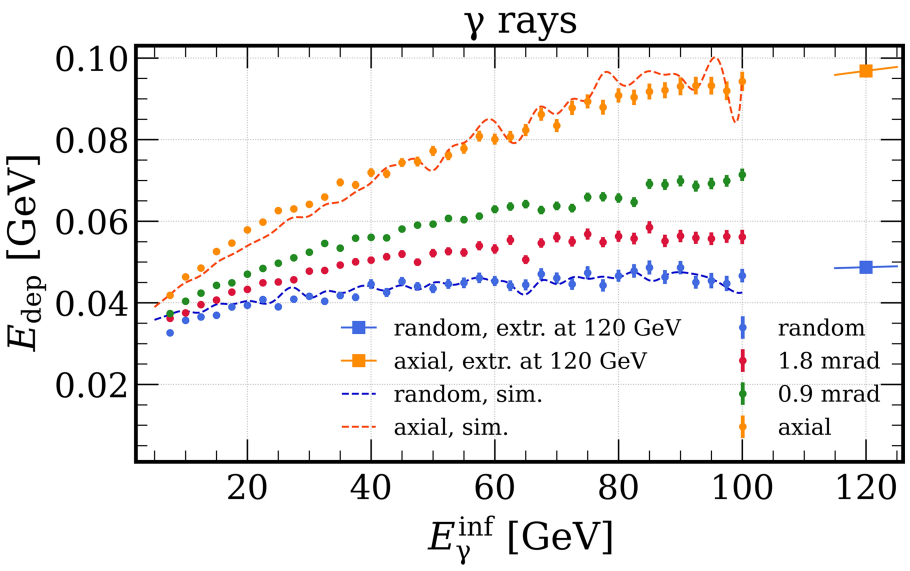

Figure 2.15: Mean energy deposit by photons as a function of their energy, at different incidence angles. Curves from the corresponding simulations (dashed lines) are also presented [40].

3

THE OREO PROJECT

Following the experimental results obtained on the acceleration of the electromagnetic shower development in oriented crystals, the OREO collaboration has assembled and tested a scintillating homogeneous calorimeter prototype based on oriented crystals.
The path towards the construction of the OREO calorimeter consists of different steps, carried out during the years:

- First, the strong field effects have been characterized in a single $PbWO_4$ crystal to quantify the enhancement in the electromagnetic shower development and thus the reduction of the radiation length. Furthermore, an alignment procedure has been standardized to ensure that the crystal is positioned so that the beam impinges along the crystallographic axis. These studies were performed during the 2022 beamtest and are described in Chapter 4.
- The most challenging aspect of an oriented calorimeter design is keeping all the crystals aligned when arranged in a matrix. In 2023, the possibility of aligning a layer of crystals along the same crystallographic direction was demonstrated with two prototypes: a single 3×1 row and a 2×2 matrix of $PbWO_4$-UF oriented crystals, both coupled to SiPM matrices (Chapter 5).
- Having established the possibility of keeping all the crystals aligned when glued together, the OREO calorimeter was finally assembled and tested in 2024 over a wide range of energies. The obtained results are presented in Chapter 6.

This chapter is divided as follows: the first part describes the crystals and the photodetection systems used in each beamtest; the second part describes the experimental setup employed to investigate the strong field effect and to characterize the OREO calorimeter.

3.1 THE $PbWO_4$ CRYSTALS

Altough $PbWO_4$ crystals are widely exploited for homogeneous electromagnetic calorimeters in high-energy physics and astrophysics (Section 1.3.1), their crystalline nature and thus the modification of the electromagnetic processes described in the previous chapter, are typically ignored.
During the years, different generations of lead tungstate crystals have been developed; the main properties of the scintillation mechanism in different generations of $PbWO_4$ are

shown in Table 3.1 [8, 26, 68, 72–75].

First-generation $PbWO_4$ ($PbWO_4$-I) presents good timing performance; its emission

	$PbWO_4$-I	**$PbWO_4$-II**	**$PbWO_4$-UF**
ρ [g/cm^3]	8.28	8.28	8.27
Scintillation max. [nm]	420	420	420
LY [ph. e^-/MeV]	8–12	17–22	7
LY rel. to NaI [%]	0.3	0.6	about 0.2
τ_{decay} [ns]	10–30	10–30	0.64

Table 3.1: Properties of the scintillation mechanism in different generations of lead tungstate.

wavelength near 420 nm (i.e. in the blue range) contains two components with a decay time of $\approx$ 10 ns and $\approx$ 30 ns for the fast and slow component, respectively. The high refractive indexes, $n_o = 2.242$ and $n_e = 2.169$, result in an additional, very prompt light component from Cherenkov emission. Compared to NaI(Tl), lead tungstate features a smaller light yield (LY) of only 0.3%.

The need for an improvement of the $PbWO_4$ light yield (such as for the $\overline{\text{P}}$ANDA experiment [26]), led to the development of second-generation $PbWO_4$ ($PbWO_4$-II).

$PbWO_4$-II features approximately twice the light yield of $PbWO_4$-I; the increase of the light output is obtained by keeping the lanthanum and yttrium ion concentration at $\lesssim$ 50 ppm and under strict control during the doping procedure. The optical transmission is the same between the two generations as well as the decay times. Furthermore, $PbWO_4$-II features better radiation tolerance.

Studies on the luminescence of lead tungstate highlighted the presence of very fast (ultra-fast or UF) scintillation components with sub-ns decay times. High-precision doping techniques [72] allow enhancing these light components, obtaining an overall $\tau_{\text{decay}} of \sim 640$ ps.

3.1.1 THE 2022 SAMPLES AND PHOTODETECTION SYSTEM

In 2022, two 4.6 X_0 thick $\langle 100 \rangle$ $PbWO_4$-I crystals, machined from a single, 15 cm thick spare crystal of the CMS electromagnetic calorimeter [24], were tested, along with the respective SiPMs and front-end electronics. The most relevant properties of the two crystals are reported in Table 3.2; they have a transverse area of 30×30 mm^2 and a surface mosaicity[1] of $\sim$ 250 μrad, measured with a High-Resolution X-Ray Diffractometer (HRXRD) in the INFN Ferrara laboratory [76, 77].

Figure 3.1 shows a photo of one crystal sample; the crystal lateral surfaces of each sample were coated using the EJ-510 white, radiation-resistant reflective paint [78].

The energy deposited inside the crystals has been measured by collecting directly the scintillation light with a dedicated photodetection system based on SiPMs. A SiPM consists

1 The mosaicity is the degree of imperfection or disorder in the alignment of the lattice planes within a crystal.

Axis	$\langle 100 \rangle$
Lattice geometry	Tetragonal [10]
Thickness [mm]	41
Thickness [X_0]	4.6
Transversal size [mm^2]	30×30
Surface mosaicity [μrad]	250
Θ_0 [mrad]	0.908
$\chi = 1$	~ 30 GeV

Table 3.2: Main properties of the 2022 crystals.

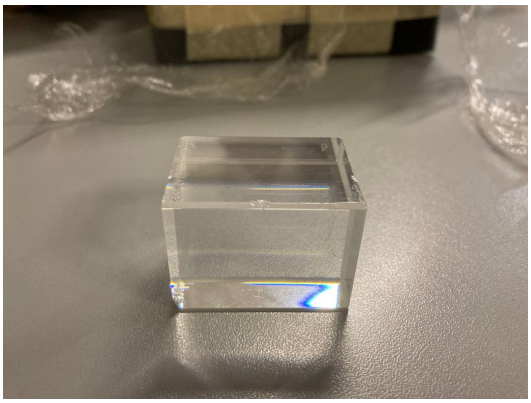

Figure 3.1: Photo of the 2022 $PbWO_4$ crystal without coating.

of an array of pixels connected to a common output; each pixel is a reverse-biased diode working in the Geiger discharge regime (Single Photon Avalanche Diode (SPAD) [79]) with its own quenching resistor. When a photon is absorbed, a Geiger avalanche is produced, causing a photocurrent to flow from the cathode to the anode thus resulting in a voltage drop across the quenching resistor, which in turn reduces the bias across the diode to a value below the breakdown. Each pixel is a digital device: when hit by a photon an avalanche is generated. Given the fact that the pixels are connected to a common output, the output signal is proportional to the number of hit pixels and thus to the number of photons: the resulting information is an analog one and allows estimating the light intensity. SiPMs are fast, linear (on a range which depends on the number of pixels), with a high gain and single photon capability. They need a low voltage bias (a few tens of Volts) and are insensitive to magnetic fields. Their drawbacks are the generally rather strong dependence of the performance on the temperature and the relatively high dark count rate (DCR), i.e., the rate of pixels that turn on because of avalanches triggered by thermally generated electron-hole pairs and free electrons in the diode depletion region.
The photodetectors used during the 2022 beamtest are shown in Figure 3.3; a single photodetection unit consists of three SiPM matrices model ARRAYC-60035-4P-BGA [80] produced by Onsemi [81] and a custom readout board designed at the InsuLab laboratory[2].

2 Università degli Studi dell'Insubria, Como, Italy.

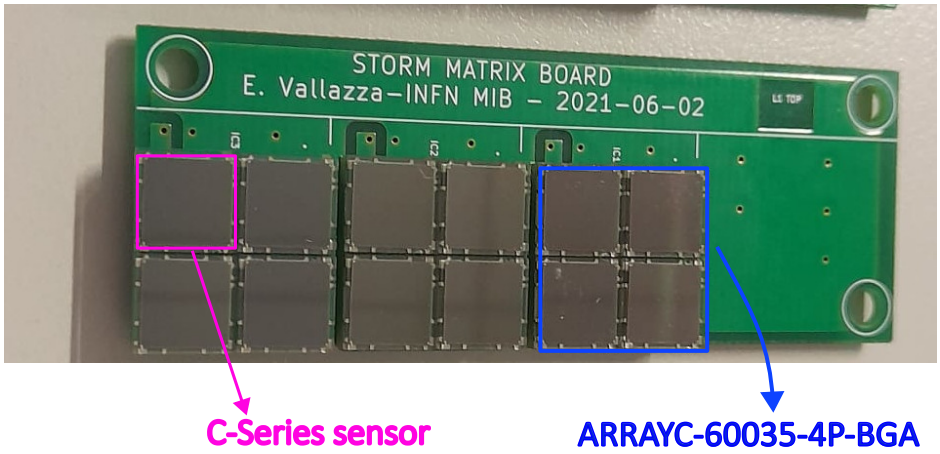

Figure 3.2: Photo of the 2022 photodetection system.

The ARRAYC-60035-4P-BGA consists of 4 individual 6 mm C-Series sensors [82] arranged in a 2×2 array. Each C-Series sensor is a low-noise, blue-sensitive and high gain SiPM with a squared pixel of 35×35 μm^2. Each sensor is mounted on a PCB that routes out the signals as a Ball Grid Array (BGA). The 4 SiPMs cathodes on the single matrix are connected together thus providing a common connection. The features of the array are summarized in Table 3.3.

The readout board has been designed at the InsuLab laboratory[3]; it is a 2 layer 63×23 mm^2

Array Size	2×2
Sensor Type	60035
Readout	Pixel
Board Size	14.2×14.2 mm^2
Pixel Pitch	7.2 mm
Cell Size (C-Series)	35 μm
No. Cells (array)	75 920
No. Connections	9
No. Connectors	3×3 BGA

Table 3.3: Main features of the ARRAYC-60035-4P-BGA [80].

1.5 mm thick printed circuit board. The sensors have been assembled on the board itself by SCEN S.r.l. [83]. The signal of each matrix is coupled with a 100 nF capacitor and is taken to the readout system with a Hirose connector/cable [84].

Four photodetection units have been combined as shown in Figure 3.3; the units have been named Ringo, George, John and Paul.

The crystals and the photodetection system are hosted in a dedicated plastic holder as shown in Figure 3.3 right. During the beamtest, only 8 matrices were connected to the digitizer. Additionally, the photosensors were connected in parallel, two by two, thus forming 4 pairs. The parallel-connected pairs were renamed as Mat_i, $i \in [1, 4]$.

3 E.Vallazza, INFN-Sezione di Milano Bicocca, Milano, Italy

The SiPM sensors were operated at a bias that was typically 10 %-25 % higher than the

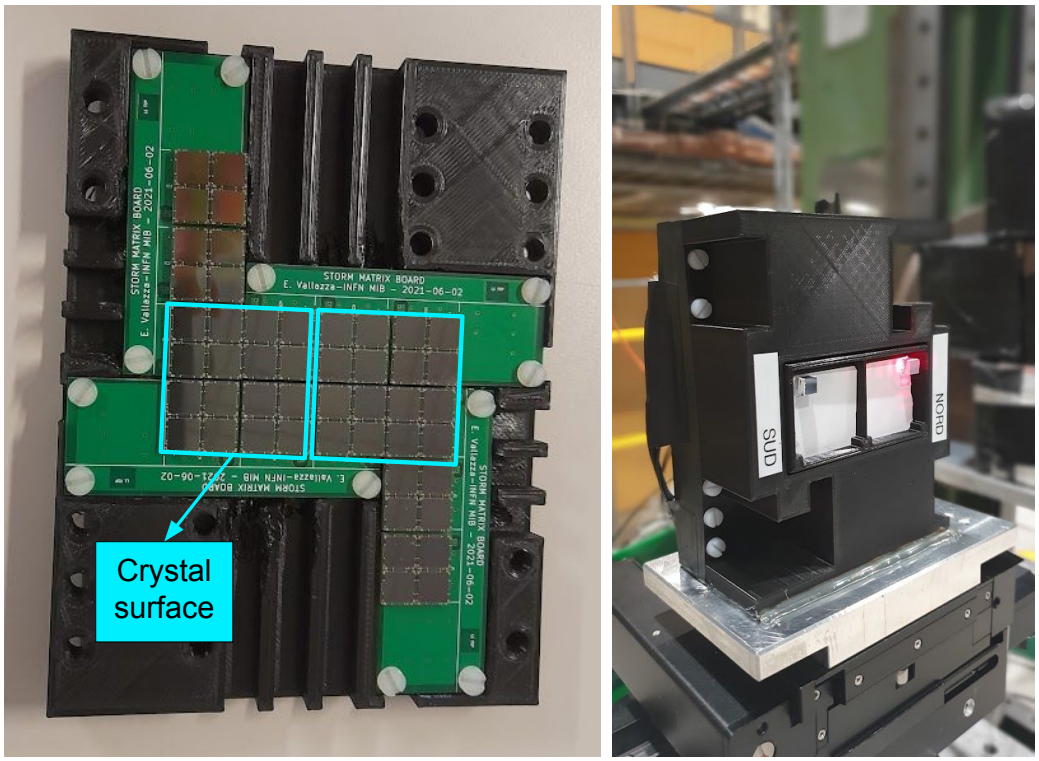

Figure 3.3: Photodetection system used in the 2022 beamtest. (left) SiPM units used for the scintillation light readout. The blue lines indicate the regions where the crystals are positioned to be coupled with SiPMs and (right) the fully assembled crystal-photodetector system installed on a plastic holder.

breakdown voltage V_{br}. The difference between the V_{br} and the bias is referred to as the overvoltage. The overvoltage value is chosen by observing the current-voltage (IV) curve of the SiPMs. Figure 3.4 shows the four units IV curves; during the beamtest the SiPM bias was 30 V.

Figure 3.5 shows an example of a waveform, acquired on the beamline with a 120 GeV electron beam. The abscissa is the digitizer acquisition window in which one clock corresponds to 2 ns, while the ordinate corresponds to the SiPM signal in ADC. The rise time of the SiPM is determined by the rise time of the avalanche formation and the variation in the transit times of the signals arriving from different points on the sensor active area. The recovery time of the sensor is determined by the pixel recharge time constant (which depends on the effective capacitance and on the quenching resistor of the pixel itself, the total number of pixels in the sensor and any resistance in series with the sensor) and by the time features of the readout circuit. In the 2022 beamtest these signals were sampled by a digitizer at 500 MHz, which allowed an acquisition time window of 500 ns; the data acquisition performed the baseline subtraction computing the maximum of the waveform and the corresponding time, saving all the information (maximum, time and waveform) in the output files. As shown in Figure 3.5, the matrices feature a large time to restore the baseline (recovery time), of the order of a μs; however for this data taking a fast recovery time was not needed.

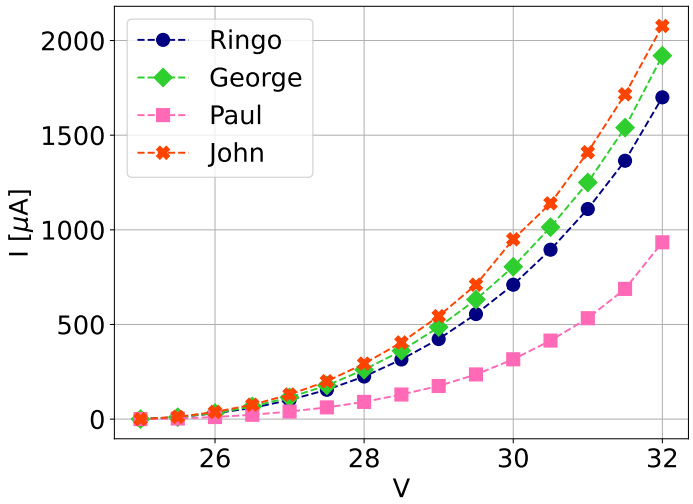

Figure 3.4: The IV curves of the four photodetection units.

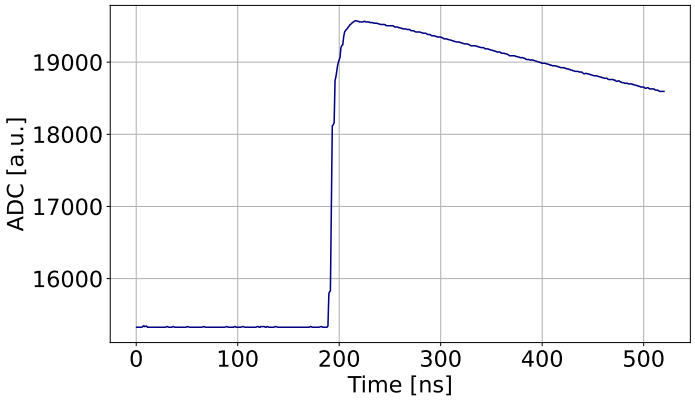

Figure 3.5: The raw waveform of Mat3 acquired on the beamline with a 120 GeV electron beam.

3.1.2 THE 2023 CRYSTALS AND PHOTODETECTION SYSTEM

The prototype samples tested during the 2023 beamtests consisted of a 3×1 row and a 2×2 matrix of $PbWO_4$-UF crystals produced by Crytur [85, 86]. Each crystal had a dimension of $2.5 \times 2.5 \times 4.4$ cm^3, corresponding to a length of 5 X_0.
Each crystal of the 3×1 row and the 2×2 matrix has been characterized and glued together at the laboratory of the Università di Ferrara with the same procedure described in [87]. The miscut angle, i.e., the angle between the lattice planes and the sample surface, was measured at the center of each crystal with microradian precision and accuracy. The variation of the crystallographic axis orientation across each sample was also mapped in order to minimize contributions from mosaicity and from inter sample miscut differences. Before bonding, all lateral faces were coated with the EJ-510 reflective paint [78].
During the alignment and bonding procedure, the samples were mounted on two separate sets of rotational and linear optomechanical stages. The profiles of each crystal surface were measured simultaneously with a wide-field laser interferometer [88] with nanometric precision, enabling to estimate of the relative inclination of the crystals with uncertainties of a few microradians. Using the previously determined miscut angles, the interplanar

angles between crystal pairs were inferred. After the axis co-alignment, an epoxy resin was applied to the lateral faces to bond the crystals together.
The photodetection system was the same employed in 2022 and described in the previous section (Section 3.1.1). The SiPMs of the 3×1 row were all biased at 31 V on the T9 beamline and 28 V on the H2 beamline. The SiPMs of the 2×2 matrix were all biased at 32 V. Figure 3.6 shows the crystals and the photodetection system mounted on a 3D-printed holder specifically designed for the beamtest.

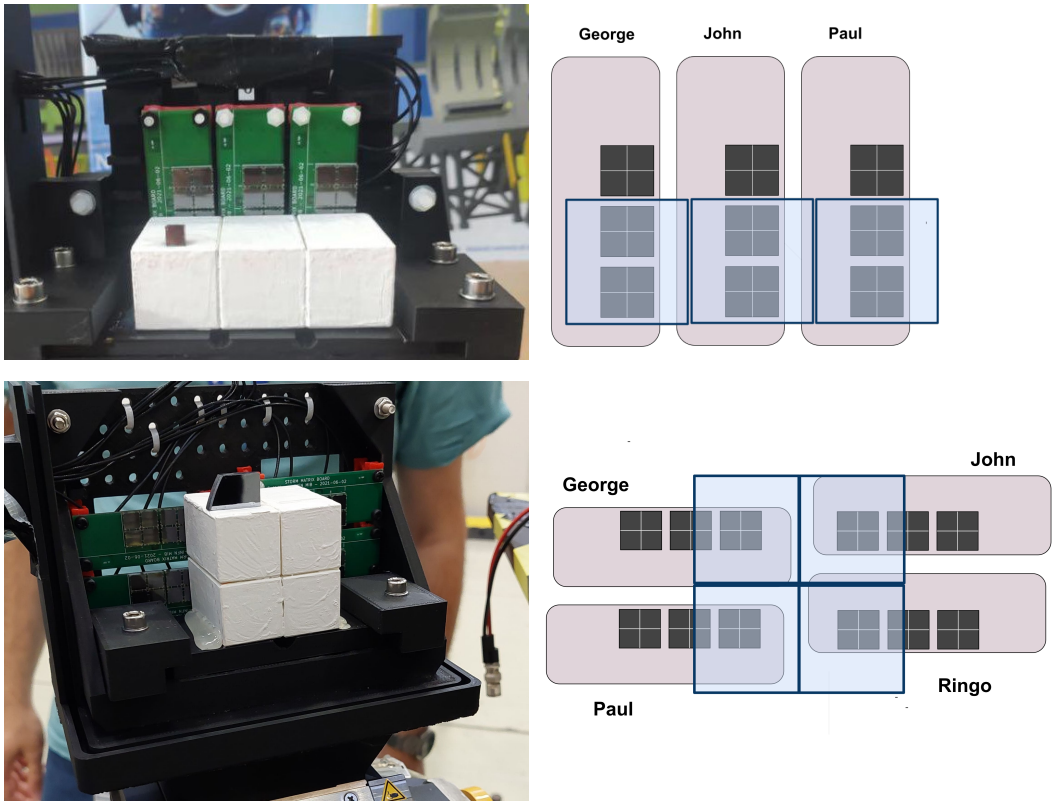

Figure 3.6: (top-left) The 3×1 raw and (bottom-left) the 2×2 matrix of $PbWO_4$-UF crystals mounted on the holder, tested during the 2023 beamtest; (top-right/bottom-right) a scheme of the prototypes coupled to the SiPM matrices.

3.1.3 THE OREO CALORIMETER

The OREO calorimeter consists of a 3×3 matrix of 5 X_0 oriented $PbWO_4$-UF crystals read out by SiPMs, followed by a layer of non-oriented crystals (Figure 3.7).
Beside the advantages of the coherent effects in the upstream layer, described in the previous chapter, another interesting feature of the OREO calorimeter is the transverse segmentation, typically absent in scintillating homogeneous calorimeters. This segmentation can be exploited to enhance the discrimination between electromagnetically interacting particles and hadrons. In oriented crystals, the strong coherent field modifies only the

electromagnetic processes, while the nuclear interaction length[4] is unaffected by the lattice orientation. Consequently, the development of the electromagnetic shower in the upstream layer is accelerated when it is oriented, whereas hadrons interact similarly in both random and axial orientations. The experimental investigation of such effect is presented preliminary in Section 5.2.3 and with the whole OREO calorimeter in Sections 6.1.5 and 6.2.7.

The upstream layer was assembled by bonding the 3×1 row to the 2×2 matrix, tested in

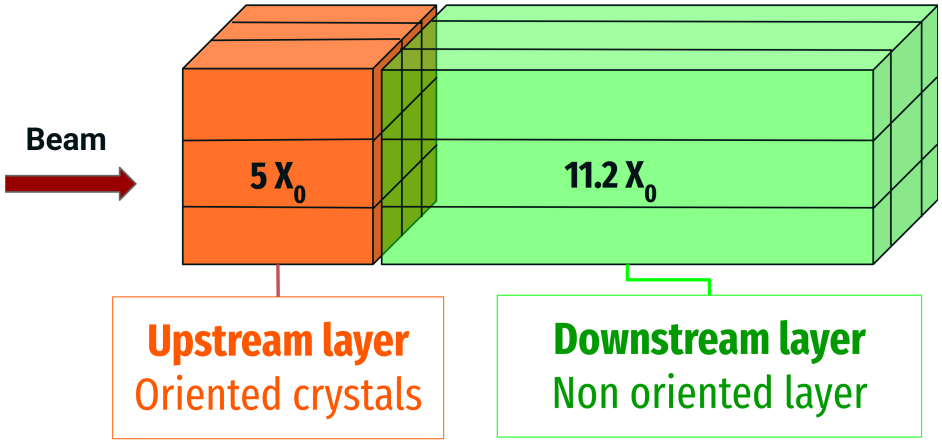

Figure 3.7: Scheme of the OREO calorimeter

2023, and then adding the remaining $PbWO_4$-UF crystals according to the bonding procedure described in the previous section [87]. The downstream layer consists of a 3×3 matrix of $PbWO_4$-UF crystals of $2.5 \times 2.5 \times 10$ cm^3, corresponding to 11.2 X_0.

Each crystal in both layers is read out by a SiPM. To avoid a gap between the two layers, the upstream layer is read out on the upstream face, while the downstream layer is read out on the downstream face, as shown in Figure 3.8. The OREO calorimeter and photodetection system were mounted on a 3D printed holder specifically designed and produced at the University of Ferrara.

3.1.3.1 THE OREO PHOTODETECTORS

The SiPMs used for scintillation light readout in the OREO calorimeter differ from those employed in 2022 and 2023.

The OREO photodetection system consists of eighteen photodetection units (nine per layer, one per crystal) embedded in a plastic holder equipped with a spring mechanism that ensures the proper SiPM-crystal coupling, as shown in Figure 3.9.

Each unit consists of four Hamamatsu Multi-Pixel Photon Counters (MPPC), model S13360-6050VE [89], in a 2×2 layout (Figure 3.10 left); each sensor has an active area of 6×6 mm^2 with 14 336 microcells (50 µm pitch) and a fill factor[5] of 74% (Table 3.4).

The four MPPCs are mounted on a PCB that uses BGA to route the signals. The four cathodes are connected together and biased positively through a 1 kΩ resistor, while the

4 The nuclear interaction length is defined as the mean free path for a high-energy hadron in a material before an inelastic nuclear interaction occurs [8].

5 The fill factor is the geometric fraction of a SiPM pixel that is actually photosensitive. It is given by the active microcell area divided by the pixel total area: $\mathrm{FF} = A_{\mathrm{active}} / A_{\mathrm{total}}$.

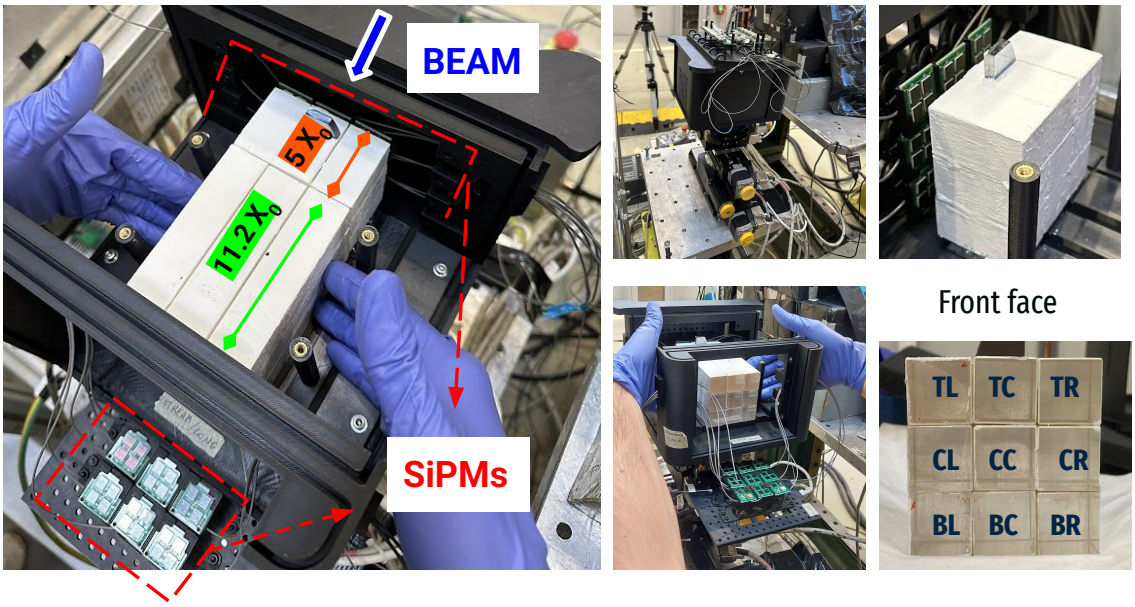

Figure 3.8: Photo of the OREO calorimeter.

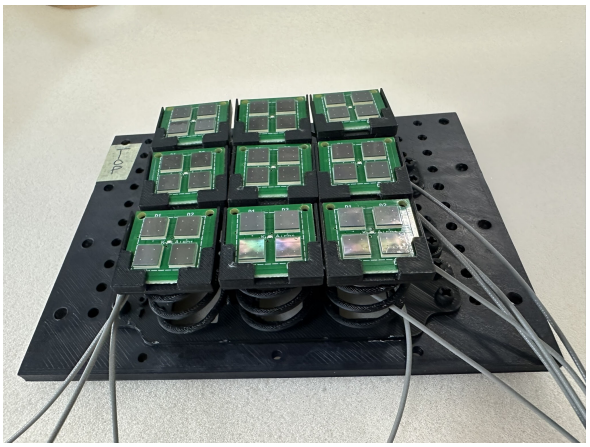

Figure 3.9: Photo of the OREO photodetection system.

anodes are held at ground. The readout board was designed at the InsuLab laboratory[6] while the sensors were assembled on the PCB by SCEN [83]. The matrix cathode (connector J2 in Figure 3.10 center) is linked to a readout board via a Hirose cable/connector [84] (Figure 3.10 right). On the readout board, the nine cathodes are AC-coupled to the digitizer inputs with 100 nF capacitors, which, together with the 50 Ω input impedance of the digitizer, form a high-pass coupling.

Figure 3.11 shows the IV curve of one unit as an example. During the beamtest the SiPMs bias was 53 V on the T9 beamline and 56 V on the H4 beamline.

On the T9 beamline the SiPMs were operated near the breakdown voltage to prevent the saturation of the SiPMs[7]. On the H4 beamline, a Kodak Neutral Density Filter [91] was

6 E.Vallazza, INFN-Sezione di Milano Bicocca, Milano, Italy

7 The saturation is a loss of linearity caused by the number of fired SiPM cells per single event exceeding approximately one-third of the total number of cells [90].

Effective photosensitive area	6×6 mm^2
Geometrical Fill Factor	74 %
No. Cells	14 336
Cell size	50 μm
Spectral response range (λ)	320–900 nm
Peak sensitivity wavelength (λ_p)	450 nm

Table 3.4: Features of the Hamamatsu S13360-6050VE MPPCs [89].

Figure 3.10: (left and center) Photo of a MPPC matrix used for the OREO readout (front and back). (right) Photo of the readout board.

applied to the front face of each layer as shown in Figure 3.12.

3.2 THE EXPERIMENTAL SETUP

The beamtests were performed on the extracted beamline T9 at the CERN Proton Synchrotron (PS) and H2 and H4 at the CERN Super Proton Synchrotron (SPS). The CERN beamtest facilities will be described in detail in Appendix C; in this section the experimental setup used to study the strong field effects and to characterize the OREO calorimeter prototype is presented.

3.2.1 GENERAL OVERVIEW

The study of the strong field effects in oriented crystals and the characterization of the OREO prototypes require a dedicated experimental setup. In particular:

- a fast trigger detector;
- a tracking system with high spatial resolution to measure the x and y impact coordinate of the particle on the crystalline sample transverse plane;

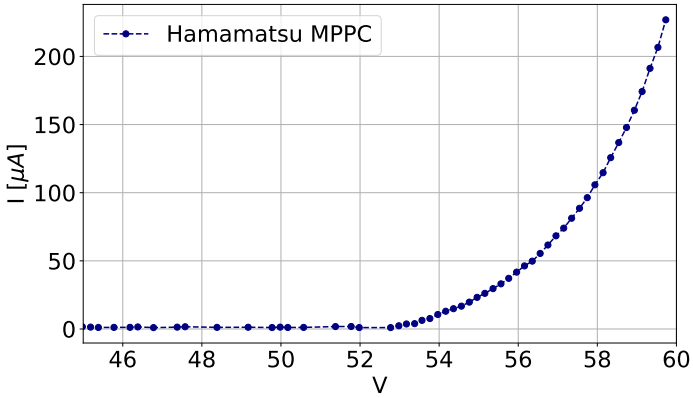

Figure 3.11: Example of a IV curve of the Hamamatsu unit.

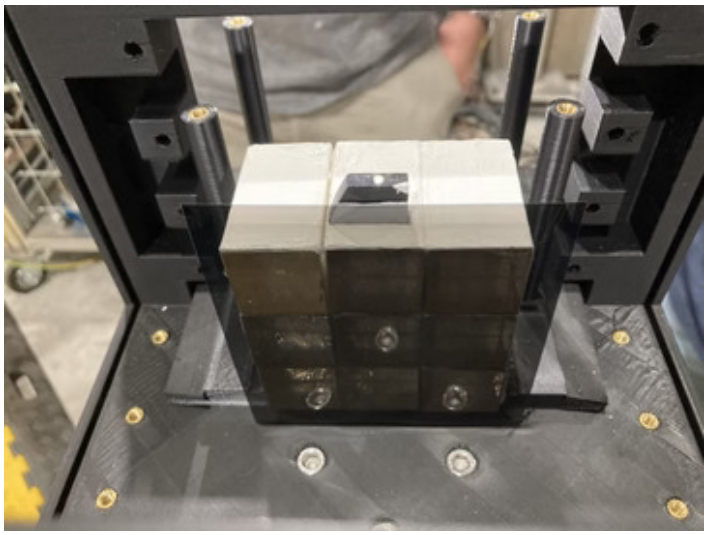

Figure 3.12: Photo of the Kodak Neutral Density Filter applied to the crystal matrix front face.

- a multistage goniometer for the precise spatial and angular alignment of the beam with the crystalline lattice;
- an electromagnetic calorimeter to measure the energy of the crystal output particles;
- a dedicated Data AcQuisition (DAQ) that works on an event-by-event basis, in order to study the correlation between all the measured quantities.

Figure 3.13 shows a simplified scheme of the experimental setup used in the beamtests described in this work. Each component is described in detail in the following sections.

3.2.2 THE TRIGGER SYSTEM

THE 2022 BEAMTEST

In the 2022 beamtest the trigger was provided by two plastic scintillators (S1 and S2) with an area of 4×9 cm^2 and a thickness of 7 mm along the z direction, both mounted on the front face of the first silicon telescope (Section 3.2.3) and read out by standard high-voltage

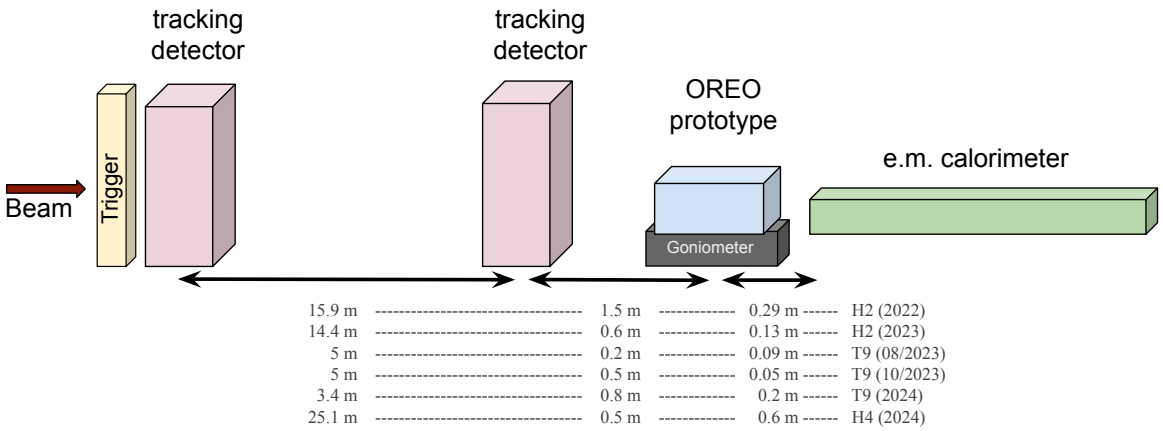

Figure 3.13: Scheme of the experimental setup used to study the strong field effects in oriented crystals and to characterize the OREO prototypes. From left to right: a trigger detector, a tracking system for the particles trajectory reconstruction, the prototype under test on a high precision goniometer and an electromagnetic calorimeter positioned downstream. The distances between the detectors in each beamtest are listed.

photomultiplier tubes (Figure 3.14, left). The S1 scintillator featured a 3.5×9 mm^2 aperture, so that the trigger condition was the coincidence between the beamline spill signal (from the accelerator monitoring system) and S2 in anti-coincidence with S1:

$$\text{Trigger} \;=\; \text{spill} \;\wedge\; \left(S2 \;\wedge\; \overline{S1} \right)$$

In this way, only particles crossing the S1 aperture were recorded, effectively collimating the beam while defining a maximum beam spot size.

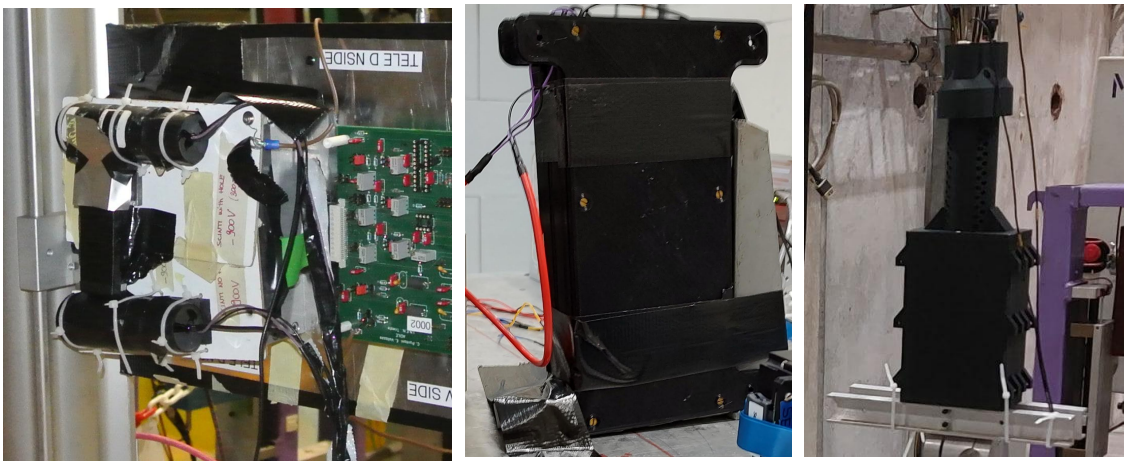

Figure 3.14: (left) The S1 and S2 trigger scintillators used in the 2022 beamtest. (Center) The plastic scintillator used in the 2023 beamtests. (right) The plastic scintillator used in the 2024 beamtests.

THE 2023 BEAMTESTS

In 2023 the DAQ trigger was generated by a plastic scintillator (Figure 3.14 center) with an area of 10×10 cm^2 and a 1 cm thickness, read out by a PMT. In both the beamtests

performed on the T9 and H2 beamlines, the trigger was given by the coincidence between the plastic scintillator discriminated signal and the beam spill signal.
The T9 beamline (SectionC.1) is equipped with two Cherenkov threshold detectors, XCET44 and XCET48, for the particle identification. During the August 2023 beamtest, the signal from the XCET44 threshold Cherenkov detector was used as a trigger in coincidence with the plastic scintillator.

THE 2024 BEAMTESTS

During the 2024 beamtest the trigger was provided by the discriminated signal of a plastic scintillator with a sensitive area of 10×10 cm^2 and a thickness of 1 cm, readout by a PMT, in coincidence with the spill signal (Figure 3.14 right).

3.2.3 THE TRACKING SYSTEM

The 2022 tracking system was composed by two modules of double side x-y small area silicon microstrip detectors (T1 and T2 telescopes [92, 93]) while in the 2023 and 2024 beamtests two single side silicon microstrip detectors (the AGILE Beam Chambers [93–97]) were used.

THE INSULAB TELESCOPES

The InsuLab Telescopes are shown in Figure 3.15. Each module consists of a double-side, high-resistivity 300 μm-thick 1.92×1.92 cm^2 silicon microstrip detector, and its frontend electronics. The junction side (p^+ side of the silicon tile) of the detector has 384 strips with a readout pitch of 50 μm, while the implant pitch is 25 μm (a floating strip readout scheme is applied, that is, only 1 strip out of 2 is actually read). The ohmic side (whose strips are orthogonal with respect to the junction one) has 384 readout strips with a pitch of 50 μm, separated by p^+ blocking strips, and no floating scheme is used. The full depletion voltage is in the 36–54 V range. Each silicon side is read out by three VA2 ASICs, 128-channel radiation-tolerant integrated circuits built with the 1.2 μm N-well CMOS technology. Each ASIC channel consists of:

- a folded-cascode low-noise/low-power preamplifier;
- a CR–RC shaper;
- a sample & hold circuit.

The 128 output signals are multiplexed on a single output line, with a maximum frequency for the readout clock of 10 MHz. The three ASICs are AC-coupled to the double-side silicon detector with external quartz capacitors. They are interfaced with the rest of the frontend electronics with a multi-layer ceramic hybrid. The *n*-side signals are level-shifted by an opto-coupler and the output signals of both sides are conditioned by a repeater card which provides the bias voltage, the power, and the control signals to the hybrid.

The high spatial resolution of the two modules (5 μm on the junction side and 10 μm on the ohmic side) allows measuring, with a high precision the trajectory and the input angle of the charged particles impinging on the crystals.

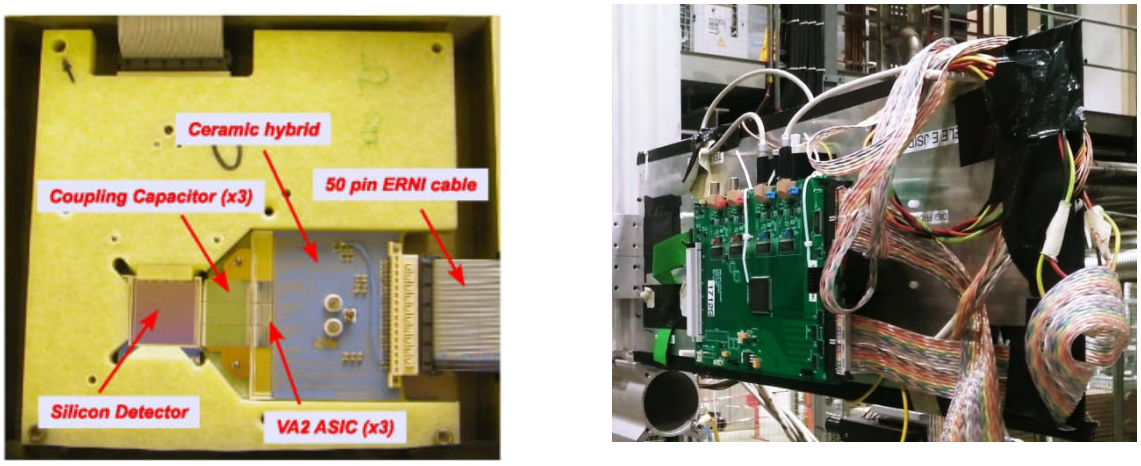

Figure 3.15: (left) The telescope module assembled on the fiberglass frame together with the readout ASICs and the ceramic hybrid. (right) The telescope box on the beamline.

THE AGILE BEAM CHAMBERS

The AGILE beam chambers are based on detectors originally developed for the AGILE satellite [94]. Each chamber consists of two 9.5 $\times$ 9.5 cm^2 single-side silicon tiles 410 μm thick, arranged in x–y configuration. The strips have a physical pitch of 121 μm, and a floating-strip readout is employed, that is, only one strip out of two is read out. The detector spatial resolution is 30 μm [95]. As shown in Figure 3.16, the sensors are assembled on 3 or 5 mm thick fiberglass supports 3 or 5 mm together with the ASIC printed-circuit board. The strips are connected via 17 μm aluminum wire bonds to a pitch adapter that matches the sensor readout pitch (242 μm) to the ASIC channel pitch (100 μm). Each sensor is read out by three 128-channel, low-noise, analog–digital TA1 ASICs fabricated in 1.2 μm N-well CMOS technology. Each channel consists of a preamplifier, a CR–RC shaper, and a sample&hold circuit; the shaper output also feeds a high-pass filter and a discriminator with a tunable threshold. Whenever any of the 128 channel signals exceeds the threshold, a digital trigger signal is generated. The differential analog output is multiplexed, with a maximum readout clock frequency of 10 MHz.

3.2.4 THE GONIOMETER

The study of the coherent effects in oriented crystals requires an accurate alignment system to orient the crystal with respect to the particle beam. A high-precision goniometric system was employed to position the crystal on the beam and to perform fine angular alignment (Figure 3.17). The goniometer consists of four different stages (produced by Physik Instrumente (PI) [98]):

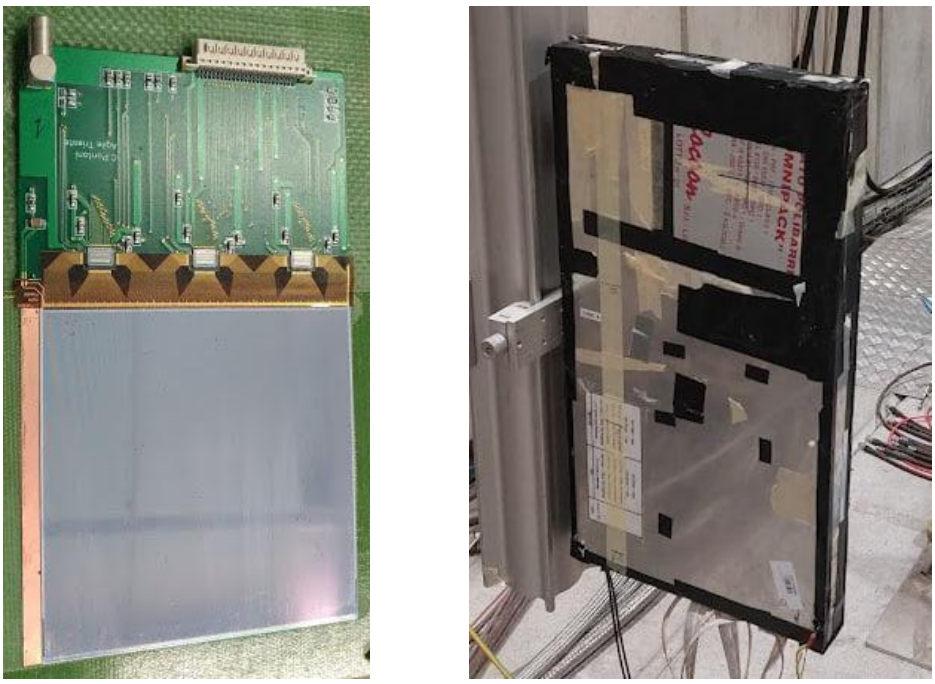

Figure 3.16: (left) An AGILE silicon microstrip layer coupled to the ASICs PCB and assembled on the fiberglass support. (right) The Agile Beam Chamber on the beamline.

- a linear stage for the horizontal translation along x, perpendicular to the beam;
- a rotational stage for the azimuthal alignment in the x-z plane;
- a second linear stage to complete the transverse positioning;
- a cradle stage for the movements in the y-z plane.

The system is remotely controlled by the DAQ computer via PI controllers (Corvus [99], Pollux [100] or Mercury [101]) directly connected to the DAQ computer. During the beamtests, the goniometer has been installed on the XSCA table [102], a remotely controlled platform, which offers two additional translational degrees of freedom along the x and y directions, that is, perpendicularly to the beam. A comprehensive description of the features of the goniometer may be found in [103].

3.2.5 THE ELECTROMAGNETIC CALORIMETER

The energy of the $e^{\pm}$ exiting the OREO prototypes was measured by a homogeneous calorimeter placed on a Desy table [102], located at the end of the beamline.
In the 2022 and 2024 beamtests the homogeneous calorimeter was composed by seven lead glass blocks, arranged as shown in Figure 3.18-right while in 2023 only one block has been used. Each block has been developed for the barrel electromagnetic calorimeter of the OPAL experiment [27]. They are made of Schott SF57 glass with 76% of lead[8]; each

8 In the lead glass calorimeter, the shower generated by the particle produces Cherenkov radiation (Section 1.3.2).

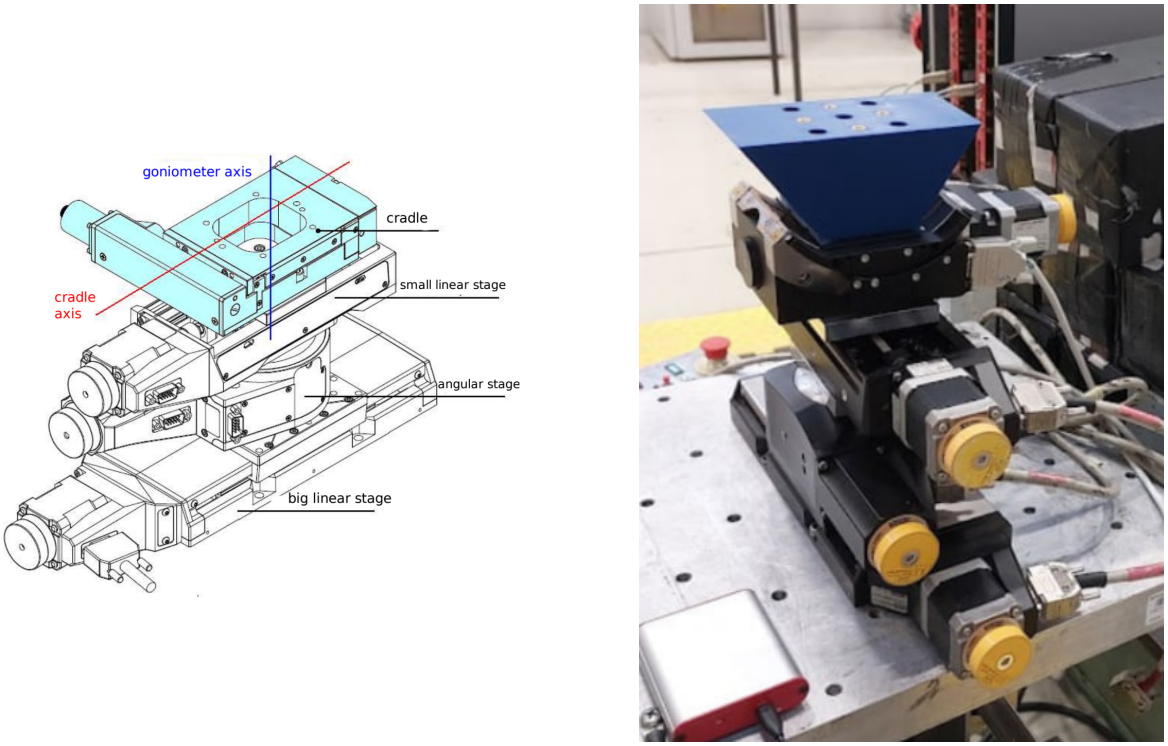

Figure 3.17: (left) A scheme of the goniometer; from top to bottom: the cradle, the small linear stage, the angular stage, the big linear stage. (right) A photo of the goniometer on the XSCA table on the beamline.

block has a thickness of 37 cm ($\sim$ 24.7 X_0), a transverse area of 10×10 cm^2 at the front face and of 11×11 cm^2 at the rear face. The transverse half-size of the active volume is $\sim$ 5.5 cm $\sim$2.13 R_M (R_M = 2.578 cm).
Each lead glass is coupled to a high voltage Hamamatsu R9880U-110 PMT [104], biased in the 900-1000 V range, and covered with an aluminum foil and a cardboard layer to protect it from the environmental light.

3.2.6 THE DAQ SYSTEM

The DAQ system is controlled by a dedicated software developed by the InsuLab group[9]. The source code consists of a set of C [105] routines which are called by a Graphical User Interface (GUI) written in Tool Command Language (Tcl) [106], which is a dynamic programming language.
The data taking procedure is the following (Figure 3.19):

- the signals of the trigger scintillator are sent to a NIM discriminator;
- the discriminated signals, are sent to a VME trigger board along with the SPS spill signal to generate the trigger;

9 M. Prest and E. Vallazza.

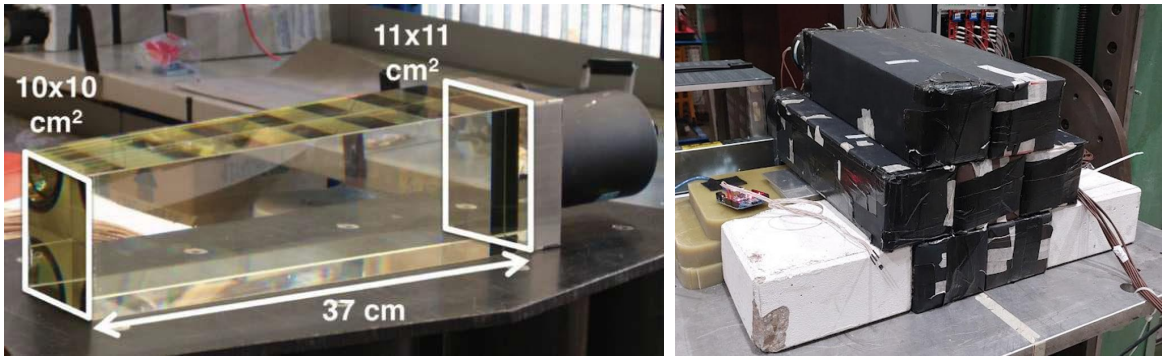

Figure 3.18: (left) Single lead glass block without the outer cover. (right) The seven lead glass arrangement used both in the 2022 and 2024 beamtests. During the 2023 beamtest only a single lead glass block has been used.

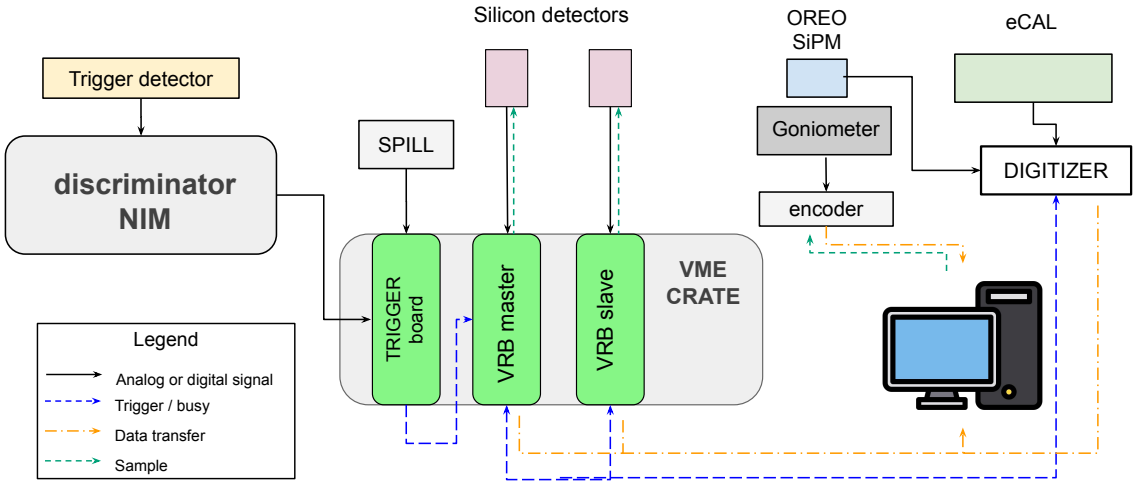

Figure 3.19: Scheme of the DAQ system.

- the VME Readout Board (VRB) of the first silicon detector (VRB master) generates a busy signal that acts as a trigger for the slave VRB (the one of the other silicon detector) and for the digitizers, that read out the signals of the other detectors (SiPMs and lead glass calorimeters);
- each VRB generates the hold signal to sample the peak of the shaper output, after a given time interval chosen to optimize the signal-to-noise ratio;
- in the readout phase, the silicon output signals are digitized by dedicated two channel Analog to Digital Converter (ADC) and sent to the corresponding VRB, where they are stored until the inter-spill period[10].

10 The beam monitor instrumentation at the SPS produces two digital signals: "warning of extraction" and "end of extraction". The first is used to start the spill signal and the second to stop it. The spill signal is used in

- in the VRB either all the strip values are stored for each event or only the strips above a given threshold are stored in the RAM (i.e in the zero-suppression mode);
- the digitizers receive the busy signal generated by the master VRB and sample the waveform from the other detectors. An online algorithm determines the maximum value of each output signal Pulse Height (PH) and the corresponding instant in time. These values, along with the baseline of the readout channels and the sampled waveforms, are stored into memories and saved to the disk in the inter-spill period;
- the readout of the angular and linear stages of the goniometric system is performed by optical encoders, remotely controlled by the DAQ;
- during the inter-spill period the data are saved in HBOOK ntuples;
- an online pre-processing procedure selects the single particle events, that is the ones with a single cluster[11] in each silicon detectors, and produces ASCII files in which every row corresponds to an event while all the information of the single event are arranged in columns: the coordinates of the silicon hit positions and the number of clusters, the PHs and the times of the digitizers, the goniometer coordinates and the event number;
- the final file is a root tree storing the ASCII file same information.

The main features of the digitizers used during the OREO beamtest are listed in Table 3.5.

Property	**DT5730** [107]	**V1724** [108]	**V1730S** [109]
Number of readout channels	8	8	8
Resolution [bits]	14	14	14
Maximum sampling frequency (f_{sampl}) [MS/s]	500	100	500
Full scale range [V_{pp}]	2	2.25 (single-ended)	2
Beamtests [year]	2022, 2024	2022, 2024	2023, 2024

Table 3.5: Features of the CAEN digitizers used in the OREO beamtests.

AND with the scintillator trigger and the end of the spill signal starts the data transfer, from the VRBs and the digitizers to the PC. At the PS, the spill signal is provided ready to be used with the same logic.

11 A cluster is defined as the groups of neighboring strips where the particle deposits its charge, for each silicon module.

4

THE 2022 BEAMTEST

The first step in developing a new prototype of electromagnetic calorimeter based on oriented crystals is to experimentally study the strong field effects in a single $PbWO_4$ crystal, in order to quantify the enhancement in the electromagnetic shower development and, thus, the reduction of the radiation length.
This chapter presents the results obtained with a single 4.6 X_0 $PbWO_4$ crystal (Section 3.1.1) during the 2022 beamtest on the H2 beamline of the CERN SPS.
The chapter starts with the description of the alignment procedure, which ensures that the crystal is positioned such that the beam impinges along the crystallographic axis. This procedure is standardized and applied to all the beamtests discussed in this thesis. Next, the acceleration of the electromagnetic shower development is studied as a function of the incidence angle θ relative to the crystallographic axis and as a function of the beam energiy, in the 80-120 GeV range. Finally, the reduction of the radiation length is evaluated.

4.1 THE CRYSTAL ALIGNMENT PROCEDURE

A crucial step in the design of an electromagnetic calorimeter based on oriented crystals is the development of a standard procedure for aligning the crystallographic axis with the incident particle beam, with an angular precision well below the strong field angular acceptance Θ_0 (Section 2.1.4.2).
The procedure consists of two steps:

- a pre-alignment step, which ensures that the sample is positioned aligned within a few mrad with the beam direction;
- an offline alignment step, which uses the SiPMs signal to achieve a final precision of a few μrad.

4.1.1 THE PRE-ALIGNMENT PROCEDURE

First, the relative orientation between the crystal lattice and the face of the sample is determined. The miscut angle (i.e., the angle between the lattice planes and the sample surface) is characterized using HRXRD techniques at the INFN Ferrara laboratory [76, 77]. This characterization can be performed with a precision of a few tenths of mrad. The

sample is then mounted on a mechanical holder, together with a reference mirror (as shown in Figure 4.1); the angular offset between the crystal and the mirror is measured with high precision.

The initial alignment of the crystal is performed in the experimental area by observing

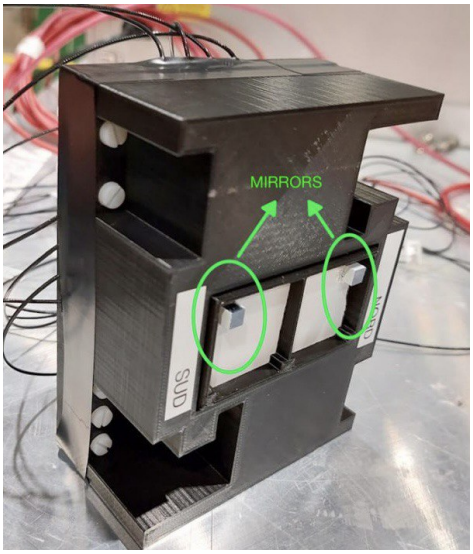

Figure 4.1: The plastic holder housing the $PbWO_4$ crystals: the mirrors are glued in the corners of their surfaces and highlighted in green.

how a laser beam is deflected by the crystal surface. The procedure, illustrated in Figure 4.2, involves the following steps:

1. the crystal sample, mounted together with the reference mirror on a holder, is positioned on the goniometer along the beamline;
2. a straight reference line, parallel to the beam direction, is marked on the floor;
3. two plummets placed along this reference line are used to align the laser beam accurately;
4. a pentaprism is set up in front of the crystal to deflect the laser by exactly 90° onto the reference mirror attached to the holder;
5. if the reference mirror is not perfectly perpendicular to the beam, the laser will not return to its original path. The mirror is adjusted using the goniometer until the reflected laser retraces its incoming path;
6. the holder is then rotated by 90° to align the mirror with the beam direction;
7. finally, the crystal is aligned to the beam using the offset value previously determined in the laboratory.

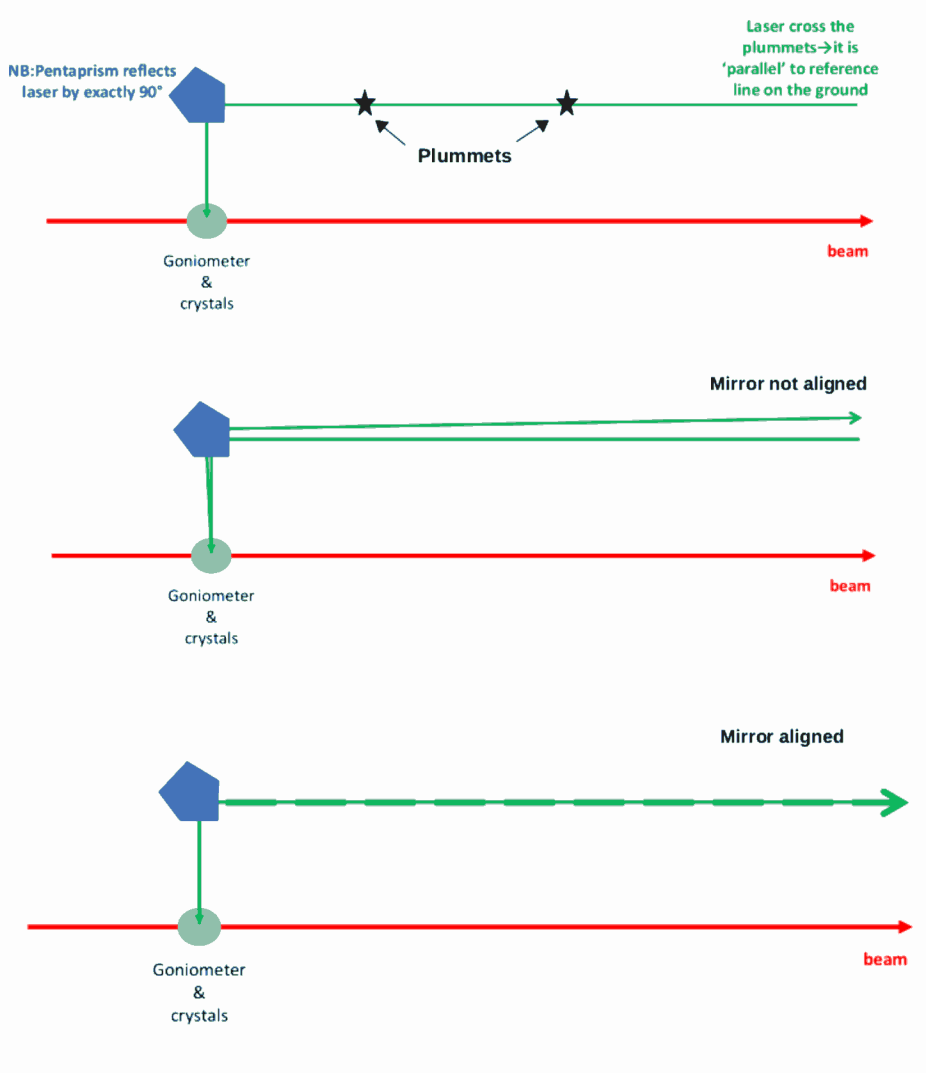

Figure 4.2: Scheme of the manual pre-alignment procedure. The sample is aligned with the beam when the laser returns along the same path.

4.1.2 OFFLINE ALIGNMENT

The found coordinates θ_x and θ_y are very close to the axis (within a few mrad). The precise alignment coordinates are determined by an offline procedure, analyzing the variations in the SiPMs response: as the angle between the beam particles and the axis of interest becomes smaller, the enhancement of the electromagnetic processes in the strong field regime becomes stronger, resulting in the increase of the number of secondary charged particles, and thus in the light output of the $PbWO_4$ crystal.
The offline procedure consists in building the so-called stereogram (Figure 4.3): the abscissa and the ordinate are the x and y coordinates of the misalignment angle i.e. the angle between the particle trajectory and the crystalline sample which is independent on the laboratory frame and is given by:

$$\theta_{\text{mis}} = \theta_{\text{track}} \pm \alpha\theta_{\text{gonio}} \tag{4.1}$$

where θ_{track} is the relative angle between the particle track and the tracking system axis (computed using Equation A.1), and θ_{gonio} is the relative angle between the crystalline sample and the laboratory frame, which is given by the geometrical coordinate of the high resolution goniometer; α is a factor that takes into account the differences in the measurement unit. In the crystallographic stereogram, the origin coincides with the axis and the black lines represent some of the crystalline planes; the axis is the interception point of all the crystalline planes.

Several angular scans were performed starting from the pre-alignment angles, by varying

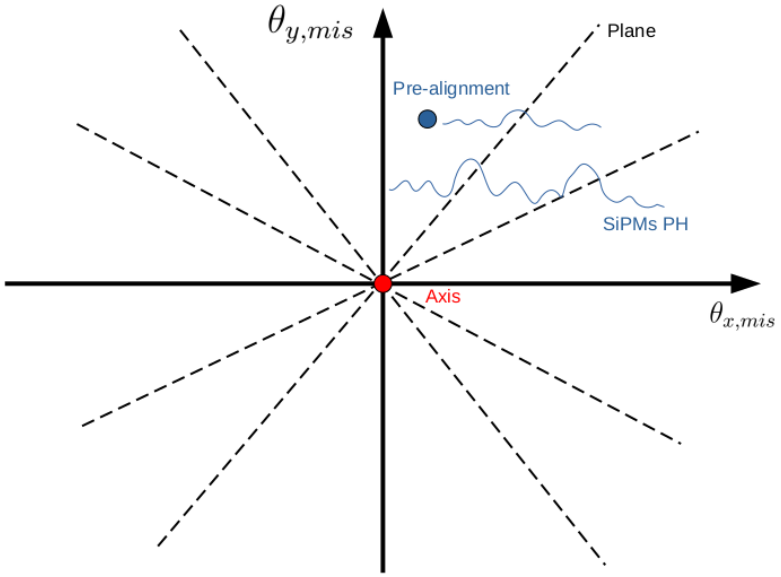

Figure 4.3: The stereogram: the abscissa and the ordinate are the x and y coordinate $\theta_{x,mis}$, $\theta_{y,mis}$ of the angles between the particle trajectory and the crystalline sample; the dashed black lines represent the crystallographic planes, whose intersection point is the axis (red dot). The pre-alignment procedure allows starting the data taking with the sample aligned within a few mrad with respect to the particle beam. The blue lines represent the SiPMs response; the pulse height of the SiPMs is larger when the beam is aligned with respect to the axis; a smaller enhancement is expected when it is aligned with planes.

the goniometer degrees of freedom, defined as θ_{rot} and θ_{cradle} (the angular coordinates of the goniometer rotation stage and the cradle stage, respectively). During each scan, the goniometer was moved either along θ_{rot}, keeping θ_{cradle} fixed, or along θ_{cradle}, keeping θ_{rot} fixed, and the mean value of the PH of the SiPM matrices[1] has been evaluated. Figure 4.4 shows the profile plot of the energy deposit in the crystal during two angular scans along the θ_{rot} and θ_{cradle} directions, performed around the alignment angles: the mean energy deposit increases as the goniometer approaches the alignment condition.

The crystallographic stereogram, obtained putting together different scans, is shown in Figure 4.5; each colored dot represents the mean value of the PHs of the SiPMs, normalized to the maximum value. The axis has been chosen between the two points with the higher PH values. Figure 4.6 shows a second crystallographic stereogram reconstructed using the

1 The PH of the SiPMs matrices are equalized and then summed on an event by event basis; details can be found in 4.2.1.

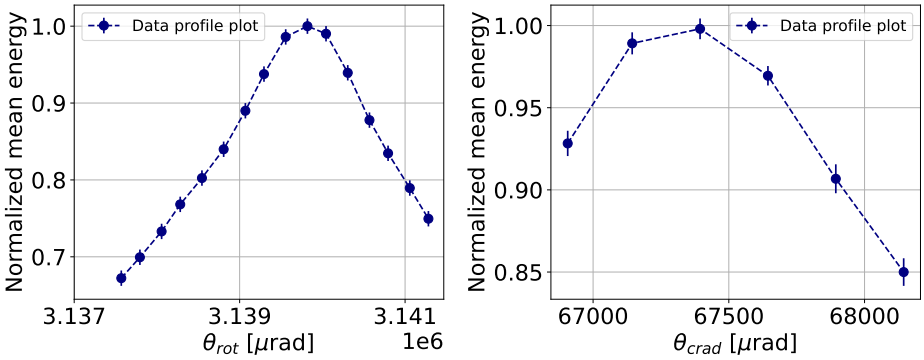

Figure 4.4: Profile plot of the PH of the SiPM matrices as a function of θ_{rot} and θ_{cradle} during an angular scan.

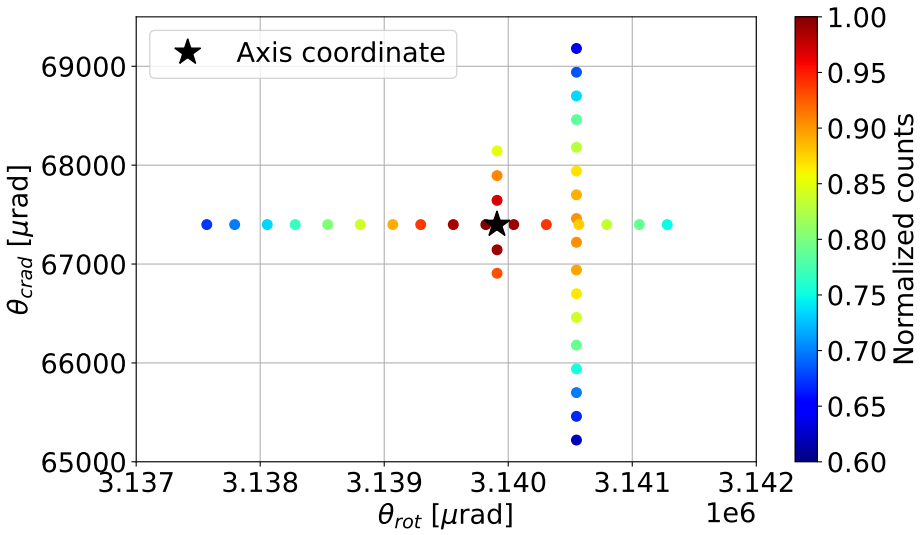

Figure 4.5: The reconstructed crystallographic stereogram; each colored dot represents the mean value of the PHs of the SiPMs, normalized to the maximum value. The axis has been chosen between the two points with the higher PH values.

misalignment angles (defined in Equation 4.1) obtained with a broader set of angular scans. Each bin in the 2D histogram corresponds to a specific range of misalignment angles. The color of the bin indicates the average SiPMs pulse height, computed using all the events falling within that angular range and normalized to the maximum value. It is possible to observe the skew planes[2] of the lattice, indicated with dashed colored lines, whose effect on the electromagnetic processes is very small compared to that of the axis.

4.2 CRYSTAL CHARACTERIZATION

Once the crystallographic axis coordinate is determined, is it possible to characterize the $PbWO_4$ crystal at different misalignment angles to study the angular acceptance of the strong field effects, and at different beam energies (80, 100, and 120 GeV), collecting data

2 The skew planes are neither parallel nor orthogonal to any crystallographic direction; they appear oblique with respect to any other crystal plane or axis.

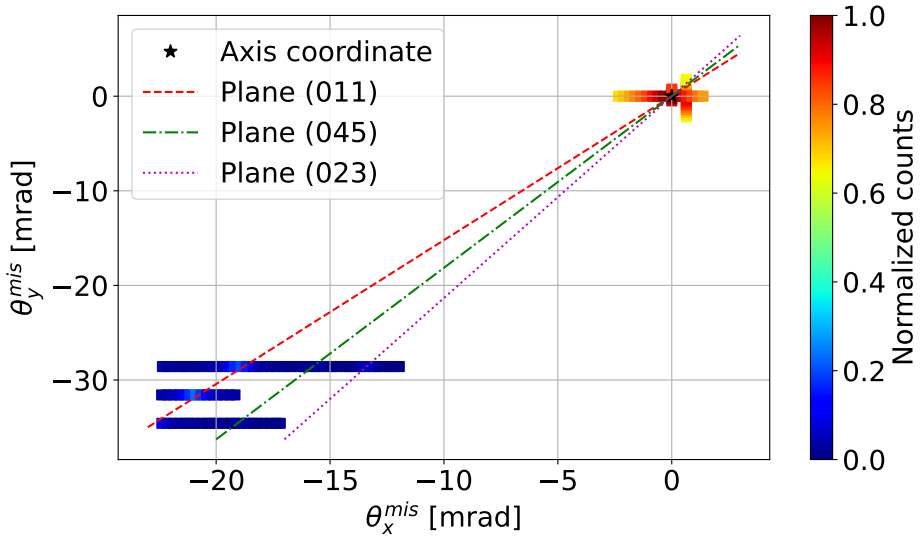

Figure 4.6: The complete crystallographic stereogram: several skew planes are observed at different distances from the axis (black cross), and are highlighted with dashed lines.

in both axial and random configuration, in order to perform a preliminary study on the acceleration of the electromagnetic shower dependence on the incident beam energy. The enhancement in the electromagnetic shower development and the resulting reduction in the effective radiation length are presented at the end of the chapter.

4.2.1 SIPMS CALIBRATION

The scintillation light produced by the electromagnetic shower in the $PbWO_4$ crystal positioned on the beamline has been readout using two SiPM matrices: Mat2 and Mat3 (a scheme is presented in Figure 4.7 while a full description can be found in Section 3.1.1). The energy deposited in the crystal measured by the Mat2 and Mat3 SiPM matrices is expressed in arbitrary units; in order to convert the signal into GeV, a calibration procedure is required. Before performing the calibration, an equalization of the response of the two SiPM matrices, is needed. This is done using the data collected with a 120 GeV electron beam in the center of the crystal. To select the events of interest, a fiducial region was defined based on the crystal efficiency map, i.e., the spatial distribution of the fraction of events in which the SiPMs recorded a signal with a large pulse height. The efficiency, shown in Figure 4.8, is calculated as the ratio between the 2D distribution of the particle tracks that crossed the crystal and produced a detectable signal, and the 2D histogram of all the tracks reconstructed on the crystal.

Furthermore, the events of interest have been selected using the time of the signal, as shown in Figure 4.9: only the particles detected by the trigger and the crystal have the same arrival time, while the other ones are due to the noise or particles that have not crossed the detector. The PH spectra of Mat2 and Mat3 have been fitted with a Crystal Ball

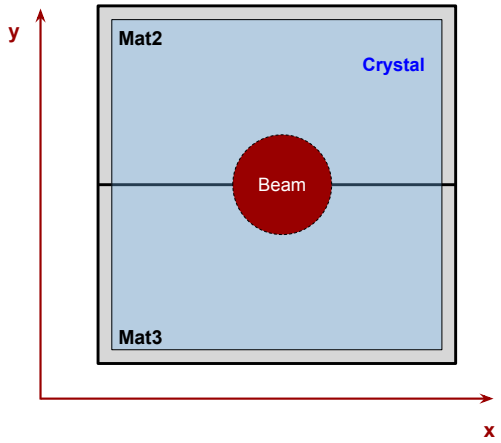

Figure 4.7: Layout of the SiPMs used to read out the scintillation light produced by the electromagnetic shower in the $PbWO_4$ crystal. The x-y direction in red is the reference system defined by the telescopes.

function, defined as follows [110]:

$$f(E;A,\overline{E},\sigma,k_L,k_H) = A \cdot \begin{cases} \exp\left(\frac{k_L^2}{2} + k_L\frac{E-\overline{E}}{\sigma}\right) & \text{if } \frac{E-\overline{E}}{\sigma} < -k_L \\ \exp\left(-\frac{(E-\overline{E})^2}{2\sigma^2}\right) & \text{if } \frac{E-\overline{E}}{\sigma} \in [-k_L,k_H] \\ \exp\left(\frac{k_H^2}{2} - k_H\frac{E-\overline{E}}{\sigma}\right) & \text{if } \frac{E-\overline{E}}{\sigma} > k_H \end{cases} \tag{4.2}$$

where E is the function independent variable while A, $\overline{E}$, σ, k_L, k_H the function parameters. It is essentially composed by a Gaussian core with two exponential tails, and it reproduces how the crystal energy spectrum is smeared due to an incomplete shower containment. The Mat3 pulse height has been rescaled, event by event, with the equalization factor computed as $Q = \mu_{Mat2}/\mu_{Mat3}$, where μ_{Mat2} and μ_{Mat3} are the two Gaussian core mean values extracted from the Crystal ball fit of the Mat2 and Mat3 pulse height; the spectra obtained after the equalization are reported in Figure 4.10.

Once the response of the two matrices has been equalized, their signals can be summed and calibrated. The calibration has been performed using a Monte Carlo simulation of the energy deposited in random orientation, with Geant4, whose details are described in Appendix B. Figure 4.11 shows the simulated energy deposit distribution obtained with electrons of 80-100-120 GeV, along with the experimental data, fitted with the Crystal Ball function. The experimental data were fitted after applying a cut in position at the center of the crystal and a cut on the signal peak time. The calibration lines fitted with a first-degree polynomial and the corresponding residuals, computed as $\text{res}[\%] = 100 \cdot (y_{exp} - y_{fit})/y_{exp}$, are shown in Figure 4.12; all the residuals are compatible with zero, indicating a good linearity.

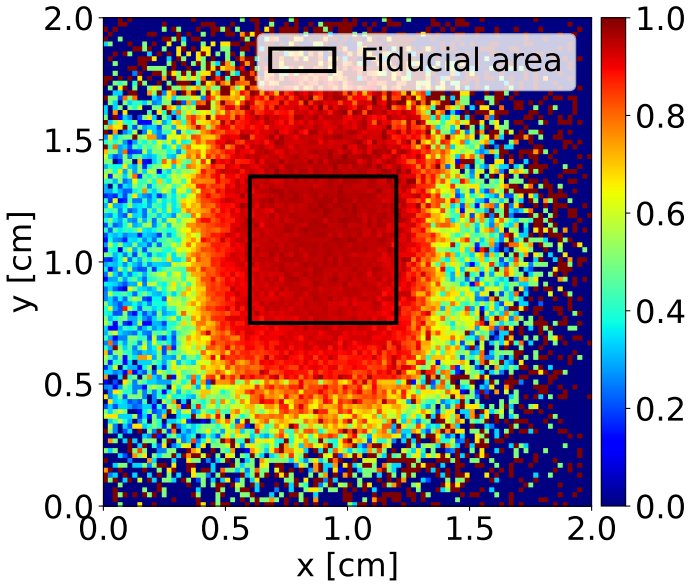

Figure 4.8: Efficiency map of the $PbWO_4$ crystal, defined as the distribution of the fraction of the events where the PH of the reference SiPM was larger than 500 a.u.. The crystal has a transverse size of 30 mm $\times$ 30 mm, which is larger than the beam size both in the x and y direction (the beam size is determined by the S1 trigger which has a transversal size of 3.5 mm $\times$ 9 mm; Section 3.2.2).

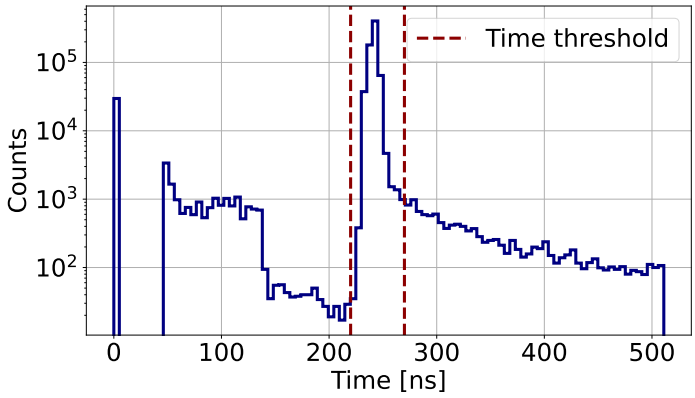

Figure 4.9: Mat2 signal peak time distribution; only the particles detected by the trigger and the crystal have the same arrival time, while the other ones are due to the noise or particles that have not crossed the detector. The red line is the threshold chosen to discriminate these events from the noise.

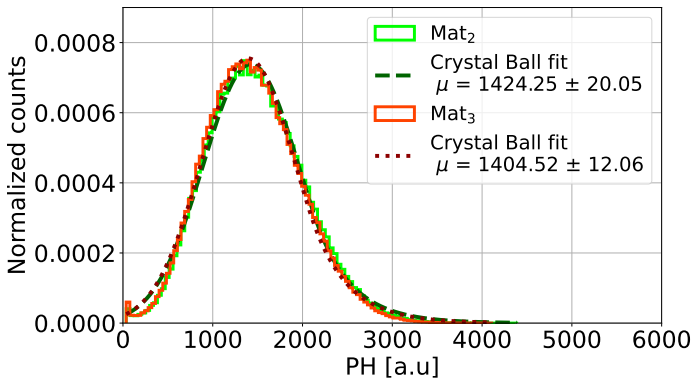

Figure 4.10: Normalized PH of the Mat2 and Mat3 SiPM matrices after the equalization.

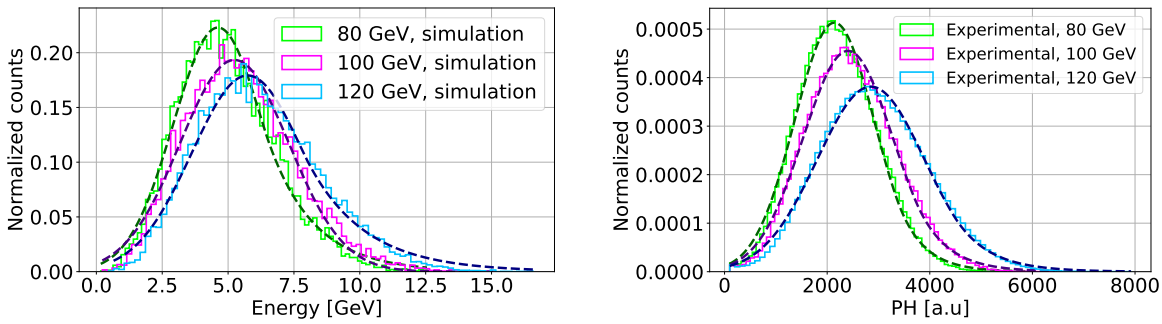

Figure 4.11: (left) Energy deposit distribution in the $PbWO_4$ crystal obtained using the Monte Carlo simulation with Geant4 described in Appendix B. (right) Experimental PH distribution in arbitrary units. Each curve has been fitted using the Crystal Ball function defined in Equation 4.2. The relative increases of the mean values (120/100, 100/80 and 120/80) are compatible between the simulation and the experimental data.

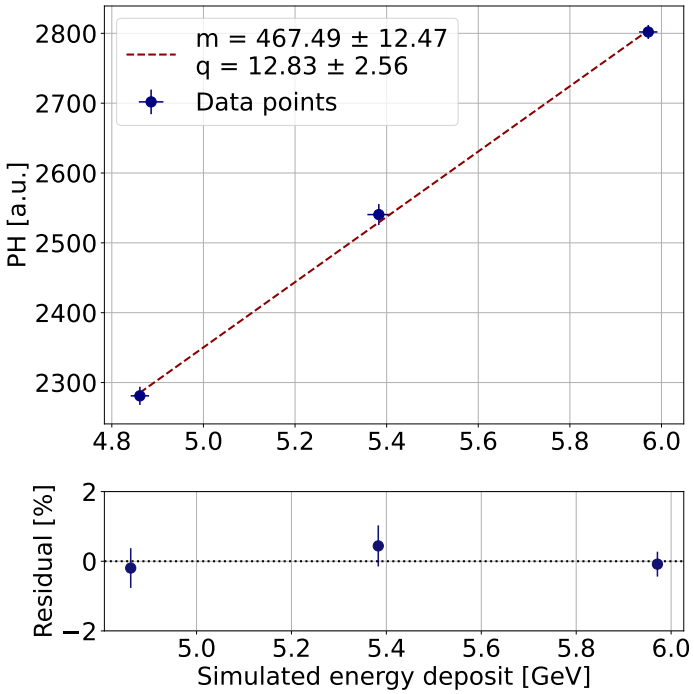

Figure 4.12: Calibration line along with the corresponding residuals.

4.2.2 ENHANCEMENT IN THE ENERGY DEPOSIT

A fundamental step in studying the strong field effects in oriented scintillating crystals is the characterization of the dependence of the coherent effects on the misalignment angle. This requires high-statistics runs with a 120 GeV electron beam directed at the center of the crystal, at an increasing angular distance from the axis and studying the resulting variation in the response of the crystal and the lead glass calorimeter as a function of the misalignment angle. A cut in position is applied to select the events that impinge at the center of the crystal. To study the dependence of the coherent effects on the misalignment angle a cut on the angular divergence is also applied (Figure 4.13). Figure 4.14 shows the energy deposited in the $PbWO_4$ crystal and in the lead glass calorimeter, positioned

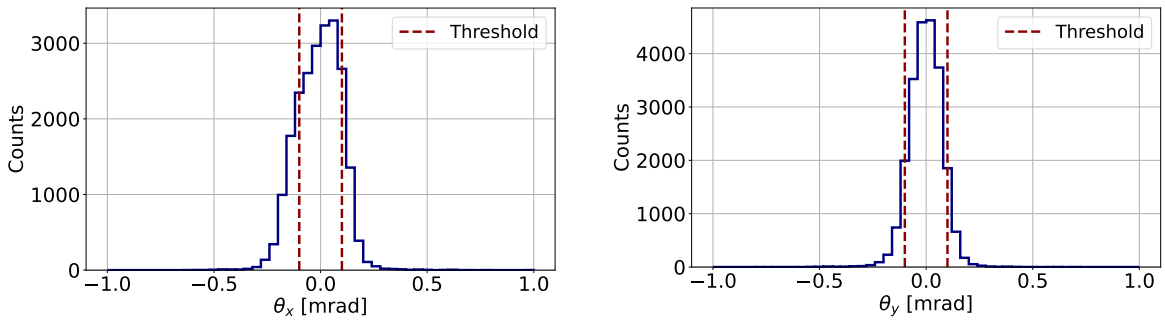

Figure 4.13: 120 GeV electron beam divergence in the x and y directions reconstructed with the silicon detectors (Equation A.1); the red lines are the thresholds chosen to select the most perpendicular events with respect to the crystal face.

0.29 m behind the crystal, as a function of the misalignment angle; as the misalignment angle approaches zero, i.e. the incident beam is aligned with the crystallographic axis, the strong field experienced by the incident electrons leads to an increase in the number of shower particles per unit thickness and thus to an enhancement in the number of scintillating photons; with the maximum of the spectrum moving to higher energies. On the other hand, as the energy deposited in the $PbWO_4$ crystal increases, a corresponding decrease is observed in the energy deposited in the lead glass calorimeter.

Figure 4.15 shows the enhancement factor, computed as the ratio between the energy de-

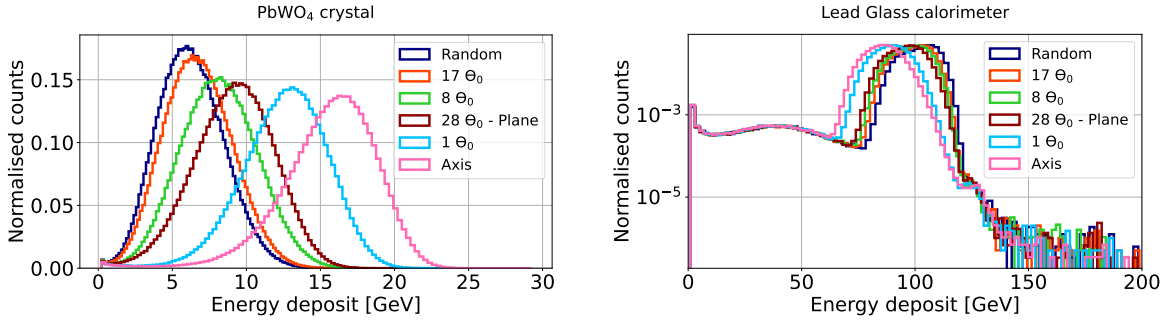

Figure 4.14: Energy deposited in (left) the $PbWO_4$ crystal and in the (left) lead glass calorimeter as a function of the misalignment angles.

posited in the $PbWO_4$ crystal and in the lead glass calorimeter at different misalignment angles and the energy deposit in random orientation, as a function of the misalignment angle; under the effect of the strong field regime, the energy deposited in the axial orientation is 2.64 $\pm$ 0.08 times the energy deposit when the crystal is not oriented. The out-of-scale behavior observed at 28 mrad is caused by the electron beam crossing a crystallographic plane.

The enhancement in the electromagnetic shower development has been studied as a function of the incident beam energy, using electron beams of 80, 100 and 120 GeV impinging on the center of the $PbWO_4$ crystal. Figure 4.16 shows:

a) the μ value extracted from the Crystal Ball fit of the energy deposited in the $PbWO_4$ crystal as a function of the incident beam energy, for both the axial and random

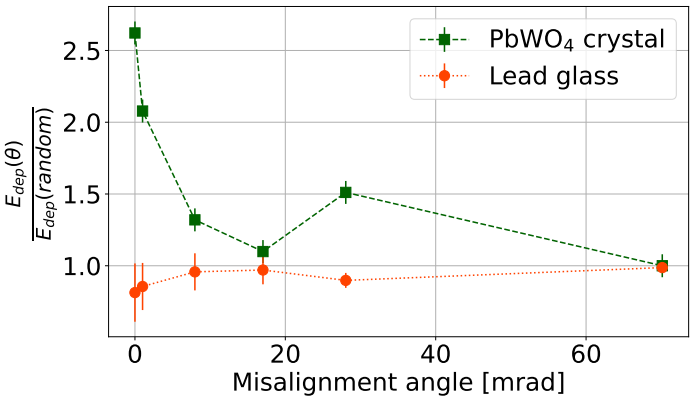

Figure 4.15: Ratio between the energy deposited in the crystal at different misalignment angles and the energy deposited in random orientation, as a function of the misalignment angle.

configurations. A clear enhancement in the deposited energy is observed when the crystal is axially oriented for all the energies.

b) the ratio between the energy deposited in the axial and random orientations. It is interesting to note that such ratio increases with the incident beam energy, from 2.29 ± 0.03 at 80 GeV to 2.64 ± 0.08 at 120 GeV.

c) the μ value extracted from the Gaussian fit of the energy deposited in the lead glass calorimeter placed downstream of the $PbWO_4$ crystal. The earlier development of the electromagnetic shower in the axially oriented $PbWO_4$ crystal leads to a reduced energy deposit in the lead glass calorimeter compared to the random orientation.

4.2.3 REDUCTION OF THE RADIATION LENGTH

Observing the deposited energy distributions, it is possible to estimate the equivalent thickness of the oriented crystal L_{axial}, expressed in units of X_0, seen by the electrons when interacting with it.
An estimation of the reduction of the radiation length[3] is given by:

$$X_0^{\text{red}}\ [\%] = 100 \cdot \left(\frac{L_{\text{axial}} - L_{\text{random}}}{L_{\text{random}}} \right) \tag{4.3}$$

where $L_{\text{random}} = 4.6\ X_0$ is the physical thickness of the crystal. The energy deposit in the $PbWO_4$ crystal was simulated using the Geant4 toolkit (Appendix B). The simulation was performed for three different initial electron beam energies (80, 100, and 120 GeV), generating 10 000 events for each energy. The thickness of the $PbWO_4$ sample was progressively increased in steps of 0.01 X_0. Figure 4.17 shows the obtained cumulative deposited energy as a function of the depth inside the detector, expressed in units of X_0, for the 120 GeV electron beam impinging on a $PbW0_4$ crystal. Given the energy deposited when the crystal is

3 The reduction of the radiation length can be computed by numerically integrating the equations of motion of the impinging particle in the crystal lattice, as described in [111].

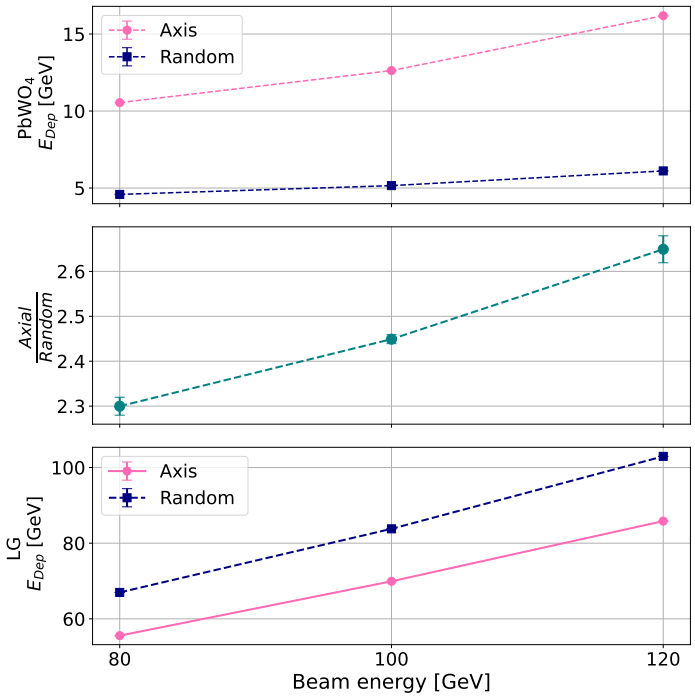

Figure 4.16: (a) The μ value extracted from the Crystal Ball fit of the energy deposit distribution in the axial and random orientation as a function of the incident beam energy in the $PbWO_4$ crystal. (b) Ratio between the energy deposit in the axial and random orientation in the $PbWO_4$ crystal. (c) The μ value extracted from the Gaussian fit of the energy deposited in the lead glass calorimeter placed downstream of the $PbWO_4$ crystal.

axially oriented, L_{axial} can be computed together with the reduction of the radiation length. The obtained values are listed in Table 4.1. For the 120 GeV electron beam, the reduction in the radiation length is $\sim 35\%$; such value is in agreement with the results reported in [68].

	80 GeV	**100 GeV**	**120 GeV**
L_{axial} $[X_0]$	5.98 ± 0.05	6.09 ± 0.03	6.20 ± 0.01
X_0^{red} [%]	30.00 ± 1.09	32.39 ± 0.65	34.78 ± 0.22

Table 4.1: Equivalent radiation length L_{axial} and corresponding radiation length reduction X^0_{red} for different beam energies.

4.2.4 UPSTREAM AND DOWNSTREAM SIPM CONFIGURATIONS

The final design of the OREO prototype consists of a 3×3 matrix composed of two layers of crystals: an oriented layer, read out by SiPMs positioned upstream with respect to the beam, followed by a non-oriented layer with the SiPMs downstream (Section 3.1.3). This configuration was chosen to avoid gaps between the two layers due to the presence of the SiPMs.

During the initial characterization phase, a preliminary measurement was performed to compare the light yield from the upstream and downstream SiPMs, since the directionality

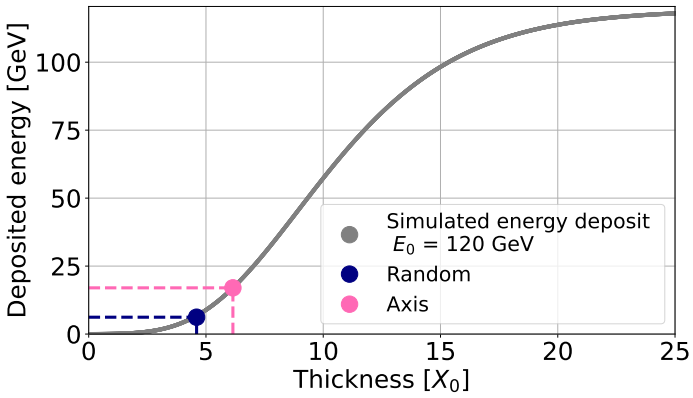

Figure 4.17: Cumulative deposited energy as a function of the thickness of the detector in units of X_0 for a 120 GeV electron beam impinging on a $PbWO_4$ crystal. The data have been obtained with a Geant4 simulation (Appendix B).

of the Cherenkov light may influence the signal detected in the two configurations. The data have been taken in the two configurations as shown in figure 4.18, with the crystal both in the random and axial orientation:

- downstream configuration, with the beam impinging on the face of the crystal and the SiPMs positioned downstream: this is the typical configuration of a calorimeter;
- upstream configuration, with the crystal and the SiPMs rotated by 180° and thus the beam impinging directly on the SiPMs.

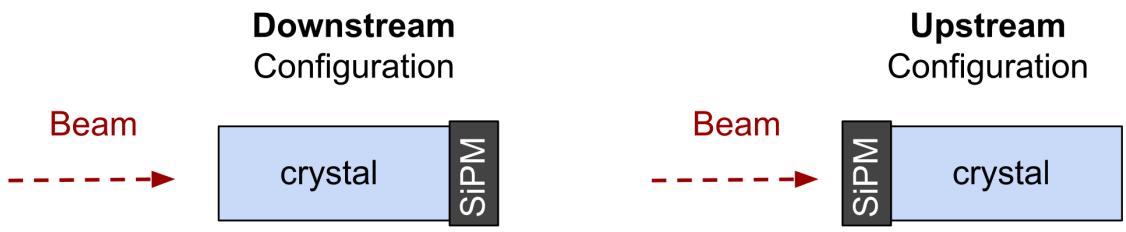

Figure 4.18: Scheme of the upstream and downstream SiPMs configuration.

For each configuration, a position cut was applied to select only the events impinging in the center of the crystal as shown in Figure 4.19. Figure 4.20 presents the energy deposited in the $PbWO_4$ crystal in the two configurations both in the axial and random orientation. The energy deposit distribution has been fitted with a Crystal Ball function: in both the axial and random orientations, the μ values extracted from the fits for the upstream and downstream configurations are not statistically compatible with each other, showing an increase in the energy deposited in the downstream configuration of approximately 8%. To investigate whether the observed enhancement in the energy deposited in the downstream configuration can be attributed to geometric effects, the normalized asymmetry between Mat2 and Mat3 was evaluated as a function of the particle hit position on the crystal plane. Such study was performed for both the upstream and downstream configurations, and for both the crystal orientations.

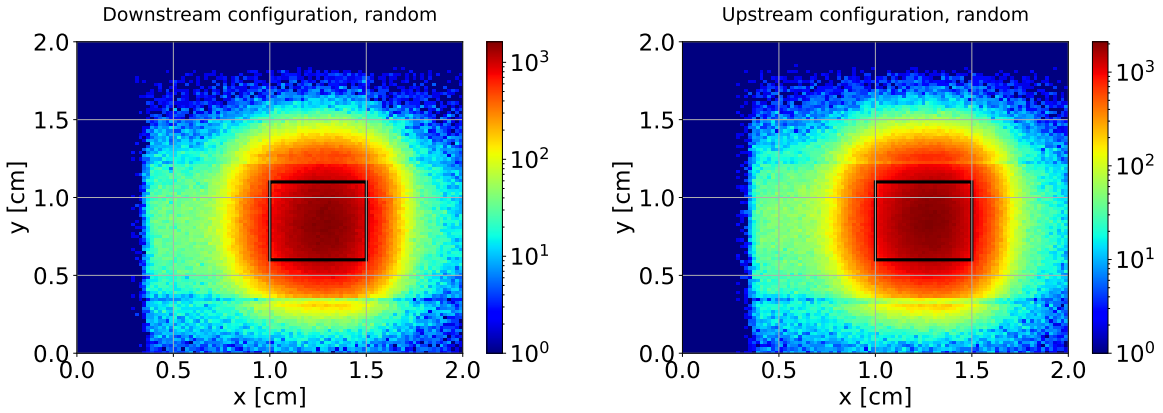

Figure 4.19: Efficiency map of the $PbWO_4$ crystal for the upstream and downstream configuration.

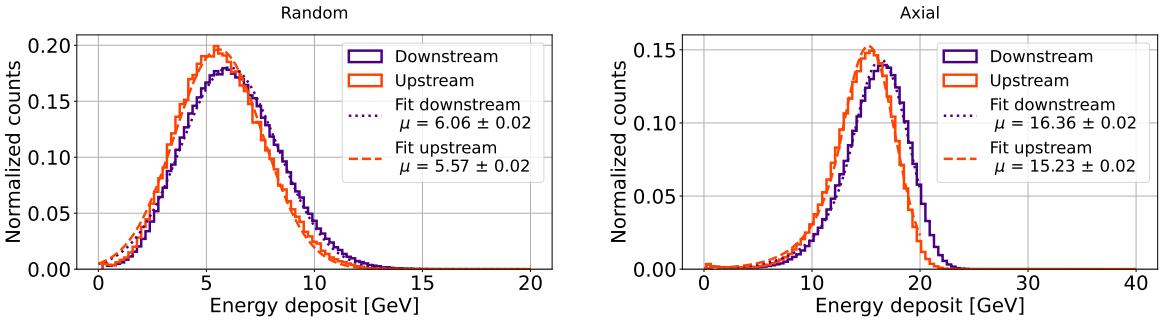

Figure 4.20: Energy deposited in the $PbWO_4$ crystal in the upstream and downstream configuration in the (left) random and (right) axial crystal orientation.

Recalling the layout shown in Figure 4.7, the normalized asymmetry is defined as:

$$\text{Asymmetry} = \frac{\text{Mat2} - \text{Mat3}}{\text{Mat2} + \text{Mat3}} \tag{4.4}$$

If the light collection is equally shared between the two matrices (i.e., Mat2 = Mat3), the asymmetry is zero. A positive value indicates a stronger signal in Mat2.
The results obtained for the random crystal orientation are shown in Figure 4.21; similar results have been obtained for the axial orientation:

- In the downstream configuration, a symmetry in the light spread between the two matrices is present: along the x-axis the light is equally distributed between Mat2 and Mat3, while along the y-axis the light initially shows a stronger signal in Mat3, then crosses zero, and finally shows a stronger signal in Mat2, as expected observing the scheme in figure 4.7.

- In the upstream configuration, the symmetry around zero is no longer evident, and a stronger signal is observed in Mat2. This effect is likely due to a possible misplacement of the crystal after the 180° rotation, resulting in the beam no longer being centered on the crystal itself.

The observed enhancement in the downstream configuration can likely be attributed to a geometric misalignment, rather than to the presence of a significant Cherenkov component

in the signal. As no clear evidence of a directional Cherenkov contribution has been found, the upstream configuration can be considered equally effective for the signal readout. This confirms the suitability of the upstream setup adopted in the final prototype.

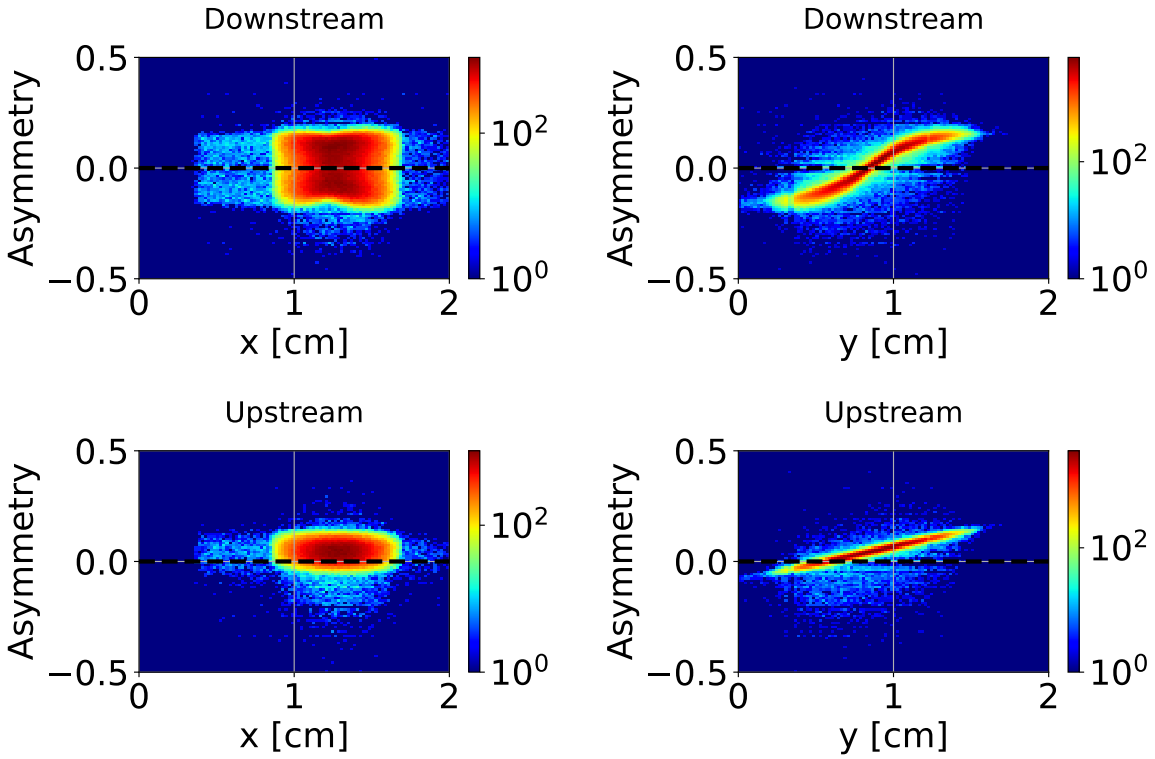

Figure 4.21: 2D histogram of the asymmetry of the two matrices PH as a function of the particles hit position on the crystal plane, in both the downstream and upstream configuration for the random crystal orientation. The same results have been obtained for the axial orientation.

5

THE 2023 BEAMTESTS

After experimentally verifying the strong field effects in a single oriented crystal, the next step toward the construction of an electromagnetic calorimeter based on oriented crystals is to test a prototype with multiple $PbWO_4$ crystals glued together. In fact, the most challenging aspect of the OREO design is to keep all the crystals aligned when arranged in a matrix structure.
In 2023, two different prototypes were developed to validate the assembly and alignment procedures: a 3×1 row and a 2×2 matrix of $PbWO_4$-UF oriented crystals, both coupled to SiPM matrices. This chapter will present the results obtained during the August 2023 beamtests with the 3×1 row on the T9 beamline at the CERN PS and on the H2 beamline at the CERN SPS, and during the October 2023 beamtest with the 2×2 matrix on the T9 beamline at the CERN PS.

5.1 THE AUGUST BEAMTESTS ON THE CERN PS T9 BEAMLINE AND ON THE SPS H2 BEAMLINE

During the August 2023 beamtests a first row of 3×1 $PbWO_4$-UF crystals has been studied with 6-15 GeV electrons on the T9 beamline at the CERN PS and with 20-150 GeV electrons on the H2 beamline at the CERN SPS.
The data analysis consists of:

- the calibration of the response of each crystal, in order to convert the raw PHs into energy deposits measured in GeV;
- the study of the energy deposit distributions in each crystal in the random and axial orientation and at different misalignment angles, in order to verify the interalignment between the three crystals;
- the study of the enhancement of the energy deposit in the axial orientation as a function of the incident beam energy, in order to characterize the prototype over a wide range of energies, from low energies up to the full strong field regime.

5.1.1 SIPMS CALIBRATION-LIKE PROCEDURE

During the 2022 beamtest, the SiPMs were calibrated using a Geant4 simulation of the energy deposited in the $PbWO_4$ crystal.
In 2023, a two-point, calibration-like procedure using Minimum Ionizing Particles (MIPs) was implemented, using a 10 GeV mixed beam on the T9 beamline and a beam of 40 GeV hadrons on the H2 beamline. The MIPs on the T9 beamline were selected using the threshold Cherenkov detectors, whose characterization is presented in Appendix A. Figure 5.1 shows the Pulse Height of the threshold Cherenkov detector XCET48: a threshold value (indicated by the dotted line) has been chosen to distinguish between events that generated a signal in the detector (electrons) and those that did not. Events with a Pulse Height lower than the threshold are classified as MIPs. On each beamline, the two calibration points were determined by collecting data at two goniometer rotation angles (0° and 90°). For each angle, the goniometer coordinates were adjusted to avoid coherent effects, ensuring that the crystals had a random orientation with respect to the beam.

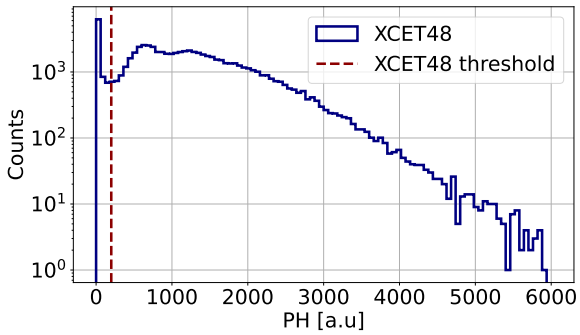

Figure 5.1: PH distribution of the threshold Cherenkov detector XCET48. The dotted line represents the selection threshold: the events with a Pulse Height lower than the threshold are classified as MIPs.

A cut in position, as shown in Figure 5.2 has been applied to each crystal to select only the events impinging on the central region. The MIPs energy deposit distribution results in a Landau-like distribution, which can be described using the Moyal approximation [112]:

$$f(\lambda) = A \cdot \exp(-0.5(\lambda + \exp(-\lambda))) \tag{5.1}$$

where λ is given by:

$$\lambda = \frac{\text{PH} - \text{MPV}}{\text{FWHM}} \tag{5.2}$$

where MPV is the Most Probable Value of the Landau curve and FWHM is the Full Width at Half Maximum, i.e. the width of the distribution at a level that is just half the maximum of the peak.
Figure 5.3 shows the MIPs energy deposit distribution on the T9 beamline along with the Landau fit for the two crossed thicknesses, i.e. 4.4 cm when the beam is centered on the crystals and 2.5 cm when the crystals are rotated by 90°. The most Probable values extracted from the Landau fit for both the T9 and H2 beamline are presented in Table 5.1.

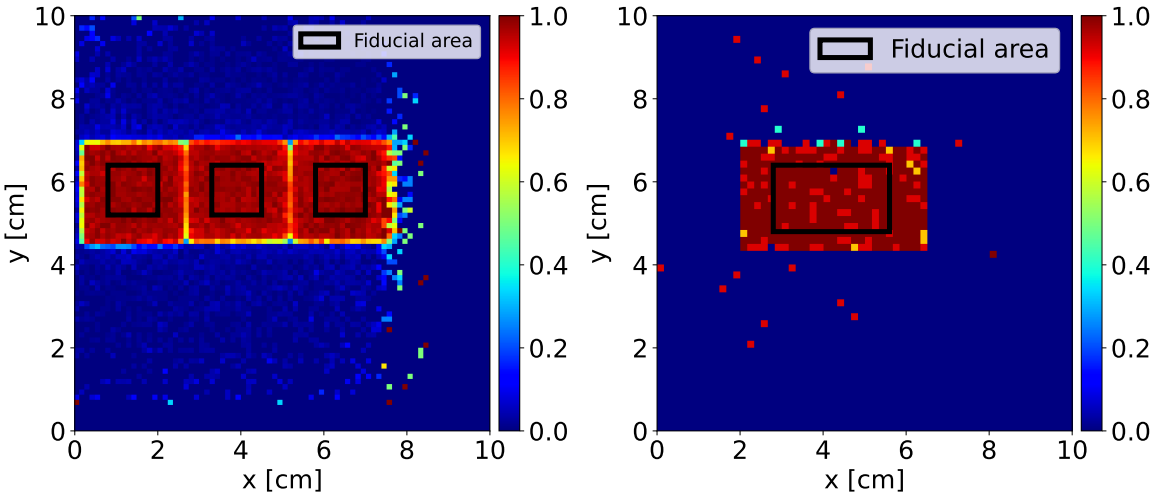

Figure 5.2: 3×1 OREO prototype efficiency map on the T9 beamline, for the two rotation angles of the goniometer: (left) 0°and (right) 90°. A cut in position has been applied to each crystal to select only the events impinging on the central region.

The calibration for each crystal has been performed simulating the MIPs energy deposit in

	Thickness	George	John	Paul
T9	4.4 cm	285.1 ± 1.47	218.37 ± 1.53	338.42 ± 1.32
	2.5 cm	169.66 ± 0.75	136.28 ± 0.96	189.97 ± 0.66
H2	4.4 cm	103.64 ± 0.58	84.01 ± 0.59	100.46 ± 0.97
	2.5 cm	61.47 ± 0.4	52.75 ± 0.5	62.03 ± 0.41

Table 5.1: Most Probable values in arbitrary units evaluated from the Landau fit of the MIPs energy deposit distribution for the two crossed thicknesses, i.e 4.4 cm when the beam is centered on the crystal and 2.5 cm when the crystals are rotated by 90°, on the T9 and H2 beamline.

the 3×1 OREO prototype using the Geant4 simulation toolkit (described in Appendix B) for the two crossed thicknesses. A beam of 10 GeV muons (generated using the Geant4 General Particle Source toolkit [113]) has been used on the T9 beamline and a beam of 40 GeV charged pions [113] for the H2 beamline. The simulated energy deposit distribution on the T9 beamline is presented in Figure 5.4. The values obtained for both the data simulated on the T9 and H2 beamline are statistically compatible with the most probable energy loss per unit length for MIPs, $\epsilon_{\text{MIP}} = 10.20$ MeVcm^{-}1, as reported in [8]. The calibration lines for each SiPM on the two beamlines are presented in Figure 5.5.

Figure 5.6 shows the energy deposit distributions for a 120 GeV electron beam impinging on the 3×1 OREO prototype, obtained by summing the energy deposited in the three crystals, together with the corresponding distributions from the Geant4 simulations. Both the experimental and simulated data, collected at the T9 and H2 beamlines, are fitted with a Crystal Ball function. At 6 GeV, the extracted μ values are statistically compatible within 1 σ while at 120 GeV the μ values differ by about 2.5 σ. The differences in the shape of the energy deposit distribution at high energy could be due to the large number of optical photons on the SiPMs, potentially leading to saturation effects in the experimental data.

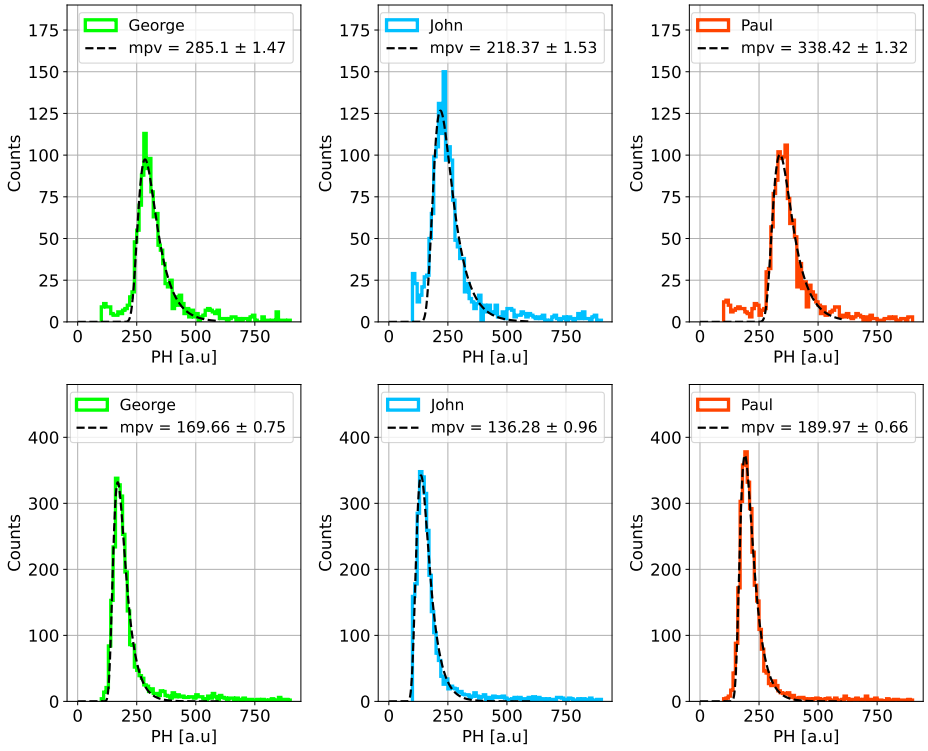

Figure 5.3: MIPs energy deposit distribution in the 3×1 OREO prototype on the T9 beamline for the two rotation angles of the goniometer: (top) 0°and (bottom) 90°, along with the Landau fit.

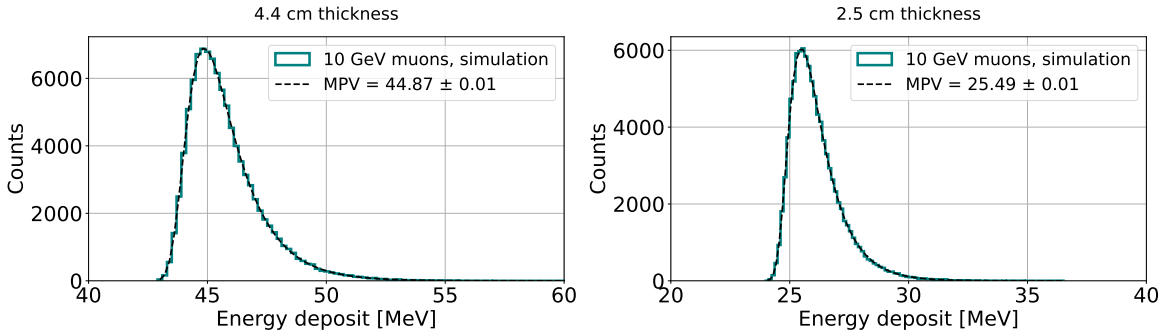

Figure 5.4: Simulation of the 10 GeV muons energy deposit in the 3×1 OREO prototype using the Geant4 simulation toolkit for the two crossed thicknesses.

5.1.2 CRYSTALS INTERALIGNMENT

A fundamental aspect in building an electromagnetic calorimeter based on oriented crystals is to ensure that the different crystals are properly aligned with each other when glued together. To investigate the relative alignment of the crystals in the 3×1 OREO prototype, the enhancement in the energy deposit between the axial and random orientations has been studied: a consistent enhancement across all the crystals indicates a uniform alignment with respect to the beam direction.

On the T9 beamline, data were collected using a 6 GeV electron beam with parallel optics (Appendix A): the beam was sufficiently wide to cover all the crystals of the 3×1 OREO

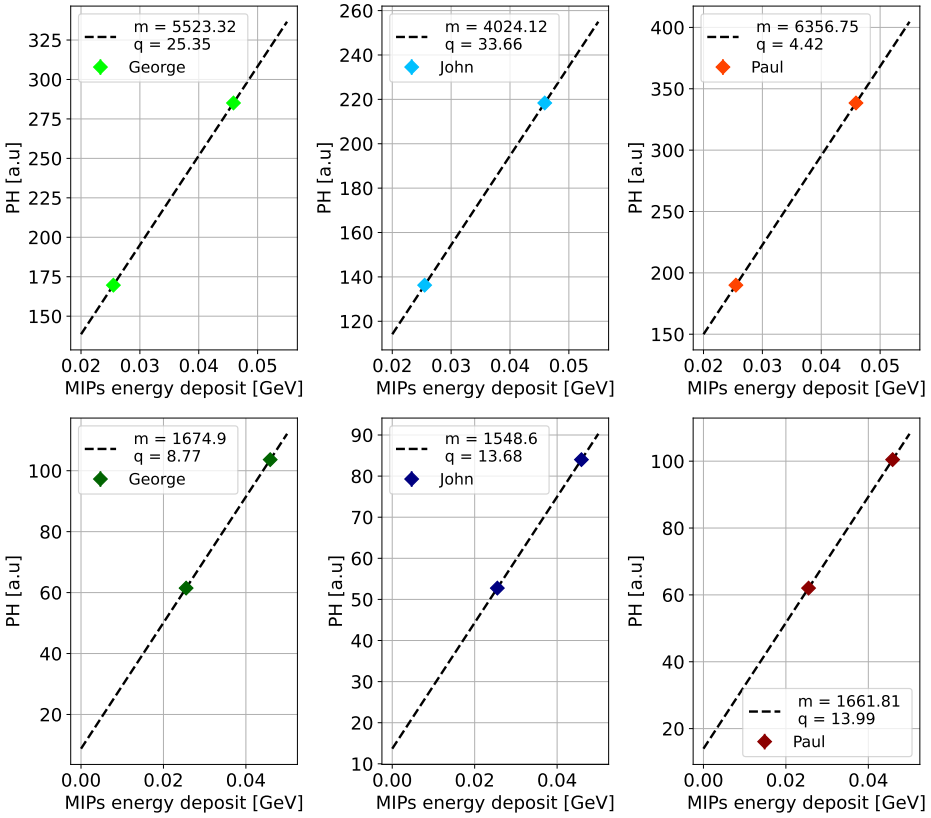

Figure 5.5: Calibration lines obtained for each SiPM (George, John, Paul) on the (top) T9 beamline and (bottom) H2 beamline.

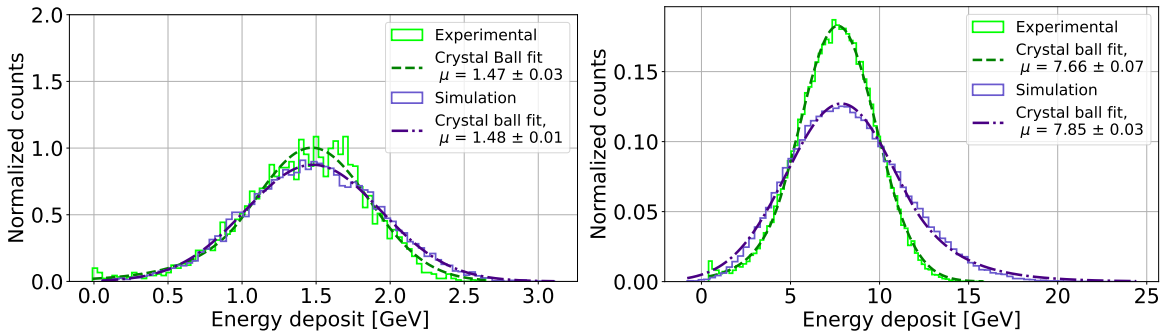

Figure 5.6: Comparison between the experimental and simulated energy deposit distribution for a 120 GeV electron beam.

prototype simultaneously. In contrast, on the H2 beamline, a 120 GeV electron beam has been used. The beam is smaller than the 3×1 OREO prototype, so the prototype was horizontally moved using the goniometer to center each crystal on the beam. A cut in position on each crystal and in beam divergence has been applied to select the events of interest. Figure 5.7 shows the energy deposit distribution in each crystal in the random and axial orientation for the T9 and H2 beamline. The μ values extracted from the Crystal Ball fits are statistically compatible across the three crystals, both in the axial and random orientation.

Figure 5.8 shows the ratio between the μ values in the axial and random orientation for each crystal on both the T9 and H2 beamline. To verify whether such ratios are consist-

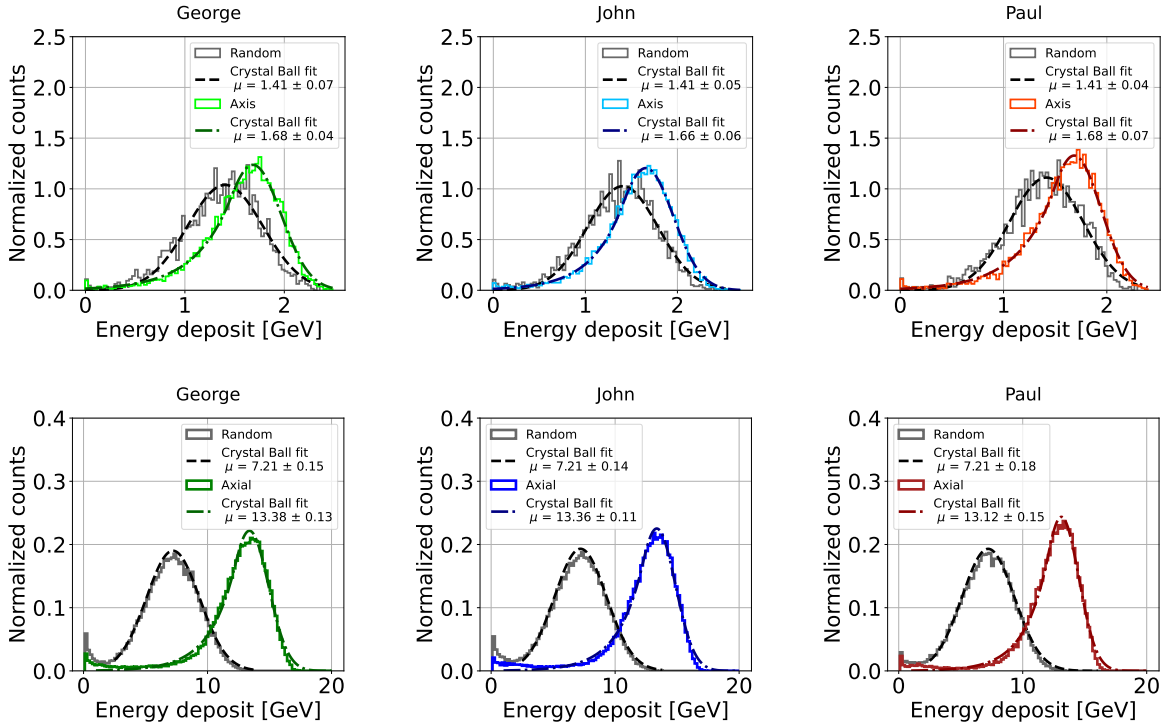

Figure 5.7: Energy deposit distribution in each crystal of the 3×1 OREO prototype in random and axial orientation. The μ values extracted from the Crystal Ball fits are statistically compatible across the three crystals, both in the axial and random orientation.

ent across the three crystals, a constant fit was performed separately for the T9 and H2 beamlines. In both cases, the χ^2/ndof[1] values are well below 1, confirming that the ratios are statistically consistent across the crystals; this indicates that the enhancement factor remains stable across different crystals and thus the crystals are aligned with each other. Moreover, the ratios computed at 120 GeV are larger than those at 6 GeV. This behavior is consistent with the fact that, at 6 GeV, the strong field regime is not yet dominant.

The interalignment between the three crystals was also studied by analyzing the enhancement factor, defined as the ratio between the energy deposited in each crystal at different misalignment angles and the energy deposited in the random orientation. Figure 5.9 shows the enhancement factor evaluate for each crystal as a function of the misalignment angle: at each angle, the enhancement factors are compatible within 1 σ, confirming the interalignment of the three crystals.

5.1.3 CHARACTERIZATION AT DIFFERENT ENERGIES

The dependence of the electromagnetic shower development acceleration on the incident beam energy has been studied over a wide energy range: with 6, 10 and 15 GeV on the T9 beamline in the sub-strong field regime, and from 40 to 150 GeV, with steps of 20 GeV, on the H2 beamline where the strong field effects dominate.

1 The χ^2 is given by $\chi^2 = \sum_{i=1}^{N} \frac{(y_i - \bar{y})^2}{\sigma_i^2}$, where y_i are the measured values, $\bar{y}$ is the value obtained from the fit, and σ_i are the associated uncertainties. The ndof are the number of degrees of freedom.

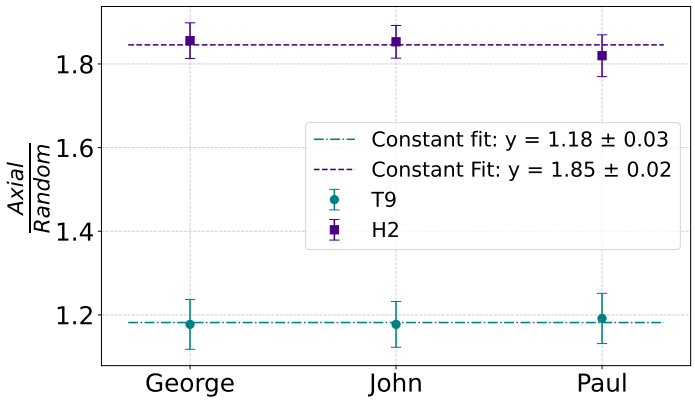

Figure 5.8: Ratio between the μ values in the axial and random orientation for each crystal measured on the T9 and H2 beamlines. A constant fit was performed for each beamline to test the consistency of the ratios among crystals. The resulting χ^2/ndof values (0.019 for T9 and 0.181 for H2) indicate that the ratios are statistically consistent.

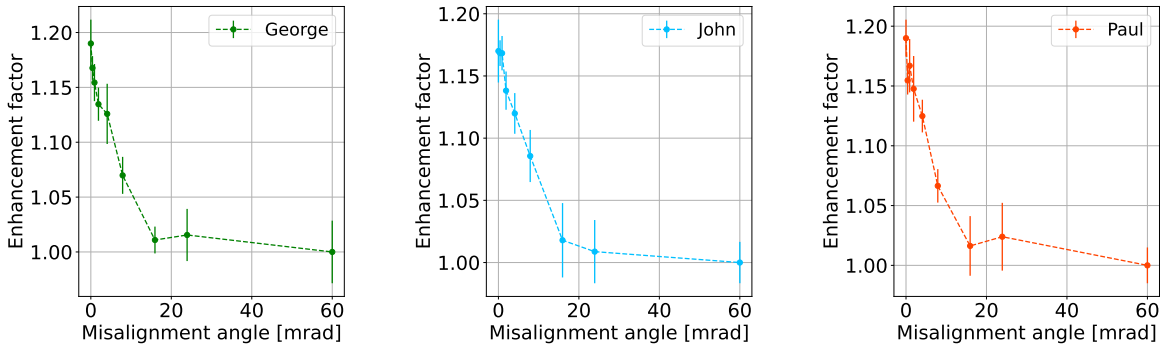

Figure 5.9: Enhancement factors of the energy deposit in each crystal of the 3×1 OREO prototype, as a function of the misalignment angle.

The beam was centered on the central crystal, and a position cut, as shown in Figure 5.10, was applied to restrict the analysis to particles crossing the central crystal region. Additionally, a cut on the beam divergence was applied to select the most perpendicular incident particles.

Figure 5.11 shows the energy deposit distribution in the 3×1 OREO prototype for the 6 GeV and 120 GeV electron beam, in random and axial orientation. The ratio between the energy deposited in the axial and random orientation increases from 1.17 ± 0.03 at 6 GeV, in the sub-strong field regime, to 1.87 ± 0.03 at 120 GeV, in the full strong field regime.
The value of the ratio at 120 GeV is significantly lower than the value of 2.64 ± 0.08 measured during the 2022 beamtest on the same beamline (Section 4.2.2). Such large discrepancy could be attributed to a possible saturation in the SiPM response when the crystals are in the axial orientation. Indeed, the SiPMs have a finite number of pixels, each of which requires a recovery time after a breakdown avalanche. A portion of the scintillation photons may hit the same pixel, resulting in a non proportionality between the number of photons and the number of hit cells. Consequently, the SiPM signal amplitude may be lower than expected, leading to an underestimation of the energy deposited in the axial orientation.
The first difference with respect to the 2022 setup is that the 3×1 OREO prototype is 5 X_0 thick, compared to the 4.6 X_0 thick crystal used in 2022, leading to a larger energy deposit

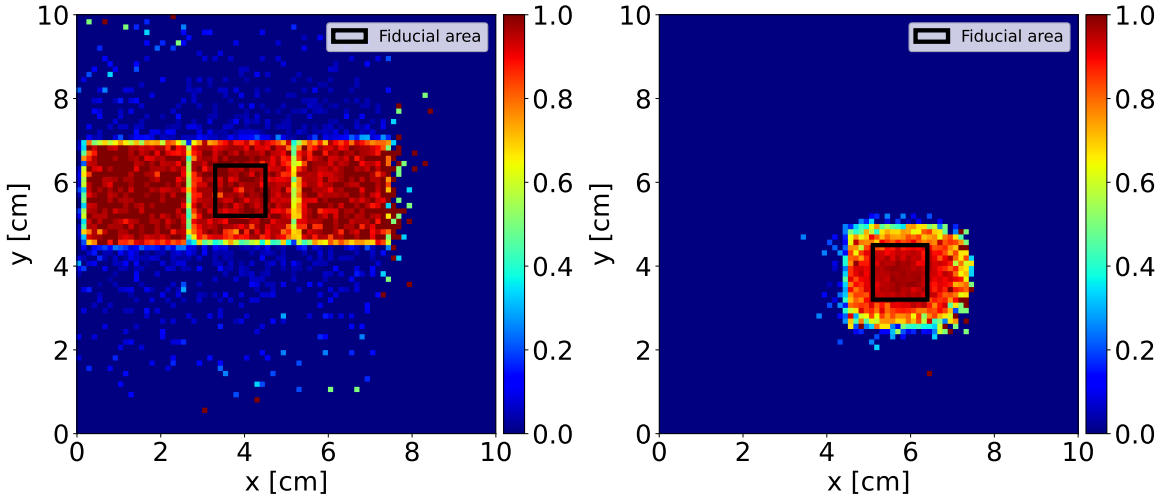

Figure 5.10: Efficiency map of the 3×1 OREO prototype on the T9 and H2 beamline. The black lines represent the cuts in position applied to select the events of interest.

and thus a larger number of scintillation photons reaching the SiPMs. Another difference with respect to the 2022 setup is the use of $PbWO_4$-UF crystals instead of standard $PbWO_4$. However, this difference can be excluded as the cause of the observed discrepancy, since, as described in Section 3.1, the electromagnetic potential of the $PbWO_4$ remains unchanged between the standard and ultra-fast crystals, thus leaving the fundamental physics of the radiation matter interaction unaltered. Furthermore, data collected in 2024 using the same $PbWO_4$-UF crystals and at the same energy of 120 GeV show an axial to random ratio exceeding 2.5 (Section 6.2.4), suggesting that the observed smaller ratio is more likely due to the saturation in the SiPMs response rather than to differences among the crystals.

Figure 5.12 shows, as a function of the incident beam energy:

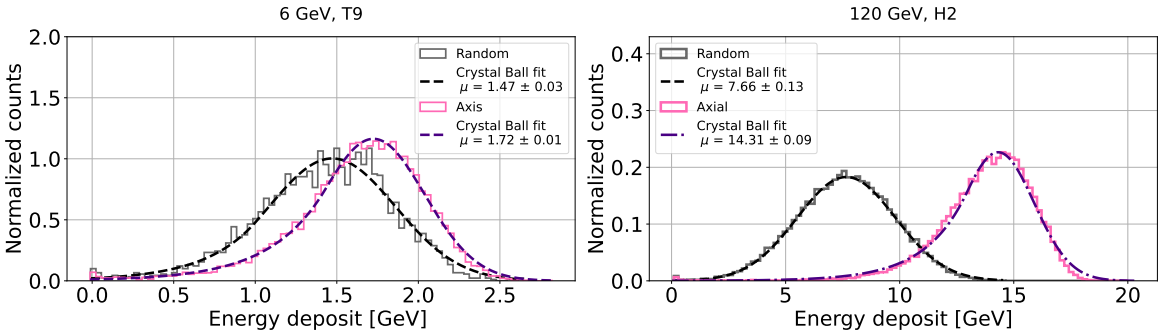

Figure 5.11: Energy deposit distribution in the 3×1 OREO prototype for the 6 GeV and 120 GeV electron beam, in random and axial orientation.

a) The μ value extracted from the Crystal Ball fit of the energy deposit distribution in the 3×1 OREO prototype in the random and axial orientation; in the axial orientation there is an enhancement of the energy deposited due to the coherent effects in oriented crystals.

b) The ratio between the energy deposit in the axial and random orientations; the ratio increases as a function of the incident beam energy.

c) The μ value of the energy deposit distribution in the lead glass calorimeter placed 0.12 m downstream the 3×1 prototype in the axial and random orientation. The energy deposited in the lead glass calorimeter is larger in the random orientation, due to the enhancement in the energy deposited in the 3×1 OREO prototype when the crystals are axially oriented.

Such results provide a very preliminary understanding of the features of the electromagnetic shower development under the effect of the strong field regime as a function of the incident beam energy. More comprehensive results have been obtained during the 2024 beamtest with the full OREO calorimeter (Section 6.2.4).

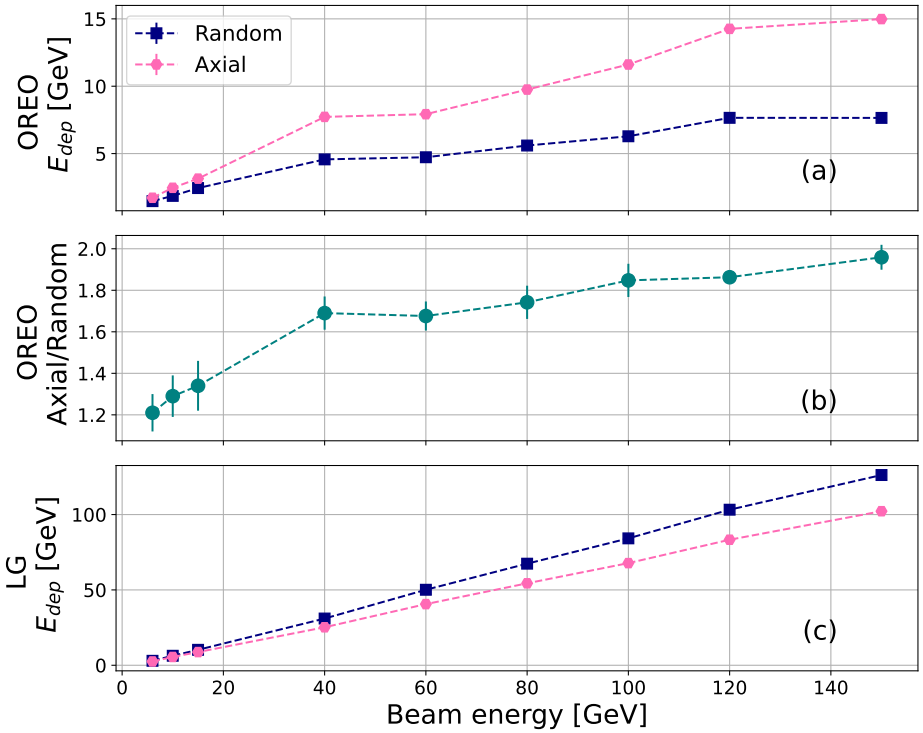

Figure 5.12: 3×1 OREO prototype. (a) The μ value extracted from the Crystal Ball fit of the energy deposit distribution in axial and random orientation as a function of the incident energy. (b) Ratio between the energy deposit in axial and random orientation in the upstream layer. (c) Lead glass calorimeter.

5.2 THE OCTOBER BEAMTEST ON THE CERN PS T9 BEAMLINE

During the October 2023 beamtest a first matrix of 2×2 $PbWO_4$-UF has been studied with 6-15 GeV electron beams on the T9 beamline at the CERN PS.
The data analysis consists of:

- the calibration of the response of each crystal;

- the study of the energy deposit distribution in each crystal in random and axial orientation and during a horizontal scan with the goniometer in order to verify the interalignment between the four crystals;
- the measurement of the total light yield and energy loss in the OREO prototype, comparing the random and axial alignment configurations and determining the energy loss enhancement;
- a preliminary study on the electron/hadron discrimination capability of the OREO prototype.

5.2.1 SIPMS CALIBRATION-LIKE PROCEDURE

The four crystals of the 2 × 2 OREO prototype have been calibrated using the same procedure described in Section 5.1.1. MIPs have been selected using the threshold Cherenkov detectors and a cut in position on the center of each crystal has been applied, as shown in Figure 5.13.
Figure 5.14 shows the calibration lines obtained for each SiPM.

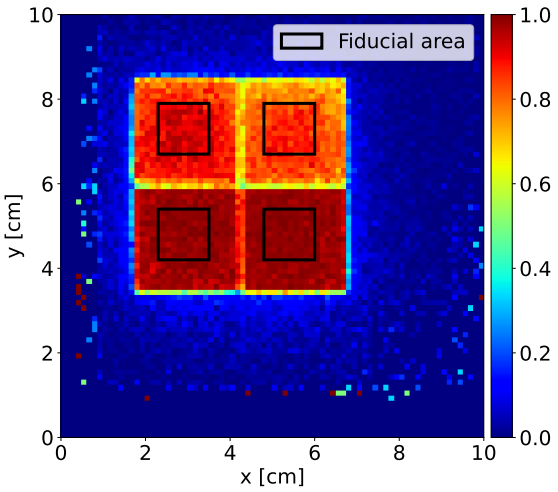

Figure 5.13: 2 × 2 OREO prototype efficiency map. The black boxes represent a fiducial cut in position to select the events of interest.

5.2.2 CRYSTAL INTERALIGNMENT

To investigate the relative alignment of the crystals in the 2 × 2 OREO prototype, the enhancement in the energy deposit distribution between the random and axial orientations has been studied for each crystal. The events of interest were selected using the threshold Cherenkov detectors and applying a cut in position in the center of the 2 × 2 OREO prototype. Figure 5.15 shows the energy deposit distribution in each crystal in the random and

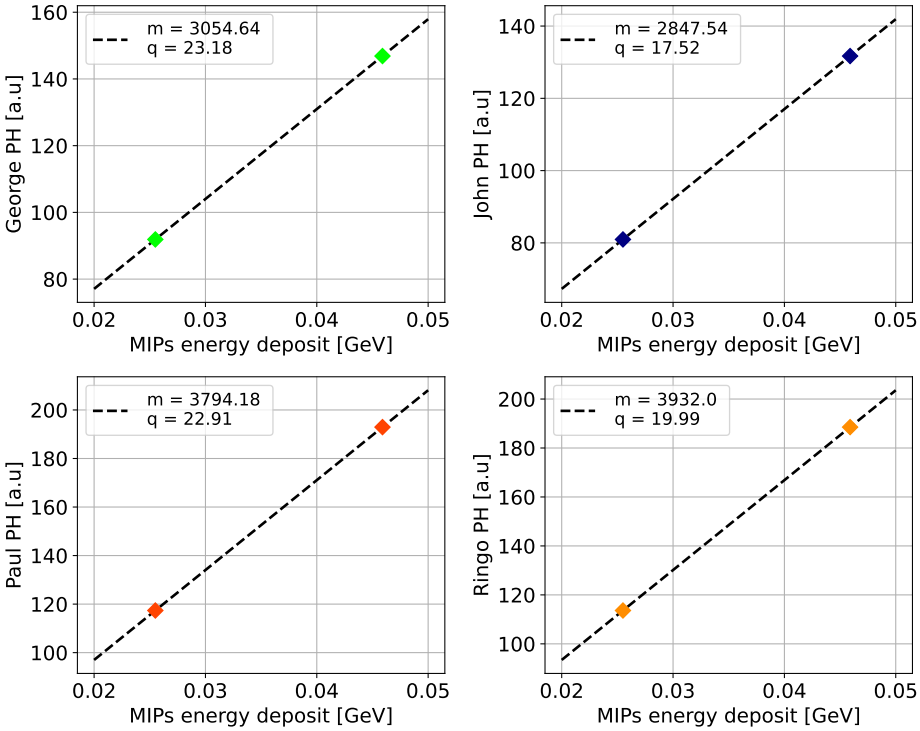

Figure 5.14: SiPMs calibration lines obtained using the same procedure described in Section 5.1.1.

axial orientation, using a 6 GeV parallel optics electron beam. All the μ values extracted from the Crystal Ball fits of the energy deposit distributions in the random orientation are mutually compatible within 1 σ; the same results are obtained for the axial orientation.

Figure 5.16 shows the ratio between the μ values in the axial and random orientations for each crystal, fitted with a constant function to evaluate the compatibility of the enhancement factor. The resulting χ^2/ndof is 0.18, indicating that the data are compatible with a constant within statistical uncertainties. This suggests that the enhancement factor is consistent across different crystals, demonstrating the good alignment of the crystals.

Figure 5.17 shows the μ values of the energy deposit distribution in each crystal as a function of the rotational coordinate of the goniometer, obtained during a rotational scan around the axis coordinate. The black dashed line represents the weighted average of the scan positions, where each position is weighted by the corresponding mean energy deposit; the maximum misalignment is of the order of 70 μrad, well below the strong field angular acceptance Θ_0 (Section 2.1.4.2).

These results suggested that the crystals were well interaligned, validating the gluing procedure in a matrix structure.

5.2.3 PRELIMINARY ELECTRON/HADRON DISCRIMINATION

To preliminarily investigate the electron/hadron discrimination capability of the 2×2 OREO prototype, runs with a 6 GeV mixed beam[2] were performed in both the random

2 The 6 GeV mixed beam produced at the T9 beamline is primarily composed of charged pions, muons, and electrons.

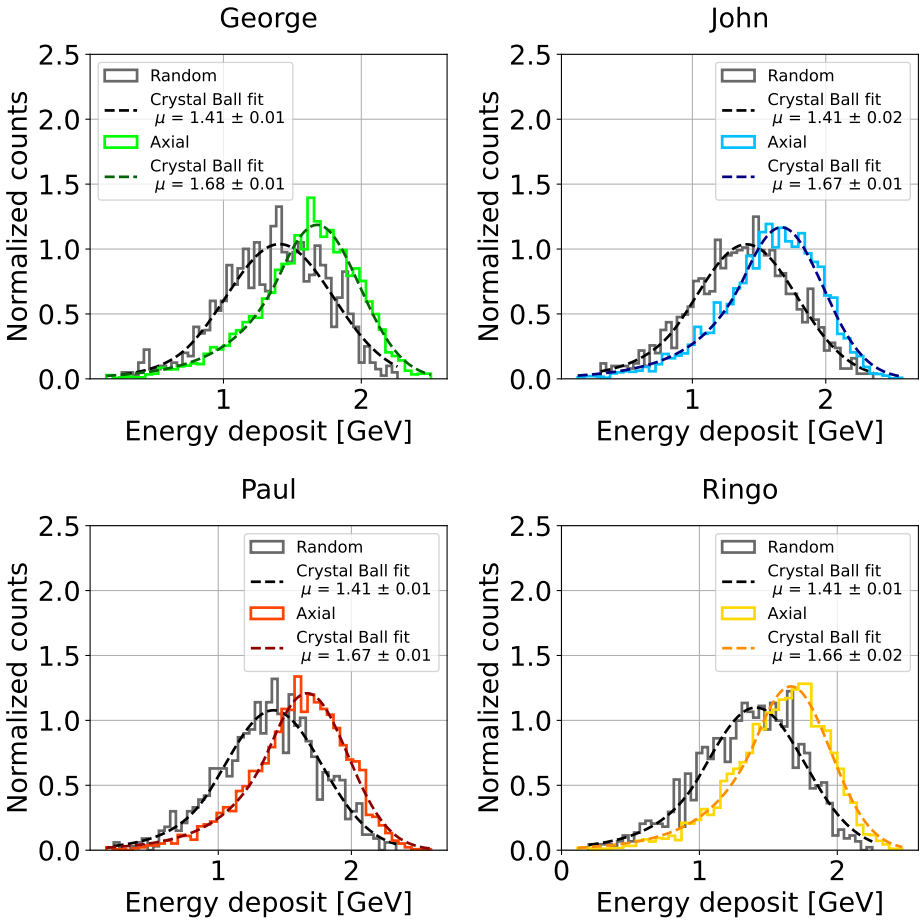

Figure 5.15: Energy deposit distribution in each crystal of the 2×2 OREO prototype in random and axial orientation.

and axial orientations. Figure 5.18 presents the two-dimensional histogram of the energy deposited in the 2×2 OREO prototype and in the lead glass calorimeter, positioned 0.23 m behind the prototype; a cut in position was applied on the center of the 2×2 matrix along with a cut on the signal peak time and on the beam divergence.

The electrons have been selected using the threshold Cherenkov detectors (whose characterization is presented in Appendix A). Figure 5.19 shows the scatter plot obtained by applying a cut on the Cherenkov threshold detectors PH, in order to discriminate electrons from hadrons. It can be observed that, since the nuclear interaction length remains unaffected by the lattice orientation, the energy deposited by hadrons (events which deposit a small amount of energy in the 2×2 OREO prototype) does not change in the axial orientation. On the other hand, under the influence of the axial crystalline field, the energy deposit distribution of electrons shifts toward higher values.

The improvement in the electron/hadron discrimination capability of the 2×2 OREO prototype has been analyzed calculating the elements of the confusion matrix TP, TN, FP and FN (summarized in Table 5.2): the actual positives correspond to the true electrons, identified using the information from the threshold Cherenkov detectors, while the predicted positives include all the events depositing in the 2×2 matrix an energy above a chosen threshold. The negatives are defined using the logical NOT operation.

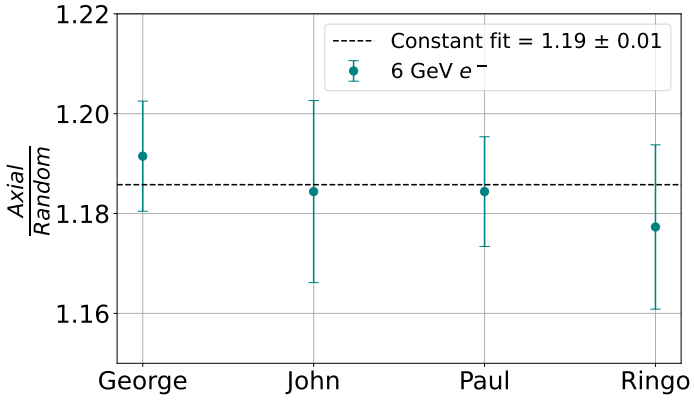

Figure 5.16: Ratio between the μ values in the axial and random orientation for each crystal measured on the T9 and H2 beamlines. A constant fit was performed for each beamline to test the consistency of the ratios among crystals. The resulting χ^2/ndof value of 3.40 indicates that the ratios are not statistically consistent.

Different threshold cuts on the energy deposited in the 2×2 OREO prototype have been

	Actual Positive	**Actual Negative**
Predicted Positive	True Positive (TP)	False Positive (FP)
Predicted Negative	False Negative (FN)	True Negative (TN)

Table 5.2: Confusion matrix: the actual positives correspond to the true electrons, identified using the threshold Cherenkov detectors, while the predicted positives include all the events depositing in the 2×2 matrix an energy above the chosen threshold. The negatives are defined using the logical NOT operation.

applied; for each threshold, the corresponding performance metrics has been evaluated:

- **Accuracy**, which is the percentage of correctly classified events (both true positives and true negatives) out of all the events. It measures how well the system distinguishes between electrons and hadrons. A high accuracy means that the system is making fewer errors in both identifying electrons (True Positives) and correctly rejecting hadrons (True Negatives):

$$\text{Accuracy} = \frac{\text{TP} + \text{TN}}{\text{TP} + \text{TN} + \text{FP} + \text{FN}} \tag{5.3}$$

- **Efficiency**, which measures the proportion of true electrons (true positives) correctly identified by the system out of the total number of true electrons. A high efficiency means the system is better at identifying the actual electrons and missing fewer of them:

$$\text{Efficiency} = \frac{\text{TP}}{\text{TP} + \text{FN}} \tag{5.4}$$

- **Purity**, which refers to the proportion of correctly identified electrons (true positives) out of all the events identified as electrons by the system. In other words, it measures how many of the events that the system classifies as electrons are truly electrons,

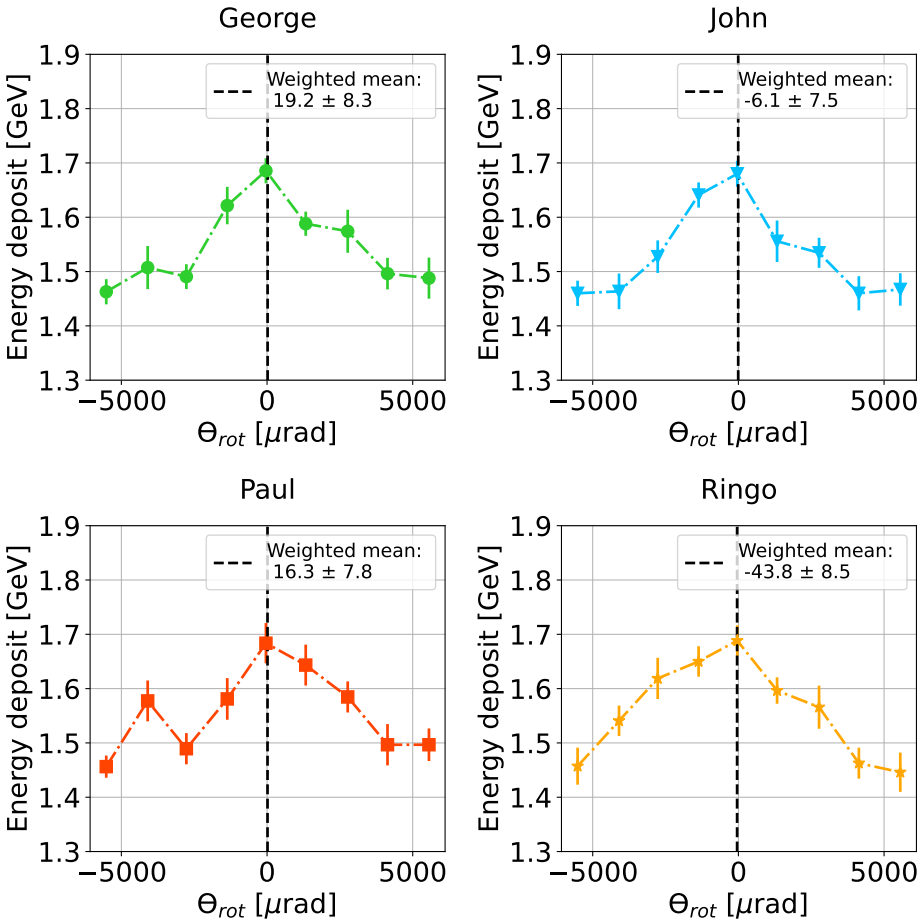

Figure 5.17: μ values of the energy deposit during a rotational scan around the axis coordinate. The black dashed line represents the weighted average of the data points.

as opposed to hadrons that might be misclassified. A high purity means that the electron candidates are more likely to be real electrons:

$$\text{Purity} = \frac{\text{TP}}{\text{TP} + \text{FP}} \tag{5.5}$$

The results obtained by applying different threshold cuts on the energy deposited in the 2×2 OREO prototype in the random and axial orientations are shown in Figure 5.20. Considering the classification process as a series of independent Poisson-distributed counts, the statistical uncertainty on each element of the confusion matrix is estimated using the square root of the corresponding number of counts. The uncertainty on the efficiency, accuracy and purity has been computed using the error propagation.

There is an overall trend indicating that the accuracy improves when the matrix is oriented, particularly at higher classification thresholds. For instance, for a threshold of 1.8 GeV, the accuracy in distinguishing electrons from hadrons increases from 42.96 ± 0.43 % in the random orientation to 70.72 ± 0.20 % when the crystals are oriented, corresponding to a difference of $+(27.76 \pm 0.48)$ % in the classification performance. This preliminary analysis suggests that the oriented configuration is more effective in distinguishing electrons from hadrons, reducing both the false positives and false negatives.

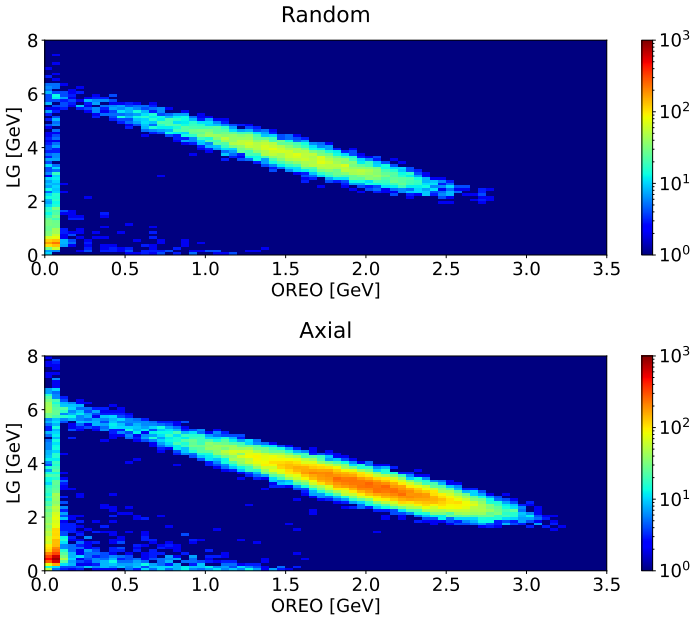

Figure 5.18: Two dimensional histogram of the energy deposited by a 6 GeV mixed beam in the 2×2 OREO prototype and in the lead glass.

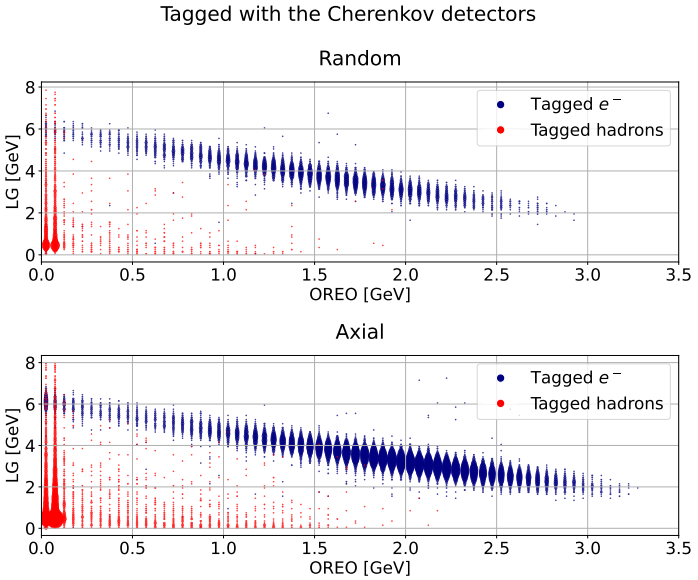

Figure 5.19: Scatter plot of the electrons (blue dots) and hadrons (red dots) tagged with the threshold Cherenkov detectors in the random and axial orientation.

The efficiency in the classification improves when the crystals are oriented; for instance for the 1.8 GeV threshold, the efficiency reaches 63.46 ± 0.24 % compared to 27.98 ± 0.44 % when the crystals are not oriented (with a $+(35.48 \pm 0.51)$ % in performance), indicating that, when oriented, the 2×2 OREO prototype performs better at correctly identifying electrons. Purity, on the other hand, appears to remain unaffected by the orientation; the values obtained in the axial orientation are statistically compatible with those from the random orientation, both approaching values close to 100 %.

Strongest effects on the electron/hadron discrimination capability using oriented crystals

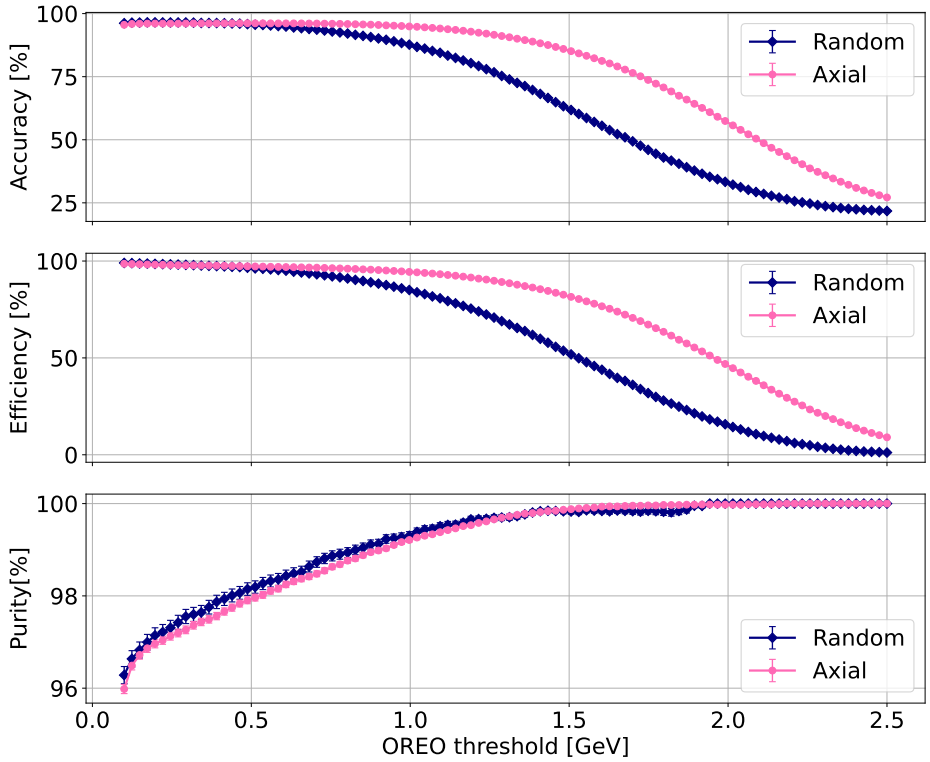

Figure 5.20: Accuracy, efficiency and purity evaluated for different threshold cuts on the energy deposited in the 2×2 OREO prototype.

occur at higher energies, where the strong field effects dominate.

6

THE 2024 BEAMTESTS

In 2024, the 3×3 OREO calorimeter was finally tested over a wide range of energies. The beamtests were performed on the T9 beamline of the CERN PS and on the H4 beamline of the CERN SPS. The main goal was to evaluate the performance of OREO as a full calorimeter, both in axial and random orientations. The first part of this chapter presents the results obtained on the T9 beamline, while the second part focuses on the higher energy data collected on the H4 beamline. The linearity and the energy resolution of the OREO calorimeter are presented at the end of the chapter.

6.1 THE JUNE BEAMTEST ON THE CERN PS T9 BEAMLINE

During the June beamtest, the 3×3 OREO prototype was tested with electron beams with energies ranging from 2 to 6 GeV at the T9 beamline of the CERN PS. The goals of the beamtest were the following:

- Measure the crystals inter-alignment after gluing; in fact, one of the most challenging aspects in the design of an oriented calorimeter is to keep the crystals aligned when arranged in a matrix structure.
- Characterize the strong field acceleration of the electromagnetic shower development in the OREO calorimeter, measuring the energy deposited as a function of the beam energy and incidence angle.
- Evaluate the potential improvement of the electron/hadron discrimination capability of OREO, in random and axial alignment.

6.1.1 VARIATION OF THE SIPMS SIGNAL OVER TIME

During the beamtest, a variation of the SiPM signal over time was observed. Since OREO does not implement an active system to compensate for gain variations over time (such as temperature monitoring and a feedback loop), the signal provided by MIPs was used to correct for these variations.
The MIP energy deposit in each crystal of both layers was studied after the pedestal sub-

traction, applying a cut in position on each crystal (as shown in Figure 6.1), and selecting the MIPs using the threshold Cherenkov detectors (whose characterization is presented in Appendix A) placed in coincidence (as shown in Figure 6.2).

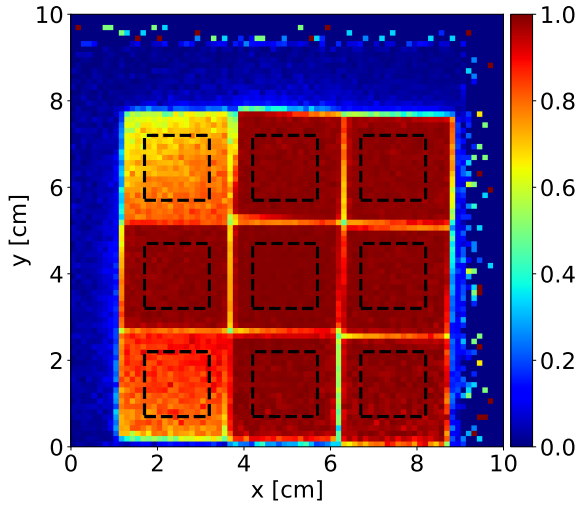

Figure 6.1: OREO efficiency map. The black lines represent the cuts in position applied to select the events of interest.

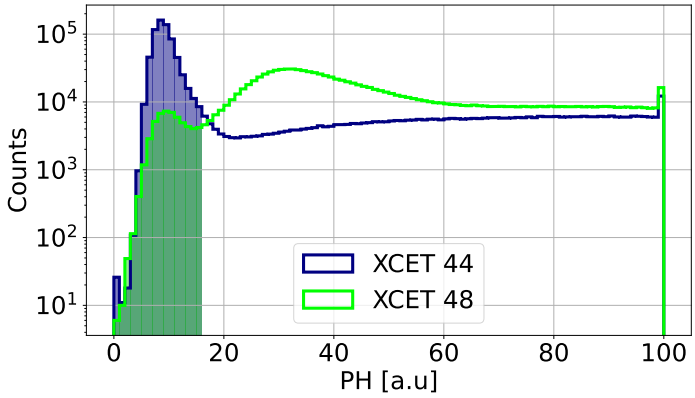

Figure 6.2: PH of the two threshold Cherenkov detectors. The colored area indicates the events selected as MIPs.

Data were collected from selected runs throughout the whole beamtest; when combined, they cover a time window of approximately two days. The dataset was divided into subsets of around 50 000 events, each corresponding to roughly two hours of data acquisition. The tertiary beam provided by the T9 beamline is essentially a pure electron beam, with only a small contamination from muons and hadrons, primarily originating from the decay of charged pions and kaons produced at the target. Figure A.32 in Appendix A shows that for energies below 6 GeV, the electron fraction exceeds 80%. Therefore, dividing the run into shorter time windows, such as one-hour blocks, was not possible due to a not large enough MIP statistics. Runs with energies below 6 GeV were also excluded, as the low MIP statistics did not allow for the subdivision into two-hour blocks.
Figures 6.3 and 6.4 show the PH distribution of the MIPs energy deposit in each crystal of the upstream and downstream layers for a given subrun, fitted with a Landau function.

The MPVs (Most Probable Values) obtained from the Landau fit, along with their associated errors (calculated as the square root of the diagonal elements of the fit covariance matrix), are shown in Figure 6.5 as a function of the subrun numbers. A clear variation in the signal over time is observed, most likely due to temperature fluctuations between night and day. An increase in gain is seen during nighttime hours, when the temperature tends to be lower; in fact, given a fixed bias voltage, the breakdown voltage decreases with the temperature, and thus the overvoltage increases. It is important to recall that the SiPMs were operated near the breakdown voltage to prevent saturation issues. The channels in the upstream layer exhibit signal variations of up to approximately 15 %, with the BR channel showing the largest change (18.72 %). In the downstream layer, the variation reaches 20 %, with the TC channel experiencing the largest change (21.94 %). The CL channel of the downstream layer exhibits a very different behavior, probably due to a non-correct voltage or a poorly connected cable.

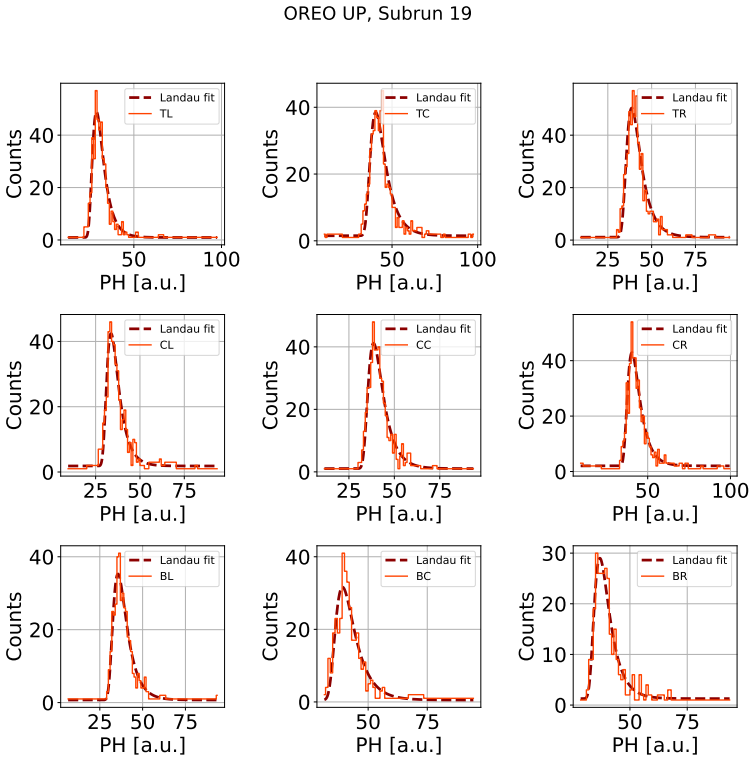

Figure 6.3: PH distribution of the MIPs energy deposit in each crystal of the OREO upstream layer, fitted with a Landau function.

During the data taking, it was not possible to normalize each individual channel separately (and thus correct for the signal variation over time) because runs with an energy below 6 GeV did not have a large enough MIP statistics. Instead of normalizing the channels individually, the signal from each channel was summed, and the total sum was then normalized. In order to sum the signal of each crystal, the equalization factors between the channels had to be computed. The variation of the equalization factors over time has

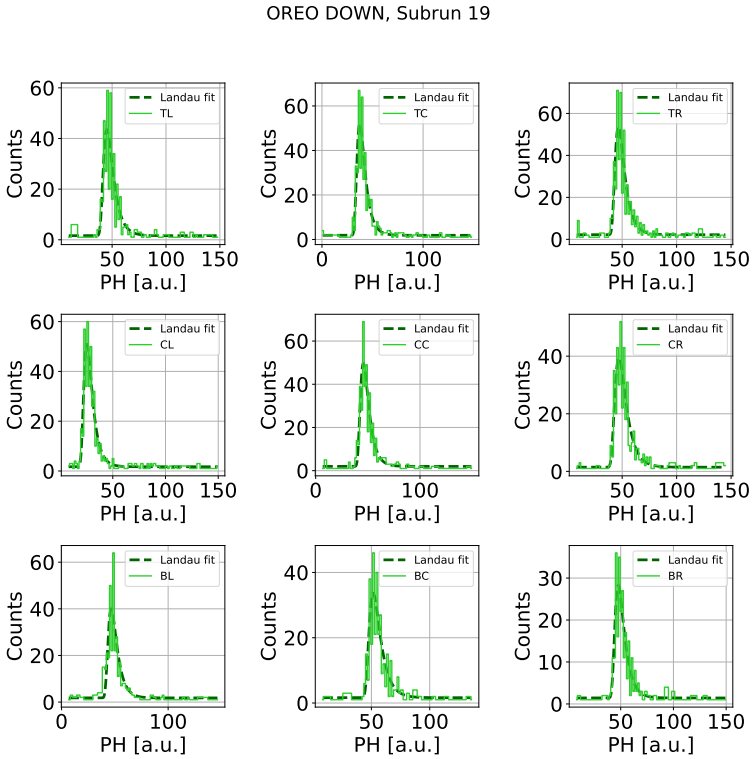

Figure 6.4: PH distribution of the MIPs energy deposit in each crystal of the OREO downstream layer, fitted with a Landau function.

been studied: if the coefficients were found to be constant, it would be possible to use fixed equalization factors Q_i for each subrun. The equalization factors have been computed as:

$$Q_i = \frac{MPV_{CC}}{MPV_i}$$

where i is the i-th channel. The computed equalization factors are shown in Figure 6.6.

To evaluate whether the equalization factors remain constant over time, a chi-square test was performed. The chi-square statistics is given by:

$$\chi^2 = \sum \frac{(Q_i - \bar{Q})^2}{\text{error}^2} \tag{6.1}$$

where $\bar{Q}$ is the mean value of the equalization factors and the error on each point has been computed through the error propagation. The p-values[1] calculated for all the channels in the upstream layer were smaller than 0.05, indicating that the variation in the equalization factors during the data-taking period for the upstream channels is not negligible. On the other hand, for the downstream layer, only the CL, TC and TL channels exhibited p-values smaller than 0.05, and thus the equalization factors for these channels remained relatively stable over time.

1 The p-value represents the probability that, under the assumption that the null hypothesis is true, a value of the chi-square statistics (χ^2) at least as large as the one calculated from the experimental data (χ^2_{obs}) is observed. It is expressed as: $p = P\left(\chi^2 \geq \chi^2_{\text{obs}}\right) = 1 - F_{\chi^2}(\chi^2_{\text{obs}})$ where F_{χ^2} is the cumulative distribution function of the chi-square distribution with ν degrees of freedom. A small p-value indicates that it is unlikely to observe, due only to statistical fluctuations, such a large discrepancy between the data and the expected model, thus suggesting that the null hypothesis may be rejected.

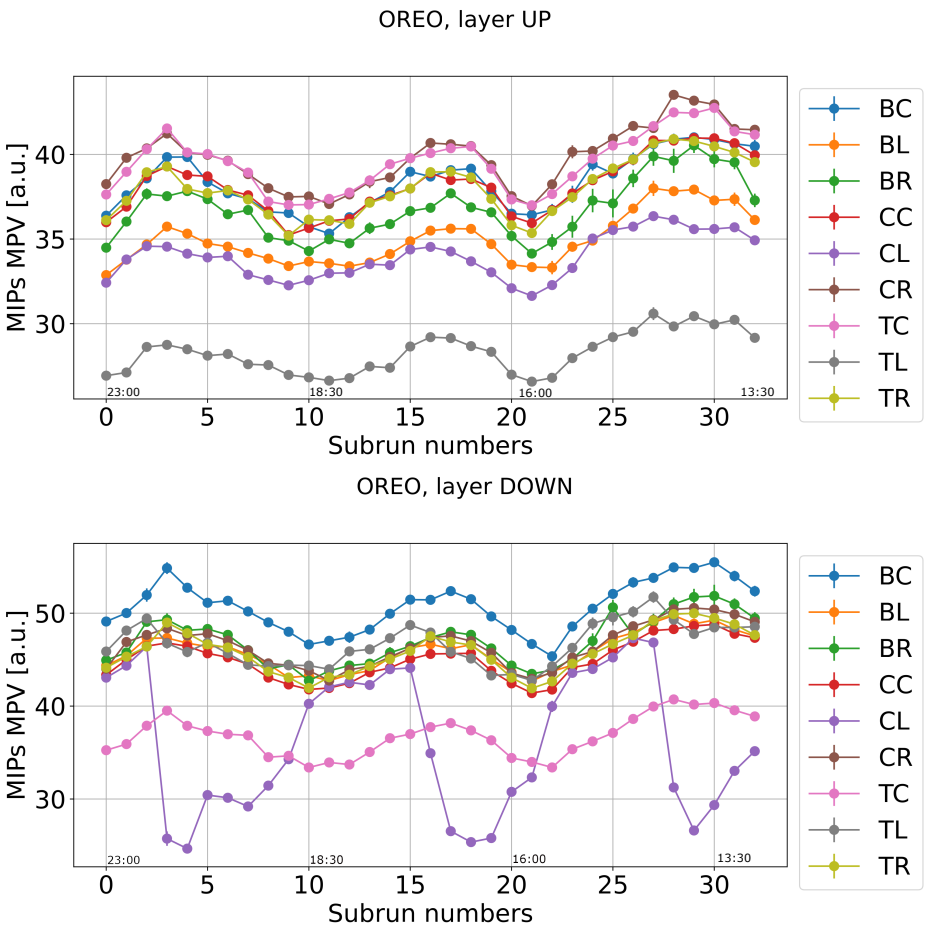

Figure 6.5: OREO Most Probable Values (MPVs) as a function of the subrun number for both the upstream (top) and downstream (bottom) layers. A clear variation of the signal over time can be observed in both layers.

Due to the variation of the equalization factors over time for the upstream layer, it was not possible to use fixed equalization factors for each subrun. The adopted equalization procedure is described in the following section.

6.1.1.1 CORRECTION PROCEDURE FOR THE JUNE BEAMTEST

For all the runs of the beamtest, the following procedure was adopted:

1. **Selection of the events of interest**
   - The pedestal is subtracted from the signal.
   - A cut in position (as the one presented in Figure 6.1) is applied to each channel to select the events of interest.
   - A cut on the threshold Cherenkov detectors PH is applied to select the MIPs (as shown in Figure 6.2).
2. **Division of the run into subruns:**
   - If the number of events in a run exceeds 50 000, the run is divided into subruns, with the number of subruns determined by rounding up the ratio of total events

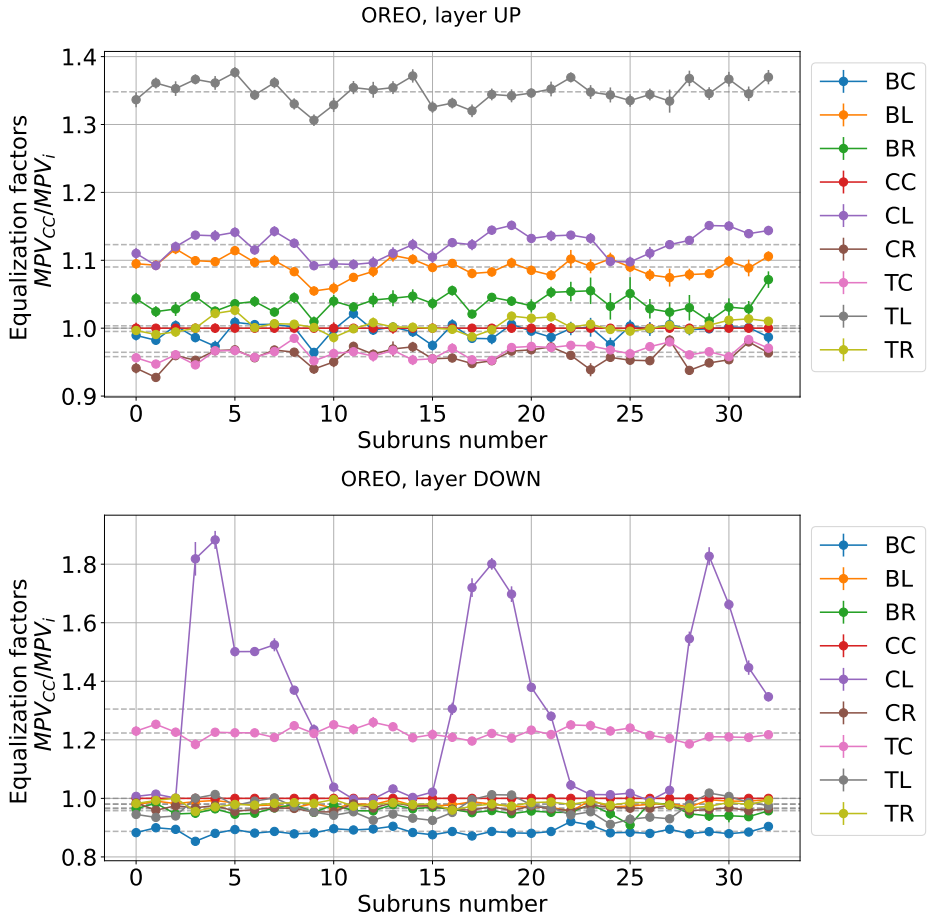

Figure 6.6: OREO equalization factors as a function of the subrun number for both the upstream (top) and downstream (bottom) layers. The error on each point was determined through the error propagation.

to the maximum number of events per subrun, ensuring each subrun contains approximately the same number of events.

3. **Equalization of the channels:**
   - For each subrun, the channels are equalized:
     - For 6 GeV runs, the equalization factors are computed for each subrun.
     - For runs at other energies (where the MIP statistics is too small), the equalization factors are computed by averaging the factors from the 6 GeV runs immediately preceding and following the run under test.
4. **Landau fit on the sum of the channels:**
   - Once the channels are equalized, the signals of all the channels in each subrun are summed. A Landau fit is then performed on the summed signal for each subrun.
5. **Normalization:**
   - The whole subrun is divided by the MPV obtained from the Landau fit to normalize the MIP peak to 1.

6. **Re-processing of the run:**

   - After the normalization, the run is reprocessed without the initial cut in position and on the Cherenkov detectors PH. Figure 6.7 shows the μ values extracted from the Crystal Ball[2] fit of the energy deposited in the upstream layer by a 6 GeV electron beam during a long axial run taken over the night. The blue squared markers represent the values obtained by dividing the run into time intervals after having applied the correction procedure, while the orange round markers correspond to the same division without applying any correction on the run. It can be seen that the electrons signal remains stable over time when the correction procedure is applied.

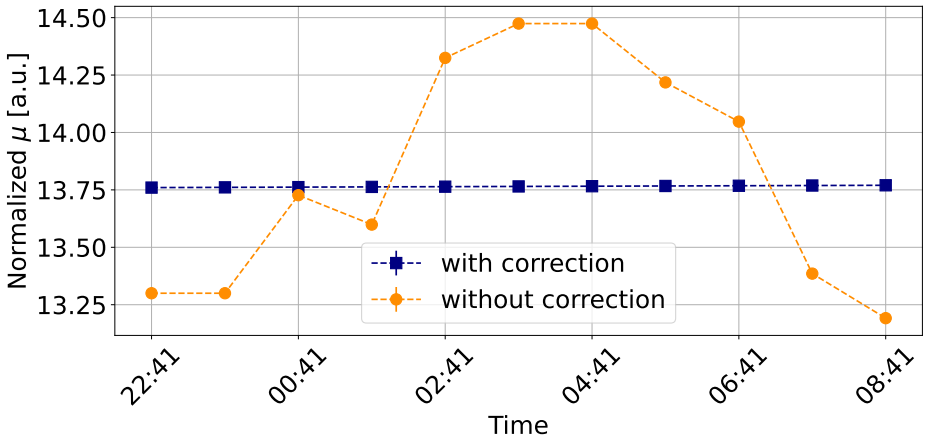

Figure 6.7: μ values extracted from the Crystal Ball fit of the energy deposited in the upstream layer by a 6 GeV electron beam during a long axial run taken over the night. The blue squared markers represent the values obtained after applying the correction procedure on the run, while the orange round markers have been obtained without applying any correction on the run. It can be seen that the electrons signal remains stable over time when the correction procedure is applied.

6.1.2 CRYSTAL INTERALIGNMENT

One of the main goals of the beamtest was to verify that all the crystals remain interaligned when arranged in a matrix structure.
A preliminary characterization has been performed at the laboratories of Università degli Studi di Ferrara using a HRXRD [76] equipped with a laser self-collimator [77]. A detailed description of the procedure can be found in [77][87][114]. The results are shown in Figure 6.8: the maximum misalignment is of the order of 100 μrad, well below the strong field angular acceptance Θ_0 of $\sim$ 0.9 mrad (Section 2.1.4).

To study the crystal interalignment, during the beamtest a scan around the axis coordinate was performed by varying both the cradle and rotational coordinates of the goniometer. A 6 GeV parallel electron beam was used to uniformly cover all the crystals. A position cut was applied on each crystal to select the events of interest, along with a cut in the threshold

2 Defined in Equation 4.2.

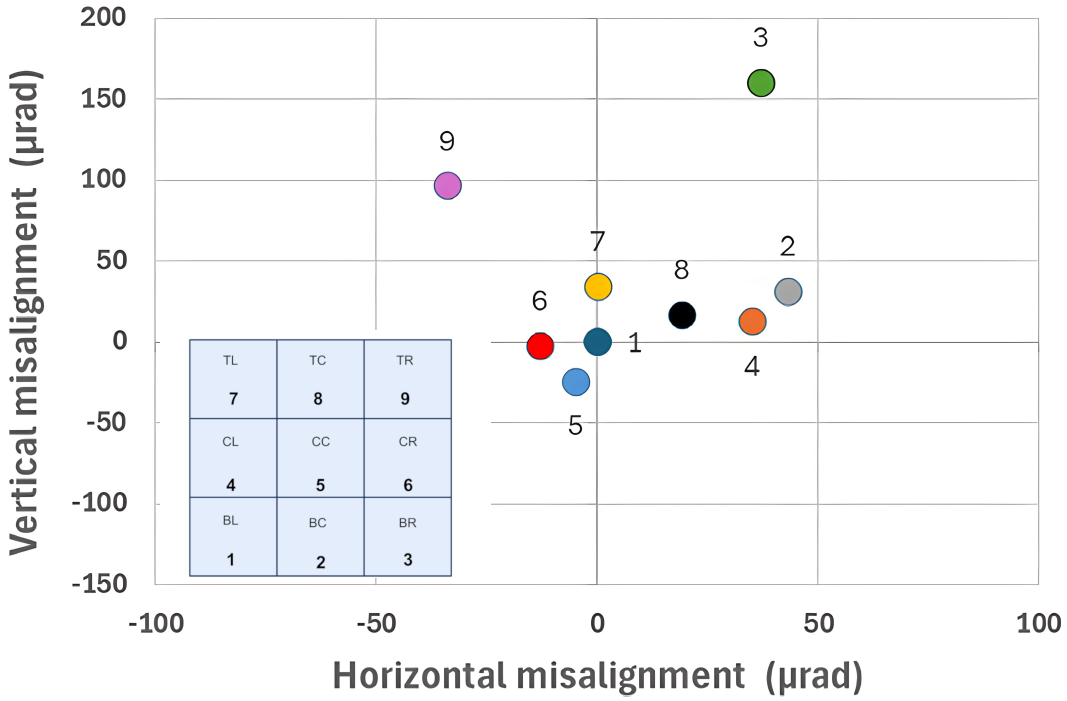

Figure 6.8: Preliminary interalignment characterization: the alignment achieved between the crystals in the final matrix is of the order of 100 μrad, well below the strong field angular acceptance Θ_0. The description of the procedure can be found in [87].

Cherenkov detector signal in order to select only the electrons, a cut in divergence and a cut in the signal peak time. For each scan point, the electron energy deposit distribution, measured in arbitrary units, was fitted using a Crystal Ball function. The results obtained during the rotational scan are presented in Figure 6.9. The pink dotted line represents the axis coordinate determined through the crystal alignment procedure described in Section 4.1.2. The green dashed line represents the weighted average of the scan positions, where each position is weighted by the corresponding mean energy deposit. The largest observed deviation was 147.19 $\pm$23.01 μrad between the TR and CL channels in the rotational scan, while in the cradle scan, the maximum deviation was 166.58 $\pm$31.09 μrad between the CC and BL channels. These results suggested that the crystals were well interaligned validating the bonding procedure.
Furthermore, the ratio between the μ value of the energy deposit in the random and axial orientations has been studied for each crystal using a 6 GeV parallel electron beam. The results are presented in Figure 6.10. The largest deviation, observed between the TL and BC channels, is $\sim$ 4%, demonstrating, once again, the good alignment of the crystals.

6.1.3 SIPMS CALIBRATION

Due to the extremely low MIP statistics when OREO is rotated by 90 degrees, the calibration method used during the 2023 beamtest could not be applied to convert each OREO layer signal from arbitrary units to energy measured in GeV. Therefore, it has been chosen

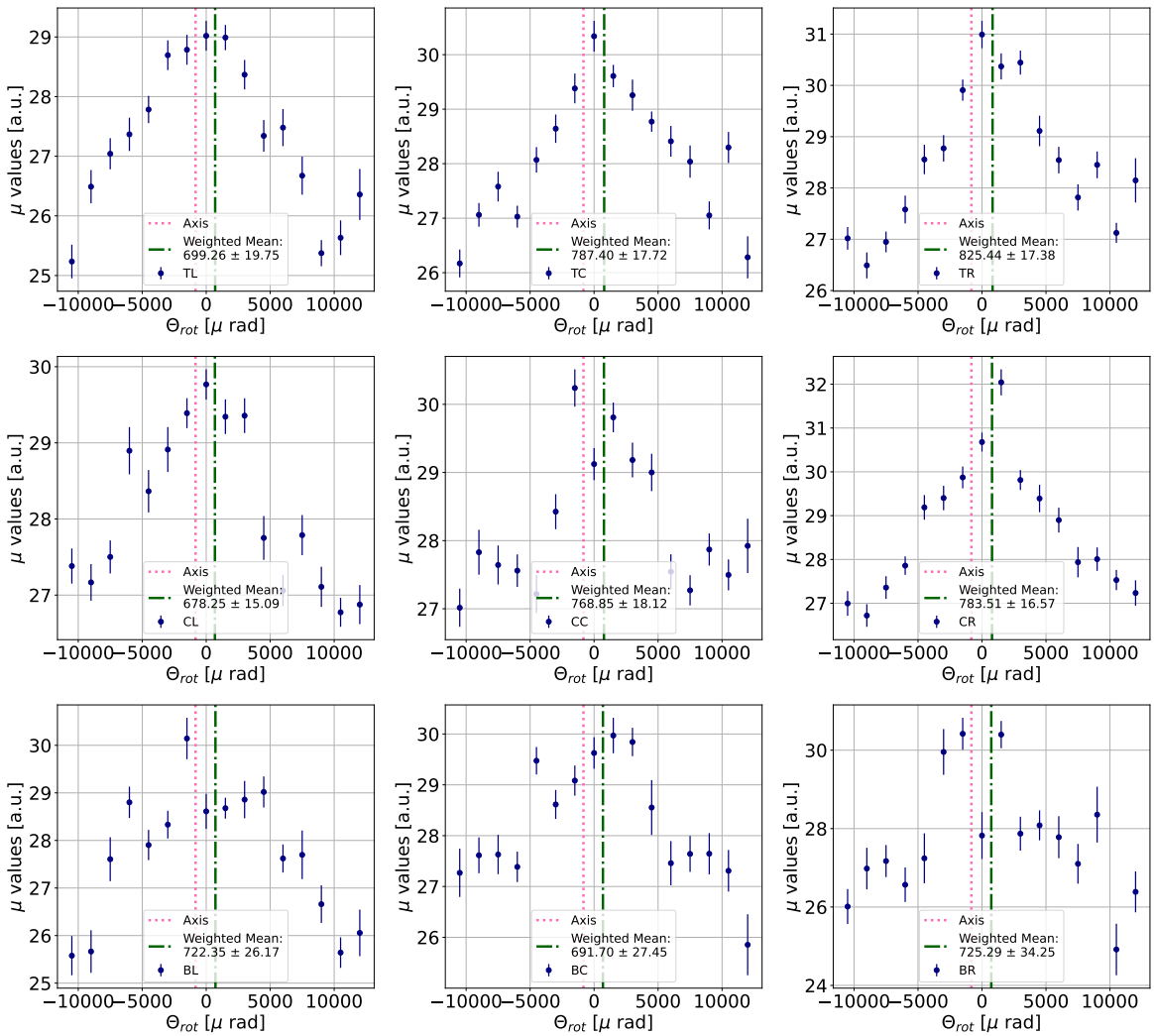

Figure 6.9: μ value of the energy deposit during a rotational scan around the axis coordinate. The pink dotted line indicates the selected axis coordinate, which was kept fixed during the beamtest, while the green dashed line represents the weighted average of the data points.

to calibrate each layer separately using a Monte Carlo simulation with Geant4, whose details are described in Appendix B.

Figure 6.11 shows the simulated energy deposit distribution in each layer obtained with electrons with energies from 2 GeV to 6 GeV, along with the experimental data, fitted with the Crystal Ball function. The experimental data were fitted after applying a cut in position at the center of the central crystal and a cut on the threshold Cherenkov detectors in order to select the electrons. The calibration lines fitted with a first-degree polynomial and the corresponding residuals, computed as $\text{res}[\%] = 100 \cdot (y_{\text{exp}} - y_{\text{fit}})/y_{\text{exp}}$, are shown in Figure 6.12. All the residuals are smaller than 2.5%, indicating a good linearity of the SiPMs response.

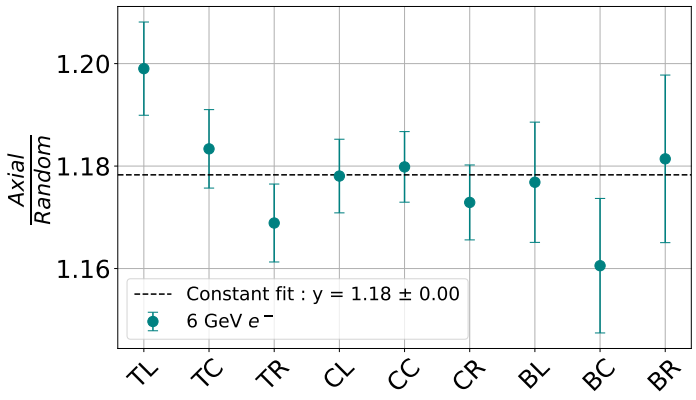

Figure 6.10: Ratio between the mean energy deposit in the random and axial orientations for each crystal. The dashed black line represents a constant fit: a χ^2/ndof value of 1.20 indicates that the ratio values are consistent across the crystals. The largest observed deviation is between the TL and BC channels.

6.1.4 CHARACTERIZATION AT DIFFERENT ENERGIES

After having studied the interalignment of the crystals, the OREO response was analyzed with different beam energies, ranging from 2 to 6 GeV. For each energy, data were collected with both axial and random crystal orientations, ensuring that the beam was centered on the central crystal. Several cuts were applied: a cut in position to select the events on the central crystal (CC), cuts on the signal peak time and on the beam divergence. The electrons were selected using the threshold Cherenkov detectors. Figure 6.13 shows the energy deposit in the two layers of OREO and in the full OREO calorimeter (obtained as the sum of the two layers) for both the random and axial orientations. The acceleration of the development of the electromagnetic shower in the axial orientation results in a slight increase[3] in the energy deposit in the upstream layer: the ratio between the axial and random orientation is 1.20 ± 0.01. In contrast to the upstream layer, the energy deposited in the downstream layer is larger in the random configuration. The energy deposited in the axial and random orientations differs by about 3σ, suggesting marginal compatibility within uncertainties.

Figure 6.14 shows as a function of the incident energy:

a) The μ value extracted from the Crystal Ball fit of the energy deposit distribution in the upstream layer in the axial and random orientation; in the axial orientation there is an enhancement of the energy deposited due to the coherent effects in oriented crystals.

b) The ratio between the energy deposit in the axial and random orientations in the upstream layer; since strong field effects dominate at high energies ($\sim$ tens of GeV), the ratio does not increase significantly as a function of the incident beam energy reaching a maximum value of 1.20 ± 0.01 for the 6 GeV electron beam.

3 The effects of the strong field regime become evident for energies above approximately 30 GeV. However, at energies of the order of GeV, coherent effects in the oriented crystals lead to an enhancement in the energy deposit.

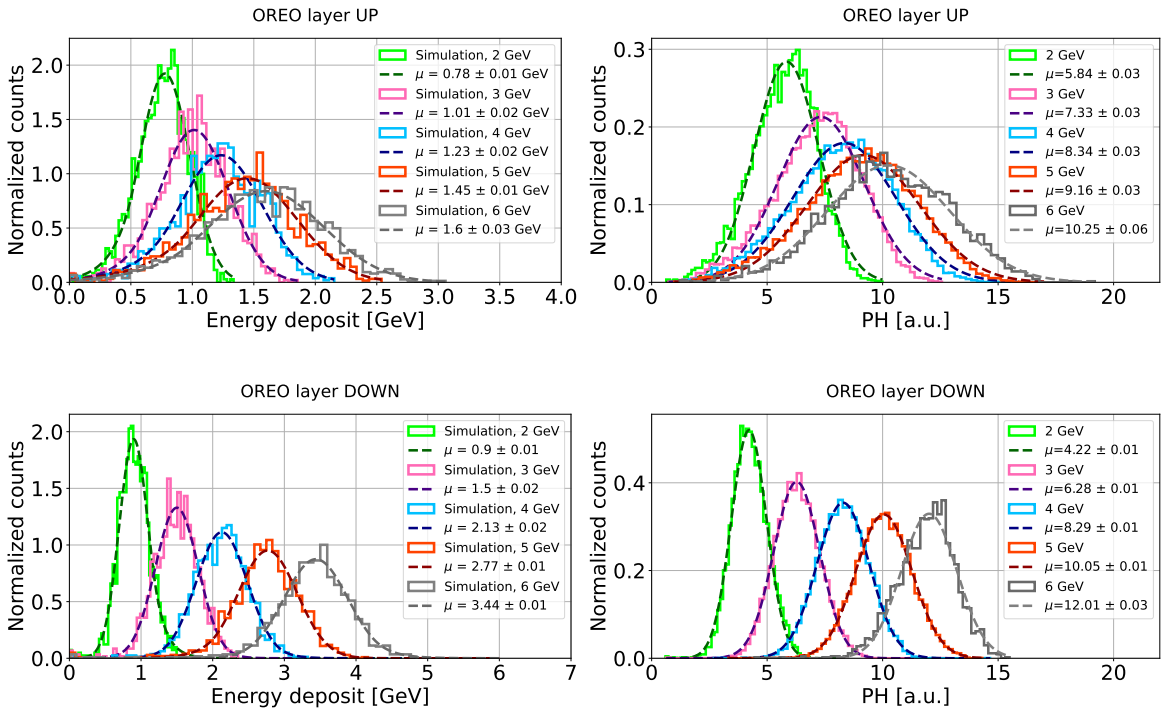

Figure 6.11: (left) Energy deposit distribution in the (top) upstream and (bottom) downstream layer obtained using the Geant4 simulation described in Appendix B. (right) Experimental PH distribution in arbitrary units. Each curve has been fitted using the Crystal Ball function defined in equation 4.2.

c) The μ value extracted from the Crystal Ball fit of the energy deposit distribution in the downstream layer in the axial and random orientation. The energy deposited in the downstream layer is larger in the random orientation, due to the enhancement in the energy deposited in the upstream part when crystals are axially oriented.

d) The μ value of the energy deposited in the full OREO calorimeter (obtained as the sum of the two layers); at these energies, the electromagnetic shower is almost entirely contained both in the random and axial configuration (Figure 6.15). All the μ values are statistically compatible with each other within one σ, indicating no significant evidence of a better containment when the upstream layer is axially oriented, except for the 6 GeV electron beam, as discussed above (Figure 6.13).

Figure 6.15 shows the energy leakage (defined as the difference between the nominal beam energy E_{beam} and the energy deposit in the OREO calorimeter E_{Dep}) and the energy deposited in the lead glass calorimeter, positioned 0.20 m behind OREO, as a function of the incident beam energy. All the energy leakage values are statistically compatible between the axial and random orientations. The energy deposit in the lead glass calorimeter, which gives an estimation of the OREO longitudinal energy leakage, was determined by fitting the energy distribution (in arbitrary units) with a Landau function and then converting it in GeV using the calibration line defined in A.3.2. At these energies, the shower is almost fully contained, resulting in a near-zero energy deposit in the lead glass. The values observed at 6 GeV reach a discrepancy slightly above one σ, remaining below the level of statistical significance. The strongest effects in the reduction of the longitudinal

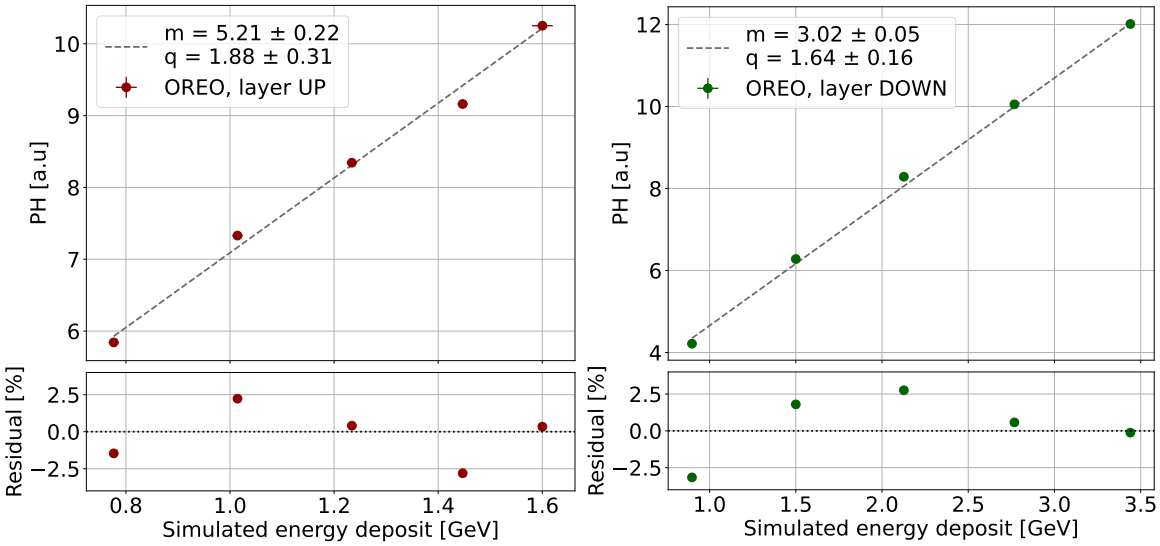

Figure 6.12: Calibration line for the (right) upstream and (left) downstream layer along with the corresponding residuals.

leakage in the OREO calorimeter are observed at higher energies, where the strong field effects dominate. These results are presented in Section 6.2.4.

6.1.5 ELECTRON/HADRON DISCRIMINATION

In 2023, a preliminary study on the electron/hadron discrimination capability of the 2×2 OREO prototype has been performed (Section 5.2.3).
To investigate the performance of the full OREO calorimeter in the electron/hadron discrimination, runs with a 6 GeV mixed beam[4] were performed in both the random and axial orientations. Figure 6.16 presents the two-dimensional histogram of the energy deposited in the upstream and downstream OREO layers; a cut in position was applied on the central crystal along with a cut on the signal peak time and on the beam divergence.
As already observed, since the nuclear interaction length remains unaffected by the lattice orientation, the energy deposited by hadrons does not change in the axial orientation. On the other hand, under the influence of the axial crystalline field, the energy deposit distribution of electrons shifts toward higher values.
The electrons were identified using the threshold Cherenkov detectors, applying an AND condition between the two detectors to ensure higher purity, as described in Appendix A. Figure 6.17 shows the scatter plot obtained by applying a cut on the threshold Cherenkov detectors PH in order to discriminate electrons from hadrons.
As for the 2×2 OREO prototype (Section 5.2.3), the improvement in the electron/hadron discrimination capability of the OREO calorimeter has been analyzed calculating the elements of the confusion matrix TP, TN, FP and FN (presented in Table 5.2).
Different threshold cuts on the energy deposited in the OREO upstream layer have been

4 The 6 GeV mixed beam produced at the T9 beamline is primarily composed of charged pions, muons and electrons.

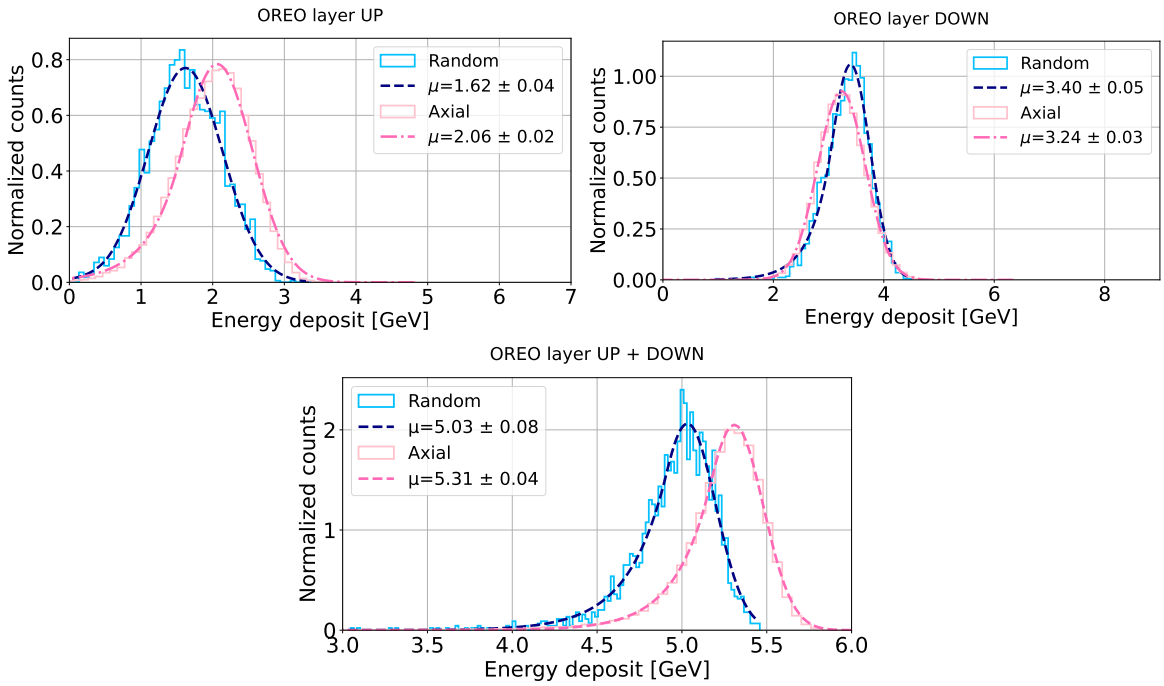

Figure 6.13: 6 GeV energy deposit in the upstream and downstream layer and in the full OREO calorimeter.

applied; for each threshold, the performance metrics defined in Section 5.2.3 has been evaluated.

The results obtained by applying different threshold cuts on the energy deposited in the OREO upstream layer in random and axial orientations are shown in Figure 6.18. Considering the classification process as a series of independent Poisson-distributed counts, the statistical uncertainty on each element of the confusion matrix is estimated using the square root of the corresponding number of counts. The uncertainty on the efficiency, accuracy and purity has been computed using the error propagation.

There is an overall trend indicating that the accuracy improves when the upstream layer is oriented, particularly at higher classification thresholds. For instance, for a threshold of 1.8 GeV the accuracy in distinguishing electrons from hadrons increases from 70.40 ± 0.29 % with random orientation to 84.74 ± 0.13 % with oriented crystals, corresponding to an improvement of $+(14.84 \pm 0.31)$ % in the classification performance. This suggests that the oriented configuration is more effective at distinguishing electrons from hadrons, reducing both the false positive and false negative cases.

The efficiency in the classification improves when the crystals are oriented; for instance for the 1.8 GeV threshold, the efficiency reaches 77.90 ± 0.18 % compared to 54.41 ± 0.39 % when the crystals are not oriented (with a $+(23.49 \pm 0.43)$ % in performance), indicating that OREO performs better at correctly identifying electrons.

Purity, on the other hand, appears to remain unaffected by the orientation; the values obtained in the axial orientation are statistically compatible with those from the random orientation, both approaching values close to 100 %.

The strongest effects on the electron/hadron discrimination capability of the OREO calori-

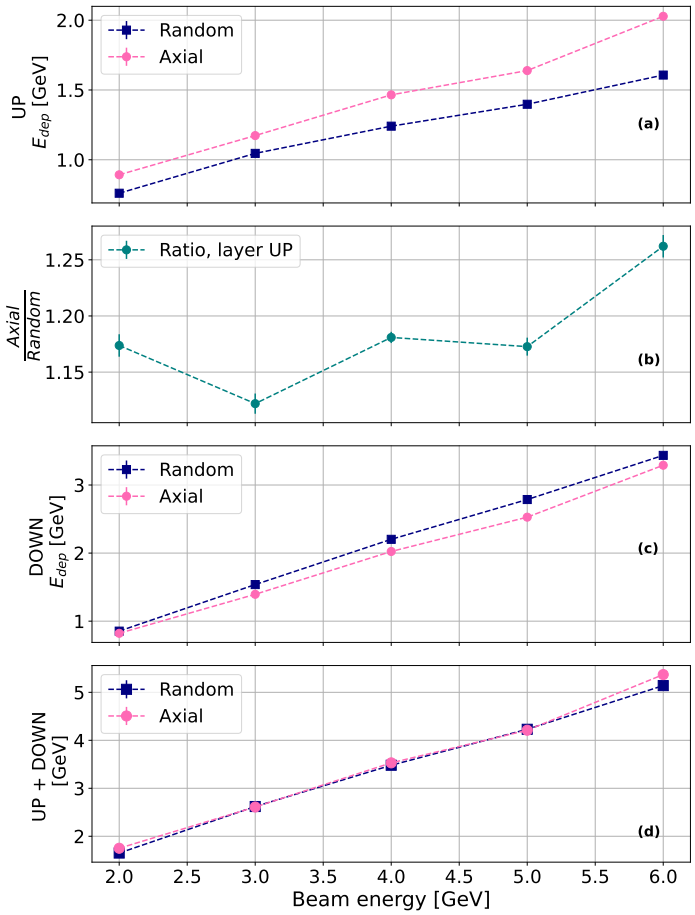

Figure 6.14: The μ value extracted from the Crystal Ball fit of the energy deposit distribution in axial and random orientation as a function of the incident energy: (a) Upstream layer. (b) Ratio between the energy deposit in axial and random orientation in the upstream layer. (c) Downstream layer. (d) Full OREO calorimeter (obtained as the sum of the two layers).

meter occur at higher energies, where the strong field effects dominate. These results will be presented in Section 6.2.7.

6.2 THE JULY BEAMTEST AT THE H4 BEAMLINE AT THE CERN SPS

During the July beamtest, the 3×3 OREO prototype was tested with beam energies ranging from 40 to 200 GeV at the H4 beamline of the CERN SPS. The goals of the beamtest were the following:

- Characterize the strong field acceleration of the electromagnetic shower in the OREO calorimeter, measuring the deposited energy as a function of the beam energy and incidence angle.
- Evaluate the angular acceptances of the strong field acceleration of the electromagnetic shower.

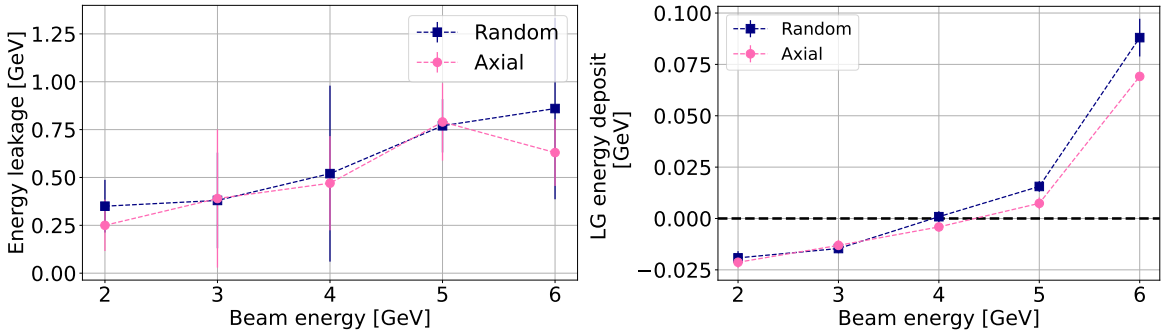

Figure 6.15: Energy leakage and energy deposited in the lead glass as a function of the incident beam energy.

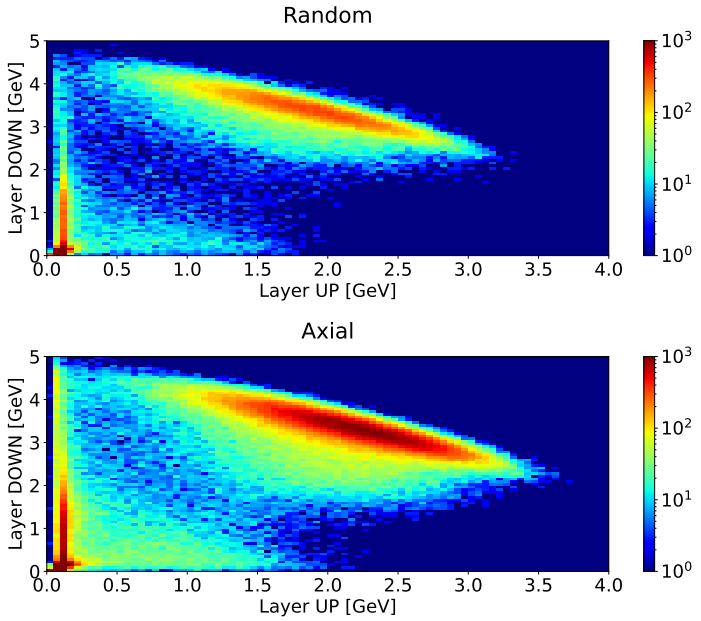

Figure 6.16: Two dimensional histogram of the energy deposited by a 6 GeV mixed beam in the upstream and downstream layer.

- Compare the behavior of electrons and positrons in oriented crystals.
- Evaluate the potential electron/hadron discrimination capability of OREO, in random and axial alignment.

6.2.1 SIPMS EQUALIZATION

The signals from the SiPMs of the upstream and downstream layer of the OREO calorimeter have been equalized separately. The equalization factors have been computed using the data taken with a 200 GeV μ^- beam impinging on the center of each crystal. The events of interest have been selected by subtracting the pedestal from the signal, applying a cut in position at the center of each crystal, as shown in Figure 6.19, and applying a cut in the signal peak time as shown in Figure 6.20.

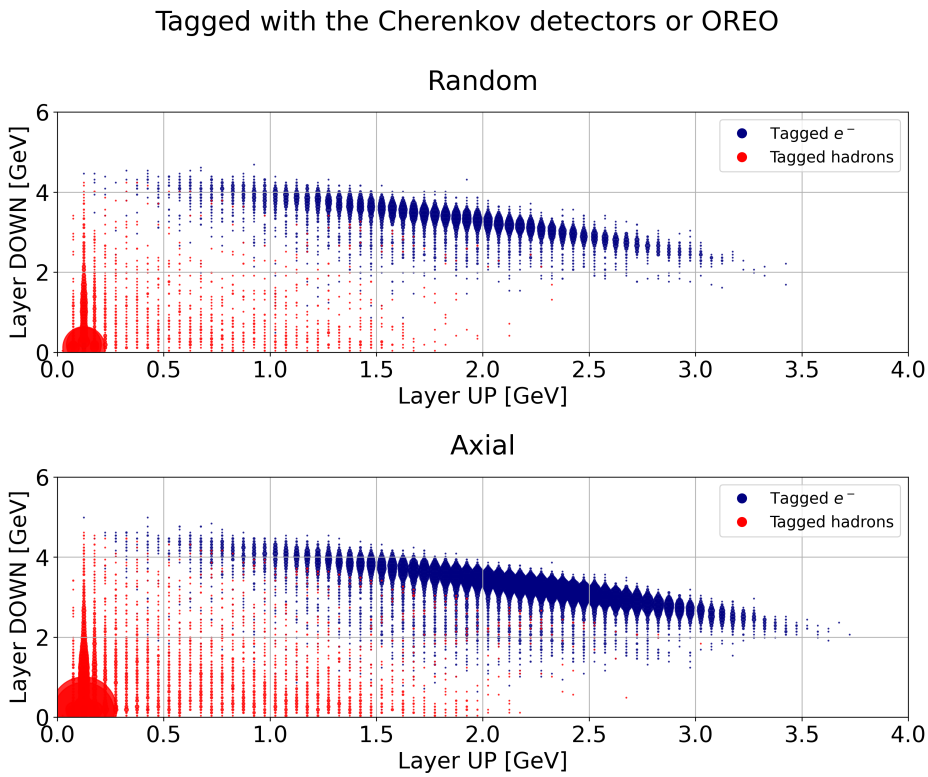

Figure 6.17: Scatter plot of the electrons (blue dots) and hadrons (red crosses) tagged using the information from the threshold Cherenkov detectors.

Figure 6.21 shows the PH spectra of the upstream and downstream layer of the central channel fitted with a Landau function. The signal of the central channel (CC) of the OREO downstream layer was electronically attenuated by a factor $\sim$ 2.5, with respect to the other channels, to avoid saturating the digitizer input voltage range. For each layer, the equalization factors have been computed as:

$$Q_i = \frac{MPV_{CC}}{MPV_i}$$

where MPV_i is the Most Probable Value extracted from the Landau fit of the i-th channel, while MPV_{CC} is taken as a reference. The equalization factors are summarized in Table 6.1.

Upstream layer

TL	**TC**	**TR**
1.073 ± 0.024	0.978 ± 0.020	1.015 ± 0.020
CL	**CC**	**CR**
0.949 ± 0.023	1.000 ± 0.021	1.075 ± 0.026
BL	**BC**	**BR**
1.412 ± 0.035	0.985 ± 0.019	1.101 ± 0.025

Downstream layer

TL	**TC**	**TR**
0.504 ± 0.020	0.519 ± 0.018	0.490 ± 0.019
CL	**CC**	**CR**
0.473 ± 0.018	1.000 ± 0.047	0.471 ± 0.018
BL	**BC**	**BR**
0.468 ± 0.018	0.460 ± 0.016	0.495 ± 0.020

Table 6.1: Equalization factors for the OREO upstream and downstream layers. The signal of the central channel (CC) of the downstream layer was electronically attenuated by a factor of approximately 2.5 using an attenuator, in order to avoid saturating the digitizer input voltage range.

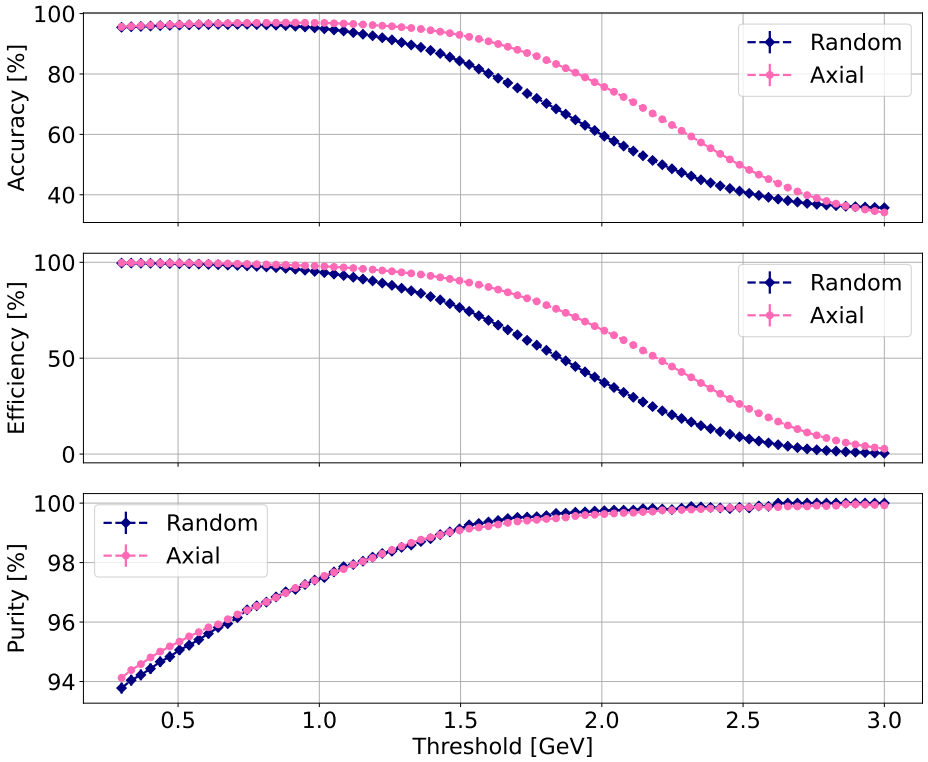

Figure 6.18: Accuracy, efficiency and purity evaluated for different threshold cuts on the energy deposited in the upstream layer of the OREO calorimeter.

6.2.2 THE SATURATION OF THE SIPMS

During the beamtest on the H4 beamline, a saturation[5] in the SiPM response was expected. For this reason, a Kodak Neutral Density Filter [91] was applied to the front face of each layer. However, during the data taking, it was observed that the saturation issue was still present. In particular, during the calibration of the two layers with simulations (as described in Section 6.2.3), a linearity in the response of the upstream and downstream layer was expected. Figure 6.22 shows the mean value extracted from the Crystal Ball fit of the energy deposit distribution in the two layers of OREO in arbitrary units as a function of the simulated energy deposit (details in Section B), in random orientation. A non-linearity in the response of the OREO downstream layer is observed. The non-linearity can be attributed to the large number of photons reaching the SiPMs. Ideally, the output charge should be directly proportional to the number of detected photons. However, SiPMs can exhibit a nonlinear response: they have a finite number of pixels. More photons can interact with the same pixel resulting in a SiPM signal with a smaller amplitude than expected. An additional indication of saturation is given by the following procedure:

- data were acquired with OREO in random and axial alignment at different energies, with 1x/1x attenuation (i.e. one optical filter for each plane);

5 Defined as a loss of linearity caused by the number of fired SiPM cells per single event exceeding approximately one-third of the total number of cells [90].

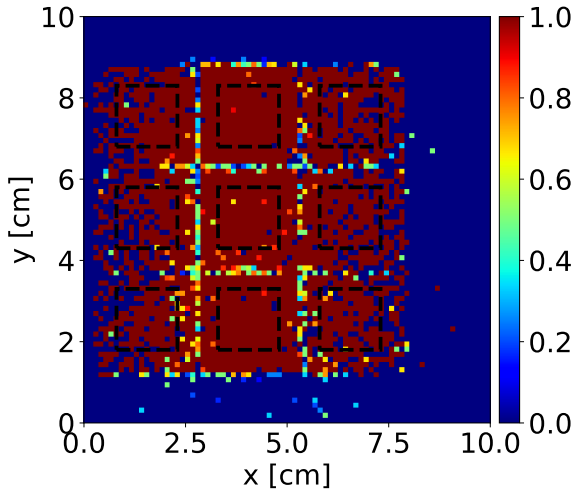

Figure 6.19: OREO efficiency map: the black lines represent the cuts in position applied to select the events of interest.

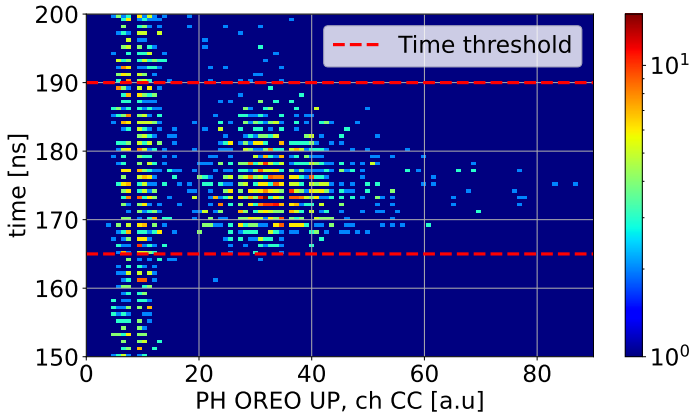

Figure 6.20: Correlation between the OREO Pulse Height and the signal peak time; the red dotted lines show the cuts in time performed to discard spurious triggers.

- for each energy, the mean value $\mu_{1x1x}(E)$, extracted from the Crystal Ball fit of the PH distribution, was computed;
- the same procedure was repeated using a 2x/2x attenuation on both layers. Due to the limited availability of the Kodak filters, it was only possible to apply a single additional Kodak filter on the downstream layer, while a green filter (previously tested in the Ferrara laboratory) was added to the upstream layer. The mean value $\mu_{2x2x}(E)$ was then computed for this configuration;
- the absorbance of the additional filter can be evaluated as:

$$A(E) = \frac{\mu_{2x2x}}{\mu_{1x1x}}(E) \tag{6.2}$$

This ratio remains constant if the detector has a linear response. Figure 6.23 shows the ratio computed for the upstream and downstream layers as a function of the incident beam energy. In both the upstream and downstream layers, the ratio is not constant, indicating

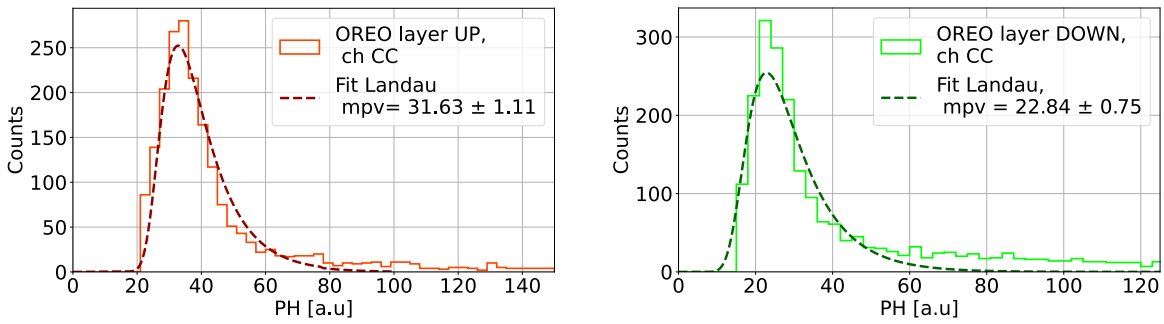

Figure 6.21: PH distribution of the MIPs energy deposit in the central crystal (CC) of the OREO (left) upstream and (right) downstream layer, fitted with a Landau function.

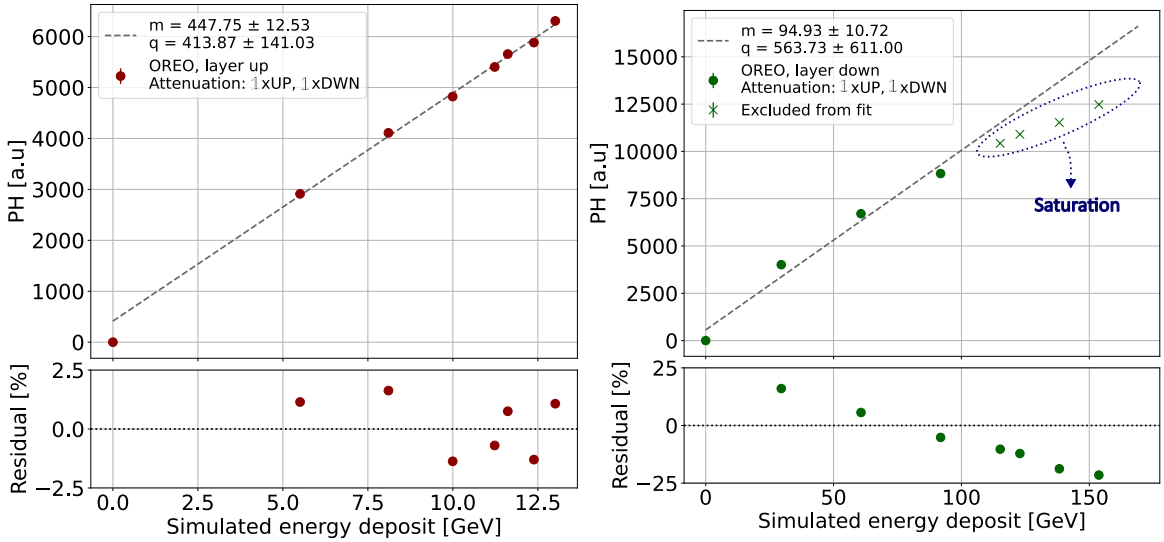

Figure 6.22: Calibration line for the (right) upstream and (left) downstream layer along with the corresponding residuals with one attenuation filter on the upstream and downstream layer. A saturation of the signal of the SiPMs of the downstream layer can be noted .

a saturation of the SiPMs signal. For this reason, the measurements were performed using the two optical filters configuration.

6.2.3 SIPM CALIBRATION

As for the June beamtest, the two layers of OREO have been calibrated separately using the Geant4 simulation presented in Appendix B. For each layer, the energy deposit distribution has been computed by summing the equalized responses of the SiPMs, with the equalization factors provided in Table 6.1, and applying a cut in position at the center of the central crystal. The simulated energy deposit distribution in each layer obtained with electrons with energies from 40 GeV to 200 GeV, along with the experimental data, have been fitted with a Crystal Ball function. The calibration lines fitted with a first-degree polynomial and the corresponding residuals are shown in Figure 6.24. The upstream layer exhibits a good linearity, with residuals below 1.5 % while the downstream layer shows

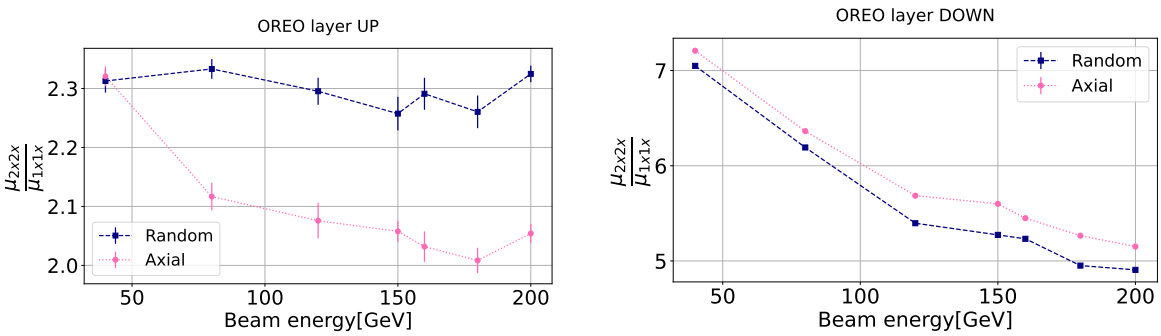

Figure 6.23: Absorbance $A(E)$ of the additional filter as a function of the incident beam energy. A non-constant behavior indicates a saturation in the SiPMs response. Note that two different additional filters were used for the upstream and downstream layers: one green filter was added for the upstream layer, and one Kodak filter for the downstream layer.

a hint of saturation at high energies; the data points with an energy above 120 GeV have been excluded from the fit.

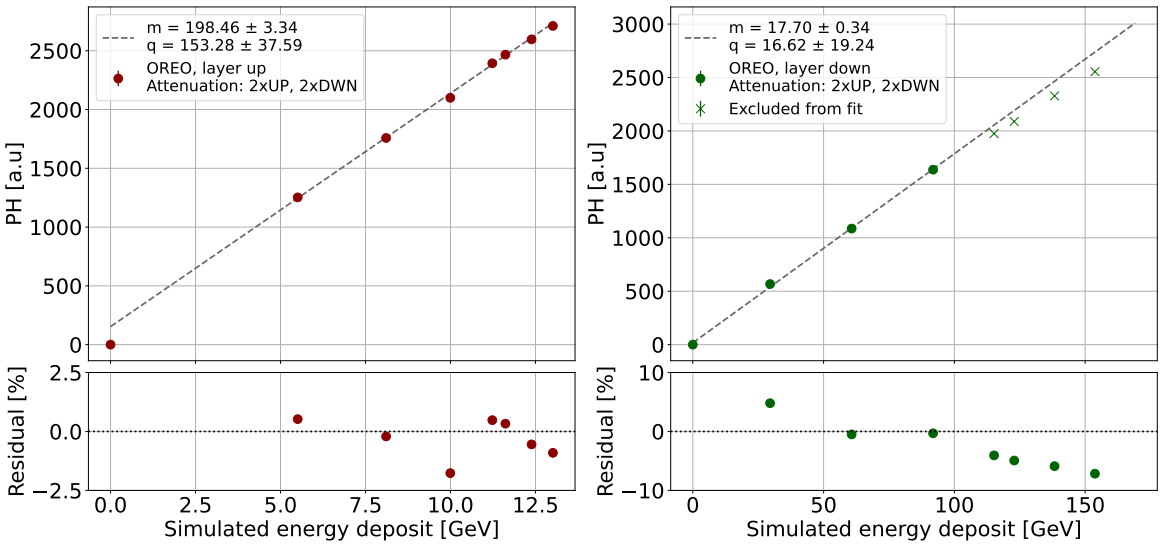

Figure 6.24: OREO calibration line for the (left) upstream and (right) downstream layer along with the corresponding residuals. The upstream layer exhibits a good linearity, with residuals below 1.5 % while the downstream layer shows a hint of saturation at high energies; the data points with an energy above 120 GeV (represented by crosses) have been excluded from the fit.

6.2.4 CHARACTERIZATION AT DIFFERENT ENERGIES

The response of the OREO calorimeter at high energies was studied using beam energies ranging from 40 to 200 GeV, in steps of 20 GeV. For each energy, data were collected with both axial and random crystal orientations, ensuring that the beam was centered on the central crystal. Several cuts were applied: a cut in position to select the events on the central crystal (CC), cuts on the signal peak time and on the beam divergence. Figure 6.25 shows the energy deposit in the two layers of OREO and in the full OREO calorimeter for

both the random and axial orientations for the 120 GeV electron beam. Figure 6.26 sum-

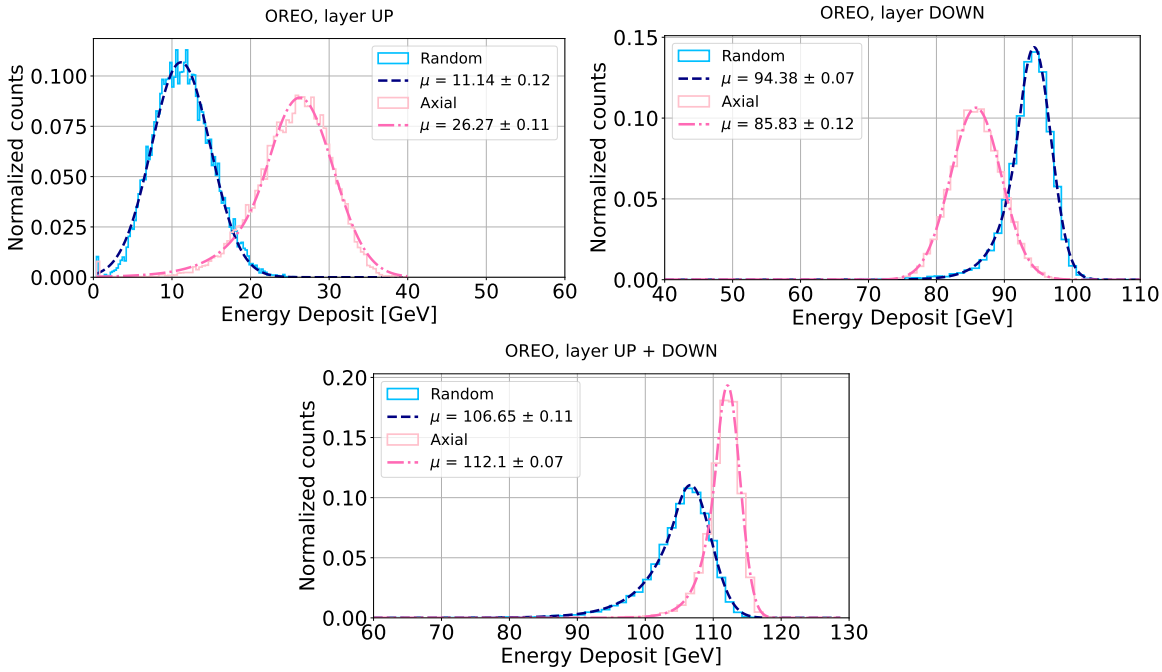

Figure 6.25: 120 GeV energy deposit in the upstream and downstream layer and in the full OREO calorimeter. The ratio in the upstream layer between the axial and random orientation is 2.36 ± 0.07. In contrast to the upstream layer, the energy deposited in the downstream layer is larger in the random configuration. The ratio between the axial and random orientation is 1.051 ± 0.011.

marizes the behavior of the OREO calorimeter at high energies: each point corresponds to the μ value extracted from the Crystal Ball fit of the energy deposit distribution in axial and random orientations as a function of the incident energy. As expected, when the crystals are axially oriented, the deposited energy increases significantly due to the strong field effects. At 200 GeV, the deposited energy in the axial configuration is approximately 2.5 times larger than in the non-oriented case. Furthermore, although at these energies the electromagnetic shower is not fully contained in the OREO calorimeter, due to the acceleration of the electromagnetic shower when the crystals are axially oriented, the energy deposited in the full OREO calorimeter increases (as shown in Figure 6.26d-e). In particular, at 200 GeV, the axial configuration results in a $7.75\% \pm 0.10\%$ larger containment compared to the random orientation, with the deposited energy increasing from 162.71 ± 0.12 in random orientation to 175.31 ± 0.08 when on-axis.

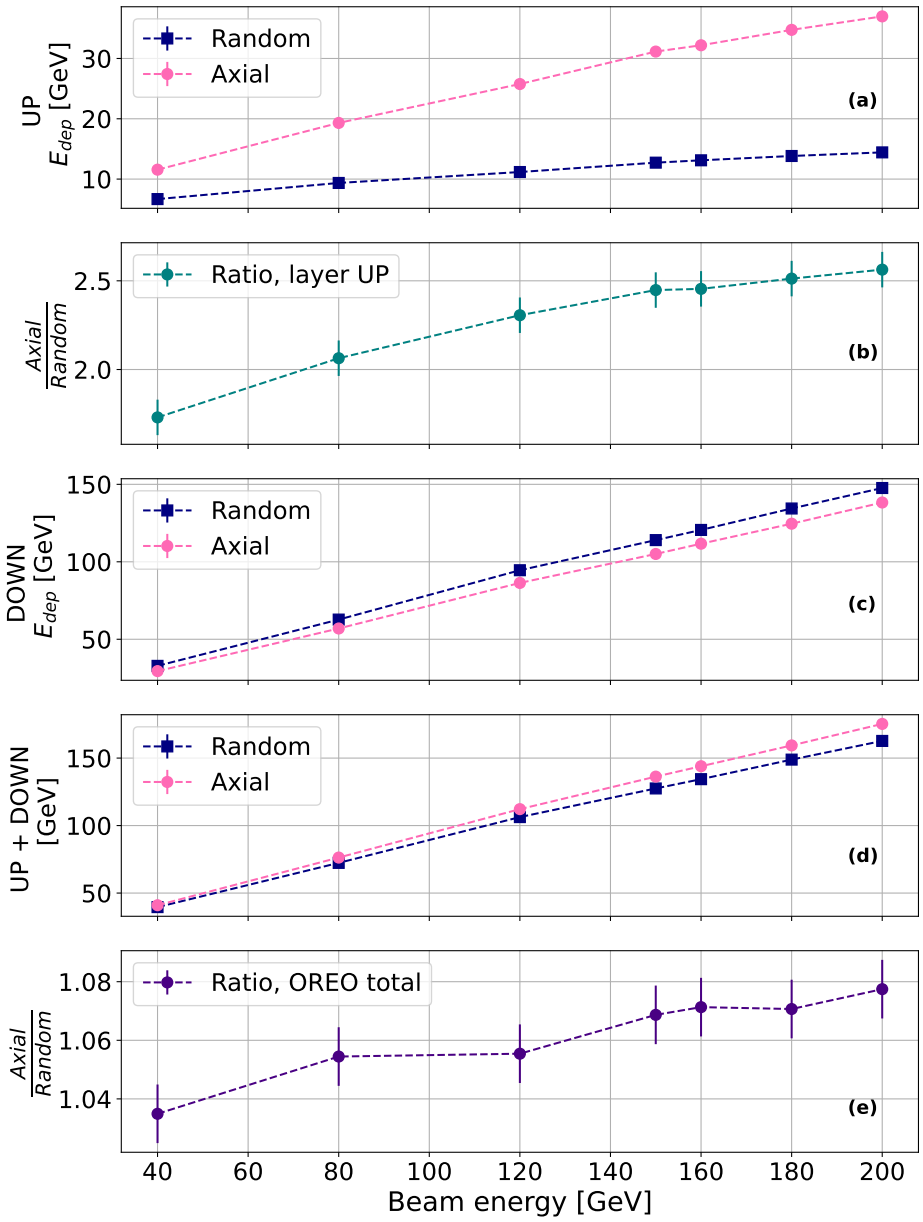

Figure 6.26: The μ value extracted from the Crystal Ball fit of the energy deposit distribution in axial and random orientation as a function of the incident energy: (a) Upstream layer. (b) Ratio between the energy deposit in axial and random orientation in the upstream layer. (c) Downstream layer. (d) Full OREO calorimeter (obtained as the sum of the two layers). (e) Ratio between the energy deposit in axial and random orientation in the full OREO calorimeter.

Figure 6.27 shows the energy leakage ($E_{beam} - E_{dep}$), and the energy deposited in the lead glass calorimeter, positioned at 0.65 m behind OREO. As the shower develops in the OREO calorimeter, a non-negligible fraction of the energy is transported by secondary particles that, due to the distance between the two detectors, do not interact with the lead glass calorimeter[6]. Nevertheless, when the beam is aligned along the axial direction of

6 A larger value in the measured energy leakage (in particular for beam energies greater than 120 GeV) could also be due to the saturation in the SiPM signal, which leads to an underestimation of the deposited energy and consequently to an overestimation of the energy leakage.

the crystals, the electromagnetic shower is accelerated and the effective radiation length is reduced, resulting in a decrease in the longitudinal energy leakage.

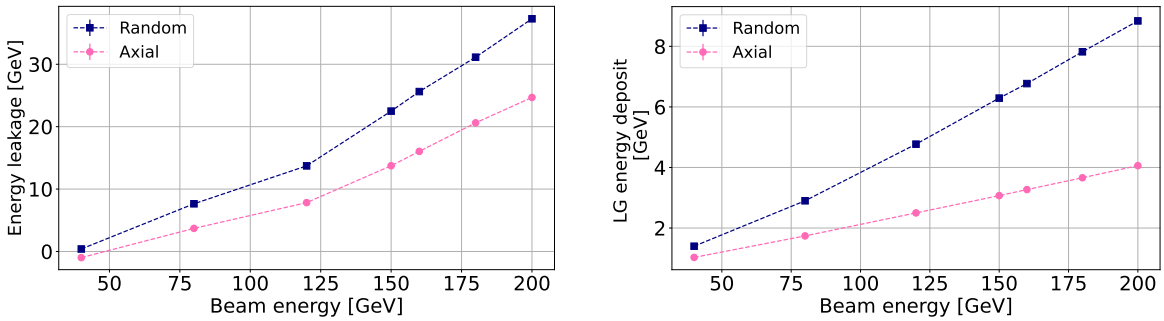

Figure 6.27: Energy leakage and energy deposited in the lead glass as a function of the incident beam energy. Under the influence of the strong field, the acceleration of the electromagnetic shower reduces the effective radiation length, resulting in a decreased energy leakage .

6.2.5 ELECTRONS AND POSITRONS INTERACTION IN ORIENTED CRYSTALS

One of the goals of the beamtest was to demonstrate that the energy measurement performed by an oriented electromagnetic calorimeter is independent on the charge of the primary particle. Although electrons and positrons behave identically under electromagnetic interaction, their behavior in oriented crystals can differ due to coherent interactions that depend on the sign of the particles charge. However, in the strong field regime, where the dominant radiation mechanism is synchrotron-like, no significant differences are expected in the radiation energy spectra between electrons and positrons. Dedicated measurements on the upstream layer have been performed with 120 GeV electrons and positrons[7]. The signal from each crystal has been equalized using the equalization factors listed in Table 6.1; the events of interest have been selected by applying a cut in position at the center of the central crystal (CC) and on the beam divergence. The results are shown in Figure 6.28: as expected, the spectra obtained with the electron and positron beam are perfectly compatible to each other in both the random and axis configuration.

6.2.6 ANGULAR TRANSITION

A very important step in characterizing an oriented calorimeter is to evaluate how coherent effects depend on the particle incidence angle.
Measurements with a 180 GeV electron beam have been performed at an increasing angular distance from the axis, along a direction that was chosen as far as possible from any strong

7 The measurements with electrons and positrons were performed before the saturation issues with the SiPMs were fully understood. For this reason, the 1x1x optical filter configuration (one Kodak filter on the upstream layer and one Kodak filter on the dowstream layer) was used. The energy deposit distribution is expressed in arbitrary units.

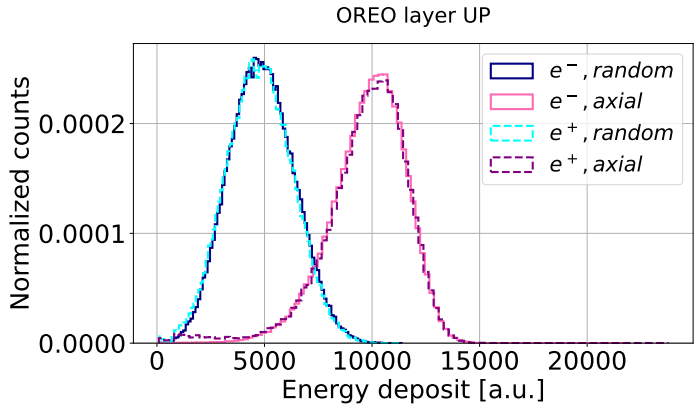

Figure 6.28: Comparison between the energy deposited in the upstream layer of the OREO calorimeter by electrons and positrons, in the random and axial configuration. The spectra are compatible to each other in both configurations.

plane. Figure 6.29 shows the ratio between the energy deposited in the upstream layer at different particles incidence angles and the energy deposit in the random orientation, as a function of the particles incidence angles θ. When the crystals are in axial orientation, the energy deposited in the upstream layer is approximately 2.5 times larger than in the non-oriented case. Coherent effects are observed up to about 1 degree of misalignment, where the enhancement in the energy deposit goes down to a factor of 1.14 ± 0.01.

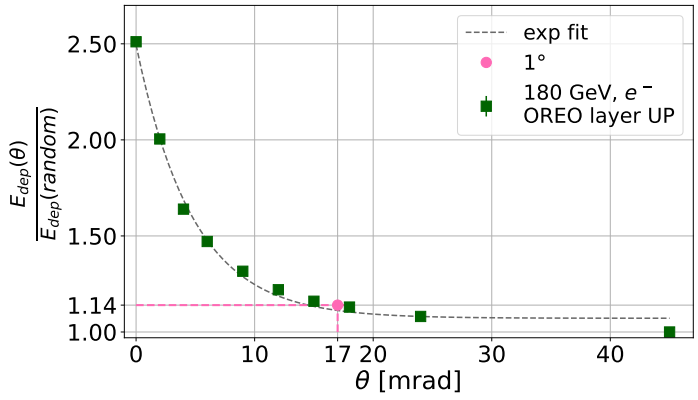

Figure 6.29: Ratio between the energy deposited in the upstream layer at different particles incidence angles and the energy deposit in random orientation, as a function of the particles incidence angles θ.

6.2.7 ELECTRON/HADRON DISCRIMINATION

To investigate the electron/hadron discrimination capability at higher energy of the full OREO calorimeter, where the strong field effects dominate, runs with a 150 GeV pion beam and 150 GeV electron beam were performed in both the random and axial orientations. The 150 GeV pion beam provided by the H4 line has a high percentage of charged pions and a non-negligible fraction of kaons, protons, and muons, while the 150 GeV electron beam always contains a fraction of hadronic contamination (Appendix C and [115]).

Unlike the T9 beamline, where the electrons can be identified using the two threshold Cherenkov detectors installed along the line, at the H4 beamline particle identification at such energies is not trivial.

For this reason, with the data collected in 2024, only preliminary considerations can be made regarding the performance of the full OREO calorimeter in discriminating electrons from hadrons at higher energies.

Figure 6.30 presents the two-dimensional histograms of the energy deposited in the upstream and downstream OREO layers, for the 150 GeV electron run and concatenating the same electron run with the 150 GeV pion beam run for both the random and axial orientations; a cut in position was applied on the central crystal along with a cut on the signal peak time and on the beam divergence.

As previously mentioned, the 150 GeV electron beam is not pure and contains a fraction of

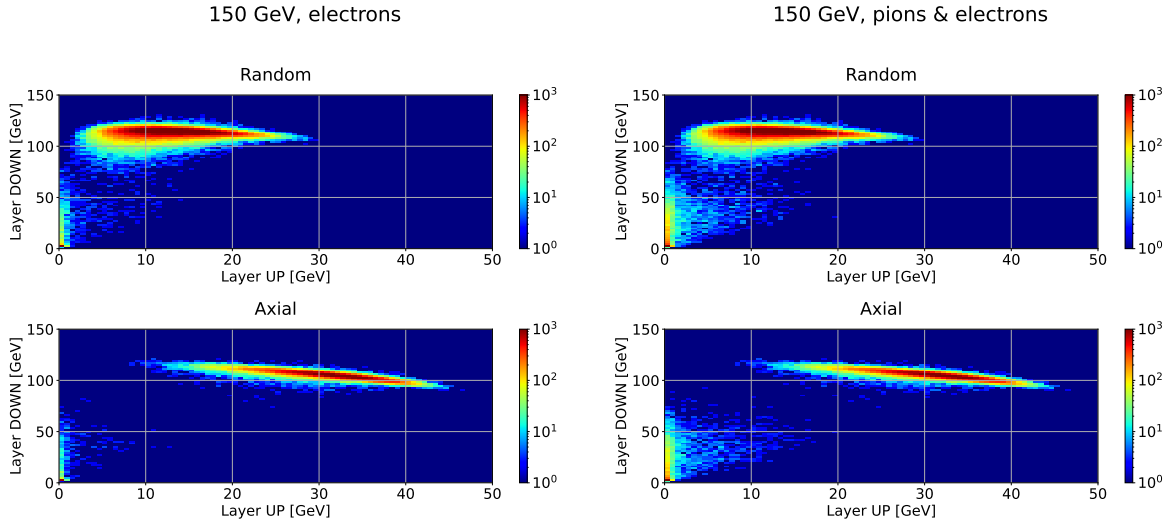

Figure 6.30: (left) Two dimensional histogram of the energy deposited in the upstream and downstream layer by (left) the 150 GeV electron beam and (right) combining the electron run with the 150 GeV pion run.

hadronic contamination. In the axial orientation, under the effect of the strong field regime, there is an enhancement in the energy deposited by the electrons in the upstream layer of OREO, resulting in a shift of the electrons spectra towards higher energies. In contrast, the hadronic contamination is unaffected by the lattice orientation. This effect facilitates the discrimination of the electrons, which produce an electromagnetic shower, from the hadrons that can be identified as the events depositing a small amount of energy in the electromagnetic calorimeter: in the random orientation such separation is less pronounced. Three representative thresholds have been chosen to discriminate the electrons from the hadronic contamination in the 150 GeV electron run, as shown in Figure 6.31:

- At the low threshold (1), the majority of electrons are selected, but a fraction of hadrons is also misidentified as electrons. In this case, the fraction of events identified as electrons (i.e. the events above the selected threshold out of the total events in the electron run) is similar for both the random and axial orientations, around $\sim$ 97 %,

while the fraction of misidentified hadrons (the events above the same threshold out of the total events in the pion run) is approximately $\sim$ 5 % in both orientations.

- At the medium threshold (2), the fraction of events identified as electrons in the random orientation decreases to $\sim$ 93 %, while in the axial orientation it remains at $\sim$ 97 %. The fraction of misidentified hadrons is compatible between the two orientations and is of the order of $\sim$ 4 %.
- At the high threshold (3), the fraction of misidentified hadrons is zero in both orientations. However, the electron efficiency in the random orientation drops drastically to $\sim$ 28 %, while in the axial orientation it remains very high at 96 %.

The enhancement of the energy deposited by electrons (or photons) under the effect of the strong field regime in oriented crystal can provide a better electron (γ) / hadron discrimination while maintaining low the fraction of misidentified events, compared to the random orientation.

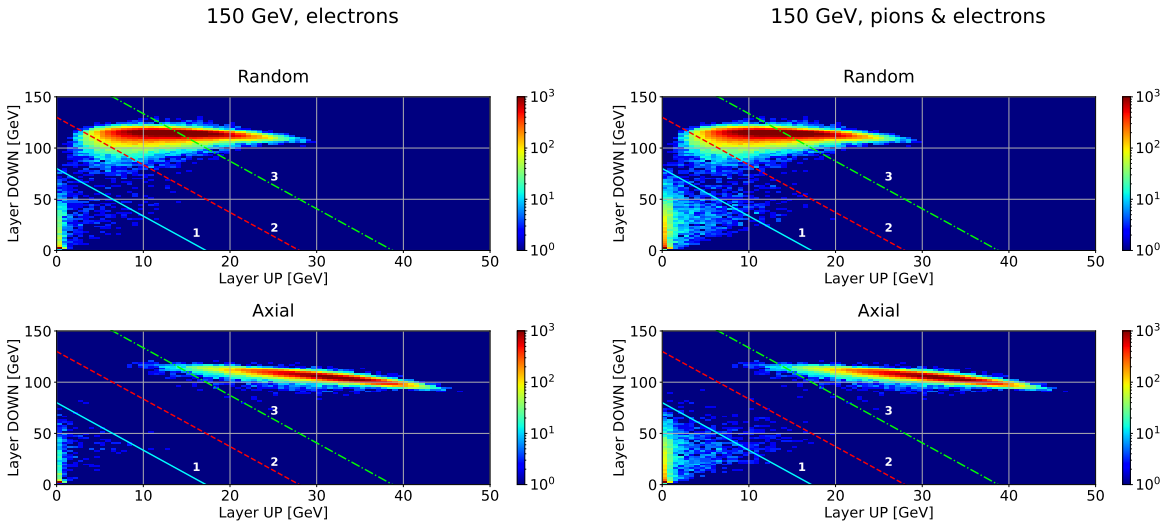

Figure 6.31: Two dimensional histograms of the energy deposited by the 150 GeV pion and electron beam in the upstream and downstream layer. Three representative thresholds have been chosen to discriminate electrons from the hadronic contamination in the 150 GeV electron run.

6.3 OREO OVERALL PERFORMANCE

In the development of an electromagnetic calorimeter based on oriented crystals, two fundamental parameters must be considered: linearity, which ensures that the measured signal is proportional to the deposited energy, and energy resolution, which reflects the ability to accurately measure the energy of the incoming particles. Since the calorimeters used in high energy physics experiments are typically required to operate over a large dynamic range, achieving both a linear response and a good resolution across a wide range of energies is fundamental. This section presents the evaluation of these two key parameters as a function of the incident beam energy, combining the results obtained from the two beamtests performed on the CERN PS and SPS beamlines.

6.3.1 LINEARITY

The linearity of the OREO calorimeter has been evaluated by combining data from both the June and July beamtests performed on the PS and SPS beamlines, using a range of beam energies from 2 to 200 GeV, and considering both the axial and random crystal orientations. A linear fit has been performed on the μ values extracted from the Crystal Ball fits of the energy deposit distributions in the full OREO calorimeter, as a function of the beam energy. To investigate the energy range over which the OREO response remains linear, the root-mean-square (RMS) of the percentage residuals, presented in Figure 6.32, was first computed as a function of the number of points included in the linear fit:

$$\mathrm{RMS}[\%] = \sqrt{\frac{1}{\mathrm{ndof}} \sum_i (\mathrm{Residual}_i)^2} \tag{6.3}$$

where the residuals are computed as res[%] = $100 \cdot (y_{exp} - y_{fit})/y_{exp}$ and ndof is the number of degrees of freedom (number of data points N minus 2).
When including points at high energy (energy > 120 GeV), the RMS of the residuals shows a steady increase, exceeding the 5 % threshold, indicating a deviation from the linear behavior. Therefore, only the points for which the RMS remained below the 5 % have been included in the final linear fit. The linearity of the OREO calorimeter is presented in Figure 6.33. The observed non-linearity at high energies, both in the random and axial orientations, could be due to the non-negligible lateral leakage of the OREO calorimeter (Figure 6.27) and to saturation effects in the SiPM signal, which may still be present even after the application of the attenuation optical filter.

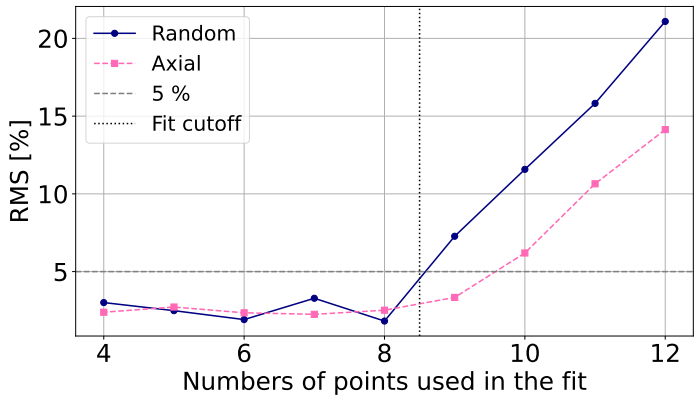

Figure 6.32: RMS of the percentage residuals as a function of the number of points in the linear fit.

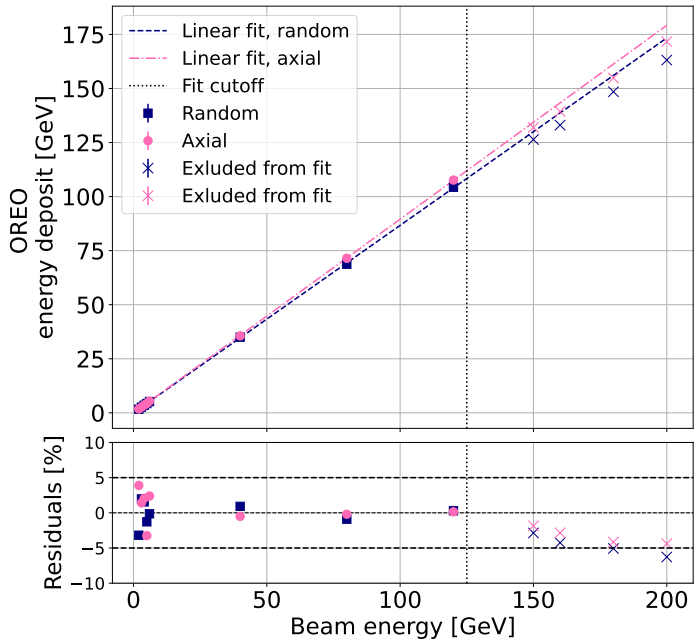

Figure 6.33: OREO linearity and residuals. The data points for energies above 120 GeV have been excluded from the fit. The observed non-linearity could be due to saturation effects in the SiPM signal, which may still be present even after the application of the attenuation optical filter.

6.3.2 ENERGY RESOLUTION

The energy resolution of the OREO calorimeter has been evaluated combining the data collected at both the PS and SPS. The electron peak at different energies has been fitted with a Crystal Ball function[8] and the energy resolution has been computed as:

$$R = \frac{\sigma_\mu}{\mu} \tag{6.4}$$

where σ_μ is the width of the Gaussian core of the Crystal Ball fit and μ is the mean energy deposited in the OREO calorimeter. The results obtained in the random and axial

8 The energy deposit distribution has not been fitted with a Gaussian function due to the low-energy tail caused by the longitudinal leakage in the OREO calorimeter, as shown in Figure 6.25.

orientation are presented in Figure 6.34. The data have been fitted using the function described in Equation 1.17, where the parameter b has been neglected; the data points corresponding to an energy above 120 GeV have been excluded from the fit, as the lateral leakage and the possible saturation in the SiPM signal led to an underestimation of the energy deposit, resulting in an unreliable estimate of the energy resolution. The stochastic and constant term obtained from the fit are presented in Table 6.2. Although the stochastic terms for the axial and random configurations are statistically compatible, the constant term exhibits a significant improvement in the axial orientation. The energy resolution curve for the axial configuration lies below that of the random configuration over the whole energy range, indicating an overall enhancement in the energy resolution performance.

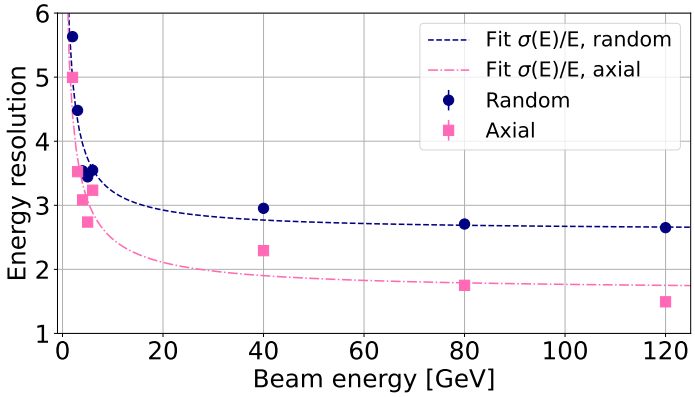

Figure 6.34: OREO energy resolution. The data points corresponding to an energy above 120 GeV have been excluded from the fit.

Orientation	a [% $\sqrt{\text{GeV}}$]	c [%]
Random	5.95 ± 0.48	2.60 ± 0.18
Axial	5.76 ± 0.52	1.66 ± 0.20

Table 6.2: OREO energy resolution terms.

CONCLUSIONS

The work described in this thesis has been performed in the framework of the OREO project, with the aim of assembling and characterizing a first prototype of homogeneous electromagnetic calorimeter based on oriented $PbWO_4$ crystals.
Lead tungstate is one of the most widely used scintillation materials in particle physics experiments, especially in the design of electromagnetic calorimeters. Nevertheless, the influence of the strong crystalline field on the features of the radiation emission by electrons and positrons and on the photon conversion into charged pairs is generally ignored.
When a particle travels inside an oriented crystal, the nearly constant and extremely intense lattice field acting on the particle, leads to an enhancement of the bremsstrahlung and pair production cross sections and thus to an enhancement of the electromagnetic shower development. Therefore, when on axis, the shower is more compact along the longitudinal direction: the reduction of the shower length in crystals can be seen as the reduction of the effective radiation length values with respect to the standard values obtained in case of amorphous or randomly oriented media.
In this work, the enhancement in the electromagnetic shower development and thus the reduction of the radiation length have been measured in a dedicated beamtest in 2022 with a single $PbWO_4$ crystal. During the beamtest, a standardized alignment procedure was also implemented, to ensure that the crystal is oriented such that the beam impinges along the crystallographic axis.
Once the strong field effects were characterized in a single oriented crystal, the next step toward the construction of an electromagnetic calorimeter based on oriented crystals was to test a prototype with multiple $PbWO_4$ crystals glued together. In fact, the most challenging aspect of the OREO design was to keep all the crystals aligned when arranged in a matrix structure. During 2023, two dedicated beamtests have been performed in order to characterize different $PbWO_4$-UF oriented crystals glued together in a single 3×1 row and in a 2×2 matrix. The possibility of aligning a layer of crystals along the same crystallographic direction has been demonstrated for the first time ever.
Finally, in 2024 the OREO calorimeter has been assembled and characterized over a wide range of energies, during two beamtests performed on the T9 and H4 extracted beamlines at the CERN PS and SPS. In particular:

- the inter-alignment of the nine crystals of the 3×3 upstream layer of the OREO calorimeter has been verified, validating the bonding procedure;
- the strong field acceleration of the electromagnetic shower development in the OREO calorimeter has been measured as a function of the beam energy and the particles incidence angle;

- the linearity and the improvement in the energy resolution of the OREO calorimeter have been evaluated.

Beside the advantages of the coherent effects obtained orienting the upstream layer, OREO is a homogeneous calorimeter with a transverse segmentation, a feature that can be exploited to enhance the discrimination between electromagnetically interacting particles and hadrons. In fact, in oriented crystals the strong coherent field modifies only the electromagnetic processes, while the nuclear interaction length is unaffected by the lattice orientation. Consequently, the development of the electromagnetic shower in the upstream layer is accelerated when it is oriented, whereas hadrons interact similarly in both random and axial orientations. Such effect has been experimentally investigated in this work.
All the measurements have been performed using a dedicated experimental setup consisting of a tracking system to reconstruct the particle trajectory, a high resolution goniometer to perform angular measurements, an electromagnetic calorimeter to measure the prototypes longitudinal energy leakage and a dedicated DAQ.
The energy deposited in the $PbWO_4$ crystals has been measured directly with dedicated photodetection systems based on SiPM. During the 2023 and 2024 beamtest it has been noted a saturation in the SiPMs response. In the beamtest performed in the summer of 2025 two additional Kodak filters have been used in order to prevent the saturation of the photodetectors; furthermore, a LED was integrated into each SiPM matrix to enable an offline correction procedure (e.g. temperature drifting of the SiPMs signals). Future developments may consider a SiPM with a larger number of cells to increase the dynamic range and mitigate the saturation. The use of a PMT is generally excluded to maintain the compactness in the design of the OREO calorimeter.

FUTURE DEVELOPMENTS

In August 2025 a beamtest has been performed on the H4 beamline at the CERN SPS. During the beamtest, the OREO calorimeter has been tested aligning the central crystal of the downstream matrix with the crystallographic axis of the upstream layer. Figure 6.35 shows a photo of the OREO prototype during the alignment procedure of the central crystal of the downstream layer. After verifying that two separate layers could be mutually aligned, the electromagnetic shower development, in random and axial orientation, has been studied over a wide energy range. Preliminary results indicate no saturation of the SiPM signals; therefore, a more comprehensive analysis of the OREO calorimeter linearity and energy resolution can be performed.
Future developments include:

- a more quantitative study on the electron/hadron discrimination capability of the OREO calorimeter at high energies. Such study requires dedicated particle identification detectors in the experimental setup;
- the measurement of the effects of the crystalline strong field on the Moliere radius in oriented crystals;

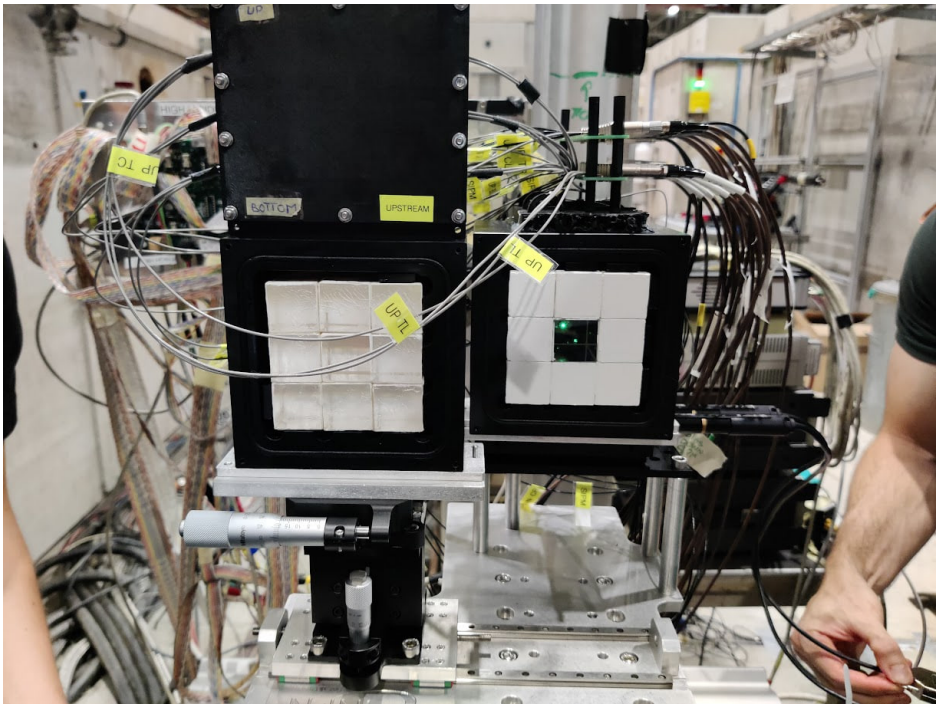

Figure 6.35: The 2025 OREO prototype during the alignment of the central crystal of the downstream layer. After the alignment the front face of the central crystal has been painted with a white reflective paint.

- the development of a Monte Carlo simulation of the coherent effects in oriented crystals (Appendix B.0.1).

The reduction of the effective radiation length and the improvement in the energy resolution with oriented crystals are very interesting features for the future development of calorimeters for high energy physics, in particular for collider experiments at very forward angles, where particles arrive directly from the interaction point with very little angular spread.

The use of oriented crystals was considered in the design of the High-Intensity Kaon Experiment (HIKE) Small Angle Calorimeter (SAC). HIKE was a proposed CERN experiment aimed at measuring the very rare decay $K_L \to \pi^0 \nu \bar{\nu}$. The SAC was to be placed directly in the neutral beamline to detect photons from π^0 decays with a small opening angle. The calorimeter was required to be as transparent as possible to neutral hadrons, with an expected hadron flux in the beamline of $\sim$ 500 MHz. The implementation of an oriented calorimeter would exploit the strong field enhancement of the pair production cross section, reducing the photon detection inefficiency without degrading the response to neutral hadrons.

The enhancement in the electromagnetic shower development, and thus the increase in the scintillation light yield during the early stages of the shower, can affect both the interpretation of data from homogeneous crystal calorimeters and their design, especially when the particles are accidentally aligned with the crystallographic axes. This is relevant to existing detectors, because commonly used scintillating crystals are often grown at a small angle with respect to a principal axis.

This study on the feasibility and the R&D of a homogeneous electromagnetic calorimeter based on oriented crystals represents a first quantitative understanding of the orientation effects in crystal calorimetry and lays the groundwork for the design of future detectors.

ACRONYMS

$\overline{\text{P}}$ANDA antiProton ANnihilation at DArmstadt

ADC Analog to Digital Converter

ALICE A Large Ion Collider Experiment

AMBER Apparatus for Meson and Baryon Experimental Research

ATLAS A Toroidal LHC Apparatus

AXIAL Axial and quasi-axial coherent interaction between charged particle beams and crystals

BGA Ball Grid Array

CHARM CERN High-energy AcceleRator Mixed-field

CLOUD Cosmic Leaving Outdoor Droplets

CMS Compact Muon Solenoid

COMPASS Common Muon and Proton Apparatus for Structure and Spectroscopy

DAQ Data AcQuisition

GUI Graphical User Interface

HIKE High-Intensity Kaon Experiment

HRXRD High-Resolution X-Ray Diffractometer

INFN Istituto Nazionale di Fisica Nucleare - National Institute for Nuclear Physics

KM3NeT Cubic Kilometre Neutrino Telescope

LEP Large Electron–Positron Collider

LHC Large Hadron Collider

LINAC4 LINear ACcelerator

MIP Minimum Ionizing Particle

MPPC Multi-Pixel Photon Counters

NEMO NEutrino Mediterranean Observatory

NESTOR Neutrino Extended Submarine Telescope with Oceanographic Research Project

NIM Nuclear Instrumentation Module

OPAL Omni-Purpose Apparatus for LEP

OREO ORiEnted calOrimeter

PH Pulse Height

PI Physik Instrumente

PMT PhotoMultipliers Tube

PS Proton Synchrotron

PSB Proton Synchrotron Booster

QED Quantum ElectroDynamics

SHINE SPS Heavy Ion and Neutrino Experiment

SiPM Silicon PhotoMultipliers

SLAC Stanford Linear Accelerator Center

SPEAR Stanford Positron Electron Accelerating Ring

SPS Super Proton Synchrotron

STORM STrOng cRystalline electroMagnetic field

Tcl Tool Command Language

TPC Time Projection Chamber

UF Ultra-Fast

VME Versa Module Eurocard

VRB VME Readout Board

WLS Wavelength shifters

A

CHARACTERIZATION OF THE BEAM AND SETUP

This appendix is dedicated to the description of the beam characterization, as well as the characterization of the lead glass calorimeter and the threshold Cherenkov detectors installed on the T9 beamline. In particular, for each beamtest, the following analysis has been performed:

- The alignment of the tracking silicon detectors: a small offset may still be present between the detectors after the manual alignment procedure on the beamline. This step is fundamental to determine the particles impact position and angle on the crystal.
- The study of the beam size and angular divergence as a function of the incident beam energy; this analysis is essential for investigating coherent effects in crystals, which strongly depend on the particles incidence angle.
- The calibration of the lead glass calorimeter.
- The characterization of the performance of the two threshold Cherenkov detectors installed on the T9 beamline.

A.1 THE 2022 BEAMTEST

During the 2022 beamtest, a single PWO crystal (Section 3.1.1) was tested at the H2 beamline of the CERN SPS. Since the crystal had a thickness of only 5 radiation lengths, the lead glass calorimeter played a crucial role in the measurement of the energy deposit. This section describes the characterization of the electron beam used during the beamtest along with the characterization of the seven lead glasses (Section 3.2.5).

A.1.1 BEAM CHARACTERIZATION

The two silicon detectors used during the beamtest are manually aligned in the plane perpendicular to the beam axis; nevertheless, a small offset may still remain between them. In

order to correct this offset, an offline alignment procedure is needed. The particle incidence angle θ_i, sketched in figure A.1, is computed event by event as:

$$\theta_i = \arctan\left(\frac{\Delta_i}{\mathrm{D_{Tele}}}\right) \tag{A.1}$$

where $i = x, y$ are the directions orthogonal to the beam, Δ_i is the difference between the hit positions measured by the second telescope and the first one, and $\mathrm{D_{Tele}}$ is the distance between the modules.

The distributions of the incidence angles have been fitted with a Gaussian function and

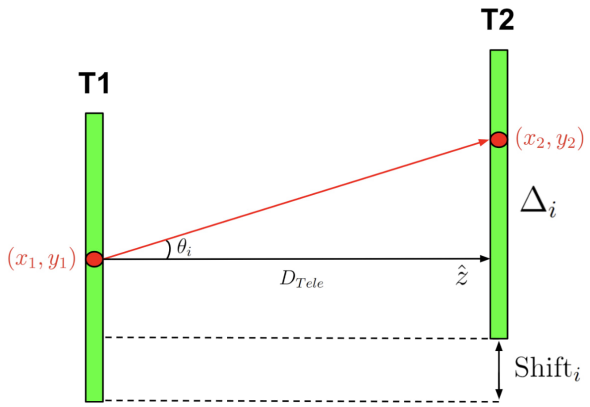

Figure A.1: Schematic representation of the particle incidence angle θ_i ($i = x, y$): the red arrow shows the particle trajectory while the red circles indicate the impact points on the two telescopes (T1 and T2). D_{Tele} is the distance between the two detectors along the z-axis, and (x, y) are the positions measured by the telescopes. A relative spatial shift between T1 and T2 along the i direction is also shown, due to a non perfect alignment in the x-y plane.

the shift parameters for the x and y coordinates have been evaluated as follows:

$$shift_i = \tan(\mu_i)(D_{Tele}) \tag{A.2}$$

where μ_i is the mean value extracted from the Gaussian fit. The measured hit positions have been corrected by subtracting the shifts. This procedure was adopted for all the beamtests. Figure A.2 shows the beam profile of the two telescopes with a 120 GeV electron beam after the alignment procedure; the shape of the beam, evident in the T1 beam profile, is due to the hole in the S1 trigger detector (described in 3.2.2). Figure A.3 presents the θ_x and θ_y distributions before and after the alignment procedure. The divergence, i.e. the standard deviation of the Gaussian fit of the T1-T2 angular distributions, as a function of the energy is presented in Figure A.4: as the energy increases, the beam divergence becomes smaller. The smallest divergences are obtained for the 120 GeV electron beam: $\sigma_x = 98.92 \pm 0.51$ μrad, $\sigma_y = 73.83 \pm 0.32$ μrad. These values are small enough to measure coherent effects in crystals, given their angular acceptance of the order of ~ 1 mrad.

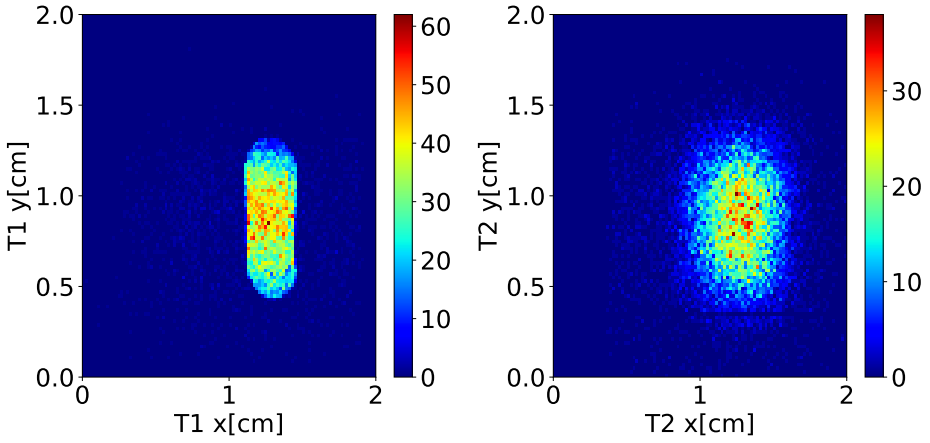

Figure A.2: 2D distributions of the x-y coordinates of the T1 and T2 silicon detectors after the offline alignment. The shape of the beam, evident in the T1 beam profile, is due to the hole in the S1 trigger detector.

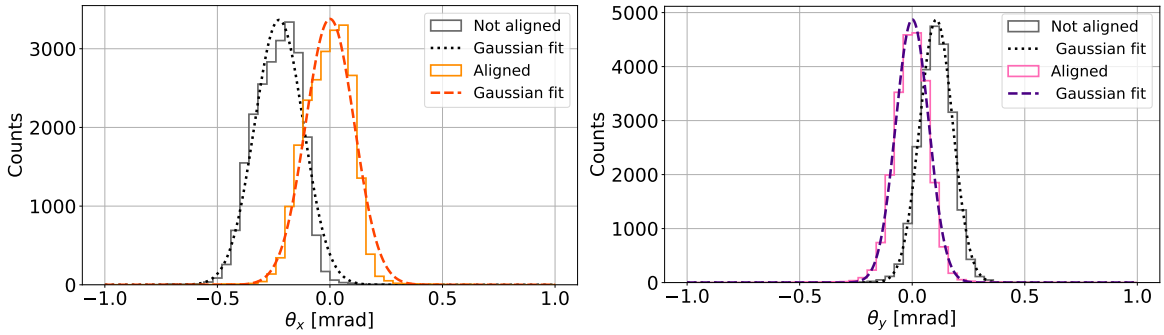

Figure A.3: Angular distributions with a 120 GeV electron beam before and after the alignment procedure.

A.1.2 LEAD GLASS CALORIMETER CALIBRATION

Each of the seven lead glass calorimeters, described in 3.2.5, must be calibrated to determine the relationship between the Pulse Height (measured in arbitrary units) and the energy (in GeV) deposited by the incoming particles. At first, the calibration was performed calibrating separately each individual lead glass, however, a non-negligible lateral spread in the shower development has been noted. Figure A.5 shows the correlation between the PH and the signal peak time for the 120 GeV electron beam aligned with the center of the central lead glass (CC). The particles detected by the trigger scintillators and by the calorimeter have the same arrival time, while the other ones are due to the noise or particles that have not crossed the calorimeter: it can be seen that a signal is also present in the lateral calorimeters suggesting that the electromagnetic shower is not completely contained in the single central block. For a standard lead glass with known properties [8] ($X_0 = 1.26$ cm, $\rho = 6.22$ g/cm^3, and $R_M = 2.576$ cm), and a transverse area of 10 cm $\times$ 10 cm (approximately $2R_M$), the expected lateral leakage is around 5%. In order to estimate the mean energy lateral spread, the following analysis has been performed:

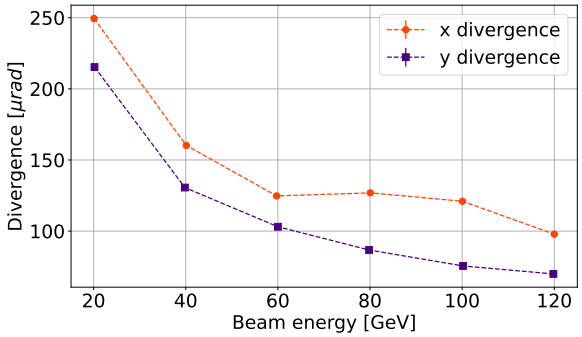

Figure A.4: Angular divergence along the x and y directions as a function of the beam energy; as the energy increases, the beam divergence decreases.

- the data were acquired using electron beams impinging on the center of the central lead glass block, with energies ranging from 20 to 120 GeV;
- cuts on the beam divergence and on the fiducial area have been performed with a fiducial area of 0.2×0.2 cm^2, in order to select only particles crossing the center of the lead glass;
- each lead glass has been equalized using an electron beam of 60 GeV impinging on the center of each block. Electrons at 60 GeV are used instead of MIPs for the channel equalization, as they better represent the operational conditions in which the lead glass detectors will be used to measure high-energy electromagnetic showers. Furthermore, the CAEN V1724 digitizer [108] (used to digitize the lead glass signals) does not have enough resolution to resolve the MIP peak while maintaining a dynamic range wide enough to also detect the electrons peak. The equalization factor is given by:

$$eq_j = \frac{\mu_{CC}}{\mu_j} \tag{A.3}$$

  where μ_j is the mean value extracted from the Gaussian fit of the j-th lead glass spectrum and μ_{CC} is taken as a reference. The equalized energy deposits in each lead glass are shown in Figure A.6 while the computed equalization factors are listed in Table A.1. It can be noted that the lead glasses energy spectra have a broad distribution, indicating a contamination in the electron momentum. An analysis of the beam components is presented in Section A.1.3;
- the percentage of the lateral energy leakage (δE) is calculated event by event for each beam energy as follows:

$$\delta E = \frac{PH_{\text{lat}}}{PH_{\text{tot}}} \times 100 \tag{A.4}$$

  where PH_{lat} is the sum of the equalized Pulse Heights of the lateral lead glasses (those surrounding the central one), and PH_{tot} is the sum of all the seven lead glasses;
- the δE distribution is then fitted with a Gaussian function, as shown in Figure A.8.

The results are shown in Figure A.8: the mean energy loss due to the finite transverse size of the calorimeter is always larger than 6%. The higher mean energy loss observed

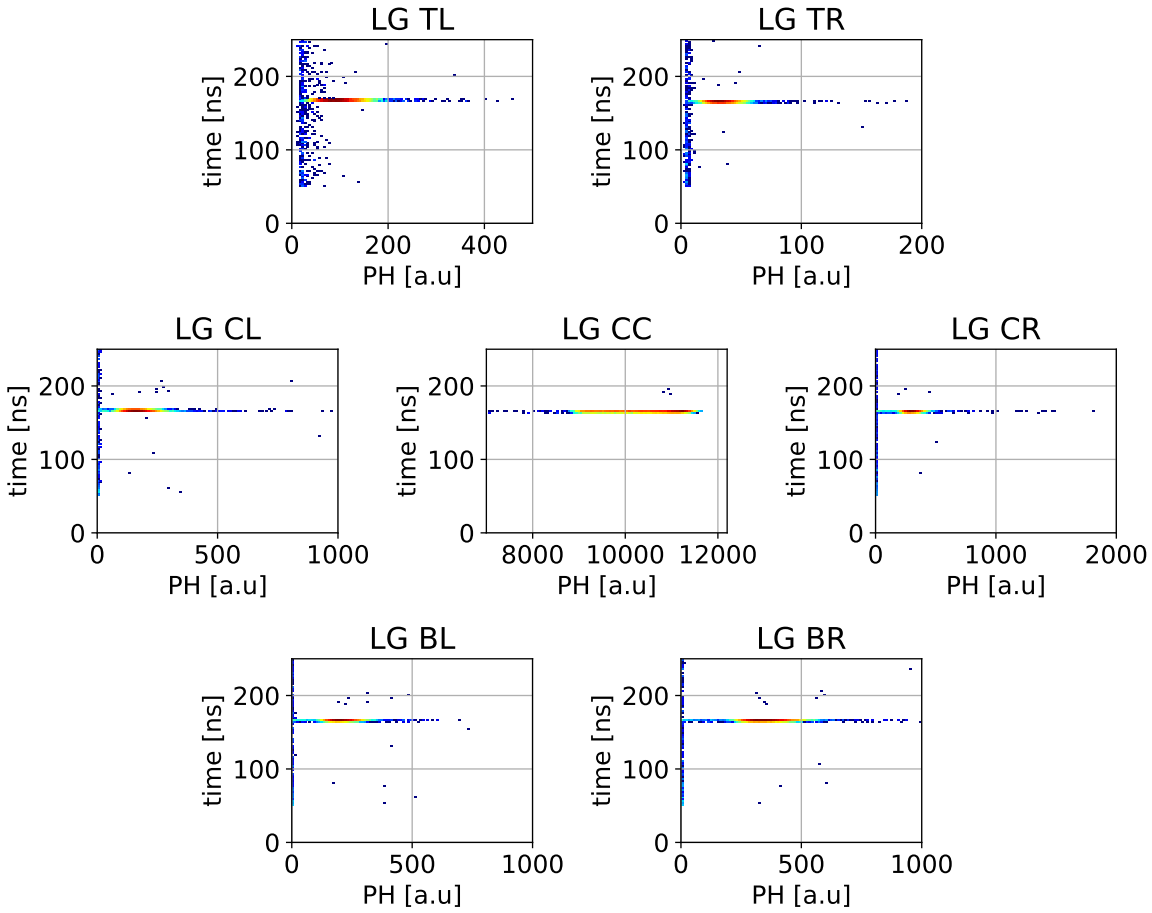

Figure A.5: Correlation between the PH and the signal peak time for the 120 GeV electron beam aligned with the center of the central lead glass (CC). The physical events, i.e. the particles detected by the trigger scintillators and by the calorimeter, have the same arrival time. It can be seen that a signal is also present in the lateral calorimeters (note that the x-scale is different for each lead glass).

Lead glass	**Equalization factor**
TL	0.743 ± 0.001
TR	0.942 ± 0.000
CL	0.610 ± 0.001
CC	1.000 ± 0.000
CR	0.965 ± 0.000
BL	1.634 ± 0.000
BR	0.854 ± 0.000

Table A.1: Equalization factors computed for each lead glass block.

at 60 GeV and 120 GeV could be attributed to a misalignment between the beam and the center of the central lead glass. This hypothesis is supported by the fact that the 60 GeV and 120 GeV runs were performed consecutively in time, suggesting that a possible misalignment might have affected both data sets. Due to the not negligible lateral energy loss, it has been decided to calibrate the whole calorimeter composed by the seven lead glasses rather than the individual detectors. The calibration line was determined using electron

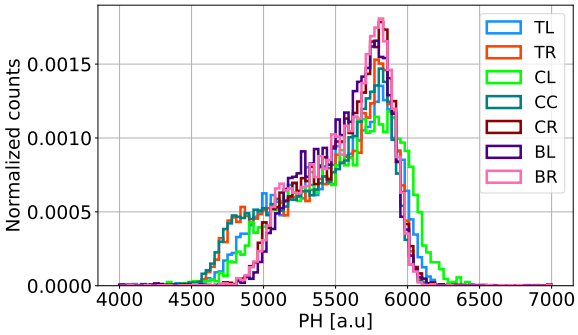

Figure A.6: Equalized energy deposit in each lead glass for the 60 GeV equalization runs.

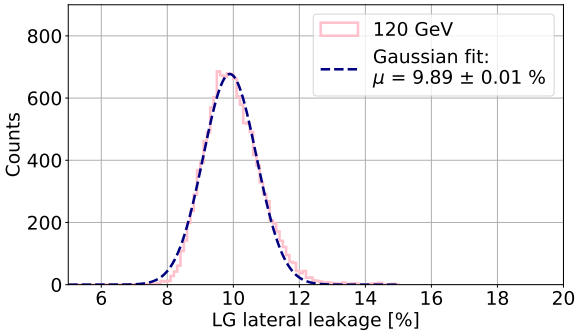

Figure A.7: Lateral energy leakage distribution with the Gaussian fit for a 120 GeV electron beam.

beams on the center of the central lead glass front face. Measurements were performed in the 40-120 GeV range, in steps of 20 GeV. For each run, the total spectrum, obtained summing the equalized PHs of each individual lead glass, is fitted with a Gaussian curve. The calibration lines and the residuals (computed as res[%] = $100 \cdot (y_{exp} - y_{fit})/y_{exp}$) are shown in Figure A.9.

A.1.3 BEAM PURITY

As mentioned in Appendix C.2, the tertiary electron beams have a variable purity (ranging from 10% to 99.5%), energies between 20 and 120 GeV, and a momentum acceptance of $\Delta p/p = 2\%$ [116]. The lead glasses energy deposit distribution, presented in Figure A.6, feature a broad distribution, highlighting a limited accuracy in the particle momentum selection. To investigate the type of particles which composed the beam, the information from both the PWO crystal and the lead glass have been taken into account. Figure A.10 presents the total energy measured by the lead glass calorimeter when the PWO crystal is on the beamline for a 120 GeV electron beam. The electron peak has been fitted with a Gaussian function. Two regions can be identified: 1) a continuous component (highlighted in red) with a PH below $\mu - 3\sigma$ where μ and σ are the mean and standard deviation of the fit of the electron peak; 2) a broad component with energies above $\mu - 3\sigma$ (highlighted in green). In order to better understand the nature of the contamination, the SiPMs spectra have been analyzed selecting events in which the calorimeter energy was either below or above the threshold. As shown in figure A.11, only the low energy continuous component

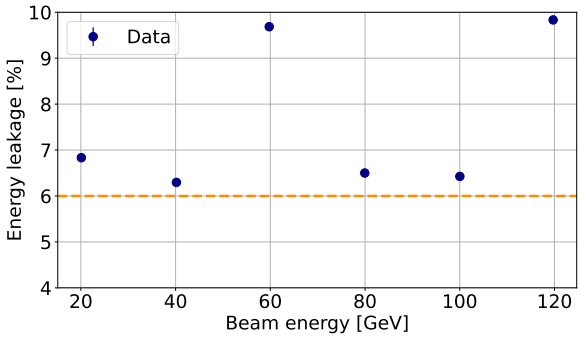

Figure A.8: Mean lateral energy leakage of the central lead glass as a function of the beam energy.

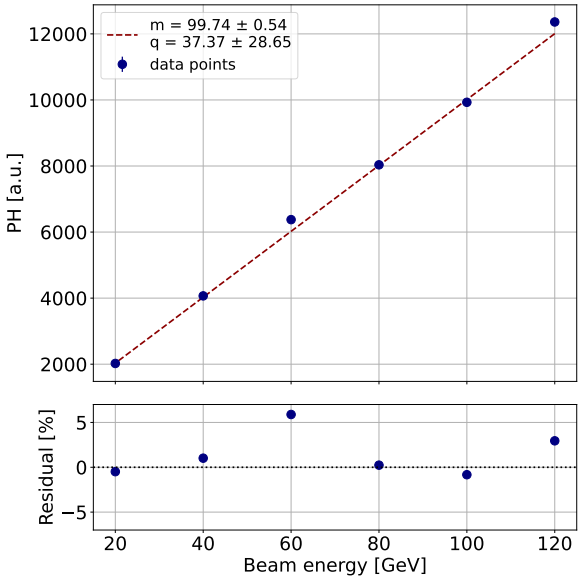

Figure A.9: Calibration line for the lead glass calorimeter with the corresponding residuals.

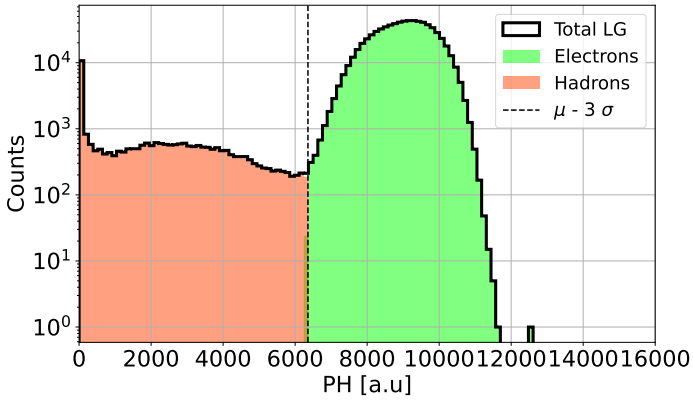

Figure A.10: Energy spectra measured by the lead glass calorimeter when the PWO crystal is on the beamline. One region of contamination with PH $< \mu - 3\sigma$ (red) can be identified under the main peak (green).

in the calorimeter does not produce a shower in the PWO crystal and thus a significant signal in the SiPMs. This can be identified as a hadronic component, likely negative pions. In fact, the pion interaction length (L_{int}) in PWO is approximately 24 cm, which corresponds to about 27 X_0 [8]. This means that the interaction scale length for pions is 27 times larger

than that for electrons. Given that the PWO crystal thickness is roughly 0.17 L_{int}, pions crossing it deposit a negligible amount of energy. On the other hand, the leas glass, with a thickness of $24.7X_0$, or approximately 0.91 L_{int}, is thick enough for hadronic particles to start a shower, resulting in a significant energy deposit. On the other hand, the spectrum above the $\mu - 3\sigma$ threshold presents a contamination in electrons momentum, since these events produce a shower in the PWO crystal.

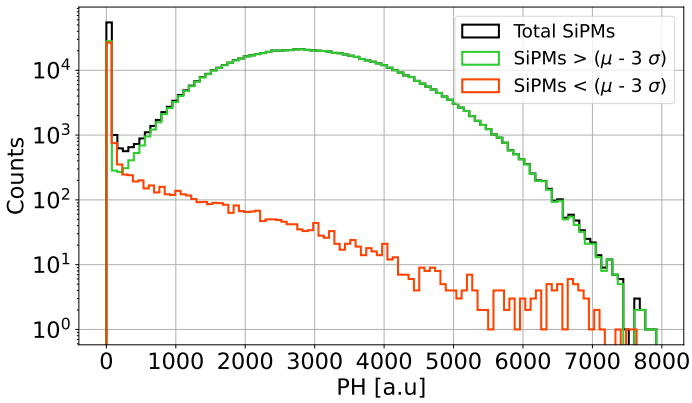

Figure A.11: SiPMs PH (a.u.) measured selecting different energy regions in the calorimeters. Energies below the $\mu - 3\sigma$ threshold do not produce a significant signal in the SiPMs, suggesting a hadronic contamination of the primary beam.

A.2 THE 2023 BEAMTESTS

During the August beamtest, the 3×1 row of PWO crystals (Section 3.1.2) was tested on both the T9 beamline at the CERN PS and the H2 beamline at the CERN SPS. During the October beamtest, the 2×2 matrix of PWO crystals (Section 3.1.2) was tested on the T9 beamline. As for the 2022 beamtest, the characterization of both the particle beams and the lead glass detectors used during the 2023 beamtests at the T9 and H2 lines was required.
A characterization of the threshold Cherenkov detectors installed on the T9 beamline is also presented.

A.2.1 BEAM CHARACTERIZATION

The silicon detectors alignment followed the same offline procedure adopted during the 2022 beamtest.
Differently from 2022, during the 2023 beamtests on the T9 and H2 beamline, the beam shape was not determined by the S1 trigger, as the trigger was provided by a plastic scintillator with a 10×10 cm^2 area (Section 3.1.2). As a result, the beam profile was characterized by measuring the Full Width at Half Maximum (FWHM) of the distributions of the impact coordinates of the particles on the silicon detectors, as a function of the incident beam energy. Figure A.12 shows the beam profile for the 120 GeV electron beam on the H2 beamline; the FWHM and the divergence are presented in Figure A.13. The beam size

decreases increasing the energy; given the fact the beam size is smaller than the crystal dimensions (2.5×2.5 cm^2) at all energies, an optimal positioning of the crystals during the beamtest was necessary. The divergence decreases increasing the energy, and it is small enough (up to 230 μrad) to ensure accurate measurements and the possibility of analyzing the strong field effects, which are highly sensitive to the incidence angle (the angular range is ~ 1 mrad).

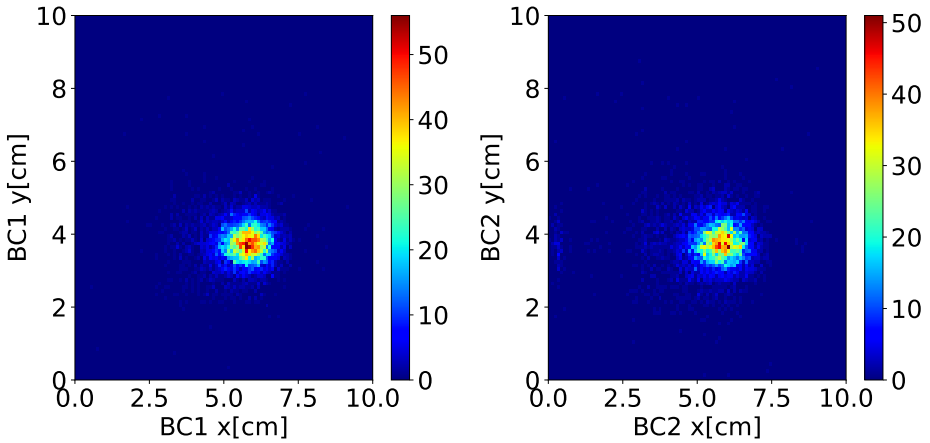

Figure A.12: 2D distributions of the x-y coordinates of the BC1 and BC2 silicon detectors for the 120 GeV electron beam of the H2 beamline.

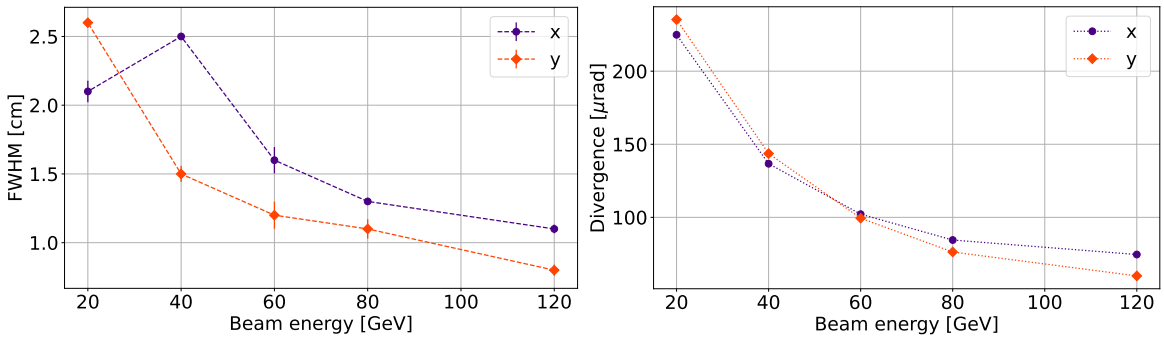

Figure A.13: (left) FWHM and (right) divergence for the H2 beamline as a function of the beam energy.

The T9 beamline allows the selection between two main beam configurations: parallel optics and focusing optics. The parallel optics configuration is designed to minimize the beam divergence by making the particles traveling along parallel trajectories. In contrast, the focusing optics configuration reduces the beam spot size by focusing the particles at a specific point, with a possible increase in divergence.
Figure A.14 shows the beam profile of the first silicon chamber for the 6 GeV electron beam in the focusing optics and in the parallel optics configuration used during the August beamtest, while Figure A.15 shows the FWHM for both configurations along with the beam divergence.

During both the August and October beamtests on the T9 beamline, the parallel optics configuration was used to minimize the divergence, at the cost of a broader beam profile.

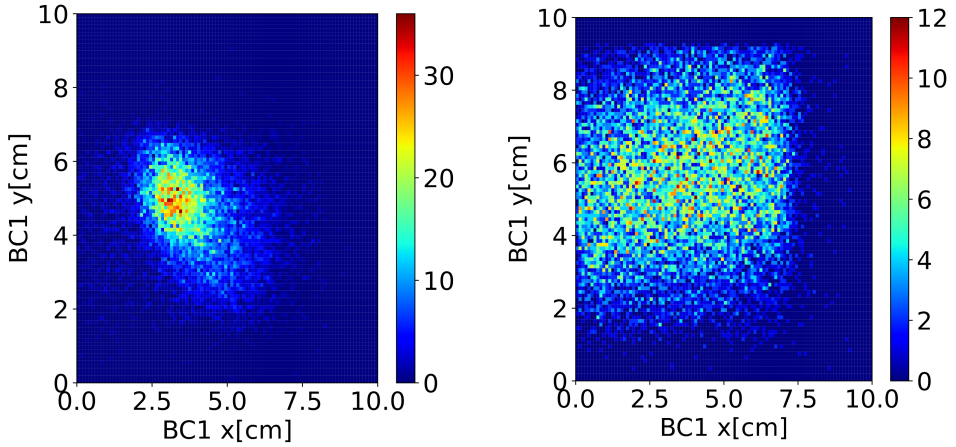

Figure A.14: 2D distributions of the x-y coordinates of the BC1 silicon detector for the 6 GeV focusing optics (left) and parallel optics (right) on the T9 beamline during the August beamtest.

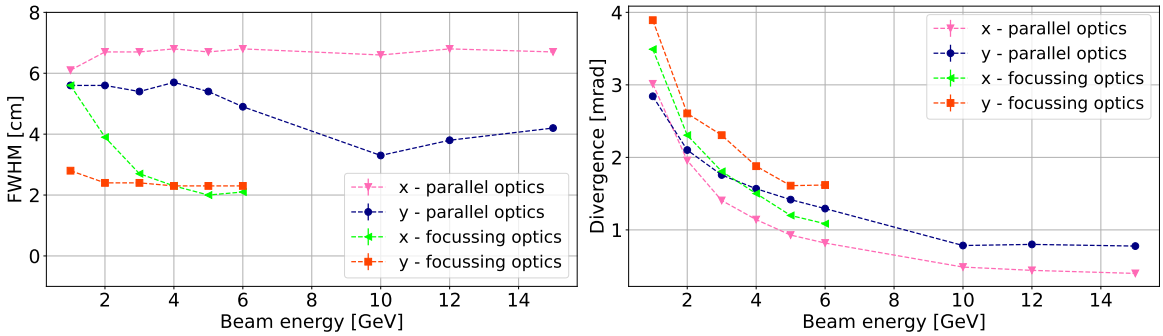

Figure A.15: (left) FWHM and (right) divergence for the focusing and parallel optics on the T9 beamline during the August beamtest as a function of the beam energy.

Figure A.16 shows the FWHM and the divergence for the parallel optics beam used during the October beamtest (2×2 matrix under test) on the T9 beamline.

A.2.2 LEAD GLASS CALORIMETER CHARACTERIZATION

Unlike the 2022 beamtest, where seven lead glass blocks were used as a single calorimeter, only one lead glass block was used during the 2023 beamtest, both on the T9 and H2 beamlines. The calibration has been performed using different electron beams aligned with the center of the lead glass:

- on the T9 line the signal has been digitized by a CAEN V1730 digitizer [109]; during the August beamtest the calibration has been performed using electron beams with energies in the 1-6 GeV range and a digitizer dynamic range of 0.5 V, and electron beams with energies of 10, 12 and 15 GeV with the digitizer dynamic range of 2 V, while during the October beamtest energies in the 1-6 GeV range and a digitizer dynamic range of 0.5 V have been used.

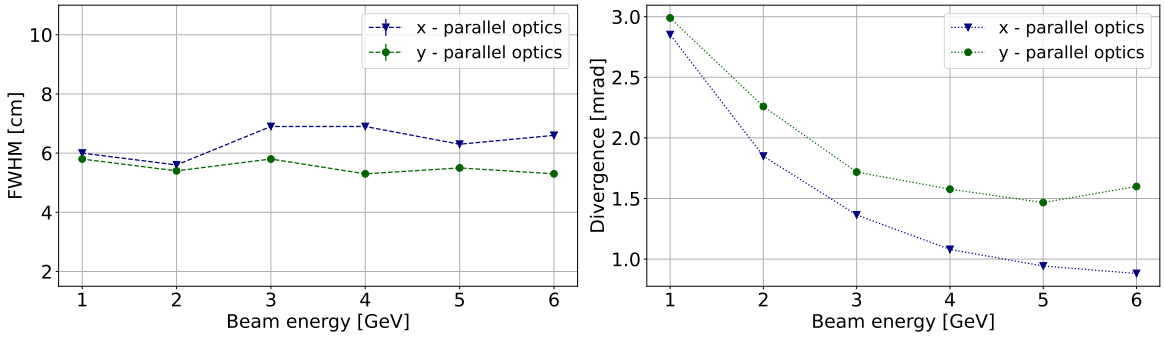

Figure A.16: (left) FWHM and (right) divergence for the focusing and parallel optics on the T9 beamline during the October beamtest as a function of the beam energy.

- on the H2 line the calibration has been performed using electron beams with energies of 20, 40, 60, 80, 120 GeV and a digitizer dynamic range of 2 V.

A set of cuts has been applied to select the good events:

- cuts on the signal peak time, in order to exclude the baseline fluctuation events;
- cuts on the beam divergence, in order to select the particles that impinge almost perpendicularly on the lead glass;
- cuts on the PH of the threshold threshold Cherenkov detectors positioned on the T9 beamline for the electron selection.

The electron peak at the different energies has been fitted with a Gaussian function. The calibration lines obtained for all the 2023 beamtests and the percentage residuals are shown in Figure A.17, A.18, A.19.

The energy resolution $R = \frac{\sigma_E}{E}$, where σ_E and E are the standard deviation and the mean energy extracted from the Gaussian fit of the energy deposited in the lead glass for each beam energy, can be modelled as:

$$\frac{\sigma}{E} = \frac{a}{\sqrt{E}} \oplus c \tag{A.5}$$

where a is the stochastic term and c is the constant term. The results are presented in Figure A.20 and summarized in Table A.2.

	a [$\% \cdot \sqrt{\text{GeV}}$]	**c** [%]
T9 08/23	8.89 ± 0.69	3.57 ± 0.25
H2 08/23	10.39 ± 0.88	1.22 ± 0.10
T9 10/23	10.53 ± 2.55	1.51 ± 0.10

Table A.2: Lead Glass energy resolution terms.

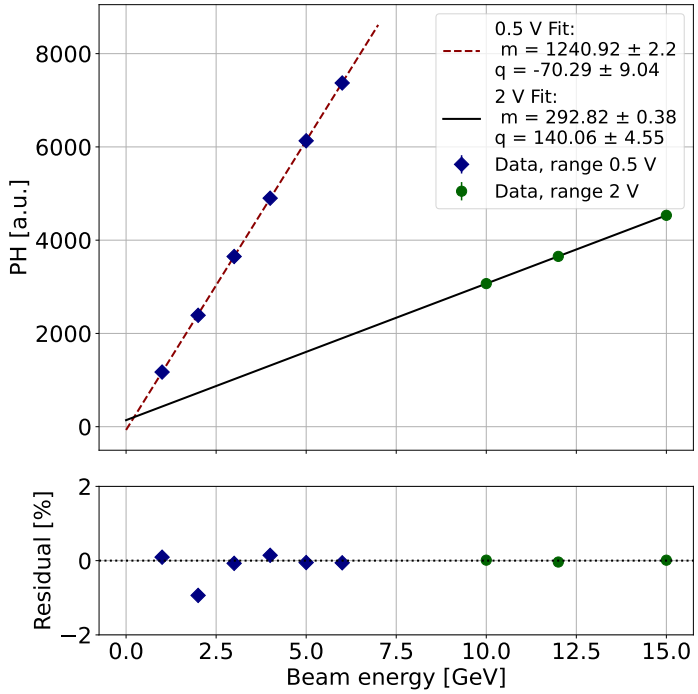

Figure A.17: Lead glass calibration line and residuals measured on the T9 beamline during the August beamtest.

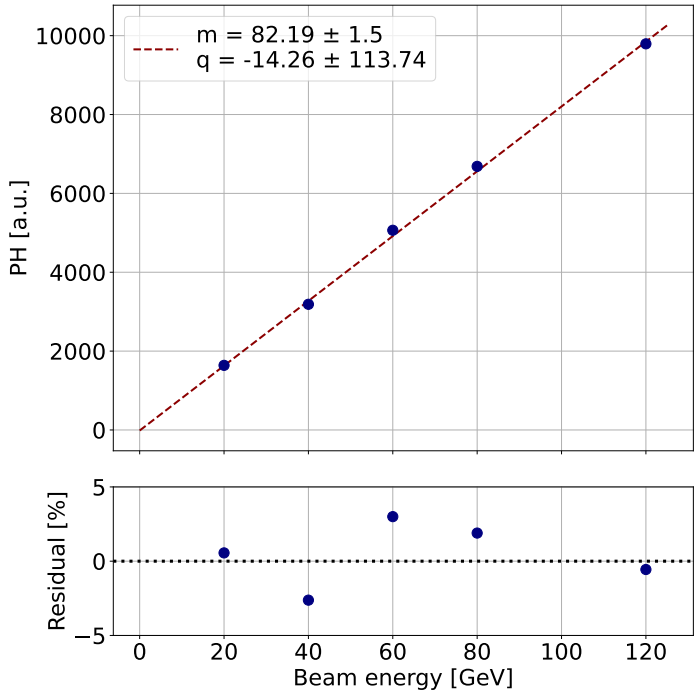

Figure A.18: Lead glass calibration line and residuals measured on the H2 beamline during the August beamtest.

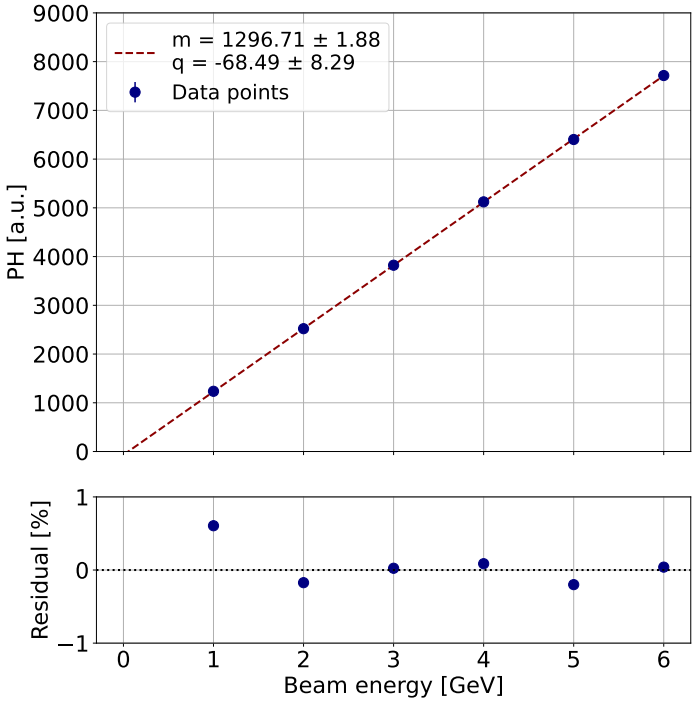

Figure A.19: Lead glass calibration line and residuals measured on the T9 beamline during the October beamtest.

A.2.3 T9 THRESHOLD CHERENKOV DETECTORS CHARACTERIZATION

The T9 beamline is equipped with two threshold Cherenkov detectors for the particle identification. Both the detectors were used to select the electrons during the beamtests. In particular, during the October beamtest, when the 2×2 matrix was under test, the threshold Cherenkov detectors have been used to compute the true positive labels corresponding to electrons in the study of the electron/hadron discrimination capability of the OREO prototype. For these reasons, the characterization of the two detectors is fundamental.
Figure A.21 presents the PH distributions of the threshold Cherenkov detector for the 6 GeV electron (October beamtest). A threshold value (indicated by the dotted line) has been chosen to distinguish between events that generated a signal in the detector and those that did not. Events with a Pulse Height exceeding the threshold are classified as electrons (shown in solid color in the plot). To evaluate the detectors performance, two key quantities have been computed:

- **purity**: refers to the fraction of particles identified as electrons by the threshold Cherenkov detector that are actually electrons.
- **efficiency**: refers to the fraction of true electrons that are correctly identified as electrons by the threshold Cherenkov detector.

The true electrons were identified using the lead glass detector. To ensure that the electromagnetic shower is fully contained, a cut in position at the center of the lead glass and a

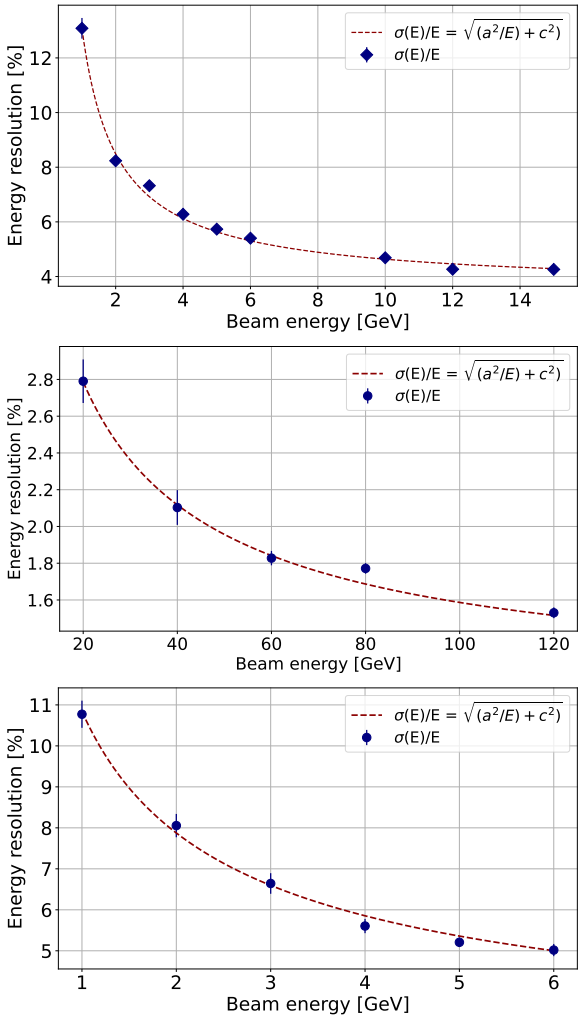

Figure A.20: Lead glass energy resolution: (top) on the T9 beamline during the August beamtest, (central) on the H2 beamline during the August beamtest and (bottom) on the T9 beamline during the October beamtest.

cut in time have been applied. The resulting Pulse Height spectrum after applying both cuts for the 2 GeV and the 6 GeV electron beam is presented in figure A.22. The electron peak was fitted with a Gaussian distribution, and events were classified as electrons if $PH_{LG} > \mu - 3\sigma$, where μ and σ are the mean and standard deviation of the fit.

Purity was calculated as the ratio of events identified as electrons by both the threshold Cherenkov detector and the lead glass, and the total number of events identified as electrons by the threshold Cherenkov detector. Efficiency was determined by the ratio of events identified as electrons by both the Cherenkov counter and the lead glass, and the events identified as electrons by the lead glass. Figure A.23 shows the purity and efficiency as a function of the beam energy.

Two additional configurations were considered in the analysis: the AND condition, where only events with both threshold Cherenkov detector above threshold are selected, and the OR condition, where events with at least one counter above threshold are included. Although the AND condition results in a lower efficiency, it ensures a higher purity and was therefore adopted for the beamtest data analysis presented in Chapter 5. During the

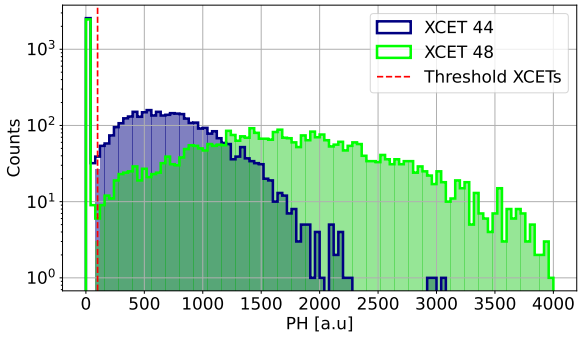

Figure A.21: PH distribution of the two threshold Cherenkov detectors (October beamtest). The dotted line represents the selection threshold: the events with a Pulse Height exceeding the threshold are classified as electrons (shown in solid color)

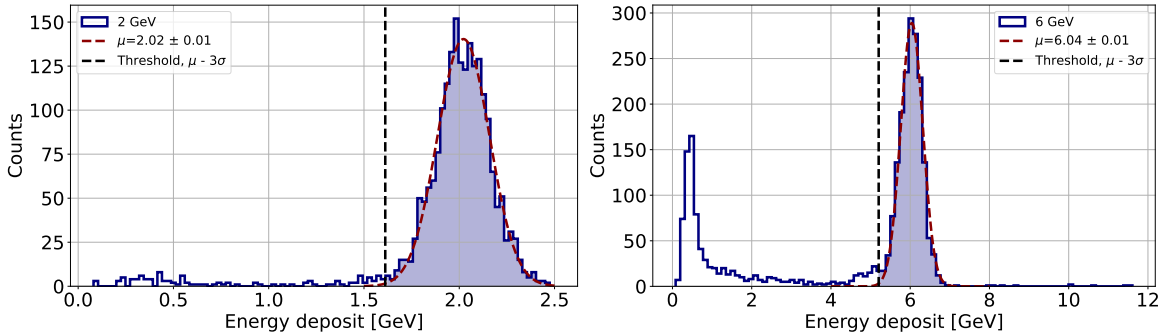

Figure A.22: Lead glass PH spectrum after applying a cut in position and in time for the (left) 2 GeV and (right) 6 GeV electron beam. The electron peak was fitted with a Gaussian function. The black dotted line represents the threshold used to identify electrons (shown in solid color).

August beamtest on the T9 beamline, the signal from the XCET 44 threshold Cherenkov detector was used as a trigger in coincidence with the APC plastic scintillator and was therefore not digitized. The efficiency and purity of the XCET 48 is presented in Figure A.24.

A.3 THE 2024 BEAMTESTS

During the 2024 beamtests the 3×3 OREO prototype (Section 3.1.3) has been tested on the T9 beamline on the CERN PS and on the H4 beamline at the CERN SPS. The characterization of the beam, the lead glass calorimeter and the characterization of the threshold Cherenkov detector installed on the T9 beamline are presented.

A.3.1 BEAM CHARACTERIZATION

As in the 2023 beamtest, the beam profile was characterized by measuring the FWHM of the distributions of the impact coordinates of the particles on the silicon detectors. During the June beamtest on the T9 beamline, the focusing optics configuration was chosen for the

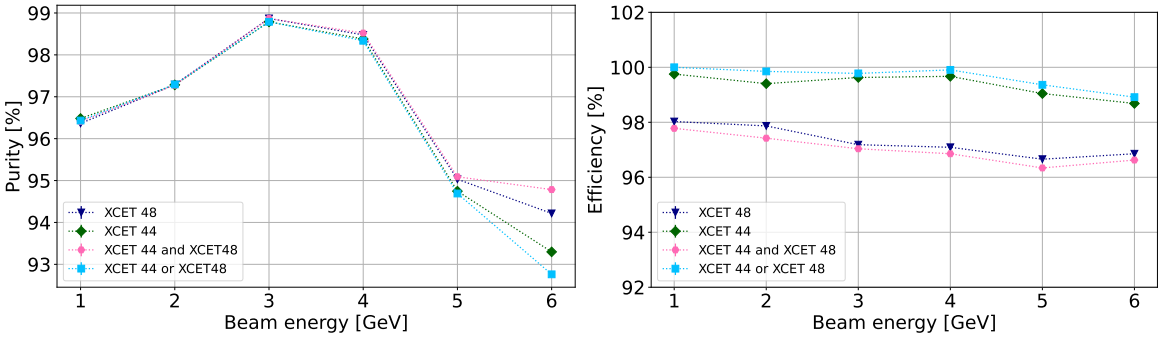

Figure A.23: (left) Purity and (right) efficiency of the threshold Cherenkov detectors.

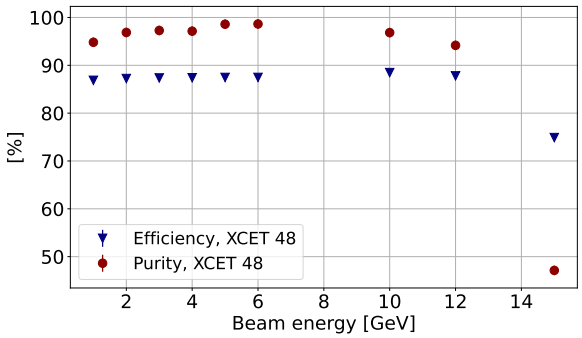

Figure A.24: Efficiency and purity of the XCET 48 during the August beamtest.

measurements. The parallel optics configuration was used only with the 6 GeV electrons to study the interalignment of the crystals (see Section 6.1.2). Figure A.25 shows the beam profile on the first beam chamber for the 180 GeV electron beam on the H4 beamline and the 6 GeV electron beam focusing optics and parallel optics on the T9 beamline.

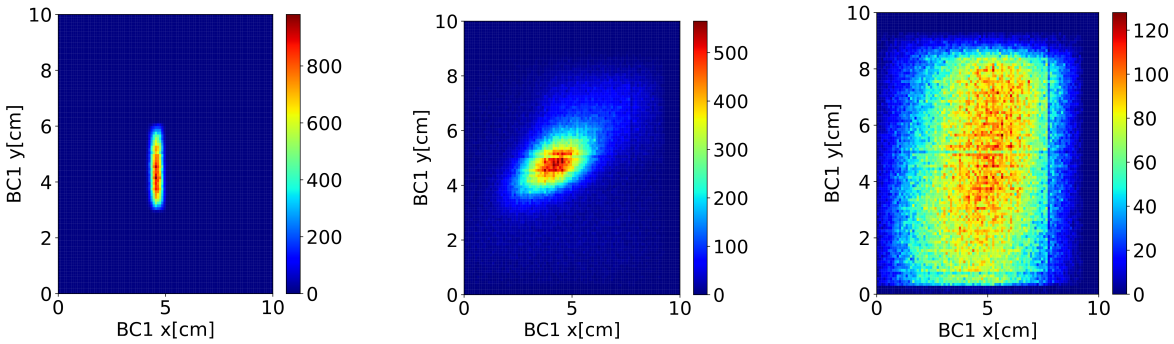

Figure A.25: 2D distributions of the x-y coordinates of the BC1 silicon detectors for the (left) 180 GeV electron beam on the H4 beamline and (center) the 6 GeV electron beam focusing optics and (right) parallel optics on the T9 beamline.

The FWHM and the divergence as a function of the beam energy are presented in Figure A.26. The 6 GeV electron beam parallel optics presents a FWHM of 5.80 $\pm$ 0.14 cm along the x direction with a divergence of 1.82 $\pm$ 0.01 mrad and a FWHM of 7.99 $\pm$ 0.14 cm along the y direction with a divergence of 1.11 $\pm$ 0.01 mrad.

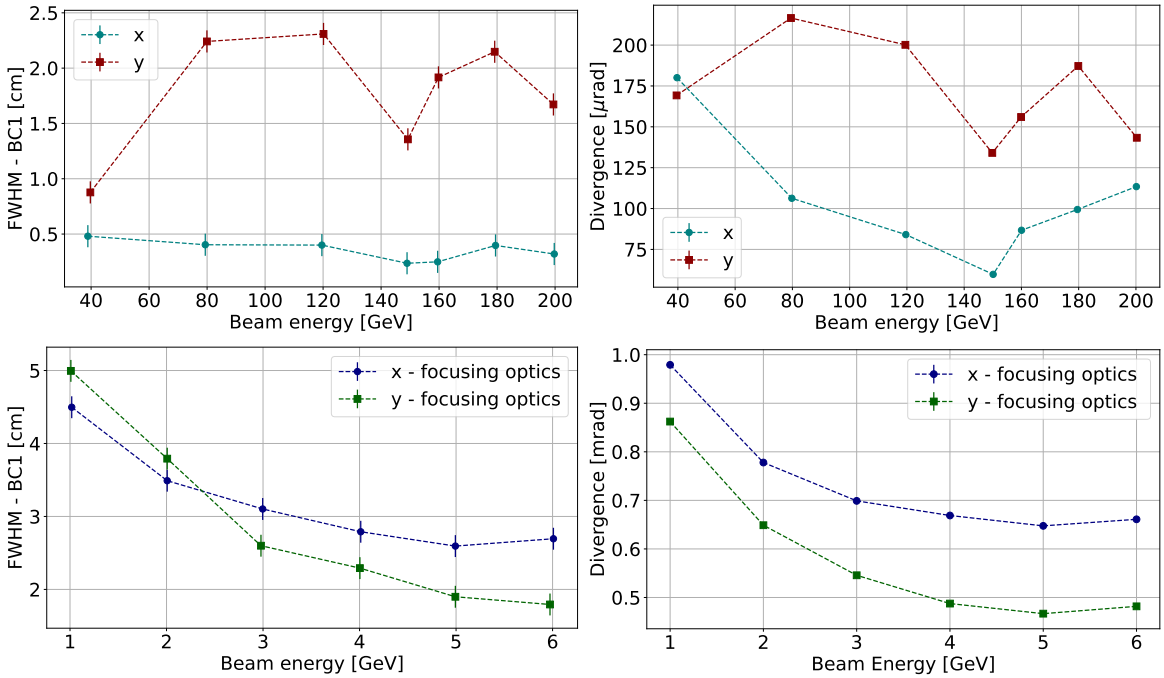

Figure A.26: FWHM and divergence of the (top) H4 and (bottom) T9 beams as a function of the incident beam energy

A.3.2 LEAD GLASS CALORIMETER CALIBRATION

During both the June and July beamtests, seven lead glasses were used as a single calorimeter during the whole data taking. As in the 2022 beamtest, due to the incomplete containment of the electromagnetic shower, it was not possible to directly calibrate each individual lead glass. Therefore, it was decided to calibrate the whole calorimeter rather than the individual detectors. To do this, an equalization procedure was first applied to the lead glass blocks, using a 1 GeV electron beam on the T9 beamline and a 40 GeV electron beam on the H4 beamline, impinging on the center of each block. The PH distribution for each lead glass has been fitted with a Gaussian function, after applying a cut in position and in signal peak time. The equalization factor is given by:

$$eq_j = \frac{\mu_{CC}}{\mu_j} \tag{A.6}$$

where μ_j is the mean value extracted from the Gaussian fit of the j-th lead glass spectrum and μ_{CC} is taken as a reference. The computed equalization factors are listed in Table A.3 Figure A.27 shows the lead glasses PH distribution after the equalization procedure.

The calibration line was determined using electron beams on the center of the lead glass block front face. The measurements were performed in the 1-6 GeV energy range, with a 1 GeV step, on the T9 beamline, and in the 40-120 GeV range, with a 20 GeV step, on the H4 beamline. For each run, the total spectrum, obtained summing the equalized PHs of each individual lead glass, was fitted with a Gaussian curve. The calibration lines and the residuals (computed as res[%] = $100 \cdot (y_{fit} - y_{exp})/y_{fit}$) are shown in Figure A.28.

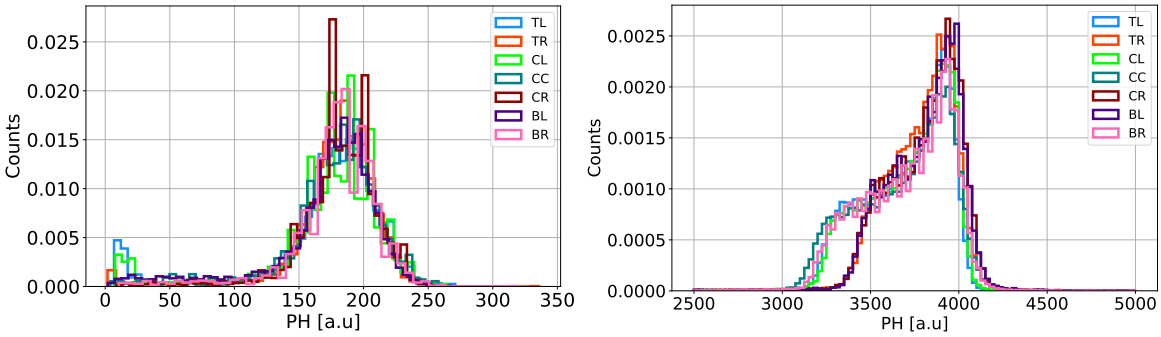

Figure A.27: Equalized energy deposit in each lead glass for the T9 (left) and H4 (right) equalization runs.

Lead glass	Equalization factor	
	T9	H4
TL	1.694 ± 0.011	0.728 ± 0.000
TR	0.587 ± 0.003	1.742 ± 0.000
CL	3.846 ± 0.056	0.513 ± 0.000
CC	1.000 ± 0.007	1.000 ± 0.000
CR	4.216 ± 0.052	3.911 ± 0.005
BL	0.671 ± 0.003	4.061 ± 0.006
BR	3.484 ± 0.027	4.473 ± 0.001

Table A.3: Equalization factors computed for each lead glass.

A.3.3 T9 THRESHOLD CHERENKOV DETECTORS CHARACTERIZATION

As in the 2023 beamtest, the T9 beamline was equipped with two gas threshold Cherenkov detectors for particle identification. Figure A.29 presents the PH distributions of the threshold Cherenkov detectors for the 6 GeV electron beam. Events with a Pulse Height exceeding the threshold (indicated by the dotted lines) are classified as electrons (shown in solid color in the plot). The purity and efficiency (defined in Section A.2.3) have been computed to evaluate the performance of the detectors. As for the 2023 beamtest true electrons were identified using the lead glass detector. Figure A.30 presents the PH spectrum of the lead glass detector, after applying cuts on the signal peak time and on the fiducial area, for the 2 GeV and the 6 GeV electron beam. The electron peak was fitted with a Gaussian distribution, and events were classified as electrons if $PH_{LG} > \mu - 3\sigma$, where μ and σ are the mean and standard deviation of the fit.
Figure A.31 shows the purity and efficiency as a function of the beam energy. Although the AND condition results in a lower efficiency, it ensures a higher purity and was therefore adopted for the beamtest data analysis presented in Chapter 6.

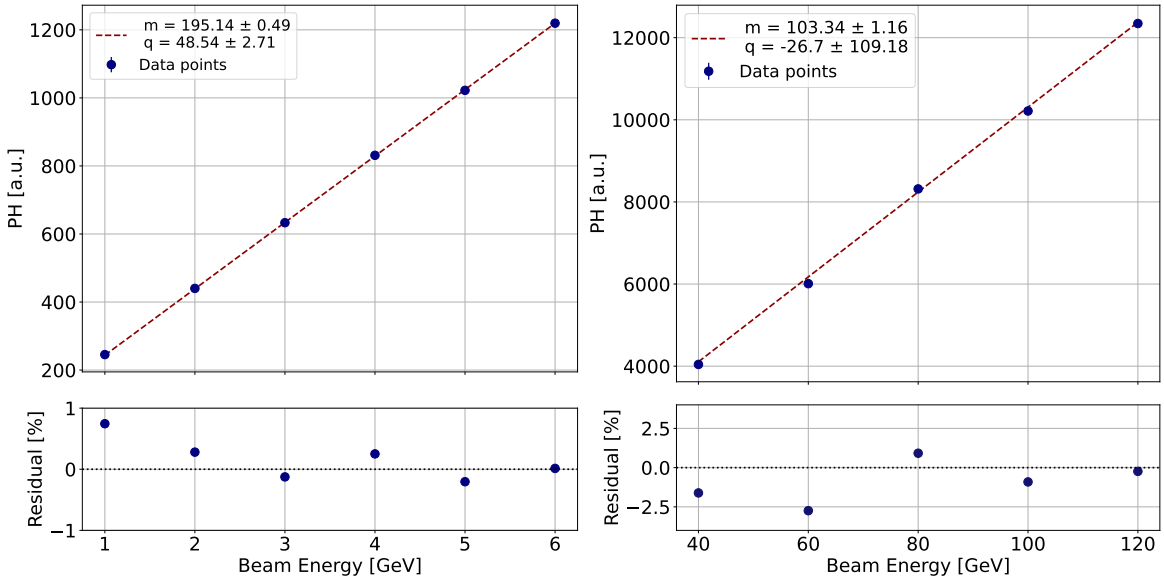

Figure A.28: Calibration line for the (left) T9 and (right) H4 lead glass calorimeter with the corresponding residuals.

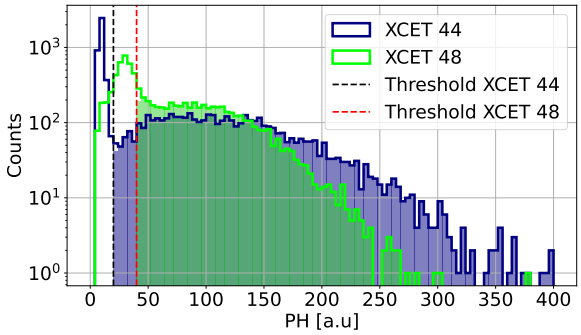

Figure A.29: PH distribution of the two threshold Cherenkov detectors. The dotted lines represent the selection threshold: the events with a Pulse Height exceeding the threshold are classified as electrons (shown in solid color).

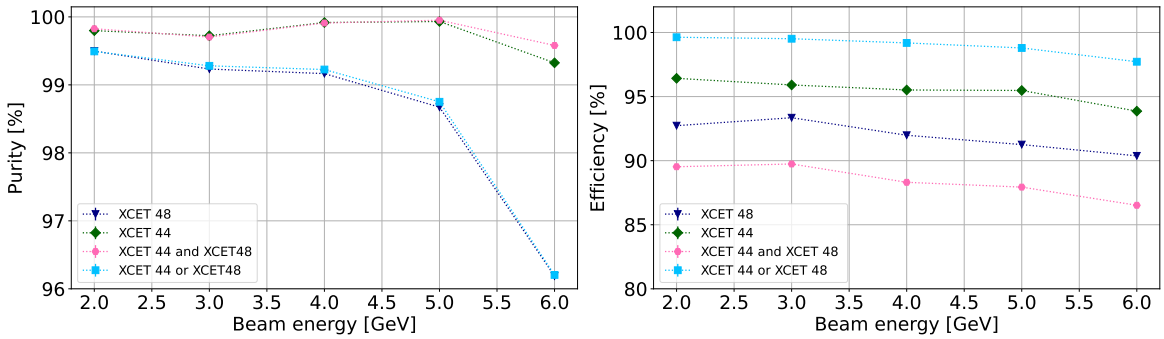

Figure A.31: (left) Purity and (right) efficiency of the threshold Cherenkov detectors.

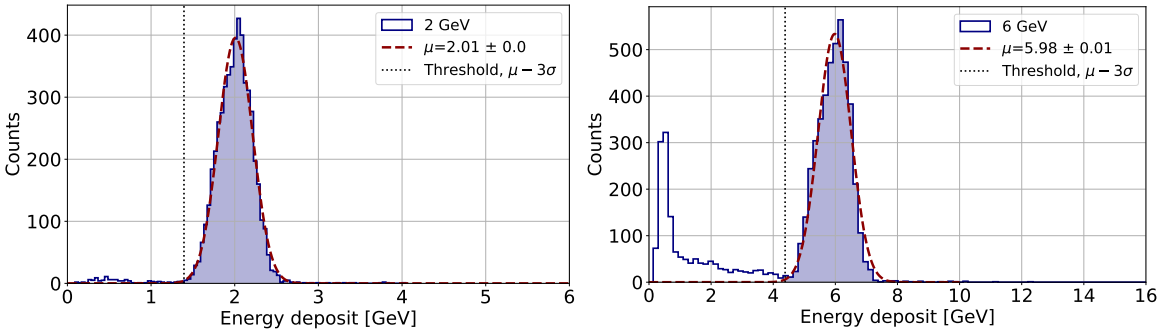

Figure A.30: Lead Glass PH spectrum after applying a cut in position and in time for the (left) 2 GeV and (right) 6 GeV electron beam. The electron peak was fitted with a Gaussian function. The black dotted line represents the threshold used to identify electrons (shown in solid color).

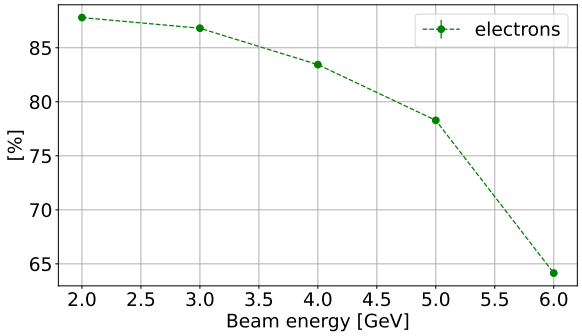

Figure A.32: Percentage of electrons as a function of the incident beam energy.

Figure A.32 shows the percentage of electrons identified by the AND condition of the threshold Cherenkov detectors as a function of the incident beam energy. As described in Appendix C, a small fraction of muons is present in the beam due to the production mechanism of the tertiary beam on the T9 beamline. Consequently, the percentage of electrons decreases increasing the beam energy.

B

GEANT4 SIMULATIONS

The simulation of the energy deposited in all the OREO calorimeter presented in this thesis work has been performed using the Geant4 toolkit [71]. The code for the simulations is available in the GitLab repositories [117] and [118][1]. The simulation code presented in this section refers exclusively to the simulation of non-oriented crystals. This is because the effects of strong crystalline fields are not yet included in any standard Geant4 physics list, although work in this direction has been performed by the OREO collaboration. Further details on simulations with axial orientation are provided in Section B.0.1.
The following points summarize the main features of the simulation code:

- The simulations were performed using the FTFP_BERT Physics List, which implements the standard high-energy electromagnetic and hadronic processes, including also photo-nuclear interactions; details can be found in [119].
- The experimental setup has been reproduced with a simplified geometry, reproducing only the active areas of the detectors without any additional materials. Figure B.1 presents the Geant4 experimental setup for the July 2024 beam test of the OREO calorimeter on the H4 beamline. The figure shows the event display of a 120 GeV electron incident on the OREO calorimeter; only particles with a momentum $p > 1$ GeV/c are drawn.
- It is important to highlight that the propagation of optical photons is not included in the simulation. The energy deposited in the crystal was simulated by modeling the physical processes responsible for the energy loss and by scoring the energy deposited in the active volumes. Neither the scintillation light production and propagation inside the PWO crystals, nor the detectors readout chain, have been implemented.
- The incident beam is modeled as monochromatic, with the spatial FWHM and the angular divergence taken from the experimental data. It is generated using the General Particle Source (GPS) [113] implemented in Geant4. In the case of an impure beam (as in the 2022 beamtest), the beam has been simulated reproducing the shape of the electron part of the energy distributions in the lead glasses, using the `hist/point` command of the Geant4 General Particle Source.

1 This work was performed collaboratively over the years within the INSULAB group at the Università degli Studi dell'Insubria. As a result, the two simulation codes differ only slightly in form, mainly in the way the output data are stored. The implementation of the physics of oriented crystals in the simulation code, as described in Section B.0.1, is available only in [117].

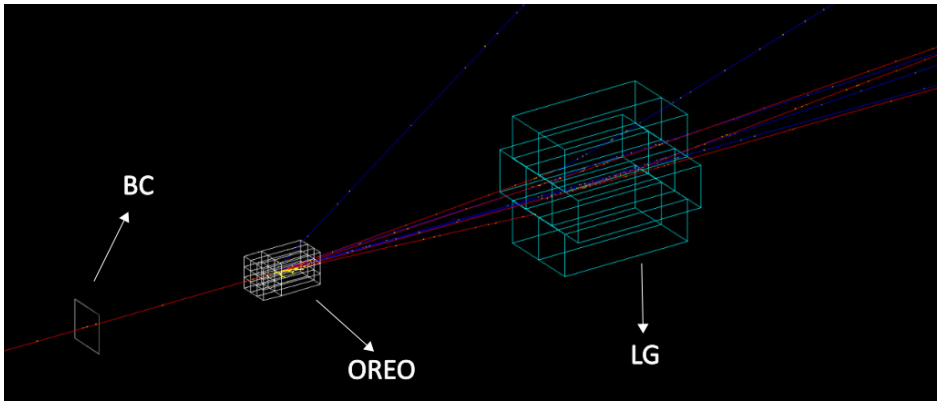

Figure B.1: Geant4 experimental setup for the July 2024 beam test of the OREO calorimeter on the H4 beamline. The figure shows the event display of a 120 GeV electron incident on the OREO calorimeter; electrons are depicted in red while photons in blue. Only particles with a momentum $p > 1$ GeV/c are drawn.

B.0.1 SIMULATION IN ORIENTED CRYSTALS

In this thesis work, the simulation of physics in oriented crystals has not been included; nevertheless, progress has been made in developing a code to incorporate crystalline lattice effects. The simulations of oriented crystals reported in the GitLab repository [117] were performed using a modified version of the FTFP_BERT Physics List, since currently Geant4 does not implement the physics of the strong field regime. In the modified version, the differential cross-sections for bremsstrahlung and pair production were scaled by a set of energy-dependent coefficients, increasing with particle energy. These coefficients were previously calculated using a full Monte Carlo simulation, in which the radiation emission and pair production probabilities in the axial field of a PWO lattice were obtained by directly integrating the quasiclassical Baier-Katkov formula on realistic particle trajectories. Additional information can be found in [56, 111, 120, 121]. The development of a full simulation based code, reproducing the crystal lattice and thus the interatomic potential wells, is performed by the `TRILLION` [122, 123] project. The project is dedicated to the implementation of the physics of electromagnetic processes in oriented crystals and nanostructures into Geant4 under a free license. Additional information on the project can be found in [124, 125].

C

THE CERN BEAMTEST FACILITIES

The CERN accelerator complex (Figure C.1) is composed by a series of machines that accelerate particles to increasingly higher energies. LINear ACcelerator (LINAC4) became

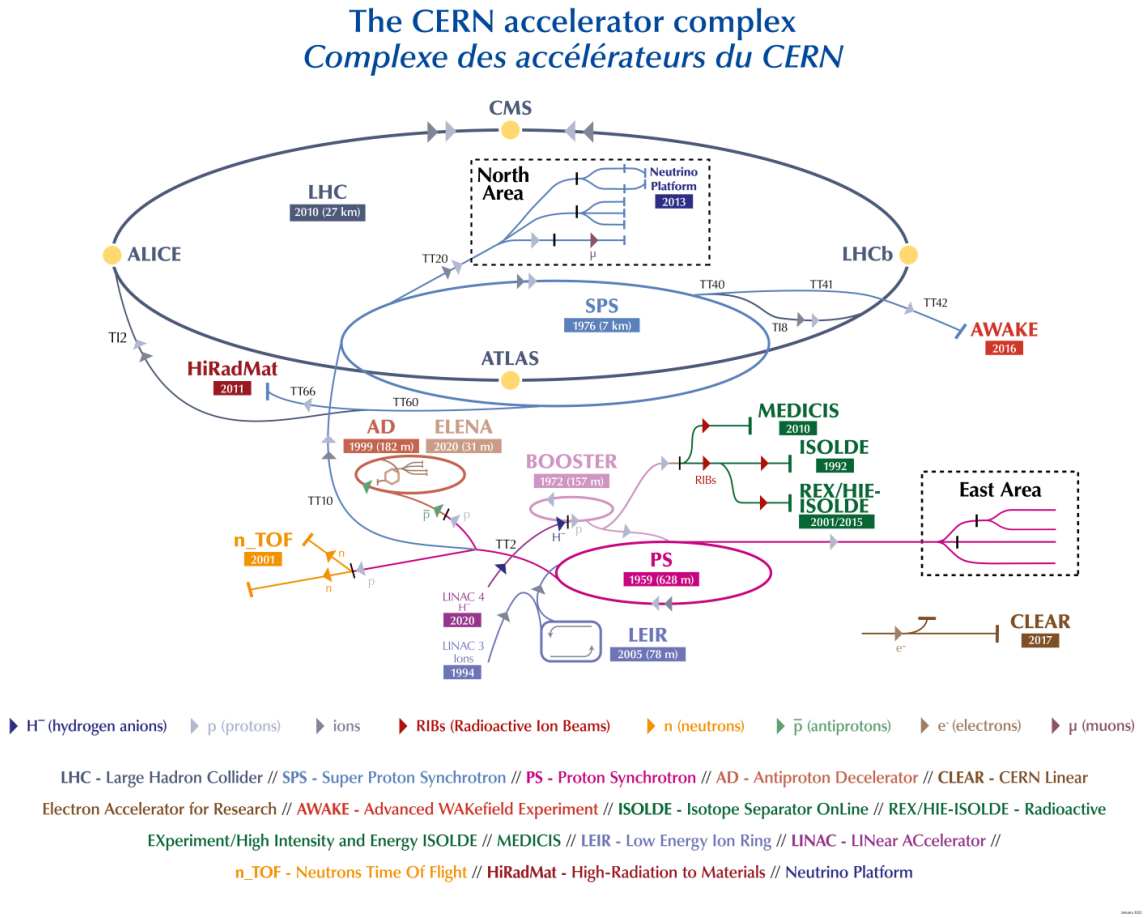

Figure C.1: The CERN accelerator complex.

the source of proton beams for the CERN accelerator complex in 2020. It accelerates negative hydrogen ions, H^-, to 160 MeV to prepare them to enter the Proton Synchrotron Booster (PSB). The ions are stripped of their two electrons during injection from LINAC4 into the PSB, leaving only protons. These are accelerated to 2 GeV to be injected into the Proton Synchrotron (PS), which pushes the beam up to 26 GeV. Protons can be either extracted to the East Area beamlines or sent to the Super Proton Synchrotron (SPS), the second-largest machine in the CERN accelerator complex, measuring nearly 7 kilometers

in circumference, which provides particles with a momentum up to 450 GeV/c to external lines, i.e. North Area, COMPASS, NA62. The protons are finally transferred to the Large Hadron Collider (LHC), where they are accelerated up to a maximum energy of 6.5 TeV. The two proton beams are brought into collision inside four detectors, ALICE, ATLAS, CMS and LHCb.

C.1 THE PS EXTRACTED BEAMLINES

The PS extracted beamlines are located in the CERN East Area (Figure C.2).
The East Area hosts two general-purpose beamtest areas, T9 and T10, the Cosmic Leaving Outdoor Droplets (CLOUD) experiment, which is studying the aerosol formation and cloud microphysics under controlled atmospheric conditions in a particle beam, the IRRAD Proton Irradiation Facility which provides a high-intensity proton beam to irradiate components and materials, and the CERN High-energy AcceleRator Mixed-field (CHARM) facility, a mixed-field irradiation area reproducing realistic radiation environments for electronics and materials.
The T9 beamline can deliver a high intensity and a high-purity tertiary beam of electron-

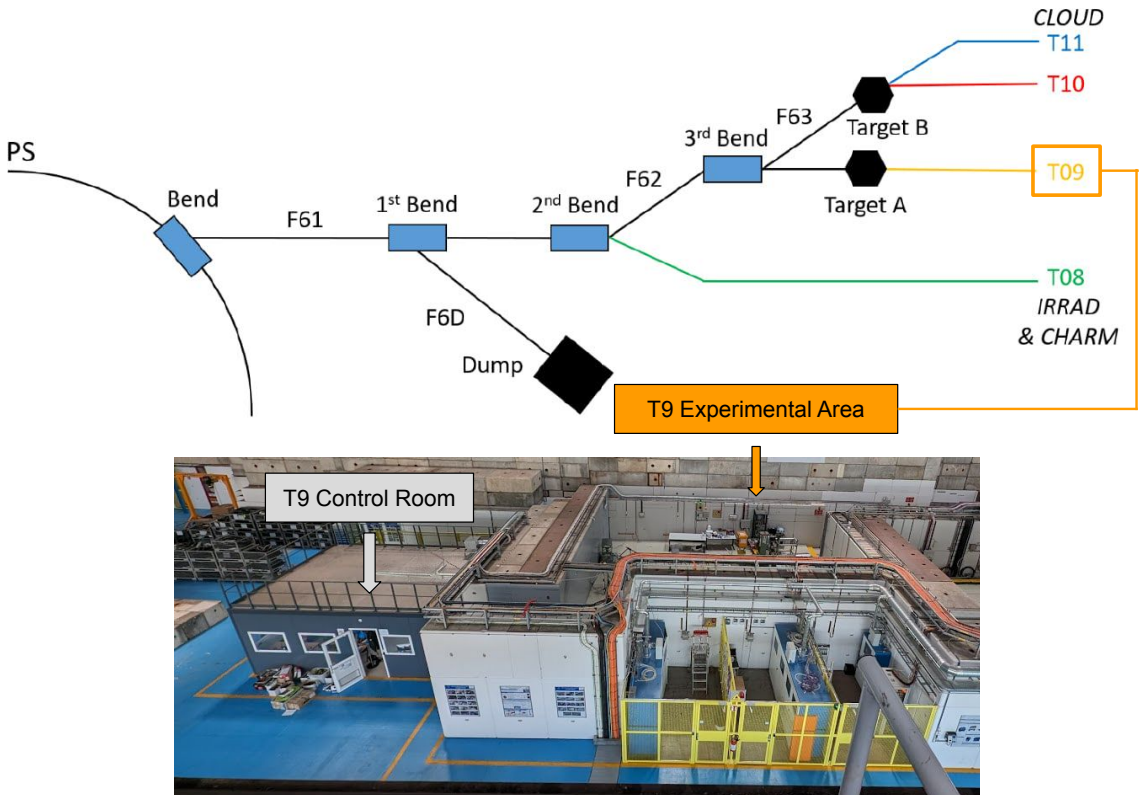

Figure C.2: The CERN PS extracted beamlines [126].

s/positrons up to 6 GeV/c. The primary protons, extracted from the PS with a momentum

of 24 GeV/c, interact with the primary target and produce neutral pions, which almost exclusively decay in flight into two high energy photons. Downstream of the target, two magnets sweep charged particles toward a beam dump. The photons are converted into $e^{\pm}$ pairs by a thin lead converter located about 8 m downstream of the magnets. The electron/-positron intensity decreases as the selected beam momentum increases, since on average they carry roughly a quarter of the parent π^0 energy; consequently, beyond 6 GeV/c only a small fraction of secondary electrons is present in the beam. Downstream of the converter, a combination of magnets and slits selects the beam charge and momentum. The muons produced in the decays of charged pions and kaons at the target interact only weakly with the thin lead converter leaving a small residual muon component in the tertiary beam. In addition, the T9 beamline can deliver a secondary mixed-hadron beam up to 15 GeV/c, typically with a small electron contamination.
The general beam parameters of the T9 beamline are listed in Table C.1.

The T9 beamline is equipped with two threshold Cherenkov detectors (XCET44 and

Parameters	**T9**
Maximum momentum (GeV/c) (hadrons / electrons)	15 / 6
Momentum resolution (%)	0.7
Maximum momentum band (%)	$\pm$15
Horizontal acceptance (mrad)	$\pm$4
Vertical acceptance (mrad)	$\pm$3.8
Max. intensity per spill (hadrons / electrons)	10^6 / $\sim 10^5$

Table C.1: Beam parameters for the T9 beamlines [126].

XCET48) to discriminate between electrons, muons, and pions (Figure C.3). Each XCET is a horizontal gas-filled tube, typically operated with He or CO_2, with thin entrance and exit windows. Given the particle momentum and type, the Cherenkov light emission depends on the gas and the selected pressure (threshold). The Cherenkov light produced by particles is collected by an internal mirror and directed to a PMT.

The T9 beamline offers two main beam configurations: in the focusing optics one, a sequence of quadrupoles and dipoles brings the beam to a focus at a chosen point, reducing the beam spot size while increasing the divergence; in parallel optics, the particle trajectories are nearly parallel, minimizing the divergence at the cost of a larger beam spot size.

C.2 THE SPS EXTRACTED BEAMLINES

The SPS has four general purpose beamlines, H2, H4, H6 and H8, located in the CERN North Area (Figure C.4), the largest experimental area at CERN. The North Area beamlines can provide different types of particle beams over a wide range of energies: attenuated primary proton beams, hadrons, muons, electrons, tagged photons, neutral hadrons,

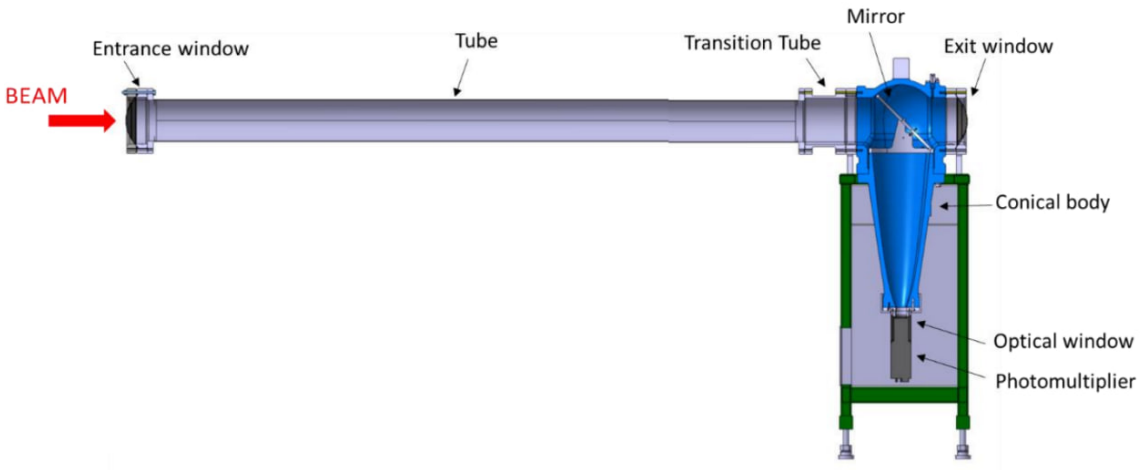

Figure C.3: A scheme of the T9 Cherenkov detector.

neutrons, primary and fragmented ion beams.

The extracted proton beam accelerated by the SPS is split and distributed over three primary targets; each target is shared between a pair of beamlines. High intensity secondary beams, given by a mix of hadrons and electrons or positrons, are produced in the primary targets. By inserting a secondary target at a focal point in the secondary beam a tertiary beam is generated composed by a very pure electron beam or a hadron beam with, depending on the momenta, an electron or positron component, which can be removed by using an absorber at a later focal point in the beamline.

Pions and kaons in a secondary beamline may decay into a muon and a neutrino.

Beyond its general-purpose beamlines, the North Area hosts major permanent experiments such as NA61/SPS Heavy Ion and Neutrino Experiment (SHINE) on H2, which measures hadron production for heavy-ion physics and neutrino flux predictions, Apparatus for Meson and Baryon Experimental Research (AMBER) (the Common Muon and Proton Apparatus for Structure and Spectroscopy (COMPASS) successor) on M2, studying hadron structure and spectroscopy with high-energy muon/hadron beams, NA64 on H4, searching for dark-sector particles with electron and muon modes; and NA62, probing ultra-rare kaon decays such as $K^+ \to \pi^+ \nu\bar{\nu}$.

Further details on the SPS beamlines and the SPS research program can be found in [127, 128].

The H2 and H4 beamlines are general-purpose beamlines that can deliver attenuated primary protons, pure electrons, mixed hadrons or muons. The extracted primary ion beam is split, using a special splitter, just upstream of the T2 target towards the H2 and H4 lines, which can receive various ion species simultaneously. The H2 beamline (Figure C.5) is divided into two separate sections by a large superconducting vertical bending magnet, M1. The H4 beamline (Figure C.6) is located on a straight line from the T2 target with respect to the incident primary beam, and it can deliver very high purity electron beams, using a strong sweeping magnet to remove charged secondaries and a downstream lead converter to transform the photons, originating mainly from π^0 decays in the target, into e^+e^- pairs. The main source of hadron contaminants in the electron/positron beam is the

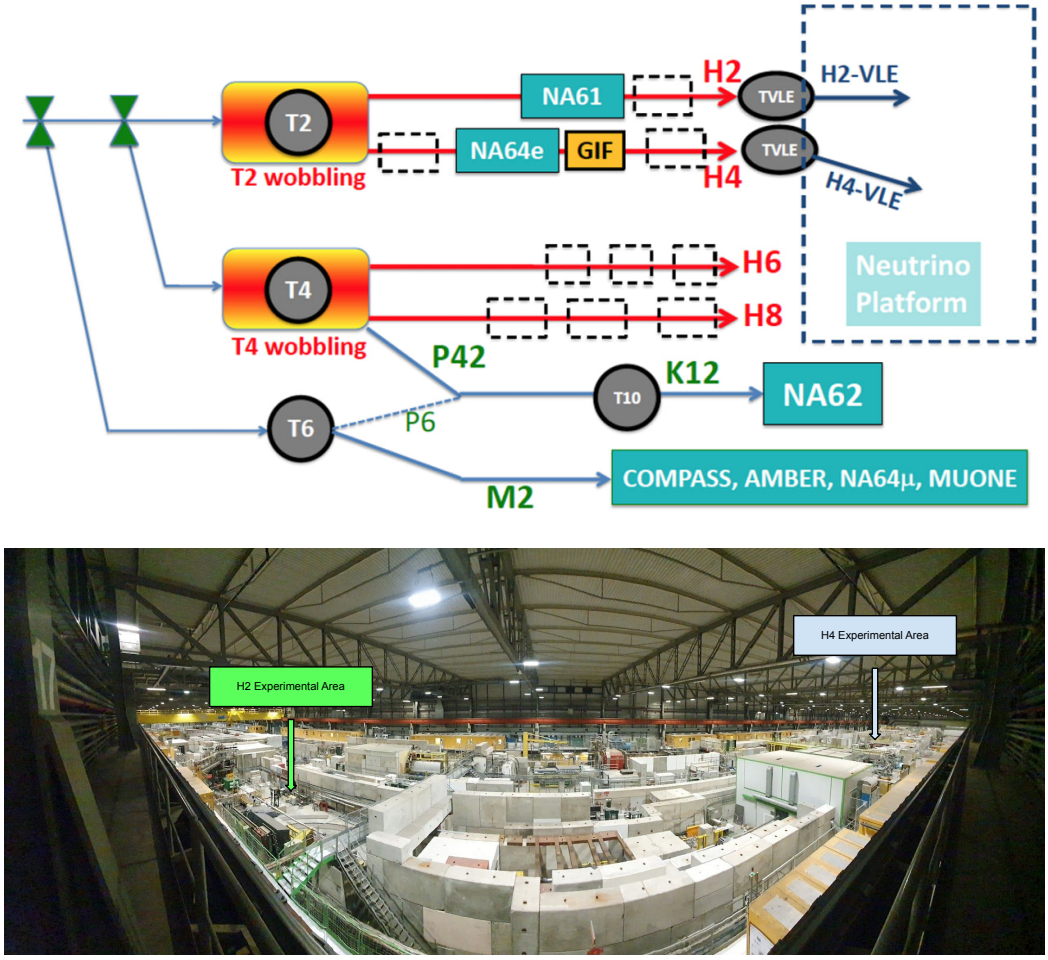

Figure C.4: (top) The CERN SPS extracted beamlines. (bottom) A photo of the North Area experimental hall.

forward production of long-lived neutral particles in the target propagating downstream and decaying to charged particles after the sweeping magnet.
It houses the GOLIATH magnet, which is available for tests of detectors under the effect of a magnetic field.
The general beam parameters of the H2 and H4 beamlines are listed in Table C.2.

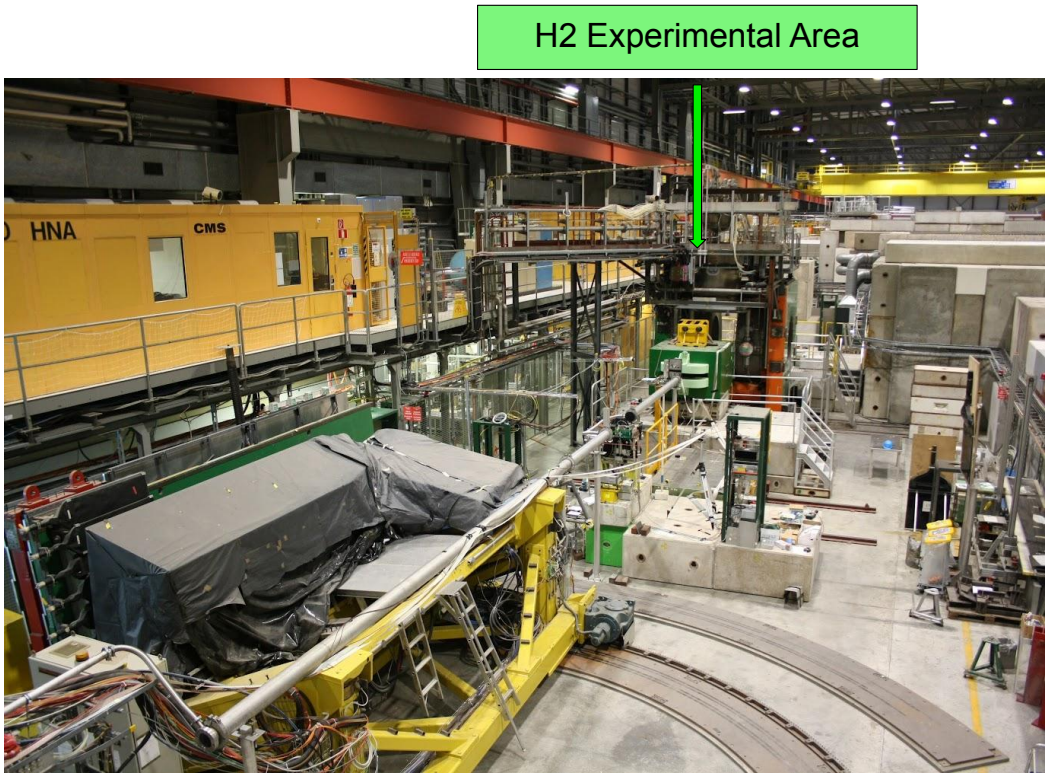

Figure C.5: The H2 beamline.

Parameters	**T2 target**	
	H2	**H4**
Maximum momentum (GeV/c) (primary / secondary mode)	400 / 360	400 / 330
Maximum acceptance (µsr)	1.5	1.5
Maximum $\Delta p/p$ (%)	± 2.0	± 1.4
Max. intensity / spill (Hadrons / Electrons)	$10^7/10^5$	$10^7/10^6$

Table C.2: Beam parameters for the H2 and H4 beamlines [127].

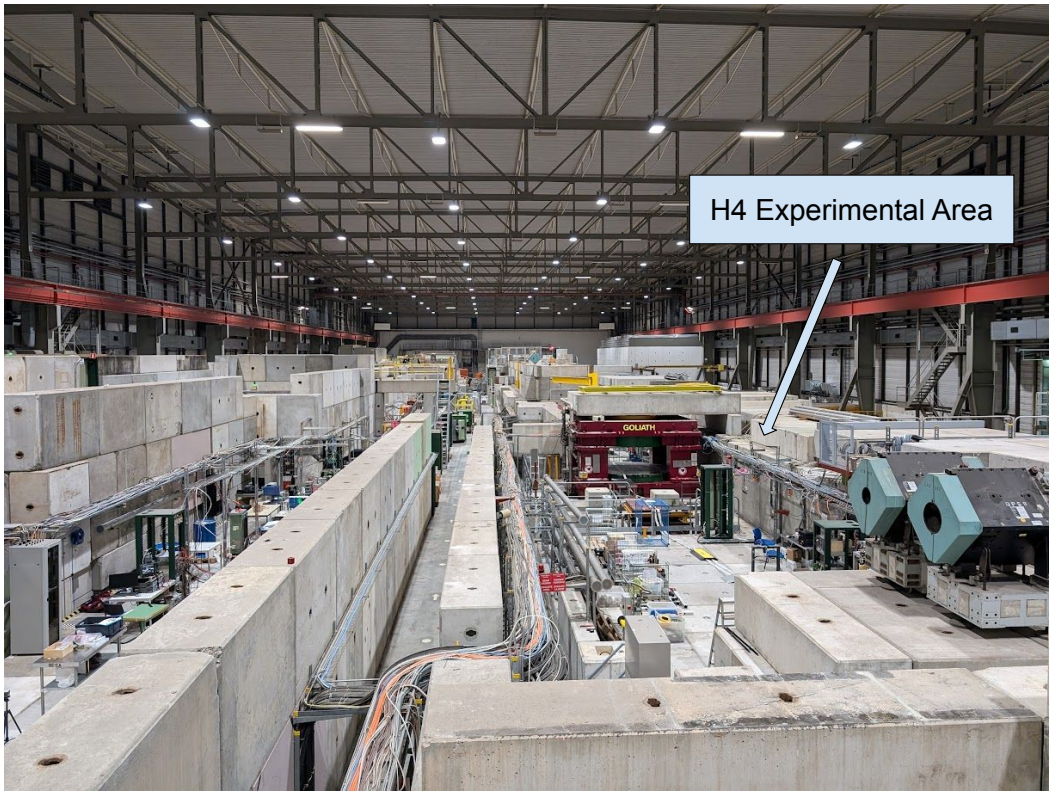

Figure C.6: The H4 beamline.

LIST OF FIGURES

LIST OF TABLES

BIBLIOGRAPHY

[1] *DRD6: Detector R&D Collaboration for Calorimeters*. CERN Greybook. Approved: 06-12-2023. 2023. URL: https://greybook.cern.ch/experiment/detail?id=DRD6.

[2] S. Chatrchyan et al. 'Observation of a new boson at a mass of 125 GeV with the CMS experiment at the LHC'. In: *Physics Letters B* 716 (2012), pp. 30–61. DOI: 10.1016/j.physletb.2012.08.021. arXiv: 1207.7235 [hep-ex].

[3] G. Aad et al. 'Observation of a new particle in the search for the Standard Model Higgs boson with the ATLAS detector at the LHC'. In: *Physics Letters B* 716 (2012), pp. 1–29. DOI: 10.1016/j.physletb.2012.08.020. arXiv: 1207.7214 [hep-ex].

[4] C. Rubbia. 'Experimental observation of the intermediate vector bosons W^+, W^-, and Z^{0}'. In: *Rev. Mod. Phys.* 57.3 (July 1985), pp. 699–722. DOI: 10.1103/RevModPhys.57.699. URL: https://link.aps.org/doi/10.1103/RevModPhys.57.699.

[5] G. Arnison and et al. 'Experimental observation of isolated large transverse energy electrons with associated missing energy at $\sqrt{s} = 540$ GeV'. In: *Physics Letters B* 122.1 (Feb. 1983), pp. 103–116. DOI: 10.1016/0370-2693(83)91177-2. URL: https://doi.org/10.1016/0370-2693(83)91177-2.

[6] M. Banner and et al. 'Observation of single isolated electrons of high transverse momentum in events with missing transverse energy at the CERN $p\bar{p}$ collider'. In: *Physics Letters B* 122.5-6 (Mar. 1983), pp. 476–485. DOI: 10.1016/0370-2693(83)91605-2. URL: https://doi.org/10.1016/0370-2693(83)91605-2.

[7] Y. Fukuda et al. 'Evidence for Oscillation of Atmospheric Neutrinos'. In: *Phys. Rev. Lett.* 81 (1998), pp. 1562–1567. DOI: 10.1103/PhysRevLett.81.1562. arXiv: hep-ex/9807003 [hep-ex].

[8] Particle Data Group. 'Review of Particle Physics'. In: *Progress of Theoretical and Experimental Physics* 2022 (Aug. 2022). ISSN: 2050-3911. DOI: 10.1093/ptep/ptac097.

[9] H. Bethe and W. Heitler. 'On the Stopping of Fast Particles and on the Creation of Positive Electrons'. In: *Proceedings of the Royal Society of London. Series A, Containing Papers of a Mathematical and Physical Character* 146 (1934). Communicated by P. A. M. Dirac, pp. 83–112. DOI: 10.1098/rspa.1934.0140.

[10] E. Tiesinga et al. 'CODATA recommended values of the fundamental physical constants: 2018'. In: *Reviews of Modern Physics* 93 (2021), p. 025010. DOI: 10.1103/RevModPhys.93.025010.

[11] B. Rossi. *High-Energy Particles*. Prentice-Hall Physics Series. New York: Prentice-Hall, 1952.

[12] U. I. Uggerhøj. 'The interaction of relativistic particles with strong crystalline fields'. In: *Reviews of modern physics* 77.4 (2005), p. 1131.

[13] E. Fiandrini. *Particle Detectors — Lecture 8*. https://www.fisgeo.unipg.it/~fiandrin/didattica_fisica/rivelatori1617/lez08_290317_riv1617.pdf. Lecture slides, University of Perugia, 29 Apr 2017. Figure: electron shower in a cloud chamber with lead absorbers. Accessed: 2025-10-07.

[14] E. Longo and I. Sestili. 'Monte Carlo Calculation of Photon-Initiated Electromagnetic Showers in Lead Glass'. In: *Nuclear Instruments and Methods* 128.2 (1975), pp. 283–307. DOI: 10.1016/0029-554X(75)90679-5.

[15] A. Ereditato. *Calorimetry In High Energy Physics-Proceedings Of The 2nd International Conference*. World Scientific, 1992.

[16] *Photomultiplier Tubes: Basics and Applications*. 4th. Fourth Edition. Hamamatsu Photonics K. K. 2017. URL: https://www.hamamatsu.com/content/dam/hamamatsu-photonics/sites/documents/99_SALES_LIBRARY/etd/PMT_handbook_v4E.pdf.

[17] F. Acerbi and S. Gundacker. 'Understanding and simulating SiPMs'. In: *Nuclear Instruments and Methods in Physics Research Section A* 926 (2019), pp. 16–35. DOI: 10.1016/j.nima.2018.11.118.

[18] J. Birks. *The theory and practice of scintillation counting: International series of monographs in electronics and instrumentation*. Vol. 27. Elsevier, 2013.

[19] C. Cochet et al. 'The central electromagnetic calorimeter of UA1'. In: *Nuclear Instruments and Methods in Physics Research Section A* 243.1 (1986), pp. 45–57. DOI: 10.1016/0168-9002(86)90820-X.

[20] A. Beer et al. 'The central calorimeter of the UA2 experiment at the CERN $\bar{p}p$ collider'. In: *Nuclear Instruments and Methods in Physics Research Section A* 224.3 (1984), pp. 360–395. DOI: 10.1016/0167-5087(84)90029-2.

[21] D. Boutigny et al. *BABAR Technical Design Report*. Tech. rep. SLAC-R-95-457. Menlo Park: SLAC, Mar. 1995. URL: https://slac.stanford.edu/pubs/slacreports/reports03/slac-r-457.pdf.

[22] A. Abashian et al. 'The Belle detector'. In: *Nuclear Instruments and Methods in Physics Research Section A* 479 (2002), pp. 117–232. DOI: 10.1016/S0168-9002(01)02013-7.

[23] C. Bebek et al. 'A cesium iodide calorimeter with photodiode readout for CLEO II'. In: *Nuclear Instruments and Methods in Physics Research Section A* 265 (1988), pp. 258–265. DOI: 10.1016/0168-9002(88)91079-0.

[24] *The CMS Electromagnetic Calorimeter Project: Technical Design Report*. Tech. rep. CERN-LHCC-97-033; CMS-TDR-4. 15 December 1997. Geneva: CERN, Dec. 1997. URL: https://cds.cern.ch/record/349375/files/ECAL_TDR.pdf.

[25] *ALICE: Technical Proposal for a Large Ion Collider Experiment at the CERN LHC*. Tech. rep. CERN-LHCC-95-71; LHCC-P-3. 15 December 1995. Geneva: CERN, Dec. 1995. URL: https://cds.cern.ch/record/293391.

[26] W. Erni et al. *Technical Design Report for the PANDA Electromagnetic Calorimeter (EMC)*. FAIR/GSI, Oct. 2008. arXiv: 0810.1216 [physics.ins-det]. URL: https://arxiv.org/abs/0810.1216.

[27] M. Akrawy et al. 'Development studies for the OPAL end cap electromagnetic calorimeter using vacuum photo triode instrumented leadglass'. In: *Nuclear Instruments and Methods in Physics Research Section A* 290.1 (May 1990), pp. 76–94. DOI: 10.1016/0168-9002(90)90346-8.

[28] S. Fukuda et al. 'The Super-Kamiokande detector'. In: *Nuclear Instruments and Methods in Physics Research Section A* 501 (2003), pp. 418–462. DOI: 10.1016/S0168-9002(03)00425-X.

[29] I. Amore. 'NEMO: A Project for a km^3 Underwater Detector for Astrophysical Neutrinos in the Mediterranean Sea'. In: *International Journal of Modern Physics A* 22 (2007), pp. 3509–3520. DOI: 10.1142/S0217751X07037123. arXiv: 0709.3991.

[30] S. E. Tzamarias. 'NESTOR: a deep-sea neutrino telescope'. In: *Nuclear Instruments and Methods in Physics Research Section A* 502.1 (2003), pp. 150–156. DOI: 10.1016/S0168-9002(03)00265-1.

[31] S. Adrián-Martínez et al. 'Letter of intent for KM3NeT 2.0'. In: *Journal of Physics G: Nuclear and Particle Physics* 43.8 (2016), p. 084001. DOI: 10.1088/0954-3899/43/8/084001. arXiv: 1601.07459.

[32] M. G. Aartsen et al. 'The IceCube Neutrino Observatory: Instrumentation and Online Systems'. In: *Journal of Instrumentation* 12 (2017), P03012. DOI: 10.1088/1748-0221/12/03/P03012. arXiv: 1612.05093.

[33] *ATLAS liquid-argon calorimeter: Technical Design Report*. Tech. rep. CERN-LHCC-96-041; ATLAS-TDR-2. Geneva: CERN, Dec. 1996. URL: https://cds.cern.ch/record/331061.

[34] S. Amerio et al. 'Design, construction and tests of the ICARUS T600 detector'. In: *Nuclear Instruments and Methods in Physics Research Section A* 527.3 (2004), pp. 329–410. DOI: 10.1016/j.nima.2004.02.044.

[35] M. Jeitler and the NA48 Collaboration. 'The NA48 liquid-krypton calorimeter'. In: *Nuclear Instruments and Methods in Physics Research Section A* 494.1 (2002), pp. 373–377. DOI: 10.1016/S0168-9002(02)01505-X.

[36] C. Fabjan and F. Gianotti. 'Calorimetry for particle physics'. In: *Rev. Mod. Phys.* 75 (4 2003), pp. 1243–1286. DOI: 10.1103/RevModPhys.75.1243. URL: https://link.aps.org/doi/10.1103/RevModPhys.75.1243.

[37] J. Stark. 'Bemerkung über Zerstreuung und Absorption von β-Strahlen und Röntgenstrahlen in Kristallen'. In: *Physikalische Zeitschrift* 13 (1912), pp. 973–977.

[38] J. Lindhard. 'Influence of crystal lattice on motion of energetic charged particles'. In: *Kongel. Dan. Vidensk. Selsk., Mat.-Fys. Medd.* 34 (Jan. 1965). URL: https://www.osti.gov/biblio/4536390.

[39] N. W. Ashcroft, N. D. Mermin et al. *Solid state physics*. Holt, Rinehart and Winston, 1976.

[40] P. Monti-Guarnieri. 'Beamtest characterization of oriented crystals for the KLEVER Small Angle Calorimeter'. Master's thesis. MA thesis. Como, Italy: Università degli Studi dell'Insubria, 2023. URL: https://cds.cern.ch/record/2850897.

[41] M. Romagnoni et al. 'Bent Crystal Design and Characterization for High-Energy Physics Experiments'. In: *Crystals* 12.9 (2022), p. 1263. DOI: 10.3390/cryst12091263.

[42] D. S. Gemmell. 'Channeling and related effects in the motion of charged particles through crystals'. In: *Reviews of Modern Physics* 46.1 (1974), p. 129.

[43] V. M. Biryukov, Y. A. Chesnokov and V. I. Kotov. *Crystal Channeling and Its Application at High-Energy Accelerators*. Vol. 133. Springer Tracts in Modern Physics. Springer, 1997.

[44] M. A. Kumakhov. 'On the theory of electromagnetic radiation of charged particles in a crystal'. In: *Physics Letters A* 57.1 (1976), pp. 17–18.

[45] J. U. Andersen, K. R. Eriksen and E. Lægsgaard. 'Planar-Channeling Radiation and Coherent Bremsstrahlung for MeV Electrons'. In: *Physica Scripta* 24.3 (1981), pp. 588–600. DOI: 10.1088/0031-8949/24/3/015. URL: https://doi.org/10.1088/0031-8949/24/3/015.

[46] H. Wiedemann. 'Synchrotron Radiation Physics'. In: *Synchrotron Light Sources and Free-Electron Lasers: Accelerator Physics, Instrumentation and Science Applications*. Ed. by Eberhard J. Jaeschke et al. Cham: Springer, 2016, pp. 3–49. DOI: 10.1007/978-3-319-14394-1_1.

[47] M. L. Ter-Mikaelyan. 'Influence of the Medium on Electromagnetic Processes at High Energies'. In: *AN Arm. SSR, Yerevan* (1969).

[48] B. Ferretti. 'Sulla "Bremsstrahlung" nei cristalli'. In: *Il Nuovo Cimento (1943-1954)* 7.2 (1950), pp. 118–134.

[49] J. Schwinger. 'On Gauge Invariance and Vacuum Polarization'. In: *Phys. Rev.* 82 (5 1951), pp. 664–679. DOI: 10.1103/PhysRev.82.664. URL: https://link.aps.org/doi/10.1103/PhysRev.82.664.

[50] M. Buchanan. 'Past the Schwinger limit'. In: *Nature Physics* 2.11 (2006), p. 721.

[51] K. Kirsebom and R. Medenwaldt. 'Investigations of the coherent hard photon yields and other QED processes for (50-300) GeV/c electrons/positrons in the strong crystalline fields of diamond, Si, Ge and W crystals: a status report'. In: *CERN-SPSLC-96-5* (1996).

[52] V. N. Baier, V. M. Katkov and V. M. Strakhovenko. 'Radiation of ultrarelativistic particles moving near crystalline axes'. In: *Physics Letters A* 95.7 (1983), pp. 403–406.

[53] M. Soldani et al. 'Next-generation ultra-compact calorimeters based on oriented crystals'. In: *Proceedings of 40th International Conference on High Energy physics — PoS(ICHEP2020)*. Vol. 390. 2021, p. 872.

[54] V. N. Baier, V. M. Katkov and V. M. Strakhovenko. 'Production of electron-positron pairs by high-energy photons in oriented crystals'. In: *Sov. Phys. JETP* 63 (1986), pp. 467–475.

[55] V. M. Katkov, V. M. Strakhovenko et al. *Electromagnetic processes at high energies in oriented single crystals*. World Scientific, 1998.

[56] V. G. Baryshevsky, A. A. Gurinovich and A. P. Ulyanenkov. 'On the influence of crystal structure on the electromagnetic shower development in the lead tungstate crystals'. In: *Nuclear Instruments and Methods in Physics Research Section B: Beam Interactions with Materials and Atoms* 402 (2017), pp. 35–39. DOI: 10.1016/j.nimb.2017.02.019.

[57] A. H. Sørensen. 'Channeling, bremsstrahlung and pair creation in single crystals'. In: *Nuclear Instruments and Methods in Physics Research Section B: Beam Interactions with Materials and Atoms* 119.1 (1996), pp. 2–29. ISSN: 0168-583X. DOI: 10.1016/S0168-583X(96)00349-7. URL: https://www.sciencedirect.com/science/article/pii/0168583X96003497.

[58] O. R. Frisch and D. N. Olson. 'Detection of Coherent Bremsstrahlung from Crystals'. In: *Physical Review Letters* 3 (1959), pp. 141–142. DOI: 10.1103/PhysRevLett.3.141.

[59] G. Diambrini-Palazzi. 'High-Energy Bremsstrahlung and Electron Pair Production in Thin Crystals'. In: *Reviews of Modern Physics* 40 (1968), pp. 611–631. DOI: 10.1103/RevModPhys.40.611.

[60] G. Bologna, G. Diambrini and G. P. Murtas. 'High-Energy Bremsstrahlung from a Silicon Single Crystal'. In: *Physical Review Letters* 4 (1960), pp. 572–575. DOI: 10.1103/PhysRevLett.4.572.

[61] R. L. Walker et al. 'Channeling and Coherent Bremsstrahlung Effects for Relativistic Positrons and Electrons'. In: *Physical Review Letters* 25 (1970), pp. 5–8. DOI: 10.1103/PhysRevLett.25.5.

[62] N. Cue et al. 'Observation of Electric Synchrotron Radiation in a Crystal'. In: *Physical Review Letters* 53 (1984), pp. 972–974. DOI: 10.1103/PhysRevLett.53.972.

[63] A. Belkacem et al. 'Observation of Enhanced Pair Creation for 50–110-GeV Photons in an Aligned Ge Crystal'. In: *Physical Review Letters* 53 (1984), pp. 2371–2373. DOI: 10.1103/PhysRevLett.53.2371.

[64] R. Moore et al. 'Measurement of pair-production by high energy photons in an aligned tungsten crystal'. In: *Nuclear Instruments and Methods in Physics Research Section B: Beam Interactions with Materials and Atoms* 119 (1996), pp. 149–155. DOI: 10.1016/0168-583X(96)00347-3.

[65] K. Kirsebom et al. 'Pair production by 5–150 GeV photons in the strong crystalline fields of germanium, tungsten and iridium'. In: *Nuclear Instruments and Methods in Physics Research Section B: Beam Interactions with Materials and Atoms* 135 (1998), pp. 143–148. DOI: 10.1016/S0168-583X(97)00589-2.

[66] X. Artru et al. 'Summary of experimental studies at CERN on a positron source using crystal effects'. In: *Nuclear Instruments and Methods in Physics Research Section B: Beam Interactions with Materials and Atoms* 240 (2005), pp. 762–776. DOI: 10.1016/j.nimb.2005.04.134.

[67] L. Bandiera et al. 'Strong Reduction of the Effective Radiation Length in an Axially Oriented Scintillator Crystal'. In: *Physical Review Letters* 121.2 (2018), p. 021603. DOI: 10.1103/PhysRevLett.121.021603.

[68] M. Soldani. 'Innovative applications of strong crystalline field effects to particle accelerators and detectors'. PhD Thesis. PhD thesis. Ferrara University, 2023. URL: https://cds.cern.ch/record/2864634.

[69] M. Soldani et al. 'Strong Enhancement of Electromagnetic Shower Development in Oriented Scintillating Crystals and Implications for Particle Detectors'. In: (2024). Version 2 (11 Jul 2025). DOI: 10.48550/arXiv.2404.12016. arXiv: 2404.12016 [hep-ex].

[70] P. Monti-Guarnieri et al. 'Development of an advanced modular setup for the on beam characterization of oriented crystals'. In: *Il Nuovo Cimento C* 46 (2023), p. 98. DOI: 10.1393/ncc/i2023-23098-5.

[71] S. Agostinelli et al. 'GEANT4—a simulation toolkit'. In: *Nuclear Instruments and Methods in Physics Research Section A: Accelerators, Spectrometers, Detectors and Associated Equipment* 506.3 (2003), pp. 250–303.

[72] M. Korzhik et al. 'Ultrafast PWO scintillator for future high energy physics instrumentation'. In: *Nuclear Instruments and Methods in Physics Research Section A* 1034 (2022), p. 166781. DOI: 10.1016/j.nima.2022.166781.

[73] P. Lecoq et al. 'Lead tungstate ($PbWO_4$) scintillators for LHC EM calorimetry'. In: *Nuclear Instruments and Methods in Physics Research Section A* 365 (1995), pp. 291–298. DOI: 10.1016/0168-9002(95)00589-7.

[74] A. A. Annenkov, M. V. Korzhik and P. Lecoq. 'Lead tungstate scintillation material'. In: *Nuclear Instruments and Methods in Physics Research Section A: Accelerators, Spectrometers, Detectors and Associated Equipment* 490.1-2 (2002), pp. 30–50.

[75] A. Borisevich et al. 'PWO-II scintillation crystals for the PANDA electromagnetic calorimeter'. In: *2008 IEEE Nuclear Science Symposium Conference Record (NSS/MIC)*. 2008, pp. 2698–2700.

[76] Malvern Panalytical. *X-ray Diffractometer*. https://www.malvernpanalytical.com/en/products/technology/xray-analysis/x-ray-diffraction. Accessed: 2025-06-11. 2024.

[77] J. Germogli. 'Bent silicon strip crystals for high-energy charged particle beam collimation'. In: *Nuclear Instruments and Methods in Physics Research Section B: Beam Interactions with Materials and Atoms* 402 (2017). Proceedings of the 7th International Conference Channeling 2016: Charged & Neutral Particles Channeling Phenomena, pp. 308–312. DOI: 10.1016/j.nimb.2017.03.053. URL: http://dx.doi.org/10.1016/j.nimb.2017.03.053.

[78] Eljen Technology. *Reflective paint EJ-510*. https://eljentechnology.com/products/accessories/ej-510. Accessed: 2025-10-01.

[79] F. Zappa et al. 'Principles and features of single-photon avalanche diode arrays'. In: *Sensors and Actuators A: Physical* 140.1 (2007), pp. 103–112.

[80] *ARRAYC-60035-4P-BGA datasheet*. url: https://www.mouser.it/datasheet/2/308/ARRAYC_SERIES_D-2309928.pdf. Accessed: 24-05-2022.

[81] *onsemi, semiconductor supplier company, Phoenix, Arizona, United States*. url: https://www.onsemi.com/. Accessed: 24-05-2022.

[82] *C-Series SiPM Sensors*. url:https://www.onsemi.com/pdf/datasheet/microc-series-d.pdf. Accessed: 24-05-2022.

[83] *SCEN s.r.l.* url: http://www.scen.it/. Accessed: 24-05-2022.

[84] *HIROSE company*. url: https://www.hirose.com/en/product/. Accessed: 24-05-2022.

[85] Crytur s.r.o. *Company website*. https://www.crytur.com. Accessed: 2025-10-01.

[86] M. Korzhik et al. 'Ultrafast PWO scintillator for future high energy physics instrumentation'. In: *Nuclear Instruments and Methods in Physics Research Section A: Accelerators, Spectrometers, Detectors and Associated Equipment* 1034 (2022), p. 166781. DOI: 10.1016/j.nima.2022.166781.

[87] L. Malagutti et al. 'High-precision alignment techniques for realizing an ultracompact electromagnetic calorimeter using oriented high-Z scintillator crystals'. In: *Nuclear Instruments and Methods in Physics Research Section A: Accelerators, Spectrometers, Detectors and Associated Equipment* 1069 (2024), p. 169869.

[88] ZYGO Corporation. *Verifire HD/HDX Laser Interferometers*. https://www.zygo.com/products/metrology-systems/laser-interferometers/verifire-hd-hdx. Accessed: 2025-10-01.

[89] Hamamatsu Photonics K.K. *MPPCs (Multi-Pixel Photon Counters) S13360 Series: S13360-2050VE, S13360-3050VE, S13360-6050VE*, etc. KAPD1053E. Datasheet; accessed 2025-10-08. Hamamatsu Photonics.

[90] V. Moya-Zamanillo and J. Rosado. 'Understanding the nonlinear response of SiPMs'. In: *Sensors* 24.8 (2024), p. 2648.

[91] Edmund Optics. *0.7 OD 100 x 300mm Neutral Density Filter*. https://www.edmundoptics.com/p/07-od-100-x-300mm-neutral-density-filter/27110/. Stock #84-002, Kodak Wratten 2, uncoated, 20% transmission, blocking range 400–700 nm. 2023.

[92] L. Celano et al. 'A high resolution beam telescope built with double sided silicon strip detectors'. In: *Nuclear Instruments and Methods in Physics Research Section A: Accelerators, Spectrometers, Detectors and Associated Equipment* 381.1 (1996), pp. 49–56.

[93] S. Carsi. 'Advanced Tracking System for Crystal Physics'. CERN-THESIS-2024-017. MA thesis. Como, Italy: Università degli Studi dell'Insubria, 2024. URL: https://cds.cern.ch/record/2892405.

[94] M. Prest et al. 'The AGILE silicon tracker: an innovative γ-ray instrument for space'. In: *Nuclear Instruments and Methods in Physics Research Section A: Accelerators, Spectrometers, Detectors and Associated Equipment* 501.1 (2003), pp. 280–287.

[95] D. Lietti. 'VISION: a Versatile and Innovative SIlicOn tracking system'. Insubria University, Como, PhD thesis, 2011. URL: url:https://cds.cern.ch/record/2626151/files/CERN-THESIS-2015-453.pdf.

[96] M. Tavani et al. 'The AGILE mission and its scientific instrument'. In: *Proceedings of SPIE, Space Telescopes and Instrumentation II: Ultraviolet to Gamma Ray* 6266 (2006), pp. 12–26.

[97] G. Barbiellini et al. 'The AGILE silicon tracker: testbeam results of the prototype silicon detector'. In: *Nuclear Instruments and Methods in Physics Research Section A: Accelerators, Spectrometers, Detectors and Associated Equipment* 490.1-2 (2002), pp. 146–158.

[98] Physik Instrumente (PI). *Physik Instrumente (PI) — Precision Motion and Piezo Technology*. Accessed: 2025-10-13. URL: https://www.physikinstrumente.com/.

[99] Physik Instrumente (PI) GmbH & Co. KG. *Corvus-eco Stepping Motor Controller-/Driver*. Datasheet; accessed 2025-10-13.

[100] Physik Instrumente (PI) GmbH & Co. KG. *Pollux: Integrated Stepper Motor with Intelligent Positioning Controller*. Datasheet; accessed 2025-10-13.

[101] Physik Instrumente (PI) L.P. *C-863 Mercury Digital Servo Controller (DC Motors)*. Product page; accessed 2025-10-13.

[102] M. Lazzaroni. *Users Tables: DESY and XSCA Tables (capacities and availability)*. https://indico.cern.ch/event/1083128/contributions/4554146/attachments/2322514/3955277/20210914_Users%20Table.pdf. EATM Meeting, CERN, 14 Sep 2021. Accessed: 2025-10-13.

[103] W. Scandale et al. 'Apparatus to study crystal channeling and volume reflection phenomena at the SPS H8 beamline'. In: *Review of Scientific Instruments* 79.2 (2008), p. 023303.

[104] Hamamatsu Photonics K. K. *Metal package photomultiplier tube R9880U series (includes R9880U-110)*. https://www.hamamatsu.com/eu/en/product/optical-sensors/pmt/pmt_tube-alone/metal-package-type/R9880U-110.html. Datasheet TPMH1321E. Accessed: 2025-10-13. 2024. URL: https://www.hamamatsu.com/content/dam/hamamatsu-photonics/sites/documents/99_SALES_LIBRARY/etd/R9880U_TPMH1321E.pdf.

[105] B. W. Kernighan and D. M. Ritchie. *The C Programming Language*. 2nd ed. Englewood Cliffs, NJ: Prentice Hall, 1988. ISBN: 978-0131103627.

[106] J. K. Ousterhout and Ken Jones. *Tcl and the Tk Toolkit*. 2nd ed. Addison–Wesley, 2009. ISBN: 978-0321336330.

[107] CAEN S.p.A. *DT5730 / DT5730S: 8-Channel 14-bit 500 MS/s Digitizer*. Product page and datasheet. Accessed: 2025-10-13. URL: https://www.caen.it/products/dt5730/.

[108] CAEN S.p.A. *V1724 - 8 Channel 14-bit 100 MS/s Digitizer*. Rev. 27. 2020. URL: https://www.caen.it/products/v1724/.

[109] CAEN S.p.A. *V1730 - 16 Channel 14-bit 500 MS/s Digitizer*. User Manual. 2020. URL: https://www.caen.it/products/v1730/.

[110] D. Souvik. 'A simple alternative to the Crystal Ball function'. In: *arXiv preprint arXiv:1603.08591* (2016).

[111] A. Sytov, V. V. Tikhomirov and L. Bandiera. 'Simulation code for modeling of coherent effects of radiation generation in oriented crystals'. In: *Physical Review Accelerators and Beams* 22.6 (2019), p. 064601. DOI: 10.1103/PhysRevAccelBeams.22.064601.

[112] J. E. Moyal. 'Theory of ionization fluctuations'. In: *The London, Edinburgh, and Dublin Philosophical Magazine and Journal of Science* 46.374 (1955), pp. 263–280.

[113] Geant4 Collaboration. *Geant4 General Particle Source (GPS)*. https://geant4-userdoc.web.cern.ch/UsersGuides/ForApplicationDeveloper/html/GettingStarted/GeneralParticleSource.html. Accessed: 2025-06-18.

[114] A. Mazzolari et al. 'Silicon crystals for steering high-intensity particle beams at ultra high-energy accelerators'. In: *Phys. Rev. Res.* 3 (2021), p. 013108. DOI: 10.1103/PhysRevResearch.3.013108. URL: https://link.aps.org/doi/10.1103/PhysRevResearch.3.013108.

[115] Yu. M. Andreev et al. 'Measurement of the intrinsic hadronic contamination in the NA64-e high-purity e^+/e^- beam at CERN'. In: *Nuclear Instruments and Methods in Physics Research Section A: Accelerators, Spectrometers, Detectors and Associated Equipment* 1057 (2023), p. 168776. DOI: 10.1016/j.nima.2023.168776.

[116] I. Chaikovska et al. 'Positron source for FCC-ee'. In: *Proceedings of the 10th International Particle Accelerator Conference (IPAC'19)* (2019), p. 424.

[117] P. Monti-Guarnieri. *OREO2024: GitLab repository*. https://gitlab.com/piemmegi/oreo2024. Private repository; contact: pietro.monti-guarnieri@cern.ch. Accessed: 2025-06-18. 2024.

[118] A. Selmi. *simulation2022-h2: GitLab repository*. https://gitlab.com/AlessiaSelmi/simulation2022-h2. Accessed: 2025-06-18. 2022.

[119] Geant4 Collaboration. *Geant4 Physics List Guide: FTFP_BERT*. https://geant4-userdoc.web.cern.ch/UsersGuides/PhysicsListGuide/html/reference_PL/FTFP_BERT.html. Accessed: 2025-06-18.

[120] L. Bandiera, V. Haurylavets and V. Tikhomirov. 'Compact electromagnetic calorimeters based on oriented scintillator crystals'. In: *Nuclear Instruments and Methods in Physics Research Section A: Accelerators, Spectrometers, Detectors and Associated Equipment* 936 (2019), pp. 124–126. DOI: 10.1016/j.nima.2018.10.147.

[121] V. Guidi, L. Bandiera and V. Tikhomirov. 'Radiation generated by single and multiple volume reflection of ultrarelativistic electrons and positrons in bent crystals'. In: *Physical Review A* 86.4 (2012), p. 042903. DOI: 10.1103/PhysRevA.86.042903.

[122] INFN Ferrara. *TRILLION – Steering and radiation effects in oriented crystals and their applications implementation into Geant4*. Marie Skłodowska-Curie Actions Individual Global Fellowships GA 101032975. 2024. URL: https://www.fe.infn.it/trillion/index.html.

[123] A. Sytov. *Alexei Sytov – CRYSTALab Team*. Accessed: 2025-06-19. 2024. URL: https://crystalab.unife.it/meet-the-team/alexei-sytov.

[124] A. Sytov et al. 'Geant4 simulation model of electromagnetic processes in oriented crystals for accelerator physics'. In: *Journal of the Korean Physical Society* 83 (2023), pp. 132–139. DOI: 10.1007/s40042-023-00834-6.

[125] A. Sytov et al. 'New full simulation model of crystal-based beam extraction using BDSim toolkit enhanced with Geant4 G4ChannelingFastSimModel'. In: *arXiv preprint* (2024). DOI: 10.48550/arXiv.2412.10715. arXiv: 2412.10715 [physics.acc-ph].

[126] J. Bernhard et al. *CERN Proton Synchrotron East Area Facility: Upgrades and Renovation during Long Shutdown 2*. Ed. by J. Bernhard. Vol. 4/2021. CERN Yellow Reports: Monographs. Geneva: CERN, 2021. DOI: 10.23731/CYRM-2021-004. URL: http://cds.cern.ch/record/2792490.

[127] D. Banerjee et al. *The North Experimental Area at the CERN Super Proton Synchrotron*. Tech. rep. CERN-ACC-NOTE-2021-0015. CERN Internal Note. Geneva: CERN, 2021. URL: https://cds.cern.ch/record/2774716.

[128] CERN. *Super Proton Synchrotron (SPS) — CERN Grey Book*. https://greybook.cern.ch/researchProgram/detail?id=SPS. Accessed: 2025-10-21.